Broadband Waveform Modeling over a Dense Seismic Network

Thesis by

Ying Tan

In Partial Fulfillment of the Requirements
for the Degree of
Doctor of Philosophy

Caltech
Pasadena, California

2006
(Defended April 17, 2006)

Acknowledgements

My stay at Caltech has been a pleasant journey, a rewarding experience, and a period of growth. I feel myself lucky to come to Seismo Lab in 1999. Since then, the broadband TriNet has expanded rapidly, without which this thesis would have been impossible.

I am very grateful to my advisor, Don Helmberger for his enthusiasm in whatever I did, his patience with me, his steady support and fathering care. Don introduced me to the broadband seismology and taught me to appreciate the beauty of the intricacies of seismograms. The excitement that Don radiates when he looks at seismograms has greatly influenced me and I am now becoming a waveform master under his guidance. Hiroo, my academic advisor, deserves my special thanks for being a constant source of help. Egill Hauksson provided me assistance with focal mechanisms and stress inversion. The other Seismo Lab faculty, Don Anderson, Joann Stock, Rob Clayton, Mike Gurnis and Mark Simons have showed me a broad view of geophysics.

I thank the people who ignited my early interest in geophysics during my undergraduate study. They are Xiaofei Chen, Jieyuan Ning, Shaoxian Zang and Liangbao Zhu at Peking University in China. Xiaofei guided my undergraduate thesis and has been a supportive friend.

Hiroo Kanamori, Joann Stock, Paul Asimow and Jeroen Tromp provided careful reviews and thoughtful comments of the whole thesis. Joann and Paul made tremendous corrections for my initial manuscript, which I truly appreciate.

Lupei Zhu, Chen Ji and Sidao Ni have provided me technique support and friendship over the years. I miss the meals at their homes.

I wish to thank Evelina Cui, Viola Carter, Elisa Loeffen, and all other Seismo Lab staff for their support and back-stage work which has made the Seismo Lab such a wonderful place.

My officemates Deborah Smith, Partria Persaud, Chen Ji, Ali Ozgun Konca, Min

Chen and Nathan Downey helped me in every aspect. My fellow students Eh, Anita, Yaru, Vala, Bruce, Brian, Anu, Sarah, Kaiwen, Qinya, ... are always fun to talk with.

Friendships outside the division has enriched my life through the years. I thank Xiaohui Gu, Jun Xie, Sijia, Yu Xiao, Hui Wu, Ming Gong, Dai Lu, Fu Liu, ... for sharing the hilarity and sadness.

Finally, I am in debt to my parents and my dear husband, Zhigang, for their support and love. They convinced me I could do anything I wanted to.

Abstract

We developed a "two-way" calibration technique for studying clustered events, particularly their mechanisms and rupture directivities. First, we demonstrate that the magnitude 4 events with known source mechanisms can be used to calibrate the path effects on the short-period (0.5-2 sec) P waves, so that the corrected P waves can be modeled for determining focal mechanisms of the smaller events within the cluster. The correction is formulated in terms of a station-specific "Amplitude Amplification Factor" (AAF), whose origin is mainly due to the site effect. Second, we show that the smaller events with radiation pattern corrections provide excellent empirical Green's functions (EGFs) for investigating the detailed rupture processes of the magnitude 4 events. In particular, we applied our methods to the 2003 Big Bear sequence. Our main results indicate that (1) Short-period (0.5-2 sec) P waves can be used for determining focal mechanisms of events as small as $M \sim 2$, provided necessary path calibration. (2) Magnitude 4 events display various detailed rupture processes.

A new technique CAPloc to retrieve full source parameters of small seismic events from regional seismograms is developed, which include origin time, epicenter location, depth, focal mechanism, and moment magnitude. Despite rather complicated propagation effects at short periods, a simple localized 1-D model can well explain signals of periods 3–10 sec if we break the three-component records into different segments and allow differential time shifts among them. These differential time shifts, once established from a calibration process or a well-determined tomographic map, can be used together with P wave travel times to refine an event's location. In Chapter 3, we tested whether our new method could produce satisfactory results with as few as two stations, so that we can improve source estimates of poorly monitored events with sparse waveform data. We conducted the test on 28 events in the Tibetan plateau. The focal mechanisms and locations determined from only two stations agree well with those determined from a whole PASSCAL array. In particular, our new method produces better locations than ISC, with the average mislocation error reduced from ∼16 km to ∼5 km. We also tested whether an event's depth and mechanism can be determined separately from its epicenter relocation in a two-step approach. We find that the two-step approach does not always give the correct solution, but the reliability of a solution can be evaluated using a reduced chi-square value.

We use 49 Tonga-Fiji events recorded at the broadband TriNet array, southern California to develop a pure path upper-mantle shear velocity model. At the epicentral distances of 70°–95°, multi-bounce S waves up to S^5, including the guided waves, such as "G-phase", are observed. Since these S wave multiplets bottom out at different depths, simultaneously modeling their differential travel times and waveforms provides strong constraints on the radial velocity structure. We parameterize the velocity model according to *a priori* information from the previous oceanic models, so that we can take a grid-search approach, to fully investigate possible interdependencies among the model parameters. This also allows us to well resolve the main characteristics of the model. We use both the SH and SV components with the synthetics constructed by a reflectivity code. Our preferred model $PAC06$ contains a fast lid (V_{sh} = 4.78 km/sec, V_{sv} = 4.58 km/sec) ∼60 km thick. The underlying low velocity zone (LVZ) is prominent with the lowest velocities V_{sh} = 4.34 km/sec, and V_{sv} = 4.22 km/sec. Besides the 406 km and 651 km discontinuities, $PAC06$ also has a small (∼1%) velocity jump at ∼516 km. We consider these main features of $PAC06$ to be well determined, since $PAC06$ explains a large data set from various events. Therefore, it is ideally suited for comparing with mineralogical models.

Contents

List of Figures

List of Tables

Chapter 1

General Introduction

Seismicity in southern California has been some of the highest in the world, which provides a natural laboratory for studying different types of earthquakes in a variety of tectonic settings. The era of broadband seismometers in southern California began in 1991. However, the broadband stations were rather sparse in the early years. Since 1999, the number of stations has increased rapidly, due to the beginning of the modern, dense, digital broadband network–TriNet. At the time of writing this manuscript, TriNet comprises over 150 three-component broadband stations.

The major advantages of having broadband, high dynamic range data have been well demonstrated in the early efforts of modeling these records. First, the broadband records enable one to identify a large number of arrivals by their frequency content, which greatly helps in understanding the velocity structure. Second, the broadband instruments of high dynamic range enable on-scale recordings of motions spanning several orders of magnitude, which allows one to relatively separate the source and propagation effect by simultaneously examining main shock and aftershocks. However, due to poor station coverage, these early studies were limited to certain paths and events. Moreover, the waveform modeling was mainly conducted at relatively long periods (>5 sec).

The rapid expansion of the TriNet array has afforded applications of the earlier developed techniques a much larger data set. Such an example is given in Fig. 1.1, where we have retrieved the source parameters of 159 earthquakes that occurred between 1998 and 2004 with the so called "cut and paste" source estimation technique (e.g., *Zhao and Helmberger*, 1994; *Zhu and Helmberger*, 1996). In particular, we break an entire record into *Pnl* and surface wave segments, and model them separately. Since differential time shifts between the principal crustal arrivals are allowed, accurate

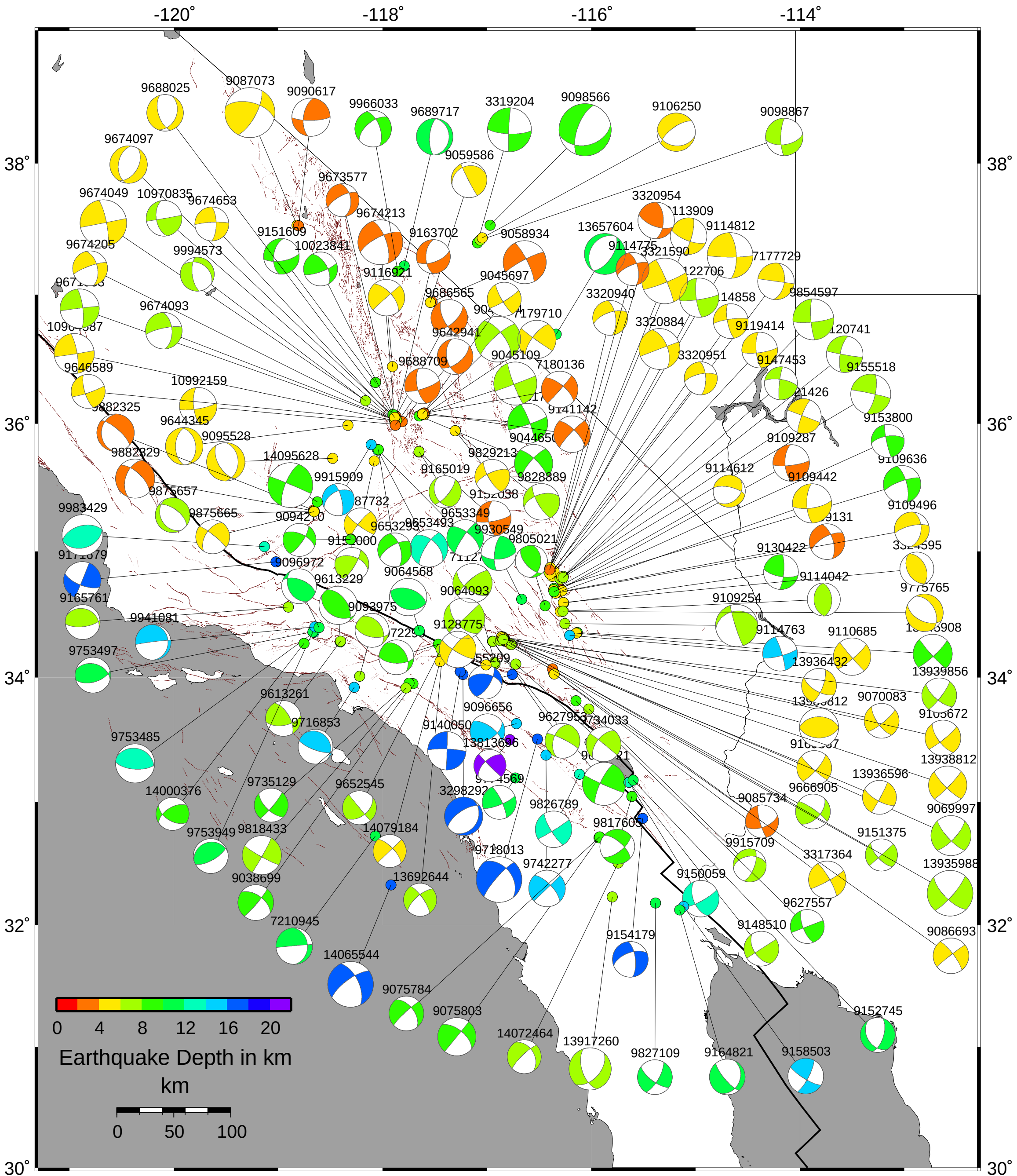

Figure 1.1: The depths and focal mechanisms of 159 recent southern California events. The detailed source parameters are given in appendix A.

source estimates could be achieved with imperfect Green's functions. Correspondingly, a byproduct from the source inversion is the path-specific phase delays of *Pnl* and surface waves.

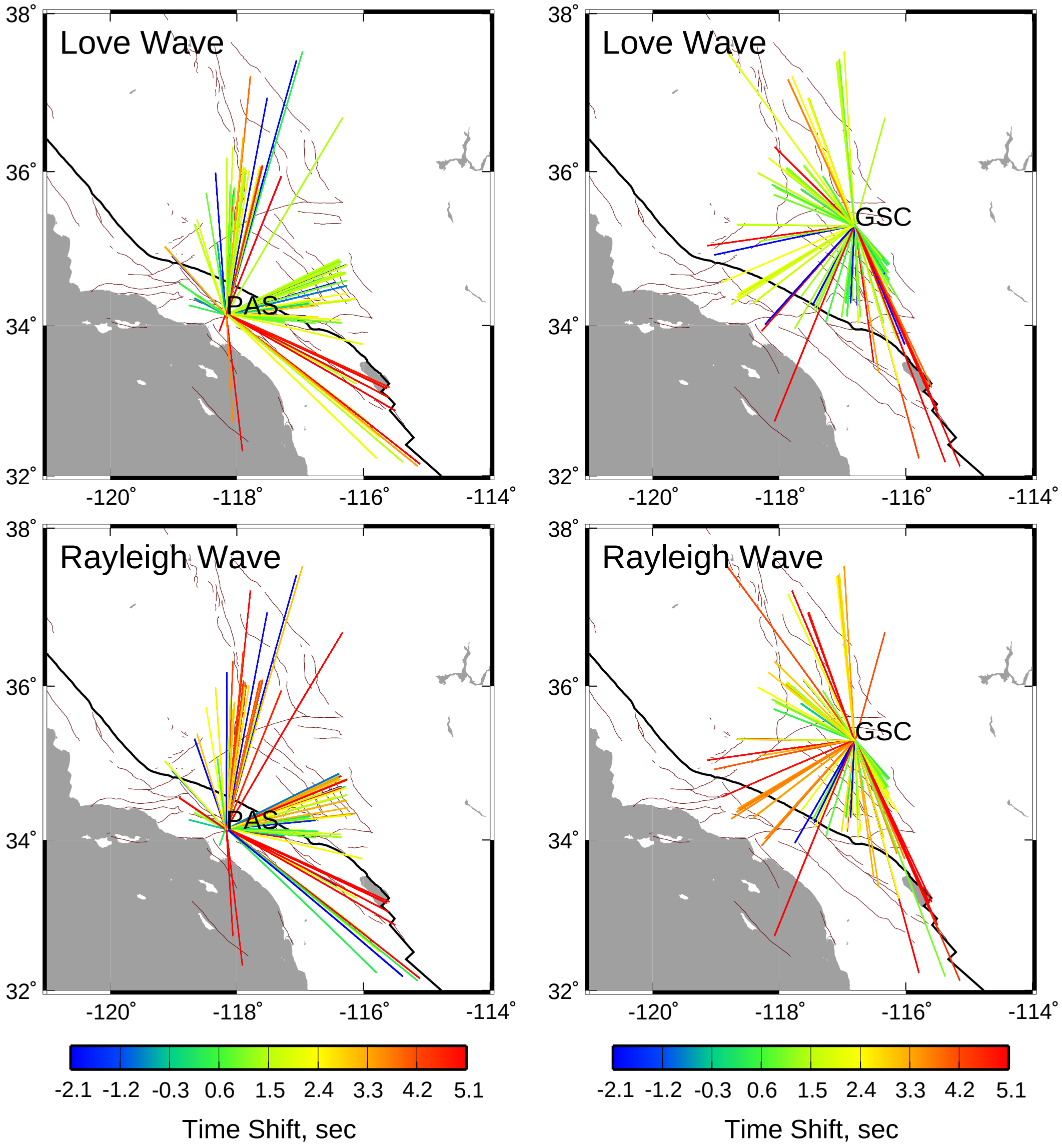

Figure 1.2: The phase delays of the surface waves at the two stations PAS (left) and GSC (right) from all the events shown in Fig. 1.1. Positive values indicate the data are slower than the synthetics while negative values mean the opposite.

Fig. 1.2 displays the Love and Rayleigh wave phase delays at two stations PAS and GSC from the events in Fig. 1.1. Note the good coverage and the stability of the time shifts along similar paths, which indicates these phase lags provide useful path calibration. An application of such path calibration for locating and modeling a regional event with sparse waveform data is detailed in chapter 3 of this thesis, where the new technique is developed and tested on the poorly monitored Tibetan plateau. However, the method is rather suited for studying historic events in southern California. The two stations PAS and GSC are of particular interest since they have been the sites for seismometers since the 1950s and the early long-period analog records from these stations are being digitized for source inversions.

Although retrieving source mechanisms of magnitude ∼3.5 or above events has become a routine process with redundant waveform data from the dense TriNet array, smaller events can hardly be addressed by such long period (>5 sec) inversions due to the poor signal to noise ratio. Besides, the second-order source characteristics of the magnitude 4 events, such as fault finiteness and rupture directivity, remain unresolved in the long-period frequency band. However, these are the key parameters for understanding the physics of earthquakes.

An effective way to address these problems is to model waveform data at shorter periods. However, the unmodeled structural effect often gets overwhelming, where one has to face the inherent trade-offs between source complexity and structural heterogeneity. Under such circumstances, analyzing clustered events of different sizes provides a practical way to "separate" the source from the structural effect. Fig. 1.3 displays a typical comparison between the records at the same station GSC from three clustered events. These events are all from the 2003 Big Bear sequence. The records from the two smaller events are dominated by noise in the long-period (5∼20 sec) frequency band, but all the three events display very similar signals in the higher frequency bands. This implies propagation stability along the path. Although what has caused the complexity is unclear, the most important information conveyed in Fig. 1.3 is the possibility of a "two-way" calibration process. First, we can use the magnitude 4 event with the known source mechanism to calibrate the path effect on short-period records, so that smaller events can be studied. Second, the smaller events can provide perfect empirical Green's functions for studying the detailed rupture process of the big event. Chapter 2 of this thesis details such a technique with the application to the 2003 Big Bear sequence. Although we only address events with magnitudes 2 and above, the same methodology has a potential for even smaller events (see Fig. 1.3).

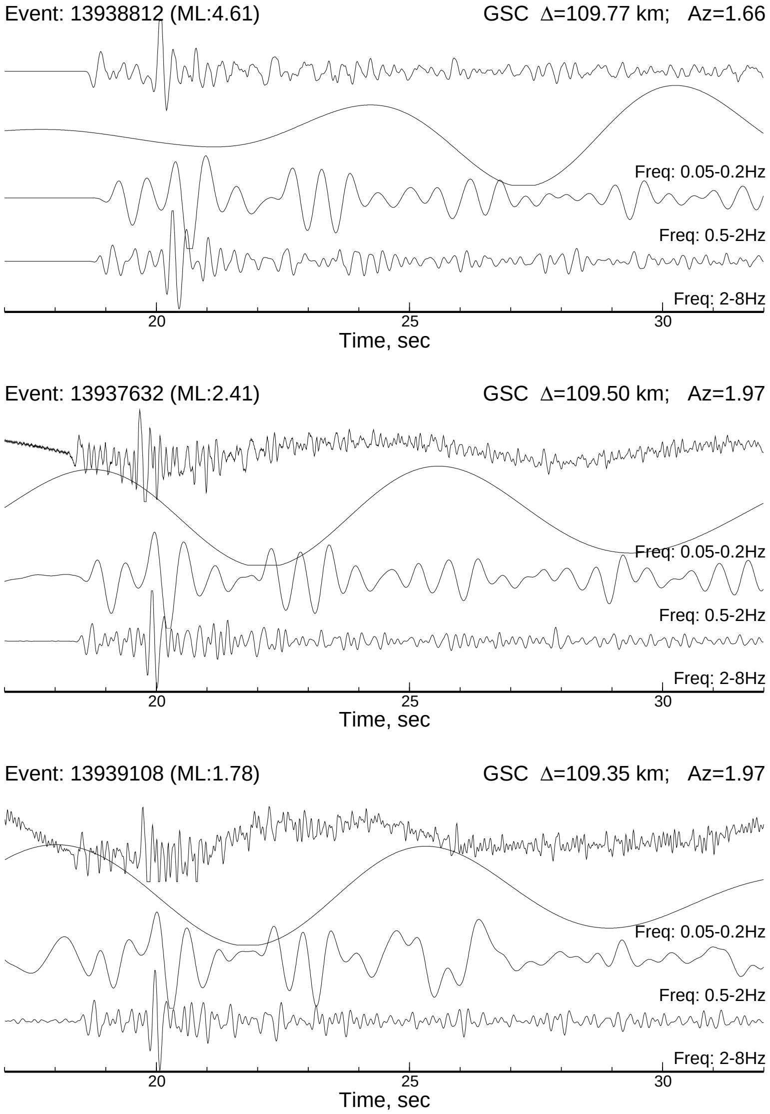

Figure 1.3: Comparison of the records from three clustered, but different-sized events at station GSC. For each event, the four traces shown from top to bottom are the original vertical component broadband record, and the filtered records featuring different frequency bands.

Although not addressed in this thesis, modeling regional broadband waveform data can cast light on resolving fine-scale crustal complexities. For example, we display in Fig. 1.4 a profile of broadband *Pnl* waves along a corridor from Big Bear

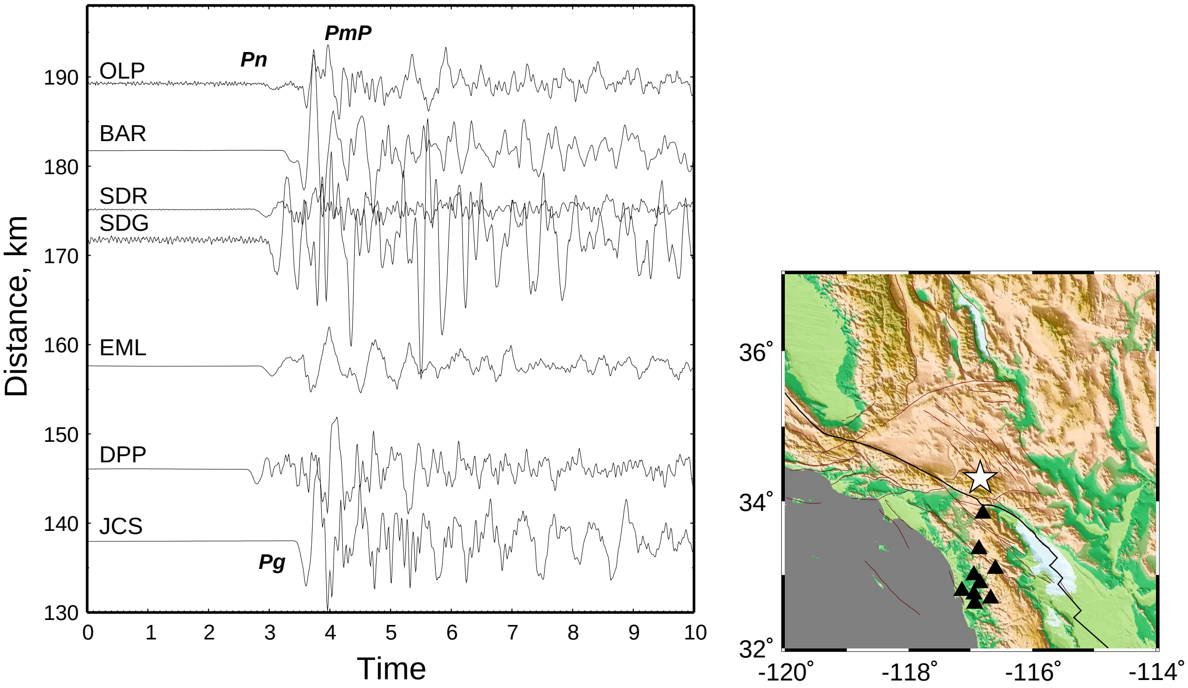

Figure 1.4: The reduced record section with a P velocity of 7.0 km/sec along a particular azimuth ($\sim$ 180°). The locations of the source (star) and the stations (triangles) are given to the right.

to San Diego. Although the waveforms become quite similar at long periods (>5 sec), they display large discrepancies at shorter periods, which indicates fine-scale crustal heterogeneities beneath the stations. Note the rapid changes in the combination of Pg, Pn, and PmP from station to station. To model these records requires accurate identification of the complicated arrivals, where a profile from clustered events as shown in Fig. 1.5 can greatly facilitate the effort.

Chapter 4 addresses an application of the teleseismic data recorded at TriNet. In particular, we modeled the multi-bounce S waves and developed a pure path upper-mantle shear velocity model for the corridor connecting the Tonga-Fiji source region to southern California. In this study, the broadband nature of the records has enabled extensive observations of the triplications or interferences of the higher order S multiplets, which provide a tight constraint on the details of the velocity structure. Moreover, the dense array produces coherent seismograms and greatly

Figure 1.5: The vertical component records at station DPP from the clustered events of the 2003 Big Bear sequence. The traces are ordered with the separations between P and PmP (measured by waveform cross correlation) increasing from top to bottom. Note the Pn phase changes sign for the thrust events due to the radiation pattern effect.

facilitates identifications of the subtle triplicated branches.

Chapter 2

A Waveform Cluster Analysis–Application to the 2003 Big Bear Sequence

2.1 Introduction

Unmodeled structural heterogeneity presents great difficulty in determining accurate locations and mechanisms of seismic events. Recently, the relative location of earthquakes has taken a quantum jump in resolution as differential travel time measurements between "similar" event pairs are effectively used to minimize the structural heterogeneity effect, and waveform cross-correlation methods substantially reduce measurement errors (e.g., *Waldhauser and Ellsworth*, 2000; *Schaff et al.*, 2004). The relocated events reveals fine fault images at depth with unprecedented resolution, which enables people to estimate fault zone width, to identify large voids in seismicity for future hazard assessment, to study repeating earthquakes and to learn foreshock and aftershock behaviors (e.g., *Waldhauser and Ellsworth*, 2002; *Schaff et al.*, 2002; *Zanzerkia et al.*, 2003). Moreover, the seismicity-defined planes, when associated with high quality focal mechanisms, can resolve the primary and auxiliary fault plane ambiguity, and provide unique information on deformation and stress states (e.g., *Waldhauser and Ellsworth*, 2002; *Prejean et al.*, 2002; *Kilb and Rubin*, 2002; *Shearer et al.*, 2003). However, discrepancies between focal planes and seismicity planes are widely noted in these studies, particularly in diffuse zones of deformation. To determine whether this is due to inaccurate focal mechanisms or whether the seismicity plane actually differs from the slip plane as suggested by *Shearer* (1998), requires reliable focal mechanisms of the clustered events. Moreover, in cases of complicated fault geometry, estimates of fault finiteness or directivity are highly desired.

Accurate source mechanisms of seismic events with $M_w \sim 3.5$ or greater can be easily determined from long-period (>5 sec) inversions of complete broadband waveforms (e.g., *Zhu and Helmberger*, 1996; *Liu et al.*, 2004), even if only sparse data are available (e.g., *Tan et al.*, 2006). However, the same strategy becomes less effective when applied to smaller events due to very low signal to noise ratio (SNR). These smaller events are particularly important to image small scale variations of stress field spatially and temporally due to their prevalence and frequent occurrence, whose mechanisms are generally obtained with focal plots from P-wave polarities (e.g.,FPFIT by *Reasenberg and Oppenheimer*, 1985; *Hardebeck and Shearer*, 2002). Since only the binary up or down of the P-wave first motions counts in these methods, a dense sampling of the focal sphere is required to form a reliable solution.

Adding amplitude information provides a way to relax the requirement on station coverage, although several corrections must be made for event magnitude, geometrical spreading, attenuation and station site effects. Early work based on simple calculation demonstrated the feasibility of determining an earthquake focal mechanism using short-period amplitude ratios of P and S waves or their absolute amplitudes (e.g., *Kisslinger*, 1980; *Kisslinger et al.*, 1981; *Ebel and Bonjer*, 1990). A later result by *Rau et al.* (1996) showed the improvement on the focal mechanism solutions of adding SH/P amplitude ratios as constraints over using P-wave polarities alone, when the attenuation effects were appropriately corrected. *Nakamura et al.* (1999) also reported success in recovering a large set of spatially coherent focal mechanisms in Japan using absolute amplitudes of P and S waves with an “amplitude station correction function”, although the resulted misfit reduction was not satisfactory. They attributed the large misfit error to short-wavelength crustal heterogeneity. The recent work of *Hardebeck and Shearer* (2003), however, raised some concern, where they reported considerable “noise” in the observed S/P ratios for the “similar” event clusters in Northridge and Anza region, California, which limited the usefulness of the S/P ratios in determining focal mechanisms. More work is therefore needed to understand the propagational distortion on P or S waves and to use this information for improving focal mechanism determination.

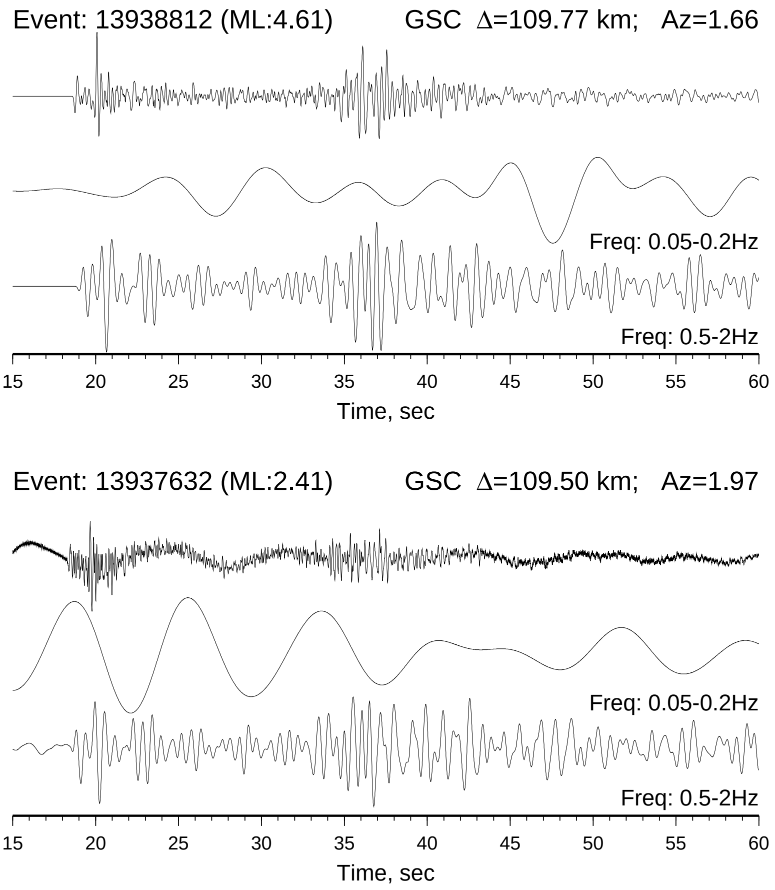

Figure 2.1: This figure compares the waveforms from two events of different magnitudes indicating the strength of both events in the short-period (0.5 to 2 Hz) band where the calibration will be made. The strong second arrival after the direct P wave is the Moho reflection P_mP.

Our strategy in this study is to analyze spatially clustered events; moreover, rather than focus on short-period amplitude measurements, we pay attention to broadband waveforms. Figure 2.1 gives an example of the broadband records at the same station (GSC) for two events of different sizes (M_L:4.61 vs. 2.41). The two events are located within ∼50 m of each other using hypoDD (*Chi and Hauksson*, 2006). The record of the smaller event is contaminated by noise in the long-period (5-20 sec) frequency band; however, the two events display very similar signals in the higher frequency band (0.5-2 sec). This implies propagational stability along the path, although how much of the complexity is caused by the entire path *vs.* locally near the station site is not known. The frequency band of 0.5-2 sec is shorter period than those used in waveform cross-correlation for travel time measurements (e.g., *Schaff et al.*, 2002). However, it proves optimal for understanding structure and radiation pattern effect on waveforms from different-sized events, since small events with M_L down to ~2.0 still have good SNR, while detailed rupture processes of bigger events are filtered out. Analyzing clustered events of different sizes is a practical way to "separate" the structure and source effect, in that the bigger events ($M_w > 3.5$) with source mechanisms well determined from long-period inversions can be used to study the structural effect and probably calibrate paths for determining focal mechanisms of smaller events. Conversely, the smaller events with known focal mechanisms provide excellent empirical Green's functions (EGF) for retrieving rupture processes of the bigger events.

The purpose of this study is to demonstrate such a "two-way" calibration process using waveform data from an event cluster. We select the 2003 Big Bear sequence (see Fig. 2.2) as the example, since there are several events with well-determined long-period solutions. Because these events occurred in the center of the southern California TriNet array, they were generally well recorded. Also note in Fig. 2.2 a number of other seismic zones suitable for such a waveform cluster analysis. In the following, we will begin with a brief review of the long-period (>5 sec) inversions for retrieving reliable source parameters of magnitude 3.5 or above events. Then we will focus on the short-period (0.5–2 sec) path calibration and derive a source inversion algorithm of short-period P wave waveforms with appropriate amplitude corrections. The results will be discussed in the remaining sections, featuring different aspects, including the stress inversion, seismic moment–magnitude scaling, source duration and stress drop, and rupture directivity.

2.2 Long-period inversions

Six events in the cluster (Fig. 2.2) have adequate SNR for long-period inversions of complete seismograms. The method we use is the "cut and paste" source estimation

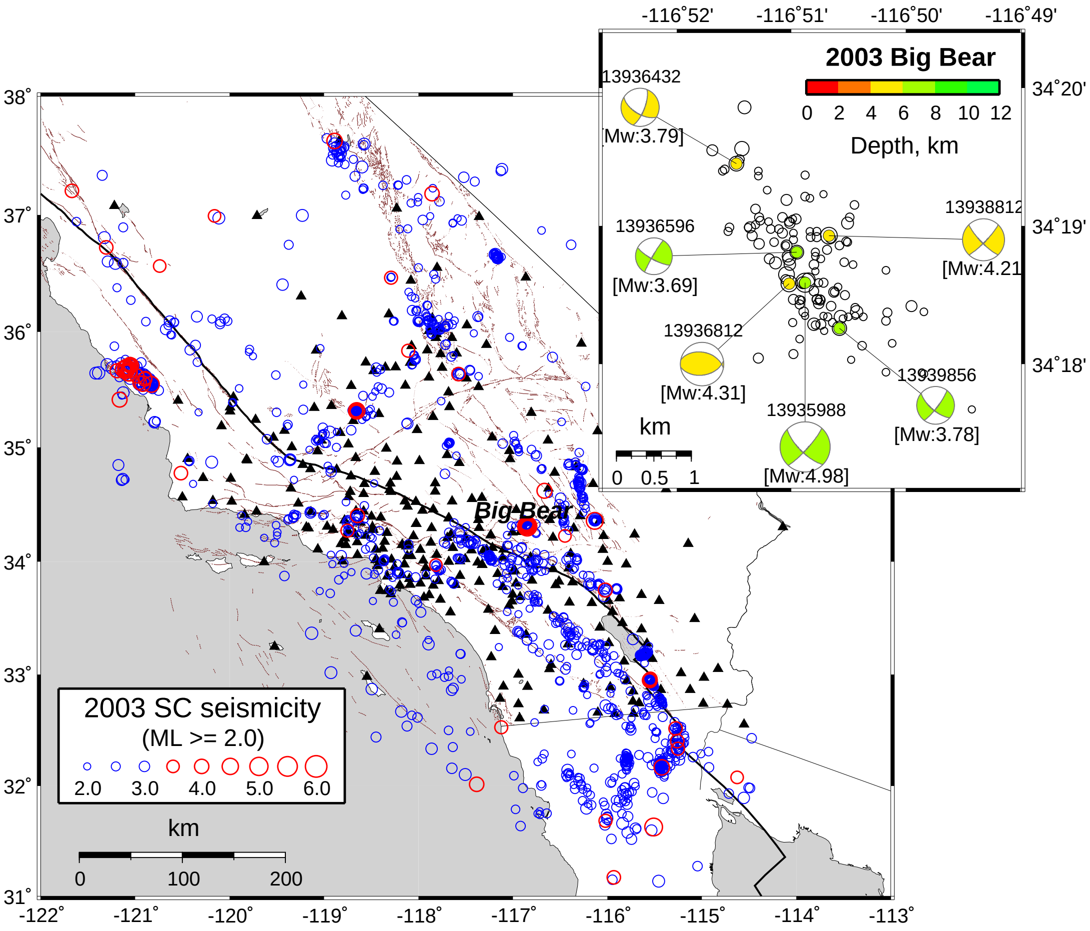

Figure 2.2: Earthquakes in the year 2003 (circles) along with the broadband TriNet stations (triangles). An enlarged Big Bear region is included with the mechanisms of events larger than Mw > 3.5.

technique by *Zhu and Helmberger* (1996). The Green's functions are computed with a reflectivity code (*Zhu and Rivera*, 2002), assuming the 1D southern California (SC) model (*Dreger and Helmberger*, 1993). One of the advantages of this technique is that it allows differential time shifts between different phase groups, mainly the *Pnl* and surface waves; hence, accurate source estimates can be obtained with imperfect Green's functions. Recently, *Tan et al.* (2006) (Chapter 3 of this thesis) enhanced the technique for sparse data sets by introducing an adaptive weight between *Pnl* and surface waves. However, since we generally have such a dense coverage with over 100 stations here, we simply weight *Pnl* waves by 2 over the surface waves following *Zhu* *and Helmberger* (1996).

The depths and focal mechanisms of the six events are displayed in Fig. 2.2. Among them, the main shock (13935988) was also investigated by *Liu et al.* (2004) using a 3D model. Their result of the source parameters agree well with ours. Some selected waveform fits for this event are displayed in Fig. 2.3, where those from the thrust aftershock (13936812) are also included for comparison. It is worth mentioning that the waveform data distinguish the pure thrust (13936812) from the strike-slip mechanism (13935988). However, the first motion focal mechanisms of the two events both contain a significant strike-slip component (*Hauksson*, 2000). We also performed the inversions using Pnl or surface waves alone. The results with these data subsets agree very well with the solutions using both Pnl and surface waves, which indicates the robustness of the resolved source parameters, and also the data redundancy, with over 100 stations. The latter warranted our effort in the next two sections to use a further reduced data set of only the direct P waves. As we will see, about 10 stations would suffice for the task.

A byproduct from the long-period waveform inversion is the phase delays of the Pnl and surface waves plus the corresponding cross-correlation (cc) coefficients sampling different paths. The phase delays are measured by waveform cross-correlation as the time shifts of the synthetics relative to the observations, where a positive shift means data is slower (see Fig. 2.3). For an example, we display in Fig. 2.4(a) the Love wave phase delays and the cc values from the main shock 13935988. Note in Fig. 2.4(a) a large number of paths show cc values above 90, while the poorer fits mainly occur when the geological boundaries are encountered, such as the paths into the Los Angeles basin and the Imperial Valley. These complex paths (cc < 90) are of great interest for understanding sharp structural heterogeneities; however, we simply discarded them in the inversion of source mechanisms.

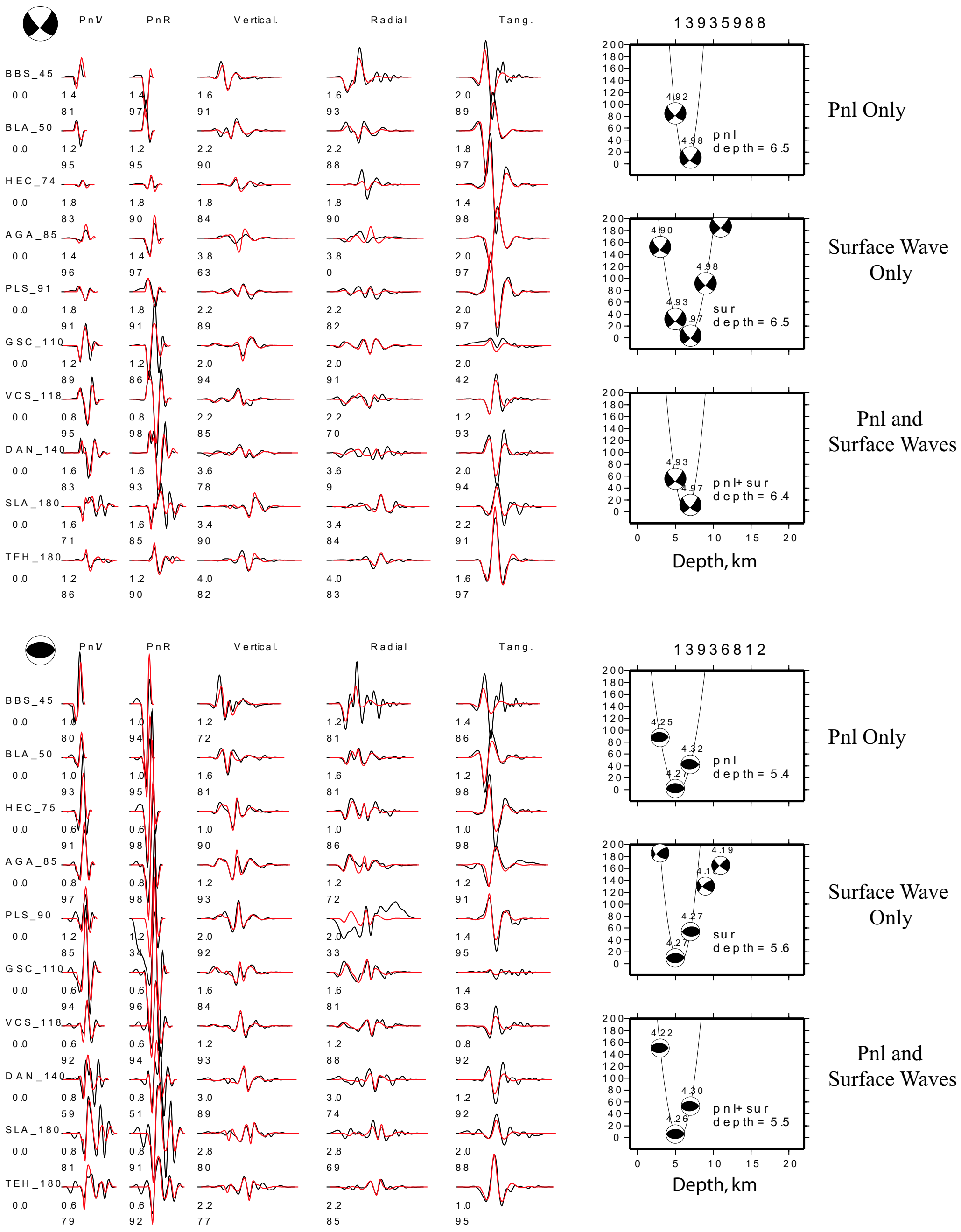

Figure 2.3: Comparison of the modeling results for two events with distinctly different focal mechanisms. The hypocenters of the two events are within 0.5 km. Over 100 records, 10 shown here, sample the entire radiation pattern. The two rows of numbers below the traces are the time shifts of the synthetics relative to the observations and the corresponding cross-correlation coefficients. The column on the right shows the inversion results using *Pnl* (only), surface waves (only) and together on the bottom. Low-pass filters with corner frequencies of 0.2 Hz and 0.1 Hz are applied to *Pnl* and surface waves respectively.

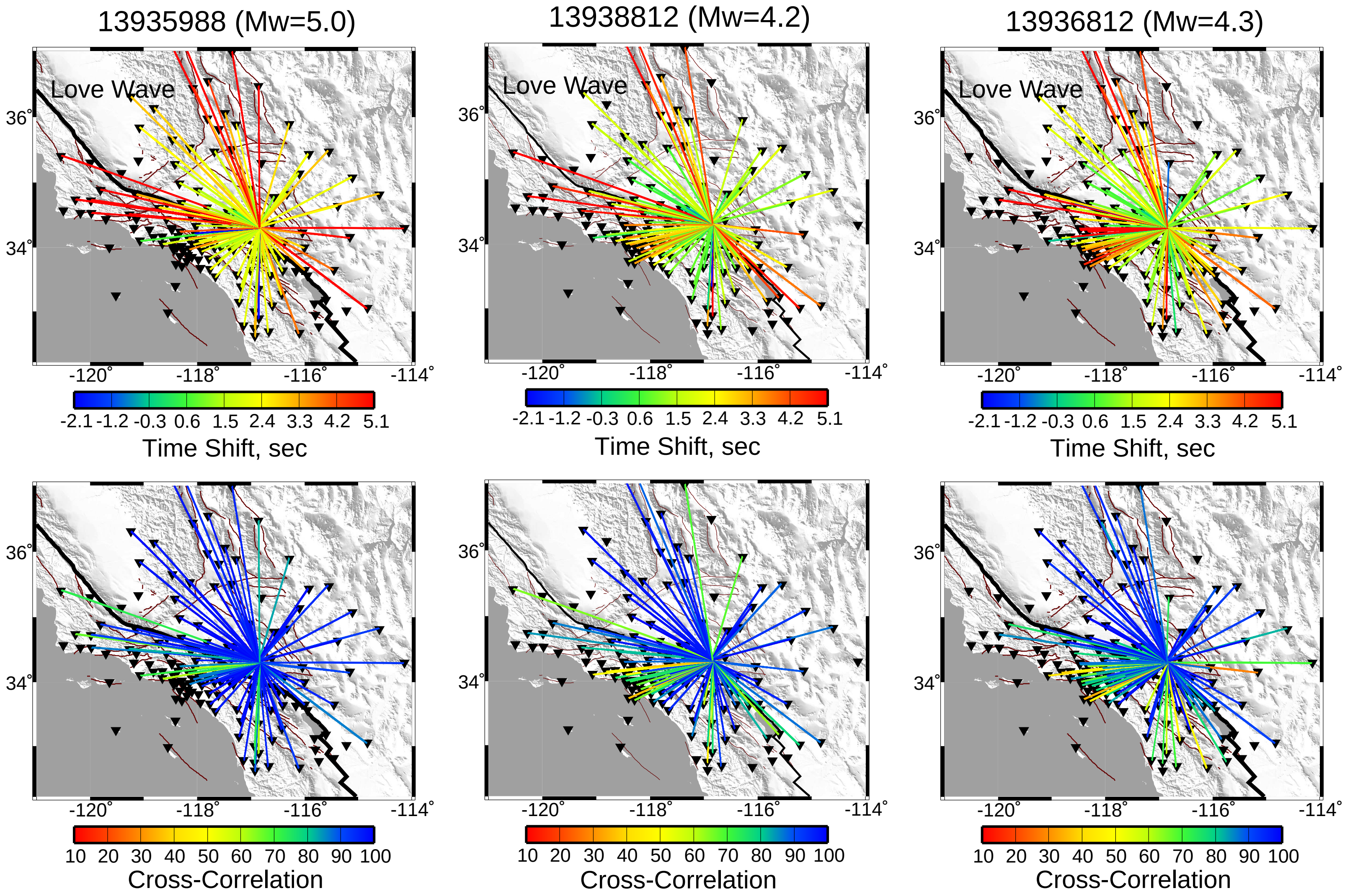

(a) (b) (c)

Figure 2.4: Love wave phase delays derived from three clustered events, 13935988, 13938812, and 13936812 (top) together with corresponding cross-correlation values (bottom).

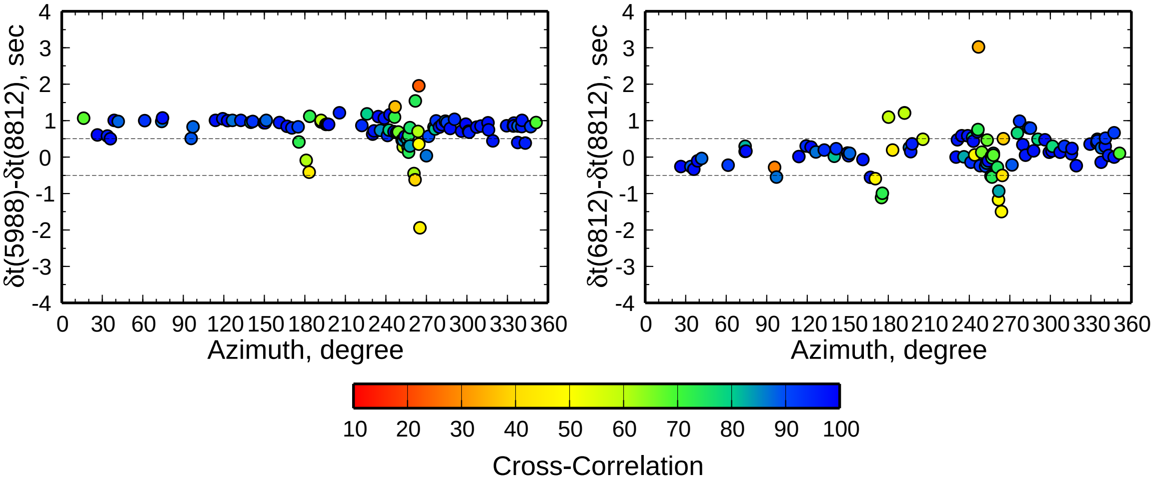

Figure 2.5: Comparison of the differential Love wave phase delays between the two events 13935988 and 13938812 (left), 13936812 and 13938812 (right).

Zhu et al. (2006) and *Tan et al.* (2006) demonstrated that the surface wave phase delays could be turned into tomographic maps or used as empirical path-specific corrections for locating and determining the source mechanism of a regional event with a very sparse data set. Occasionally, the phase delays can also be indicative of source complexity. Such an example is given in Figs. 2.4 and 2.5, where the Love wave phase delays derived from the three clustered events are compared. The three events (see Fig. 2.2) are located within 1 km × 1 km × 1 km. Two of them (13935988 and 13938812) are strike-slip events, while the third (13936812) is a pure thrust event. The Love wave phase delays from the three events display similar azimuthal variations. Although there is some scatter, the phase delays from the main shock 13935988 are consistently larger than those from the two aftershocks by over 0.5 sec. The discrepancy becomes more clear when we calculate their differences at the same stations (Fig. 2.5). The lack of obvious azimuthal patterns of these differential phase delays confirms that the events are well located relative to each other. The scatter is mainly due to fine-scale features in the observed Love wave waveforms of major frequencies of $\sim$ 8–16 sec. It tends to be smaller when the two events of similar source mechanisms are compared, suggesting it might be caused by 3D propagation effects excited differently for different source types.

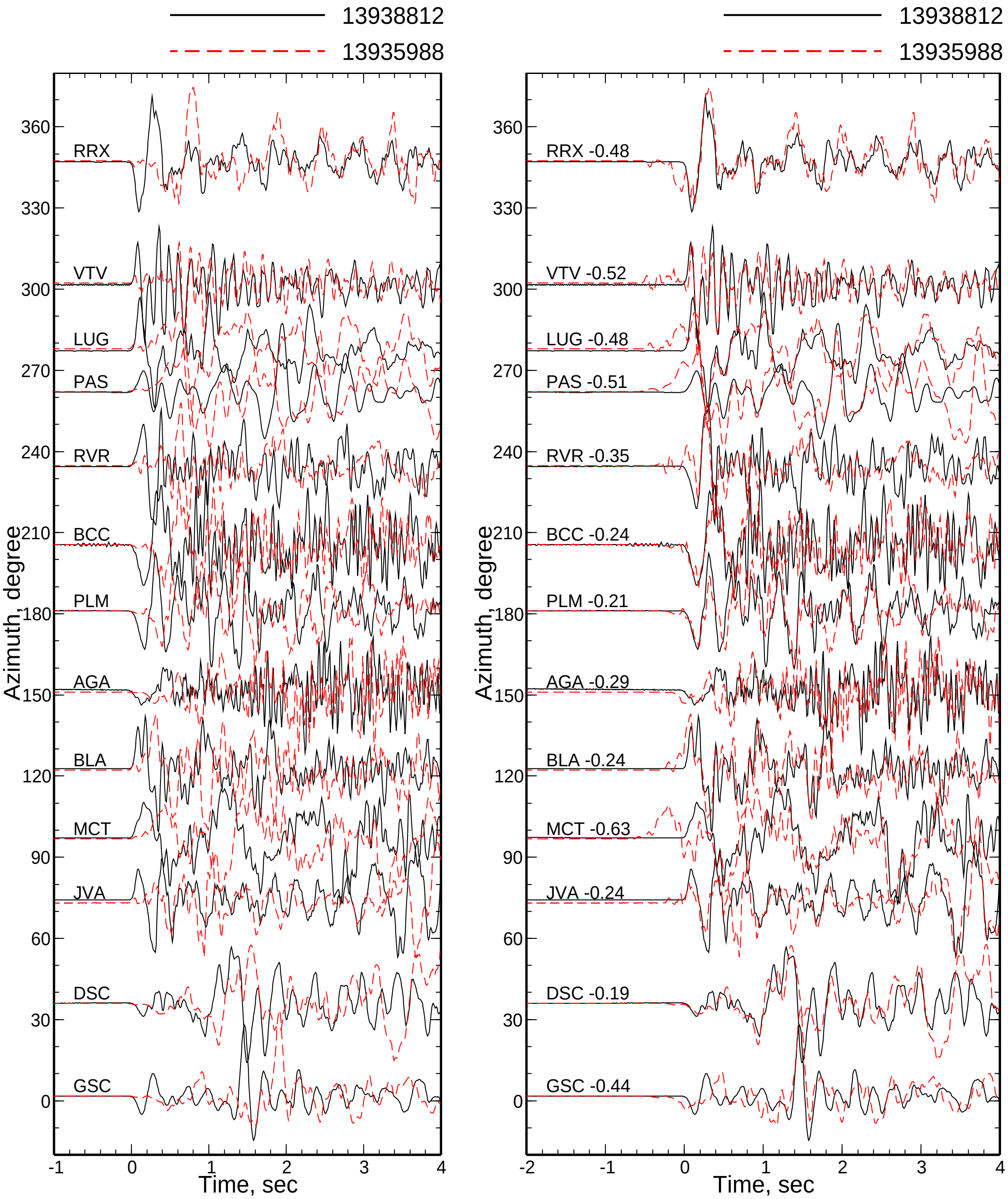

Figure 2.6: Comparison of the selected broadband records (vertical component, $\Delta <$ 100 km) from the main shock 13935988 (Mw $\sim$ 5.0) and the aftershock 13938812 (Mw $\sim$ 4.2). Plotted are the normalized amplitudes. In the left panel, the records from both events are aligned on their hand-picked first P arrival. In the right panel, the main shock records are shifted as determined by waveform cross-correlation, with the exact time shifts given after the station names.

Similar discrepancies between the phase delays from the main shock and the aftershocks are also observed for the *Pnl* and Rayleigh waves. In addition, *Liu et al.* (2004) noted unusually large time shifts were required to fit data with 3D synthetics when they studied the main shock source mechanism, which they simply attributed to an origin time problem. Besides a possible origin time offset, Fig. 2.6 reveals some more interesting contribution when we examine the broadband records directly. Note the two events compared in Fig. 2.6 have similar source mechanisms. However, there is always considerable mismatch between the major arrivals from the two events when we align the records on the first *P* arrival. The waveform cross-correlation suggests a small precursor embedded in the main shock rupture, which becomes invisible at long periods, but still causes time shifts. The apparent azimuthal pattern of the time shifts determined by waveform cross-correlation suggests that the mainshock rupture propagated towards the southeast on the NW-SE fault plane. However, future efforts are warranted to study the detailed rupture process.

This example underlines the importance of understanding the source process before we can calibrate the propagation effect, even at long periods. Therefore, the main shock (13935988) is discarded for the following short period investigation. Moreover, its long rupture time cannot be ignored in the frequency band 0.5–2 Hz.

2.3 Short-period path calibration

The idea of using magnitude 4 events with known source parameters to calibrate regional paths has been introduced earlier by *Song and Helmberger* (1998), where they attempted to build pseudo Green's functions by perturbing individual generalized ray responses from a 1D model. Here we restrict our attention to short-period (0.5-2 sec) *P* waves, since we plan to use these *P* waves (mainly P_g and P_n phases) for determining focal mechanisms of smaller events. Moreover, they are the parts of the seismograms that are most easily isolated and understood in terms of crustal complexity. For example, we compare in Fig. 2.7 the observed *P* waves (black) and the synthetics (red) for a strike-slip event (13938812). To avoid the waveform complexities that are

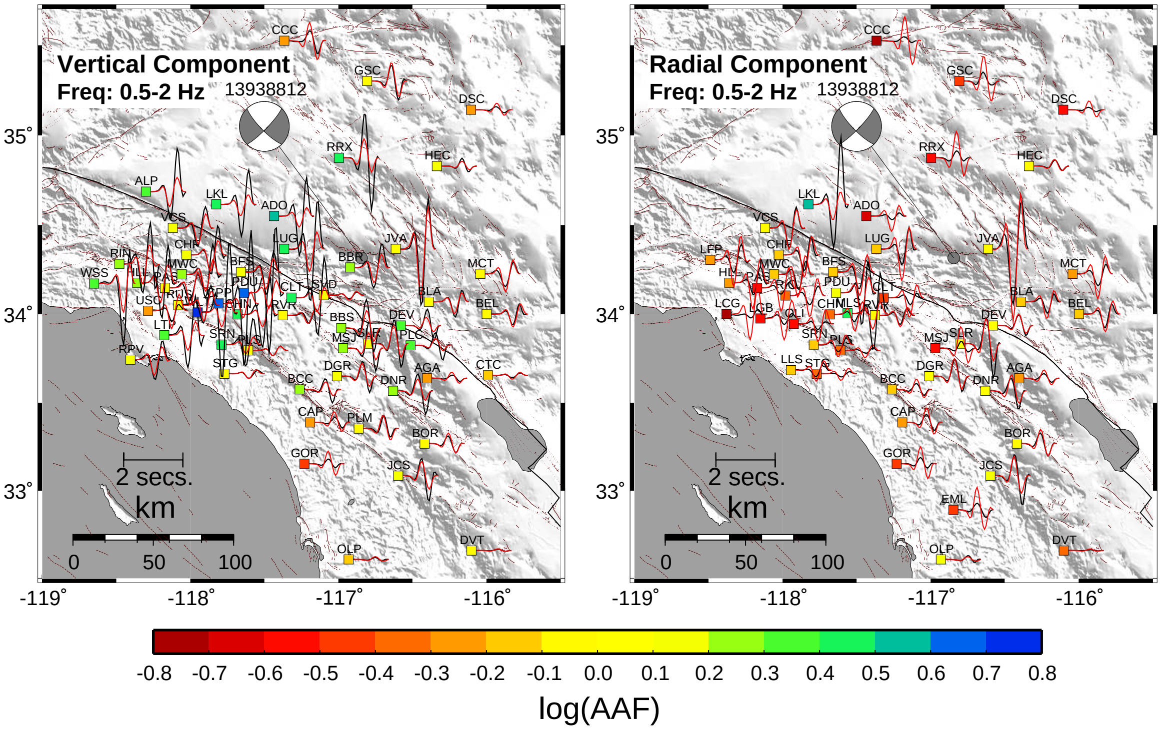

Figure 2.7: P wave comparison between the data (black) and synthetics (red) for a strike-slip event (13938812) on the vertical (left) and radial (right) components.

not easily explained at some stations, we simply discard them and concentrate on the high quality fits with cross-correlation values larger than 90. This resulted in a loss of about 1/3 of the recording stations; however, we still have good azimuthal coverage. A smoothed version of the SC model (Fig. 2.8) is used to calculate the synthetics with a reflectivity code (*Zhu and Rivera*, 2002), in order to simplify the high-frequency triplications associated with the layered boundaries. This smoothed SC model does produce an overall better fit to the observations. However, at long periods (e.g., >5 sec), the differences between the synthetics from the two models are hardly discernible. For simplicity, a 0.2 sec triangular-shaped source time function has been assumed, which fits the observed P-wave waveforms at most stations.

The discrepancies between the observed P waves and the synthetics (Fig. 2.7) are mainly manifested as amplitude differences. To quantify these, we define the function

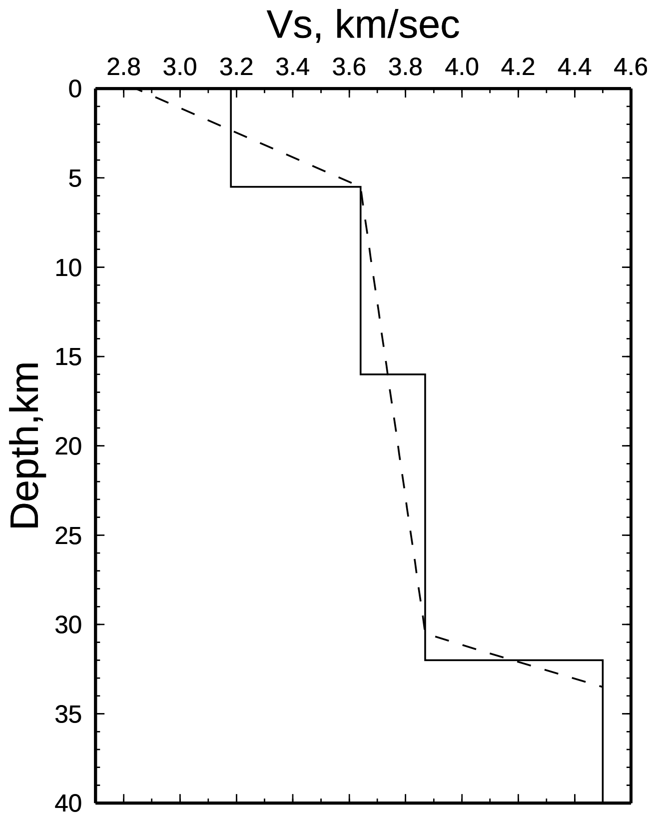

Figure 2.8: Comparison of the layered SC model from *Dreger and Helmberger* (1993) (solid line) and the smoothed one (dotted line) used in this study.

of "Amplitude Amplification Factor" (AAF) as

$$AAF = \sqrt{\frac{\int u^2(t)dt}{\int s^2(t)dt}}, \tag{2.1}$$

where $u(t)$ and $s(t)$ are the data and synthetics, respectively. It appears in Fig. 2.7 that the most anomalous AAFs occur at stations in the extended Los Angeles Basin. Particularly, these stations are consistently characterized by large AAFs (>1) on the vertical component, but small AAFs (<1) on the radial component. This discrepancy between the vertical and radial components has been noted by many previous investigators (e.g., *Savage and Helmberger*, 2004). They attributed it to a low velocity layer beneath the stations that bends the rays to be nearly vertical approaching the surface, hence greatly reducing the P wave strength on the radial component. There is also a tendency for the radial-component P waves to become broader and arrive late. Besides the "soft rock" sites in the basins, similar features are also observed at some other stations, even "hard rock" sites (e.g., GSC). However, the P wave radiation pattern is unfortunately blurred due to the laterally varying AAFs. So the AAFs have to be appropriately corrected before we can use these short-period P waves for determining focal mechanisms. Moreover, there are two key questions we need to answer: are the AAFs simply due to structural distortions independent of source mechanisms? and, secondly, are the AAFs relatively stable for the whole cluster?

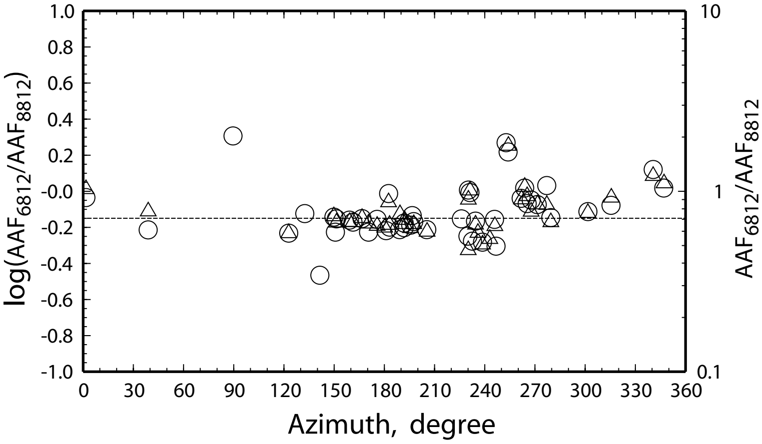

Figure 2.9: Comparison of the AAFs derived from the strike-slip event (13938812) and the thrust event (13936812) for the same stations. Shown are their log $log(AAF_{6812}/AAF_{8812})$ and linear AAF_{6812}/AAF_{8812} ratios *vs.* azimuth. The circles are for the vertical component while the triangles for the radial.

The few events in the cluster with known source mechanisms from long-period inversions enable us to address these questions. The three events (9069997: 1998/10/27, 01:08:40.6; 9070083: 1998/10/27, 15:40:17.1; 9105672: 1999/09/20, 07:02:49.2) that occurred within the cluster in the past are also included (see Fig. 2.11 (a)). As an example, we compare the AAFs derived from a strike-slip event (13938812) and the distinctly different thrust event (13936812) (Fig. 2.9). Although there is some scatter, the ratios between the AAFs at the same stations tend to follow a straight line, which supports the argument that the AAFs are independent of the source mechanism. The

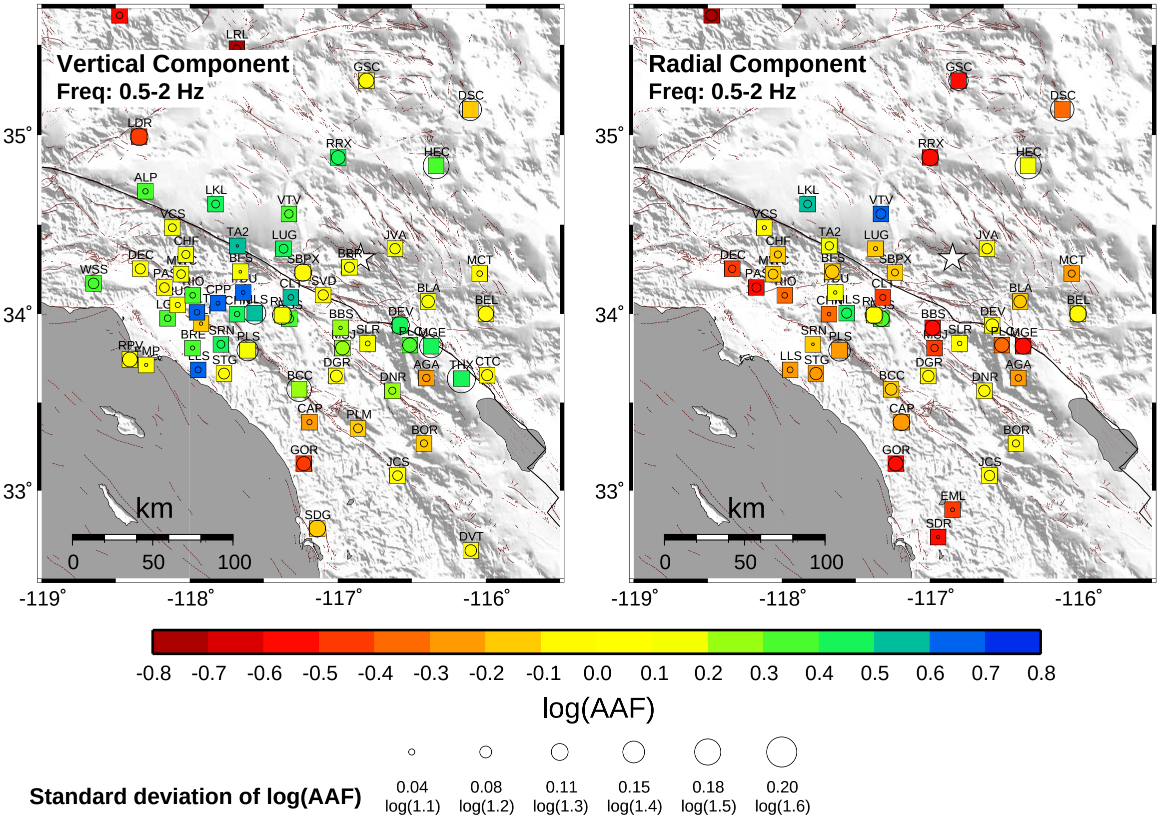

Figure 2.10: The averaged amplitude amplification factors (AAFs) for the vertical (left) and radial (right) components derived from the eight calibration events along with the standard deviations.

few outliers are mainly due to the P wave nodes of the events. The small offset of $\sim$ -0.15 in $log(AAF_{6812}/AAF_{8812})$ implies that the AAFs derived from the thrust event (13936812) are consistently smaller than those from the strike-slip event (13938812) by a factor of $\sim 30\%$, which suggests that the thrust event might have a relatively longer, but lower-amplitude source time function. Experiments indicate that the observed offset in $log(AAF_{6812}/AAF_{8812})$ can be reconciled by simply assuming a 0.4 sec triangular source time function in constructing the synthetics for the thrust event. The longer source duration also fits the observations slightly better. This again underlines the importance of understanding seismic source complexities in calibrating the structural effect. However, since fairly good agreement without significant offsets is observed when we compare the AAFs derived from the other events with those from the strike-slip event 13938812, the simple triangular source time function of 0.2 sec might present a safe approximation in the selected 0.5-2 sec frequency band. There are a few possible causes of the scatter, including small errors in the events' locations, source mechanisms, the rupture complexities as well as small-scale structural heterogeneity.

To summarize the comparisons, we calculate the averages and deviations of the AAFs derived from all the eight events as

$$\overline{log(AAF)} = \frac{1}{8}\sum_{i=1}^{8} log(AAF_i) \tag{2.2}$$

$$s^2_{log(AAF)} = \frac{1}{8-1}\sum_{i=1}^{8}(log(AAF_i) - \overline{log(AAF)})^2. \tag{2.3}$$

Particularly, the AAFs derived from the thrust event (13936812) have been corrected with the $\sim$ -0.15 offset in $log(AAF_{6812}/AAF_{8812})$ with respect to the rest of the events. However the correction hardly made a difference, simply because the offset itself is not significant compared with the scatter in the AAFs. The results are displayed in Fig. 2.10. The stations shown all have AAF estimates associated with high quality fits (cc $\geq$ 90) from at least three events. The larger deviations observed at the few stations might suggest more complicated local structure beneath the sites. However, the small deviations associated with most stations indicate the stability of the propagational effect from the whole cluster. Hence, the structural effect on the short-period (0.5-2 sec) P waves can be appropriately corrected.

2.4 Short-period inversions

Our strategy of using P waves to determine focal mechanisms is to invert the short-period (0.5-2 sec) P-wave waveforms. Since the process is highly nonlinear, we take a similar grid-search approach as in the long-period inversion, where we minimize the

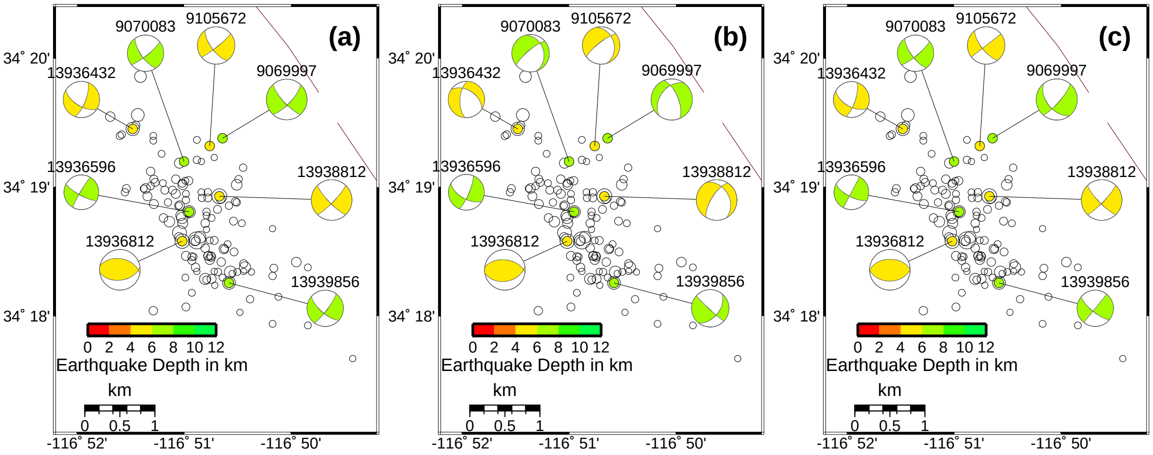

Figure 2.11: Comparison of focal mechanisms derived from (a) complete long-period waveform inversions (including both Pnl and surface waves), (b) P waves only, and (c) P waves with the AAF-corrections. Note the remarkable agreement between (a) and (c).

L_2 norm of the misfit between the data and synthetics:

$$e = \|u(t) - AAF \cdot s(t)\|. \tag{2.4}$$

The AAFs are taken from Fig. 2.10 to correct the structural effect. As a validation test, we first apply the approach to the eight calibration events (Fig. 2.11(a)) with the known focal mechanisms from the long-period inversions. This is also the best check of how well the P-wave waveforms can constrain focal mechanism.

For each event, only the stations that show stable AAFs ($s_{log(AAF)} < 0.20$) in Fig. 2.10 are utilized. Moreover, to avoid possible up-going and down-going phase interference at the crossover distance ($\sim$ 150 km), we also discarded the few stations with $130 < \Delta < 170$ km. We invert the P-wave waveforms from both the vertical and radical components, although they basically carry the same constraints. The depths of the events are set at their long-period solutions. However, almost the same focal mechanisms are obtained when we move the events up or down by 1 km due to the poor sensitivity of P waves to event depth. The inversion results show remarkable agreement with the events' known mechanisms (Fig. 2.11). Particularly, the small variations in the focal mechanisms of the strike-slip events are accurately recovered.

To demonstrate the importance of the AAF corrections in Eq. 2.4, we also conducted the inversions without them using the same stations (Fig. 2.11(b)). Although the thrust event remains a thrust, there are significant differences in the solutions of the strike-slip events compared to Fig. 2.11(a). Moreover, the inversions with the AAF corrections produce significantly reduced uncertainties with the resolved fault parameters (e.g., Fig. 2.12, event 13936432). The magnitudes of the events, however, are less biased, since the AAFs have nearly the opposite signs on the vertical and radial components (Fig. 2.10).

The above results have demonstrated the effectiveness of using the P-wave waveforms in constraining focal mechanisms. However, there is a more important question: what is the minimum number of stations that are needed to ensure an accurate mechanism? The station coverage generally gets poorer as an event becomes smaller and it is for these smaller events that improvements on focal mechanism determination are most needed. Therefore, before we routinely apply the approach to the smaller events of the cluster, we simulate the situation of expected poorer station coverages by using data from only subsets of stations for the calibration events. Four such tests for event 13936432 are shown in Fig. 2.13. In each test, 500 samples of randomly chosen stations of a certain number are used to constrain the event's focal mechanism, and the resulting P- and T-axes are compared with the known values. When only five stations are used, where the primary azimuthal gaps are generally larger than 150°, there is severe scatter in the obtained P- and T-axes. However, significant improvements are observed with the addition of more stations. As the number of stations increases to 10, the obtained P- and T-axes are much more clustered. In particular, about 80% of the P-axes are within 15° of the known value, while the T-axes show slightly more scatter with more than 60% within 15° of the known value. Furthermore, when there are fifteen or more stations used, uncertainties of the obtained P- and T-axes can be taken as 15° with $\sim 90\%$ confidence. Similar conclusions are reached with the other events. These tests provide important benchmarks to assess accuracy of the focal mechanisms when we apply the approach to the smaller events. However,

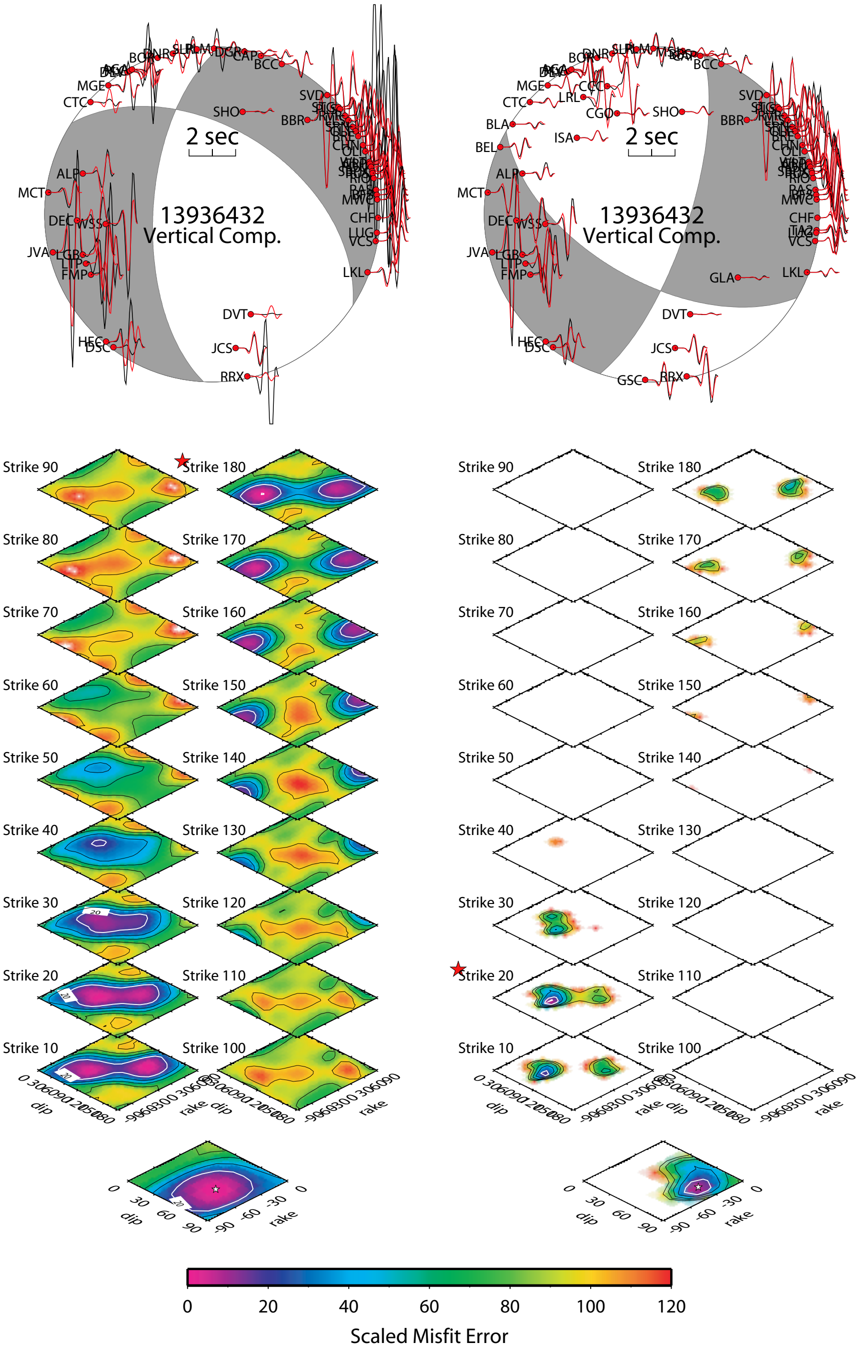

Figure 2.12: (top) The resulting P wave waveform fits on the vertical component from the short-period inversions without (left) and with AAF corrections (right) for the event 13936432. (bottom) The resolution of the solutions from short-period inversions for the event 13936432 without (left) and with AAF corrections (right) is displayed as the scaled waveform misfit errors. A red star indicates where the best solution resides with the blow up of the slice at the bottom. The white contours of 20% variance increase are displayed as the uncertainty estimates.

they might represent a raised threshold of the minimum number of stations that are indeed required, since the available stations are unevenly distributed azimuthally (see Fig. 2.10).

We then apply the approach to the smaller events with M_L down to 2.0 within the cluster. The magnitude threshold is chosen to ensure adequate SNR in the selected frequency band (0.5-2 sec). We use the event depths determined by *Chi and Hauksson* (2006) plus a +1 km static correction, since their depths for the bigger events are consistently shallower by ∼1 km than those determined from long period waveform inversions. This discrepancy is mainly due to the different velocity models used in the two studies. However, it produces nearly invisible effect on the resolved focal mechanism solutions. Fig. 2.14 displays the obtained focal mechanisms of 83 events, together with the long-period solutions of 9 bigger ones (including the main shock). We consider the uncertainties of the strike, dip and rake angles of these solutions to be within 15° with 90% confidence, since these are the events with either over 15 stations effectively used in the inversion or over 10 stations with the largest azimuthal gap $\Delta\varphi \leq 90^\circ$. Such a restriction disqualifies about 20 events (the open circles in Fig. 2.14), most of them contaminated by the coda of other events.

It appears in Fig. 2.14 that the whole sequence is dominated by strike-slip events. There are thrust and normal events, but they only occupy a rather small percentage. This overall pattern of source mechanisms is consistent with earlier reports in this region (e.g., *Hauksson et al.*, 1993). We plot the events at their refined locations by *Chi and Hauksson* (2006) with a double-difference approach. The clear northwest-trending swath of seismicity is probably associated with the mainshock (13935988) rupture. However, the seismicity does not collapse onto a single fault; there are multiple fault segments (*Chi and Hauksson*, 2006). There is, in general, good correlation between the seismicity lineations and focal planes. In particular, most of the deeper events (> 6.0 km) to the south show northwest-striking nodal planes consistent with the seismicity trend, which might indicate that the ruptures are indeed on a single fault plane. To the north, the shallower events display larger variations in the focal mechanisms; quite a few events have nodal planes that depart significantly from the

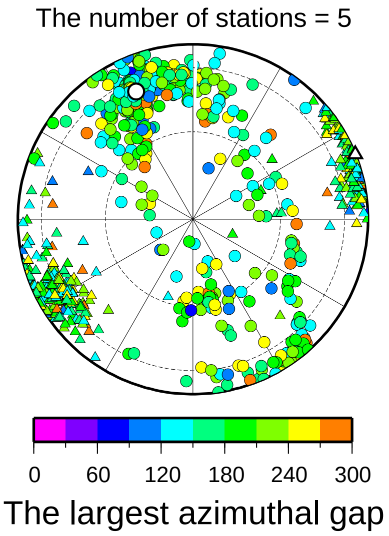
The number of stations = 5

	$\Delta\varphi \le 90^\circ$	$\Delta\varphi \le 120^\circ$	$\Delta\varphi \le 360^\circ$
$P < 10^\circ$	0/2	14/33	191/500
$P < 15^\circ$	1/2	19/33	247/500
$T < 10^\circ$	0/2	8/33	121/500
$T < 15^\circ$	0/2	12/33	196/500

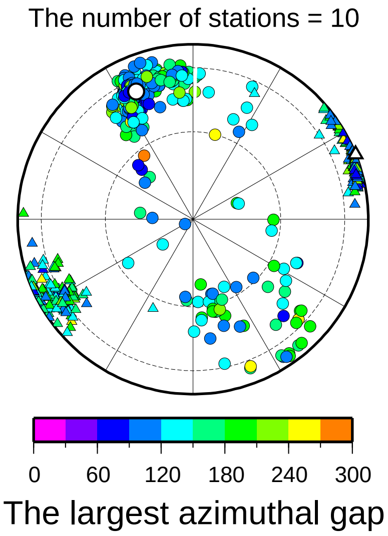
The number of stations = 10

	$\Delta\varphi \le 90^\circ$	$\Delta\varphi \le 120^\circ$	$\Delta\varphi \le 360^\circ$
$P < 10^\circ$	46/53	160/200	350/500
$P < 15^\circ$	48/53	170/200	392/500
$T < 10^\circ$	30/53	110/200	229/500
$T < 15^\circ$	41/53	143/200	319/500

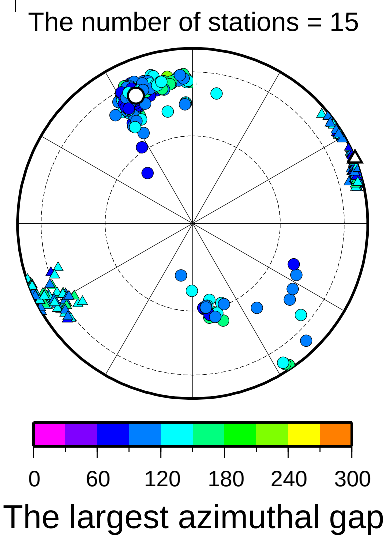
The number of stations = 15

	$\Delta\varphi \le 90^\circ$	$\Delta\varphi \le 120^\circ$	$\Delta\varphi \le 360^\circ$
$P < 10^\circ$	132/141	293/327	431/500
$P < 15^\circ$	134/141	300/327	451/500
$T < 10^\circ$	102/141	222/327	324/500
$T < 15^\circ$	139/141	306/327	440/500

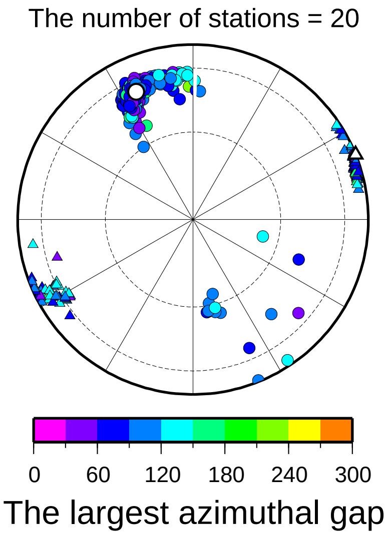
The number of stations = 20

	$\Delta\varphi \le 90^\circ$	$\Delta\varphi \le 120^\circ$	$\Delta\varphi \le 360^\circ$
$P < 10^\circ$	237/251	378/408	446/500
$P < 15^\circ$	244/251	388/408	469/500
$T < 10^\circ$	202/251	307/408	363/500
$T < 15^\circ$	242/251	387/408	454/500

Figure 2.13: The four panels of this figure display the comparison between the obtained P- and T-axes with the known values (open circle) for event 13936432, when we randomly chose a certain number of stations in the inversion.

general northwest trend. This implies complexity in the fault zone. Another small, but interesting feature in Fig. 2.14 is the sharp rotation of fault plane, such as implied by the two events 13936416 and 13943624. These two events are located almost at the same spot (Fig. 2.14), however, their focal mechanisms clearly show a $\sim 30^\circ$ difference in strike of the fault plane, which is reliably recovered by the waveform inversion (see Fig. 2.15). Note in Fig. 2.15 the obviously different P-wave radiation patterns for the two events. Besides, polarity reversals are observed at a few stations, such as HEC, SVD and BBR. This kind of change in fault plane geometry indicates there are crossover faults or fracture zones at depth, which is useful in mapping detailed fault structure.

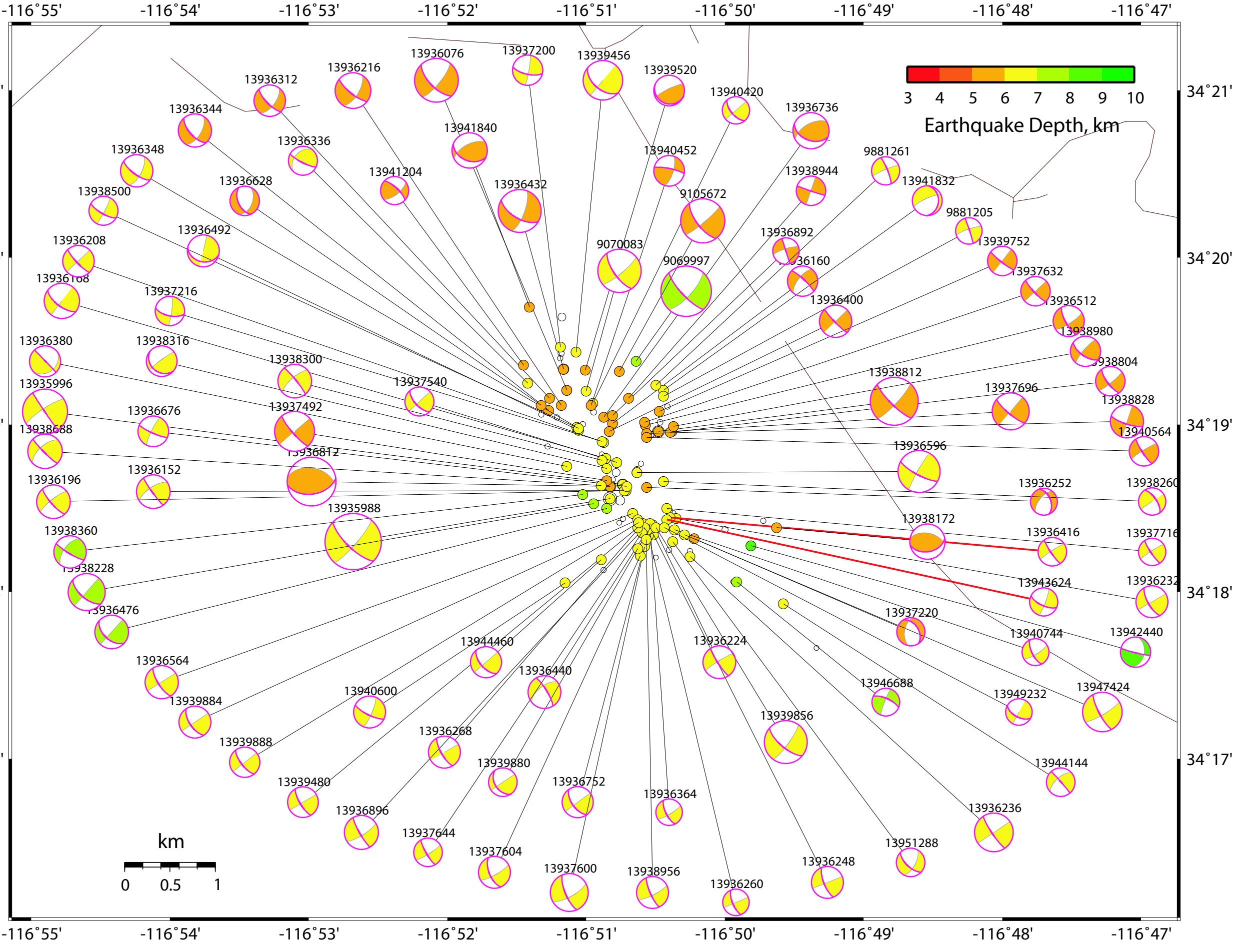

Figure 2.14: Map containing 92 events with mechanisms and moments (size of beach balls). The event locations are from *Chi and Hauksson* (2006) with a double-difference approach. Note the general NW-SE trend of seismicity, consistent with the main shock rupture. The two events (13936416 and 13943624) highlighted by red will be compared in Fig. 2.15.

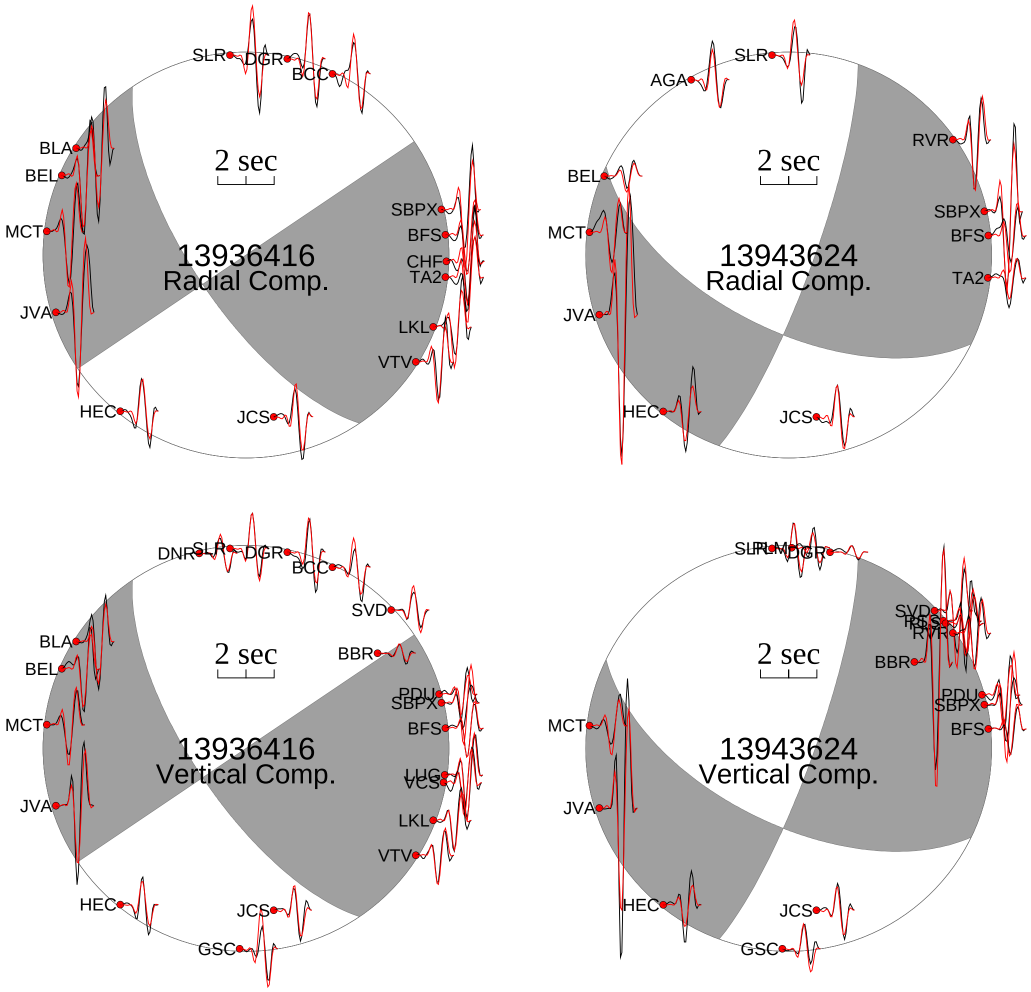

Figure 2.15: Comparison of P-wave waveform fits from the short-period inversions between the two events, 13936416 (left) and 13943624 (right), located almost at the same spot (see Fig. 2.14). Note the different azimuthal variations of P wave amplitudes for the two events. Besides, polarity reversals are observed at a few stations, such as HEC, SVD, and BBR.

2.5 Stress inversion

An important application of earthquake focal mechanism is to infer the stress field, or crustal deformation at depth (e.g., *Hauksson*, 1994; *Hardebeck and Hauksson*, 2001a). Resolving the spatial and temporal variations in the stress field, especially after a large earthquake, is probably the key step before we can understand the occurrence of the aftershocks. Although there are different stress inversion methods using focal mechanisms (e.g., *Gephart and Forsyth*, 1984; *Michael*, 1984, 1987), the two common basic assumptions are that (1) the stress field is homogeneous, i.e., a constant tensor for the sampled region, and (2) An earthquake slips in the direction of the shear stress acting on the fault plane. Hence, the objective of a stress inversion is to minimize the discrepancy between the shear stress direction and the slip direction on the fault planes for all the events in a data set, where the minimum misfit provides a natural way to examine the uniform stress field hypothesis (e.g., *Michael*, 1991). Of the resolved deviatoric stress tensor, however, only the orientations of the three principal stress axes, namely, the maximum (σ_1), intermediate (σ_2), and minimum (σ_3) compressive stresses, plus their relative magnitude ($\phi = (\sigma_2 - \sigma_3)/(\sigma_1 - \sigma_3)$) are determined, because only geometrical information is used.

A reliable stress inversion requires adequate focal mechanism diversity, since a single focal mechanism or a set of similar focal mechanisms can only constrain the quadrants containing the maximum and minimum principal stresses (*McKenzie*, 1969). However, it is generally rather difficult to distinguish real diversity in the focal mechanisms from their large uncertainties. Particularly, a stress inversion can be misleading if the apparent variations of the focal mechanisms are mostly due to their uncertainties. Moreover, the uncertainty of a stress inversion, although it can be assessed from the known focal mechanisms in a statistical sense (e.g., *Hardebeck and Hauksson*, 2001b), might be unrealistic, since the complex uncertainties of individual focal mechanisms are difficult to propagate into the stress inversion. To address these issues, various methods have been developed where P-wave first motion observations are directly used to invert for stress rather than the derived focal mechanisms (e.g., *Rivera and Cisternas*, 1990; *Abers and Gephart*, 2001). Among them, *Abers and Gephart* (2001) gave the resolved stress tensor with more complete uncertainties. *Abers and Gephart* (2001) applied their method in southern California using first motion data from the SCEC catalog, where they found typical uncertainties in stress orientation exceeded 20°-30° at the 95% confidence level. This implies that previously reported small stress rotations of 20° or less (*Hauksson*, 1994; *Hardebeck and Hauks-*

son, 2001a, e.g.,) using derived focal mechanisms from similar first motion data may not be resolvable. *Abers and Gephart* (2001) attributed the relatively large uncertainties in their stress estimates to the poor constraint of first motion data on focal mechanisms. Therefore, better-constrained focal mechanisms are required to detect small spatial or temporal variations of the stress field.

Here we present the stress inversion of 92 focal mechanisms (see Fig. 2.14) determined by comprehensive waveform modeling. We use the method developed by *Michael* (1984), since *Hardebeck and Hauksson* (2001b) demonstrated that this method produces accurate stress orientations with reasonable uncertainty estimates from known focal mechanisms. The actual fault planes for the strike-slip events are selected as the northwest-striking, right-lateral planes (denoted by purple lines in Fig. 2.14), which is consistent with the general seismicity trend. For the few thrust events, the south-dipping planes are assumed. To account for the fact that some fault planes might be incorrectly picked, we assume 10% of the fault planes are picked incorrectly in calculating the uncertainties of stress orientation with bootstrapping. In general, the erroneous choices of fault planes most likely change the shape of the stress ellipsoid and the size of the uncertainty ranges (*Michael*, 1987). Fig. 2.16(a) and (b) display the selected fault planes and the resolved stress. The average misfit angle $\overline{\beta}$ of $\sim$15° validates the uniform stress tensor assumption (*Michael*, 1991). The maximum compressive stress σ_1 is horizontal, trending $\sim$N3° W. The intermediate stress axis σ_2 is closest to vertical, and the relative stress magnitude $\phi \sim 0.6$ is consistent with the dominance of strike-slip faulting (see Fig. 2.14). The fact that σ_2 deviates from vertical with 95% confidence, however, warrants further study, since it might imply the modulation of a weak thrust fault at depth, such as the North Frontal Thrust, which did not seem to be active in earlier studies (e.g., *Hauksson*, 1994).

In general, there is good agreement between the resolved stress state and previous reports with earlier data sets in the same region (e.g., *Hauksson*, 1994; *Hardebeck and Hauksson*, 2001a). However, detailed comparisons for inferring temporal variations of the stress field are not appropriate, since the focal mechanisms are determined at a different level of accuracy. For example, we conduct the same inversion procedure

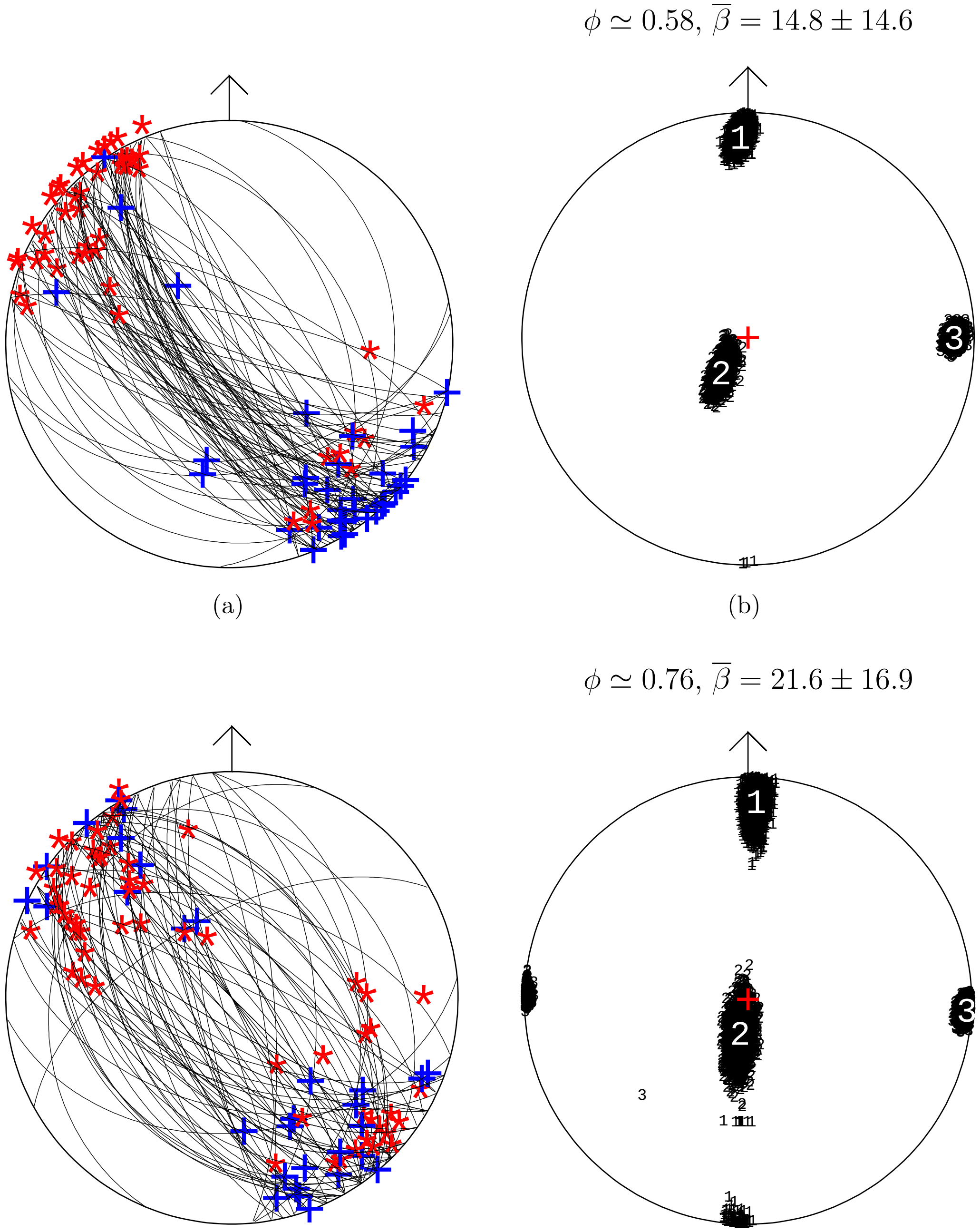
$\phi \simeq 0.58$, $\overline{\beta} = 14.8 \pm 14.6$

$\phi \simeq 0.76$, $\overline{\beta} = 21.6 \pm 16.9$

(a) (b)

(c) (d)

Figure 2.16: (a) The selected fault planes (lines) together with the slip directions (stars) from the focal mechanisms of this study are plotted on a stereonet. The red stars indicate a normal fault component, while the blue crosses indicate a thrust component. (b) The stress field inverted from the slip data shown in (a). Displayed are the three principal stress axes of the maximum (1), intermediate (2) and minimum (3) compressive stresses plus their uncertainties with 95% confidence. (c) and (d) are for the focal mechanisms determined by *Hauksson* (2000) with the same inversion procedure.

using the first motion focal mechanisms determined by *Hauksson* (2000) for the same events. The results are given in Fig. 2.16(c) and (d). We use the same fault plane selection criterion and still assume 10% of the fault planes are incorrectly picked for an uncertainty estimate. Considering the larger variations of the first motion focal mechanisms, which has complicated the fault plane selection, this might underestimate the stress uncertainty. The resolved stress (Fig. 2.16(d)) shows compatible features as seen in Fig. 2.16(b). However, the relative stress magnitude ϕ has a larger value of ∼0.76, indicating the faulting regime is a combination of strike-slip and normal faults. The larger uncertainties in the stress orientations are mainly due to the larger errors in the dip and rake angles of the focal mechanisms, which has blurred the discrepancy between σ_2 and vertical in Fig. 2.16(b). This underlines the importance of well-constrained focal mechanisms in resolving fine features of the stress field.

2.6 Seismic moment (M_0) *vs.* M_L

Quantification of an earthquake size has been one of the oldest problems in seismology. The earliest effort started as *Richter* (1935) introduced the local magnitude scale M_L in southern California based on 1 Hz waves recorded by a Wood-Anderson seismograph at an epicentral distance of 100 km. Although the old Wood-Anderson seismographs have been replaced by the modern instruments of higher dynamic ranges and broader bandwidths, M_L remains widely used. There are, however, severe intrinsic limitations on M_L, because it is based on limited instrumental measurements over a fixed frequency band. Furthermore, M_L is not easily related to physical characteristics of the earthquake source. In contrast, the seismic moment M_0 and the moment magnitude M_w (*Hanks and Kanamori*, 1979) are fundamentally superior in that they are defined based on a well accepted shear dislocation source model and can be estimated from the amplitudes of seismic radiations recorded by all suitable seismographs (*Bakun*, 1984).

Since the early 1970's, the scaling relation between M_0 and M_L has been an important aspect of earthquake studies. *Hanks and Boore* (1984) summarized earlier results in central and southern California. They suggested that the observed differences in the $log(M_0) - M_L$ relations between central and southern California were not a geographic reality, but resulted from the preponderance of different sized events that form the bulk of the two data sets. As a proof, they presented theoretical evidence for the continuous curvature of $log(M_0)$ *vs.* M_L in the magnitude range of $0 < M_L < 7.0$ based on stochastic simulations of high-frequency ground motions (*Boore*, 1983). They attributed the non-linear scaling factor between $log(M_0)$ and M_L to a complex interaction in the frequency domain, resulting in three essential bandwidths:

$$\begin{array}{lll} (i) & f_0 \ll f_s & log(M_0) \sim 3.0 M_L \\ (ii) & f_s \ll f_0 < f_{max} & log(M_0) \sim 1.5 M_L \\ (iii) & f_0 > f_{max} & log(M_0) \sim 1.0 M_L, \end{array} \tag{2.5}$$

where f_s is the natural frequency of the standard Wood-Anderson torsion seismograph (1.25 Hz), f_{max} is a high-frequency cutoff (15 Hz) and f_0 is the earthquake corner frequency. The significant departure from the usually assumed or theoretically expected $log(M_0) \sim 1.5M_L$ relationship occurs for both large ($f_0 \ll f_s$) and small ($f_0 > f_{max}$) events. For large events, it is because the M_L measurement suffers the high-frequency falloff of the source spectrum, while for small events, it implies the M_L dependence on M_0 is insensitive to stress drop. The later results of *Bakun* (1984) in central California, *Vidal and Mungúia* (1991) in the Peninsular Ranges of Baja California and *Abercrombie* (1995) with recordings in the deep Cajon Pass borehole are compatible with the results of *Hanks and Boore* (1984) (see Table 2.1). Instead of the seismic moment M_0, *Ben-Zion and Zhu* (2002) studied the scaling between the potency P_0 ($P_0 = M_0/\mu$) and M_L in order to sidestep assumptions on source material rigidity μ. They assembled a large data set, including 418 events ($3.5 < M_L < 6.0$) with seismic moments determined by inverting broadband waveforms (*Zhu and Helmberger*, 1996) and the 18 events from the borehole data set (*Abercrombie*, 1995). They found significant change in slope when attempting linear least-squares fits between $log(P_0)$ and M_L for the two data sets respectively, and a quadratic scaling relation better explained a few bigger events ($M_L > 6.0$) (Table 2.1). They also suggested a

Table 2.1: Seismic moment (M_0) – Local magnitude (M_L) relations

Study	Relation		# of events
Bakun (1984)	$log(M_0) = 1.5M_L + 16$	$3 \leq M_L \leq 6$	40
	$log(M_0) = 1.2M_L + 17$	$1.5 \leq M_L \leq 3.5$	59
	$log(M_0) \propto (2/3 - 1)M_L$	$0.5 \leq M_L \leq 1.5$	23
Vidal and Mungúia (1991)	$log(M_0) = 1.11M_L + 17.32$	$2 \leq M_L \leq 4$	72
	$log(M_0) = 1.63M_L + 14.87$	$4.0 \leq M_L \leq 6.8$	24
Abercrombie (1995)	$log(M_0)(N \cdot m) = 1.0M_L + 9.8$	$1 \leq M_L \leq 4$	18
Ben-Zion and Zhu (2002)	$log(P_0) = 1.0M_L - 4.72$	$1 \leq M_L \leq 3.5$	18
$P_0 = M_0/\nu(cm \cdot km^{-2})$	$log(P_0) = 1.34M_L - 5.22$	$M_L > 3.5$	418
Prieto et al. (2004)	$log(M_0) \propto\sim 3/2M_L$	$1.8 \leq M_L \leq 3.4$	over 400
This study	$log(M_0) = 1.12M_L + 17.29$	$2.0 < M_0 < 5.0$	92
	$log(M_0) = 1.13M_L + 17.47$	$M_L > 3.5$	161
	$log(M_0) = 1.57M_L + 15.43$	$M_L > 4.5$	31

The seismic moment M_0 is in $dyn \cdot cm$, otherwise, as indicated.

possible alternative explanation of the non-linearity in $log(P_0) - M_L$ scaling based on their simulations of earthquake patterns with strong heterogeneities (e.g., *Ben-Zion and Rice*, 1993). There is, however, a pitfall in their analysis due to the lack of data points within $2.0 < M_L < 3.5$, which also hinders their further clarification of the true moment–magnitude relation. Recently, *Prieto et al.* (2004) analyzed a cluster of over 400 events ($1.8 < M_L < 3.4$) recorded by the Anza seismic network and obtained a larger $log(M_0) - M_L$ scaling factor of $\sim$3/2.

Here we are presenting the $log(M_0) - M_L$ relation for the 92 events ($2.0 < M_L < 5.0$) within the cluster that we have studied (Fig. 2.17). The large number of events within $2.0 < M_L < 3.5$ fit well in the magnitude gap of the *Ben-Zion and Zhu* (2002) data. Besides, our moment estimates of this size of events are more reliable than the previous studies, since we have removed the radiation pattern effect, and the *AAF* corrections we incorporated in the inversion (see Eq. 2.4) eliminated the structural effect. The least-squares fit of $log(M_0) = 1.12M_L + 17.29$ explains all the data points (black symbols) spanning three orders of magnitude ($2.0 < M_L < 5.0$), except for only a few outliers (Fig. 2.17). The slope of 1.12 is consistent with the results of *Bakun* (1984), *Vidal and Mungúia* (1991), and *Hanks and Boore* (1984). The fact that the slope is slightly bigger than that derived for the borehole data

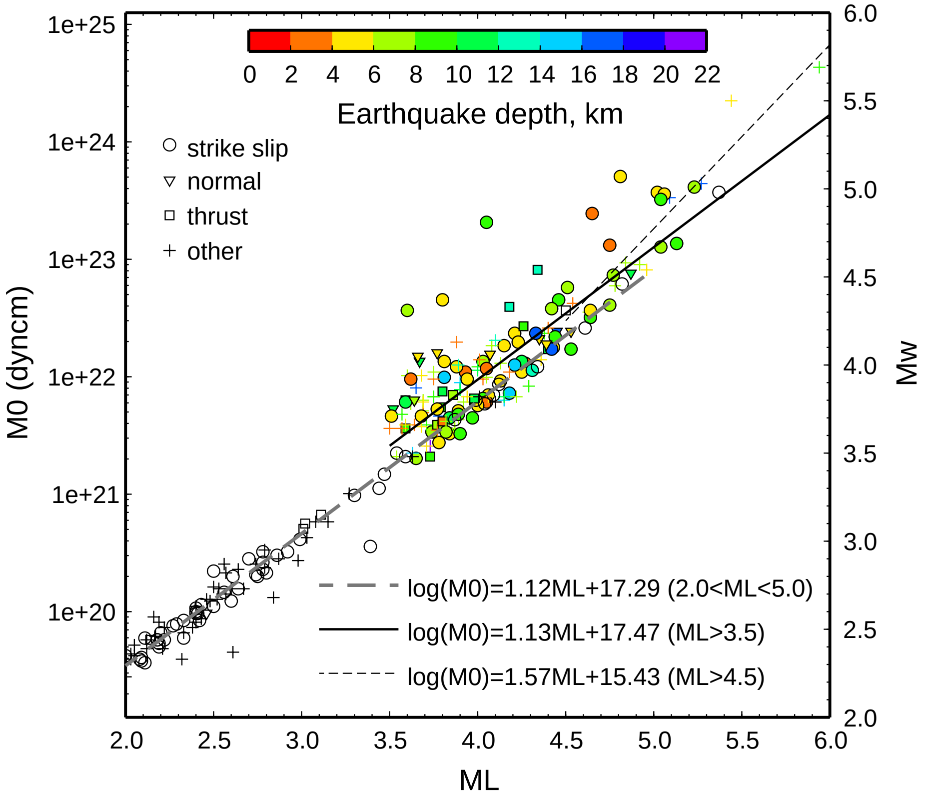

Figure 2.17: M_0 *vs.* M_L relationship. The 92 events within the Big Bear cluster from this study are displayed as black symbols. Color-coded in depth are the bigger events throughout southern California since 1999 determined from long period inversions.

set (mainly $1.0 < M_L < 2.0$) (*Abercrombie*, 1995; *Ben-Zion and Zhu*, 2002) might imply a gradual transition. However, to confirm the robustness of the slope change requires more observations with $M_L < 2.0$. We group the events according to their different fault types following *Frohlich* (1992) and find no obvious dependence on fault types of the $log(M_0) - M_L$ relation. For comparison, we also include in Fig. 2.17 159 events with $M_L > 3.5$ throughout southern California between 1999 and 2004 (color coded symbols). The seismic moments of these events are determined by inverting long-period complete seismograms as we have discussed in section 2.2. Details of the source parameters of these events are given in Appendix A. Although the linear least-squares fit gives a similar slope of 1.13, the scatter is apparently larger. No obvious event depth dependence of the $log(M_0) - M_L$ relation is observed. The slope of 1.13 is smaller than the result of *Ben-Zion and Zhu* (2002); however, it is in agreement with the result of *Clinton et al.* (2006). We also separate the 31 events with $M_L > 4.5$ and obtain a significantly larger slope of 1.57 with the linear least-squares fit, which supports the argument of the continuous $log(M_0) - M_L$ curvature by *Hanks and Boore* (1984).

2.7 Source duration and stress drop

Physical dimension is one of the basic parameters for describing the static properties of an earthquake source. From it, the seismic moment M_0 and an assumed fault geometry, the static stress drop $\Delta\sigma$ can be estimated (*Kanamori and Anderson*, 1975). Particularly for small events without surface break, there are mainly two ways of estimating source dimension: from the source duration by directly measuring the P-wave pulse width (e.g., *Frankel and Kanamori*, 1983; *Jones and Helmberger*, 1998) or from the corner frequency by analyzing the source spectrum(e.g., *Abercrombie*, 1995; *Prieto et al.*, 2004). Since the stress drop scales with the cube of source duration or corner frequency, a tenfold error in the stress drop can easily be resulted from the errors in source duration or corner frequency estimates. This has rendered the fundamental questions regarding the stress drop of small events ($M < 5$) controversial, such as whether stress drop is a constant with seismic moment, and whether stress drop varies with tectonic setting or depth. In the previous sections, we have been assuming a simple 0.2 sec triangular source time function for the whole cluster, which in fact can hardly be resolved in the frequency band of 0.5–2 sec. Here we will investigate the source durations of the individual events with a procedure, where we attempt to equalize the energy content across different frequency bands between data and synthetics (*Zhao and Helmberger*, 1996; *Song and Helmberger*, 1997; *Jones and Helmberger*, 1998). This approach of estimating source duration is more efficient than directly measuring source pulse for a large data set, while simpler than analyzing source spectra. The resulted source durations are model-dependent, and possibly biased by various factors, such as crustal attenuation, rupture directivity and source complexity. However, considering the compact size of the cluster, the relative source durations of most events are reliable. A good correlation has been found between the source durations via this approach and those determined by directly measuring the P-wave pulse widths, except for an offset (*Song and Helmberger*, 1997). The offset, however, is expected because the synthetics do not contain scattering as the data do, especially at high frequencies.

In detail, we search through the source time functions of a range of durations from 0.02 sec up to 0.4 sec. For simplicity, a triangular shape is assumed. With each source time function, we calculate the ratio between the data $d(t)$ and synthetics $s(t)$ of the energy contrast over short-period "$_{sp}$" and long-period "$_{lp}$" frequency bands:

$$r = \frac{\int d^2(t)_{sp} dt}{\int d^2(t)_{lp} dt} / \frac{\int s^2(t)_{sp} dt}{\int s^2(t)_{lp} dt}, \tag{2.6}$$

and the best source duration is found when r approximates unity. In the previous applications of the approach, where intermediate-sized events ($M > 4$) were addressed, the extended Pnl waves were used (e.g., *Song and Helmberger*, 1997; *Jones and Helmberger*, 1998). However, here we restrict the calculation on the direct P waves by choosing a 2 sec window centered on the first P-arrival. Besides, the frequency band of 2–20 Hz for short period and 0.5–2 sec for long period are selected which are suited to the events' sizes.

The obtained source durations are displayed in Fig. 2.18, where the value for each event is the average over several tens of stations. We performed simple iterations on the result in an attempt to separate possible "station terms" due to propagation effects. We solve for the events' durations (τ_is) and the stations' corrections (c_js) in each run as

$$\tau_i = \frac{\sum_{j=1}^{n_i} (t_{ij} - c_j)}{n_i}, \tag{2.7}$$

$$c_j = \frac{\sum_{i=1}^{N} (t_{ij} - \tau_i)}{N}. \tag{2.8}$$

The n_i in Eq. 2.8 is the number of available stations for an event i, and N is the number of total events. The t_{ij}s are the individual measurements for an event i at a station j. However, fairly small station corrections resulted and the scatter in Fig. 2.18 remained nearly the same, which might suggest that the scatter is mainly a source reality. Note the source durations we obtain here represent “a lower bound”, since *Song and Helmberger* (1997) reported that the durations via such energy comparisons are systematically smaller than those from direct measurements. The apparent slope between the logs of source duration and seismic moment appears significantly smaller than “1/3” of a constant stress drop, which could be caused by the inadequate “Q” structure in the velocity model ($Q_\alpha = 2Q_\beta = 1200$). Particularly, our experiments with reduced “Q” values have produced larger slopes between the logs of source duration and seismic moment. Hence, the slope in Fig. 2.18 is not capable of rejecting the earthquake self-similarity hypothesis or the “constant stress drop” model.

We group the events in Fig. 2.18 according to their depths, and find the deeper events ($>$ 6 km) consistently have larger durations, hence, lower stress drops than the shallower events. Since the events’ depths correlate well with their geographic locations (see Fig. 2.14), such a tendency is also observed in the map view of the stress drops (Fig. 2.19). The stress drops in Fig. 2.19 are calculated assuming a circular fault following *Jones and Helmberger* (1998) as

$$\Delta\sigma(bar) = \frac{1.84 \times 10^{-22} M_0(dyncm)}{\tau^3}. \tag{2.9}$$

Particularly, we compare the broadband records from two events (13938228 and 13937696) of a similar size, but different stress drops (Fig. 2.20). The P wave pulse widths from the event 13938228 are consistently larger than those from the event 13937696, which suggests that the contrast between their source durations is robust.

What has caused the variation of the stress drop in Fig. 2.19 is intriguing, since it can hardly be attributed to the structural or attenuation effects, considering the compact size of the whole cluster. Recently, *Li and Zhu* (2006) reported well-constrained Landers fault zone (FZ) structure from modeling the waveform data of the after-

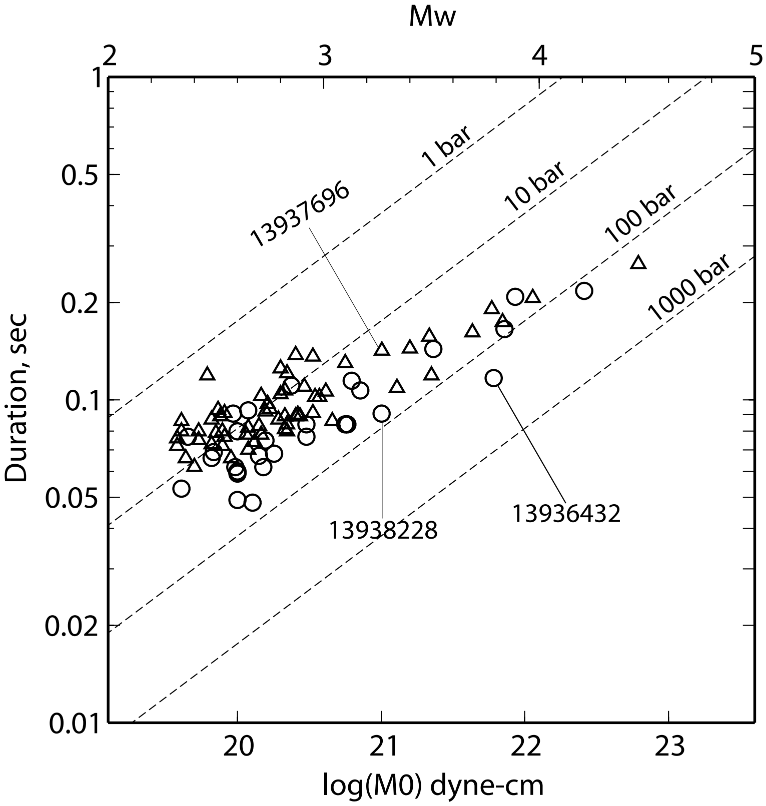

Figure 2.18: Source durations *vs.* seismic moments for the 2003 Big Bear sequence. The triangles are for the deeper events in the south ($\geq$ 6 km), with the circles for the shallower events in the north (see Fig.2.14). The lines of constant stress drops of 1, 10, 100 and 1000 bars are plotted from top to bottom. The outlier (event 13936432) of apparently the largest stress drop will be further discussed later. Also labeled are the two events 13937696 and 13938228 compared in Fig. 2.20.

shocks. They reported a low-velocity FZ of 250-340 m in width with a 45% reduction in seismic wave velocities. If we assume the crustal density is relatively uniform, the shear wave velocity reduction would imply a sharp drop in the crustal rigidity or strength in the fault zone. Correspondingly, earthquakes that occur in pre-existing fault zones would tend to have lower stress drops.

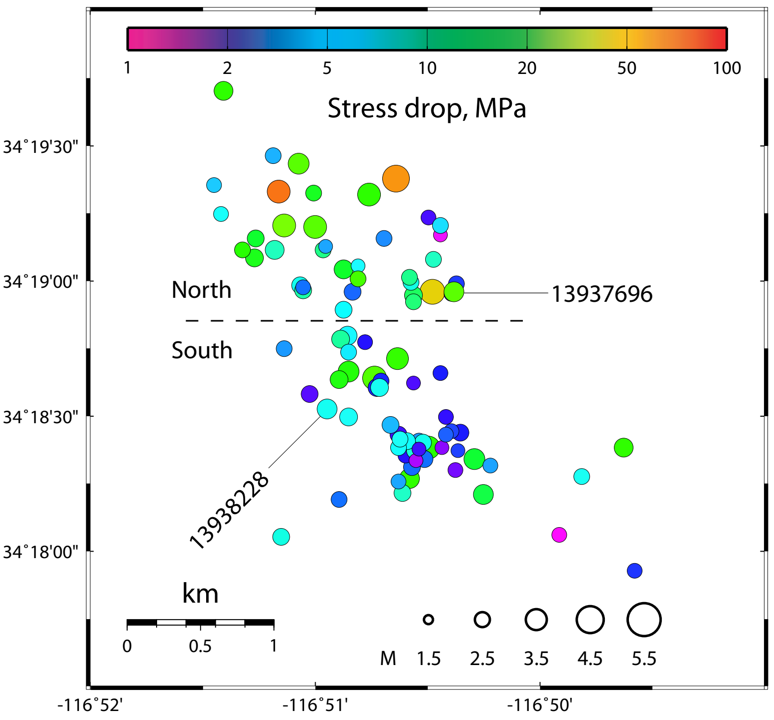

Figure 2.19: Stress drop estimates for the 2003 Big Bear sequence. Note the northern events tend to have higher stress drops than the southern ones of similar sizes. Labeled are the two events 13937696 and 13938228 compared in Fig. 2.20. The apparent tendency that larger events have higher stress drops is possibly due to the inadequate "Q" structure in the velocity model.

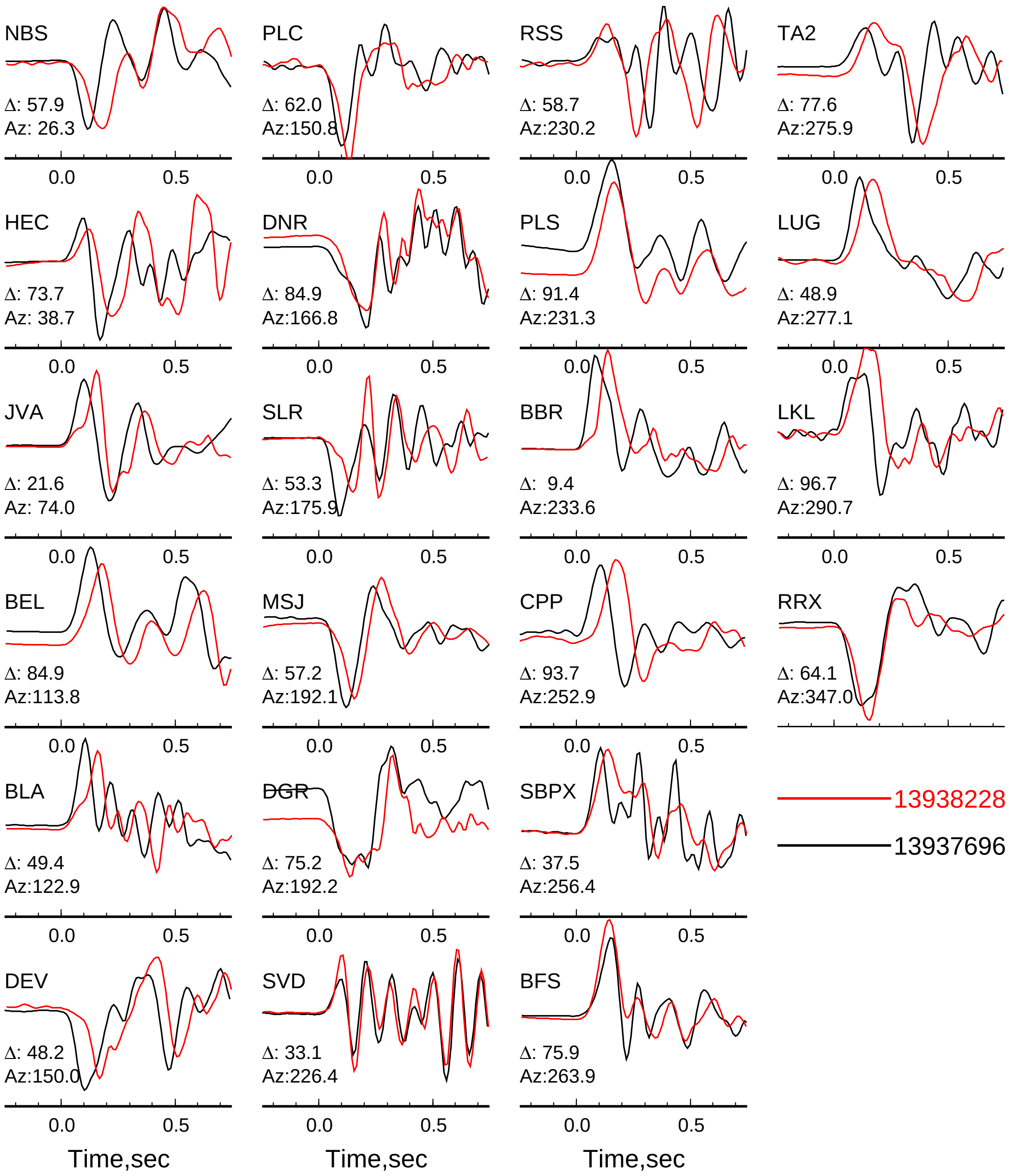

Figure 2.20: Comparison of the broadband displacement records from the event 13937696 (black) and 13938228 (red). Shown are the stations where we are able to accurately measure the on-set of P waves, by which the records are aligned. Note the P-wave pulse widths from the event 13938228 (red) are consistently larger than those from the event 13937696. This supports the duration contrast between the two events via the energy ratio approach in Fig. 2.18.

2.8 Rupture directivity

A direct consequence of rupture propagation on a fault plane is the azimuthal dependence of the observed source time function (STF). In brief, if a seismic station is located along the rupture propagation direction, the STF is narrower and has a higher amplitude. For a station located such that the rupture is propagating away from it, the STF will be spread out and have a smaller amplitude (*Lay and Wallace*, 1995). Retrieving such an azimuthal pattern of the STFs, however, is not easy, due to the difficulty in separating the STFs from the entanglement of propagational effects. The problem becomes even more severe for small events ($\mathrm{M} < 5$), where a typical STF length drops below ∼0.5 sec, and the analysis has to be conducted at high frequencies ($> 2\mathrm{Hz}$).

Instead of using inaccurate Green's functions from an inadequate velocity model, *Hartzell* (1978) early demonstrated the feasibility of modeling the strong ground motion of a large earthquake using records from its own aftershocks as Green's functions. This empirical Green's function (EGF) approach assumes the large event and the EGF events occur at a similar location and have a similar focal mechanism, so that they share nearly the same propagational effect, and a linear scaling between their source terms exists at the same stations. Therefore, the relative source time functions (RSTFs) of the large event can be obtained by simply deconvolving the EGFs from the records of the event. These relative estimates, however, can equal to the true values if the source duration of the EGF event is short enough to approximate a delta function. Since the early 1990's, the EGF method has been widely used to retrieve source parameters and rupture processes of both large (e.g., *Hough and Dreger*, 1995) and small (e.g., *Lanza et al.*, 1999; *Venkataraman et al.*, 2000; *McGuire*, 2004) earthquakes, where the deconvolution technique was the main means of extracting RSTFs.

In this section, we will take the magnitude 2 events as EGFs to investigate the rupture processes of the larger strike-slip events ($Mw > 3.5$) within the cluster. Rather than using deconvolution, we propose an alternative approach of forward modeling to retrieve the RSTFs. Let $d(t)$ and $g(t)$ be the records from a large event ($Mw > 3.5$) and the associated EGF event at the same station, which can be related by the relative source time function, $RSTF(t)$ of the large event as:

$$d(t) = g(t) * RSTF(t). \tag{2.10}$$

Assuming a simple trapezoidal shape of $RSTF(t)$ according to the 1D Haskell model (*Haskell*, 1964), where a $RSTF(t)$ can be parameterized as the convolution of two boxcars, featuring the rise time τ_1 and the rupture time τ_2, we can solve for the $RSTF(t)$ in a grid search manner by minimizing the misfit defined as:

$$e = \|d(t) - \Delta M_0 g(t) * RSTF(t)\|, \tag{2.11}$$

$$where RSTF(t) = \tau_1(t) * \tau_2(t). \tag{2.12}$$

Here the parallels denote the L_2 norm. ΔM_0 is an amplitude scaling factor to account for the two events' difference in size and radiation pattern.

We first use the event 13937492 to illustrate the whole process, which is also the smallest ($M_w \sim 3.5$) among our analyzed events. The event has a nearly pure strike-slip focal mechanism, and we have chosen a smaller event (13937632, $M_w \sim 2.5$), which has almost the same focal mechanism (see Fig. 2.14) for the EGFs. The two events are located within 500m × 500m × 500m by *Chi and Hauksson* (2006). We conducted the grid search to minimize "e" in Eq. 2.12 in the parameter space of 0.02–0.2 sec for τ_1 and 0.02–0.4 sec for τ_2 with a step of 0.02 sec. A bandpass filter of 0.5–6Hz was applied to avoid rather small-scale rupture heterogeneities. Although we could solve for τ_1 and τ_2 at each station separately, we took τ_1 as a common parameter and obtained its best value (0.08 sec) when the summation of misfit errors from all the stations was minimized (Fig. 2.21(a)). The corresponding τ_2s for the individual stations are displayed in Fig. 2.21(b), where τ_2 reaches a pronounced minimum at an azimuth of $\sim 140°$. The azimuthal variation of τ_2 indicates that the rupture is on the NW striking plane and propagates unilaterally towards the southeast. To estimate

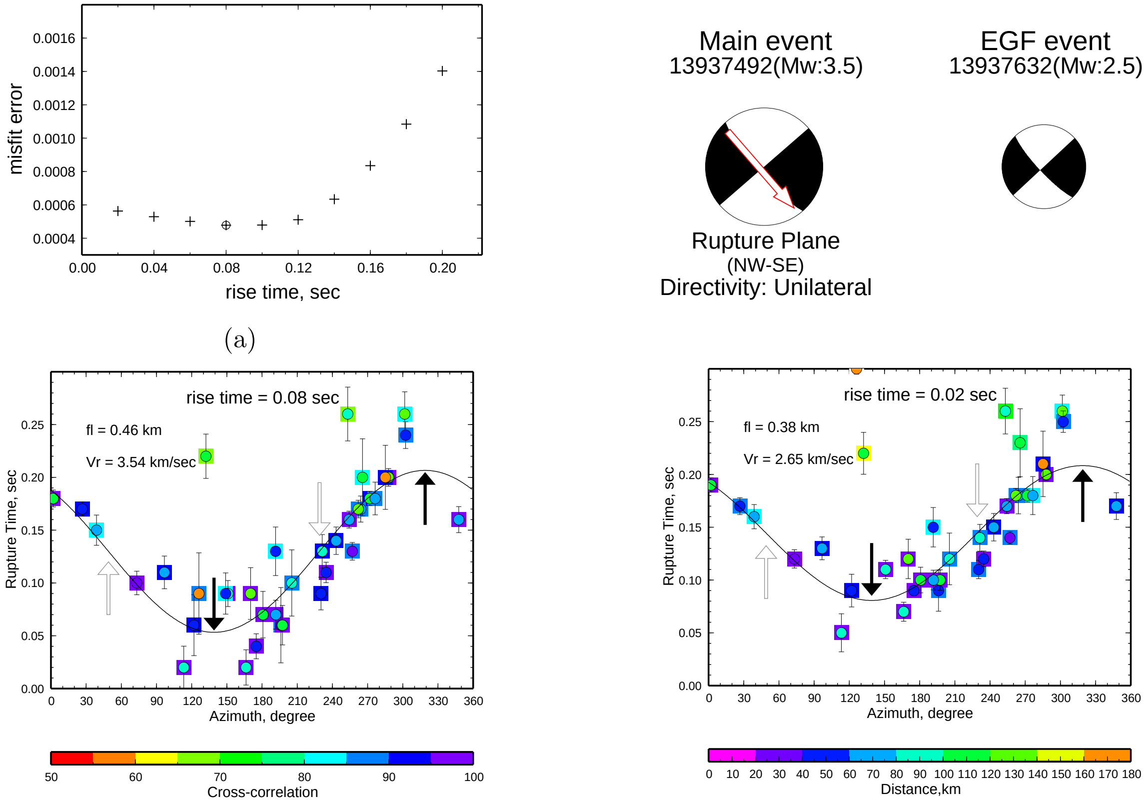

(a)

(b)

(c)

Figure 2.21: (a) The summation of misfit errors as defined in Eq. 2.12 from all the stations *vs.* rise time τ_1. The best estimate of τ_1 occurs where the total misfit error approaches the minimum, in this case, 0.08 sec. (b) The τ_2s corresponding to a 0.08 sec τ_1 *vs.* azimuth. The color of the squares denotes the waveform cross-correlation between the records from the main event (13937492) and the EGF event (13937632) convolved with the RSTFs. The color of the inner circles denotes the station distances. The uncertainties of the τ_2s are estimated by a 10% decrease in variance reduction. The solid line indicates the least-squares fit of the unilateral rupture towards SE on the NW striking fault plane (the black arrows) following Eq. 2.13. (c) The τ_2s corresponding to a 0.02 sec τ_1 *vs.* azimuth.

the fault length (fl) and rupture velocity (V_r), we fit the observed azimuthal pattern of τ_2 with the calculated values from the simple 1D model:

$$\tau_2 = \frac{fl}{V_r}\{1 - \frac{V_r}{v_p}[cos(\varphi - \phi)cos(\lambda) - sin(\varphi - \phi)sin(\lambda) * cos(\delta)]\}, \tag{2.13}$$

where we have assume the rays are essentially taking off horizontally from the source. φ in Eq. 2.13 is the station azimuth, while ϕ and δ are the strike and dip of the rupture plane. λ is the rake of the rupture propagation direction. Here we simply assumed the rupture propagates horizontally, *i.e.*, $\lambda = 0°$ or $180°$. Any vertical component of rupture directivity, however, can hardly be resolved on a nearly vertical fault plane (Eq. 2.13), since we did not make distinctions between up-going and down-going rays. The least-squares fit from this simple model well explains the azimuthal pattern of τ_2 (Fig. 2.21(b)). We color-coded the stations with their distances; however, we found no obvious dependence of τ_2 on station distance, which implies no significant vertical rupture directivity. We obtain a fault length of $\sim$ 0.5 km and a relatively large rupture velocity of $\sim$ 3.5 km/sec (Fig. 2.21(b)). However, the constraint on them is weak, simply due to the large scatter near the τ_2 minimum. Besides, there are trade-offs between the fault length, rupture velocity and the rise time. Taking these into account, we obtain the lower bounds of the fault length ($\sim$ 0.4 km) and rupture velocity ($\sim$ 2.7 km/sec) with the 0.02 sec rise time (Fig. 2.21(c)).

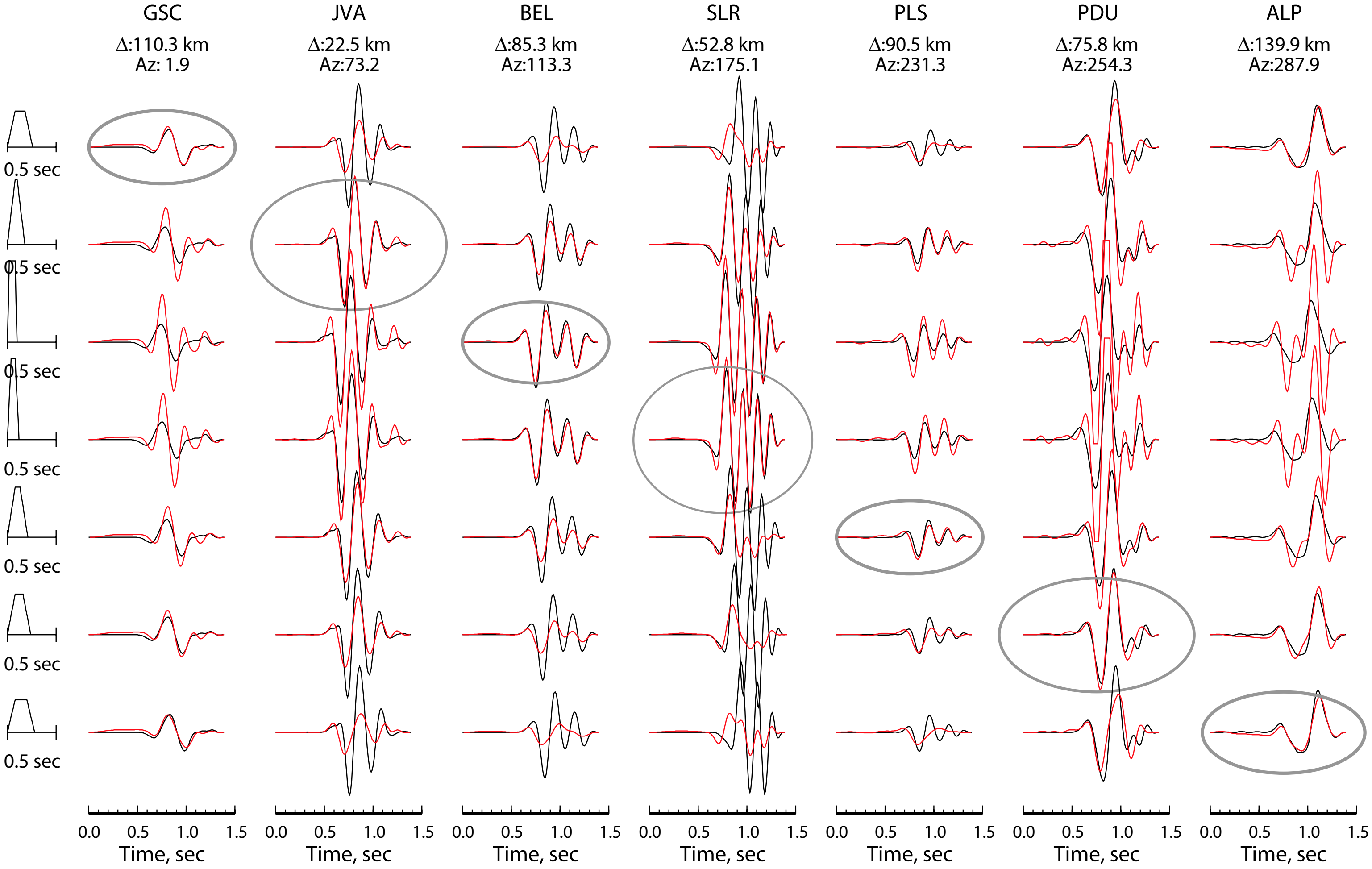

Figure 2.22: The selected waveform fits (vertical P waves) between the records from event 13937492 (black) and the "synthetics" (red) constructed with EGFs from event 13937632. The relative source time functions (RSTFs) are given to the left. Plotted are the absolute amplitudes, except that a scaling factor of 1/4, 1/2 and 2 has been applied to the stations JVA, PDU and PLS respectively for the display purpose. The obtained best RSTFs for the stations are circled. Note the apparent azimuthal pattern of the RSTFs.

The azimuthal variation of the rupture time for event 13937492 can also be visualized directly in the waveforms (Fig. 2.22). The selected stations well sample the whole azimuthal range. Apparently, the stations GSC and ALP that are located opposite from the rupture propagation direction require the largest rupture times. On the contrary, those stations located along the rupture propagation direction, such as BEL and SLR, display significantly shorter source time functions. Note in Fig. 2.22 that the minimum rupture times, such as for the stations BEL and SLR, are mainly resolved from amplitude comparisons, due to the high frequency cutoff (6 Hz) we have applied. This also explains the relatively large scatter near the τ_2 minimum in Fig. 2.21.

In the following, we will briefly discuss the results for the few other events that we have investigated. Another example of unilateral rupture, event 13936596, is given in Fig. 2.23. Although there is some scatter, the obtained rupture time displays systematic azimuthal variation, and reaches a well-developed minimum at $\sim 210^\circ$(Fig. 2.23(a)). Such an azimuthal pattern of τ_2 suggests a unilaterally propagating source on the northeast-striking fault plane towards the southwest. The least-squares fit of the τ_2s with Eq. 2.13 produces a fault length of ~0.4 km and a large rupture velocity, approximately 3.8 km/sec, though the constraints on them are weak. We compare in Fig. 2.23(b) the source time functions of event 13936596 relative to event 13938500 by projected landwebber deconvolution (PLD) (e.g., *Lanza et al.*, 1999). Although the exact durations of the RSTFs are rather subjective due to the sidelobes in the RSTFs, the stations within the azimuthal range of ~140°–300° display distinctly shorter source durations, consistent with the forward modeling result (Fig. 2.23(a)).

Event 13936076 (Fig. 2.24) appears a "doublet" when compared to a smaller event 13936344 with a similar focal mechanism. In particular, the records from event 13936076 consistently display doubled pulses of those from event 13936344. Such discrepancies can not be due to structural effects, since the two events are closely located (within 500 m). Moreover, the azimuthal stability strongly suggests a source effect. As shown in Fig. 2.24, the simple source time function "stf1" composed of two subevents well explains the observed P-wave waveforms from event 13936076

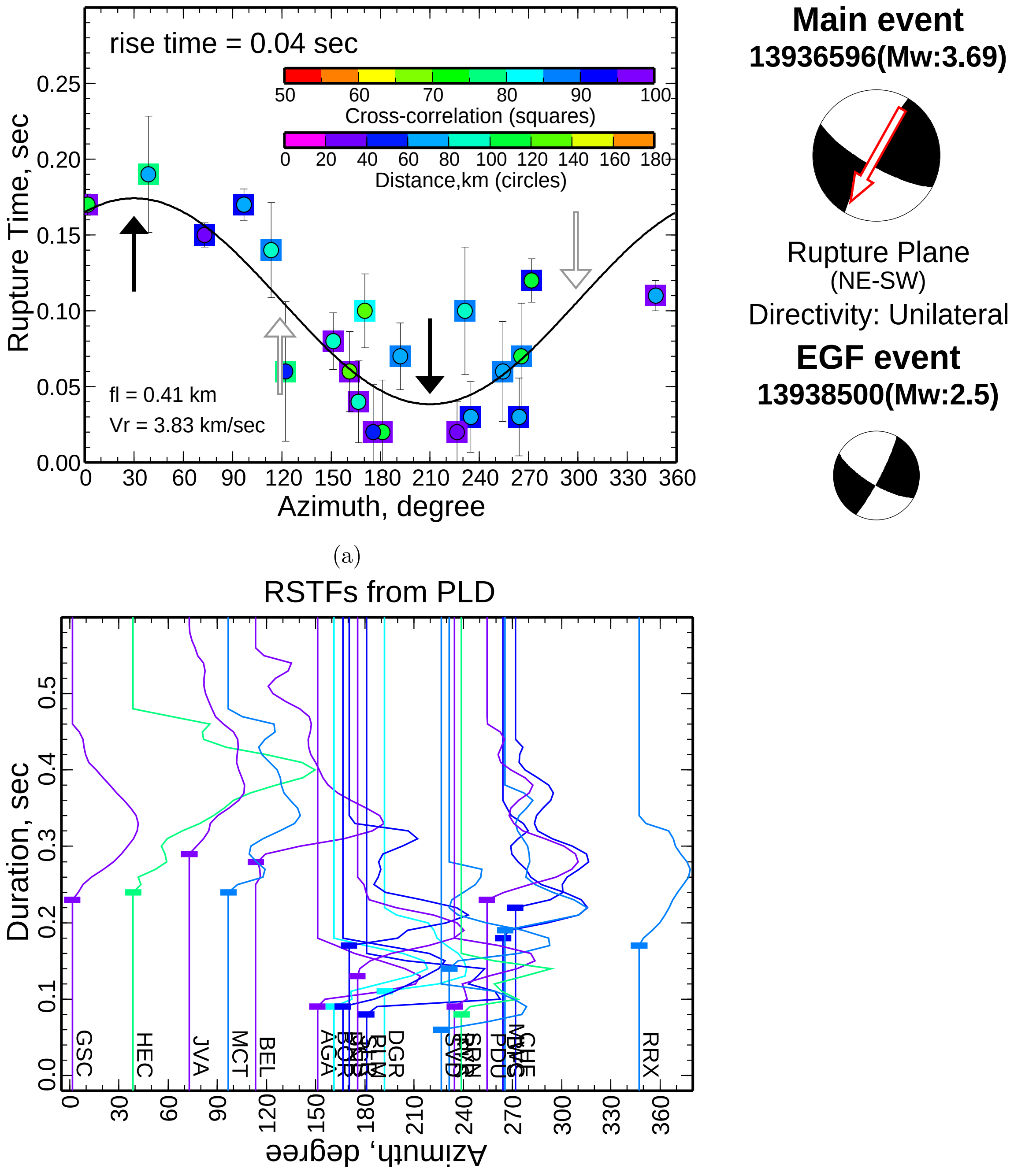

(a)

(b)

Figure 2.23: (a) The rupture time *vs.* azimuth corresponding to the best τ_1 estimate of 0.04 sec for event 13936596. (b) The source time functions (RSTFs) of event 13936596 relative to the EGF event 13938500 obtained by deconvolution. The short bars marking the onsets of the RSTFs indicate the durations of the RSTFs. The traces are color-coded by cross-correlation.

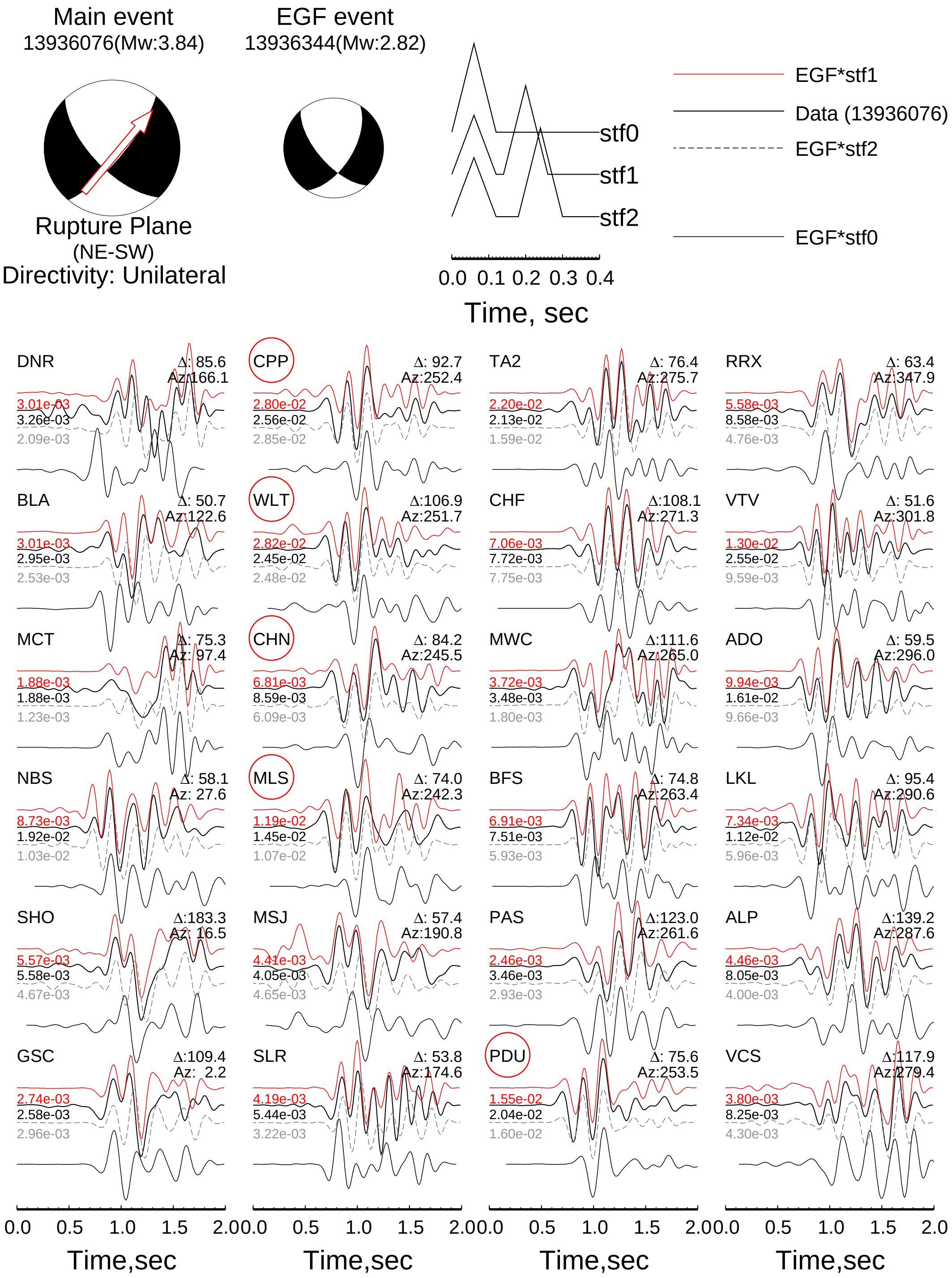

Figure 2.24: The waveform comparison between the records from event 13936076 and the associated EGF event 13936344. The four traces for each station, from top to bottom, are the EGF record convolved with source time function "stf1", the record from event 13936076, the EGF record convolved with "stf2" and the EGF record convolved with the single pulse source time function "stf0" respectively. Note the double-pulse source time function "stf1" applies well to most stations. However, the few stations (circled) that are located to the southwest end of the NE-striking fault plane require larger separations between the subevents.

for most of the stations. However, the few stations (circled in Fig. 2.24) within a certain azimuthal range clearly prefer the larger separation between the subevents as in the source time function “stf2”. Such azimuthal discrepancy is robust although the details of the subevents, or their “exact” separation are not well resolved due to the intrinsic trade-offs between them. The easiest interpretation suggests rupture propagation towards the northeast on the NE-striking fault plane (Fig. 2.24). The details of the rupture process for event 13936076 still warrant further study.

Event 13938812 has the largest magnitude among the studied events. However, it does not display any clearer signal of a unilaterally propagating rupture than we have seen for event 13937492 (Fig. 2.21) or 13936596 (Fig. 2.23). Figure 2.25(a) shows the τ_2 estimates for this event from the forward modeling approach. The rise time τ_1 has been assumed to be 0.10 sec, which minimized the total misfit error from all the stations. Although the azimuthal variation in τ_2 is considerably smaller compared to the typical unilateral ruptures (event 13937492 or 13936596), it is systematic and well resolved. In particular, τ_2 reaches a well defined minimum at $\sim$215°. Moreover, the relative source time functions (RSTFs) obtained from deconvolution provide complementary evidence (Fig. 2.25(b)), where the durations of the RSTFs display a similar azimuthal pattern as the τ_2s in Fig. 2.25(a). We first fit the τ_2s with a unilaterally propagating rupture towards the southwest on the NE-striking fault plane (the dashed line) following Eq. 2.13. The least-squares fit well explains the general azimuthal trend of τ_2, though some details are missed, such as for the couple of stations near the predicted τ_2 maximum. The resulted rupture velocity of $\sim$1.0 km/sec suggests very slow rupture propagation, while the small fault length (0.17 km) implies considerable vertical dimension of the ruptured area or high stress drop. We also investigated the other interpretation of a bi-lateral rupture, where the

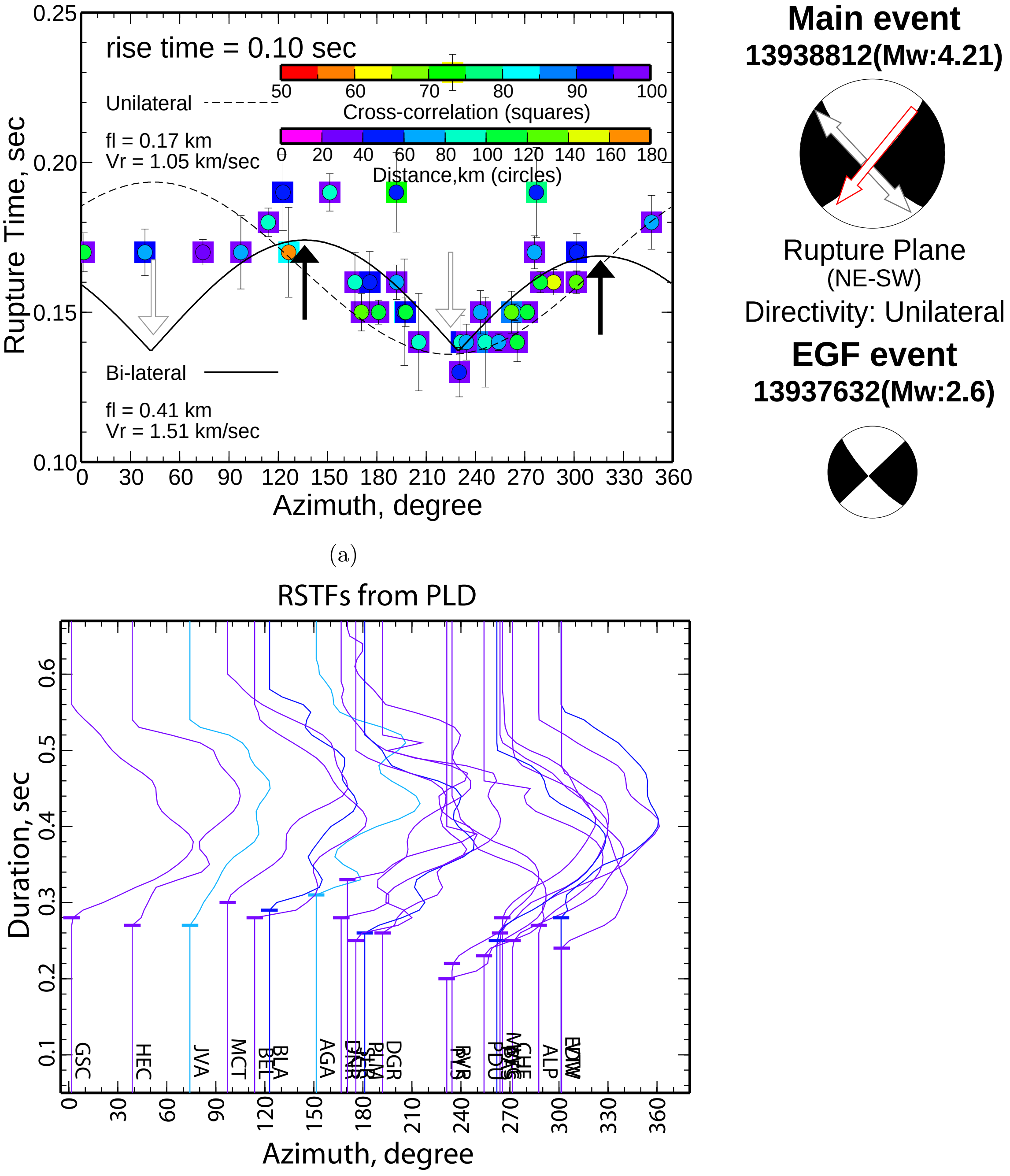

(a)

(b)

Figure 2.25: (a) The rupture time τ_2 corresponding to the best τ_1 estimate of 0.10 sec from the forward modeling approach *vs.* azimuth for event 13938812. The solid line indicates the least-squares fit of a bi-lateral rupture, while the dashed line stands for the unilateral rupture. The black arrows denote the NW-striking fault plane for bi-lateral rupture while the gray arrows denote the NE-striking fault plane for unilateral rupture. (b) The source time functions (RSTFs) of event 13938812 relative to the EGF event 13937632 obtained by deconvolution.

τ_2s can be predicted as

$$\tau_2 = max(\tau_2^{(1)}, \tau_2^{(2)}), where \tag{2.14}$$

$$\tau_2^{(1)} = Ra \cdot \frac{fl}{V_r}\{1 - \frac{V_r}{v_p}[cos(\varphi - \phi)cos(\lambda) - sin(\varphi - \phi)sin(\lambda) * cos(\delta)]\}, \tag{2.15}$$

$$\tau_2^{(2)} = (1 - Ra) \cdot \frac{fl}{V_r}\{1 - \frac{V_r}{v_p}[cos(\varphi - \phi)cos(-\lambda) - sin(\varphi - \phi)sin(-\lambda) * cos(\delta)]\}. \tag{2.16}$$

"*Ra*" introduced in Eq. 2.16 is a length ratio indicating where the rupture has initiated between the two ends. The least-squares fit of a bi-lateral fault (the solid line) produces equally well fit to the τ_2s as the unilateral fault (Fig. 2.25), since the fits are mainly controlled by the data points with azimuths over ∼150°. The resulting fault length becomes compatible (0.41 km) with the event's size, while the rupture velocity remains rather slow (∼1.5 km/sec). To make a distinction between the unilateral fault and bi-lateral fault in Fig. 2.25 mainly depends on the observations within the azimuthal range of ∼0°–120°. We prefer the unilateral rupture, since we did not observe any significant decrease in τ_2 within that particular azimuthal range when we used other events for EGFs; instead, higher τ_2s were common. Besides, the τ_2 minimum at ∼215°was well defined in all these experiments. The detailed rupture process, and particularly the vertical extent of the ruptured area needs further study.

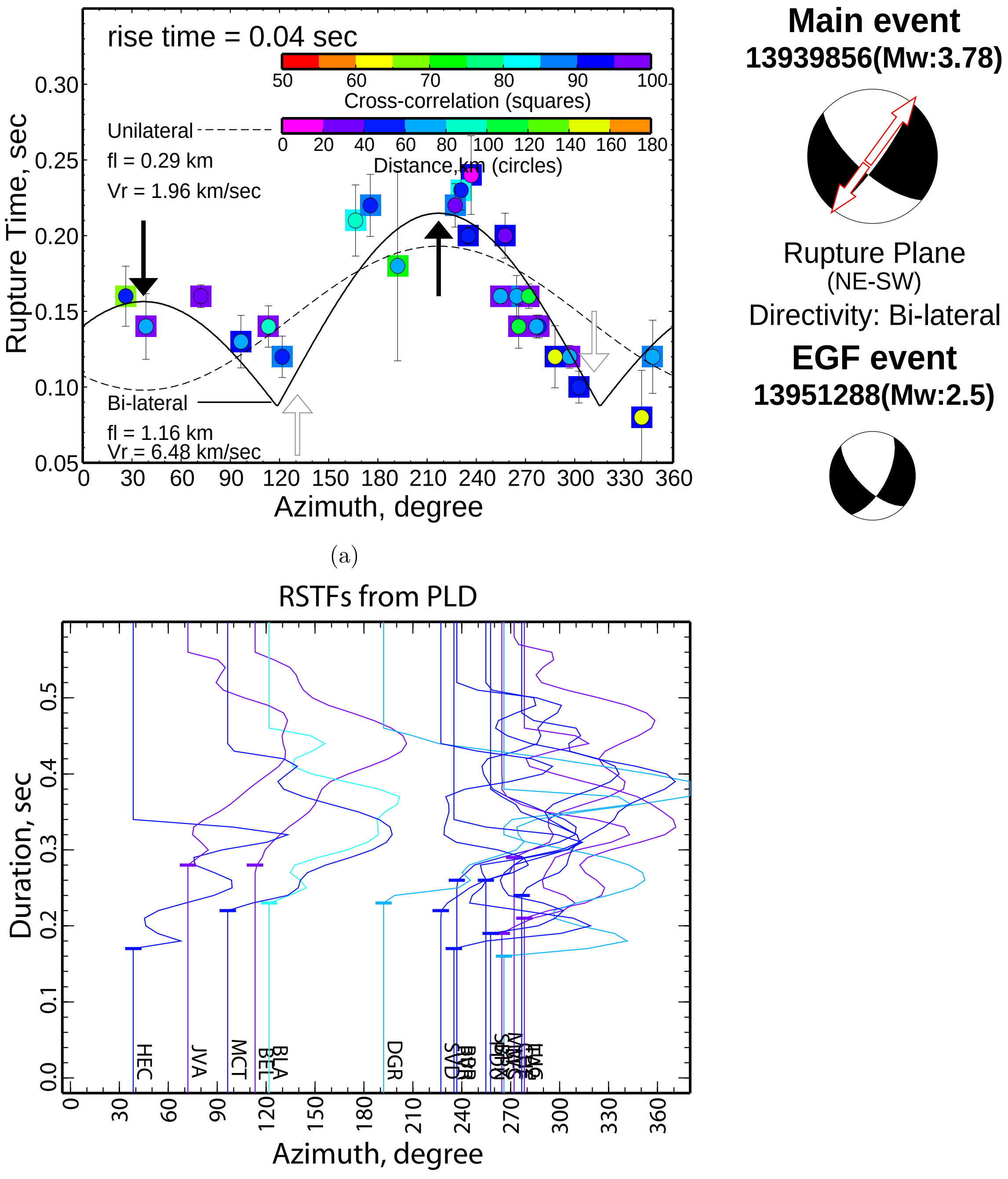

(a)

(b)

Figure 2.26: The rupture time τ_2 corresponding to the best τ_1 estimate of 0.04 sec from the forward modeling approach *vs.* azimuth for event 13939856. The solid line indicates the least-squares fit of a bi-lateral rupture, while the dashed line stands for the unilateral rupture. Note the bi-lateral rupture explains the azimuthal pattern of τ_2 much better. (b) The source time functions (RSTFs) of event 13939856 relative to the EGF event 13951288 obtained by deconvolution.

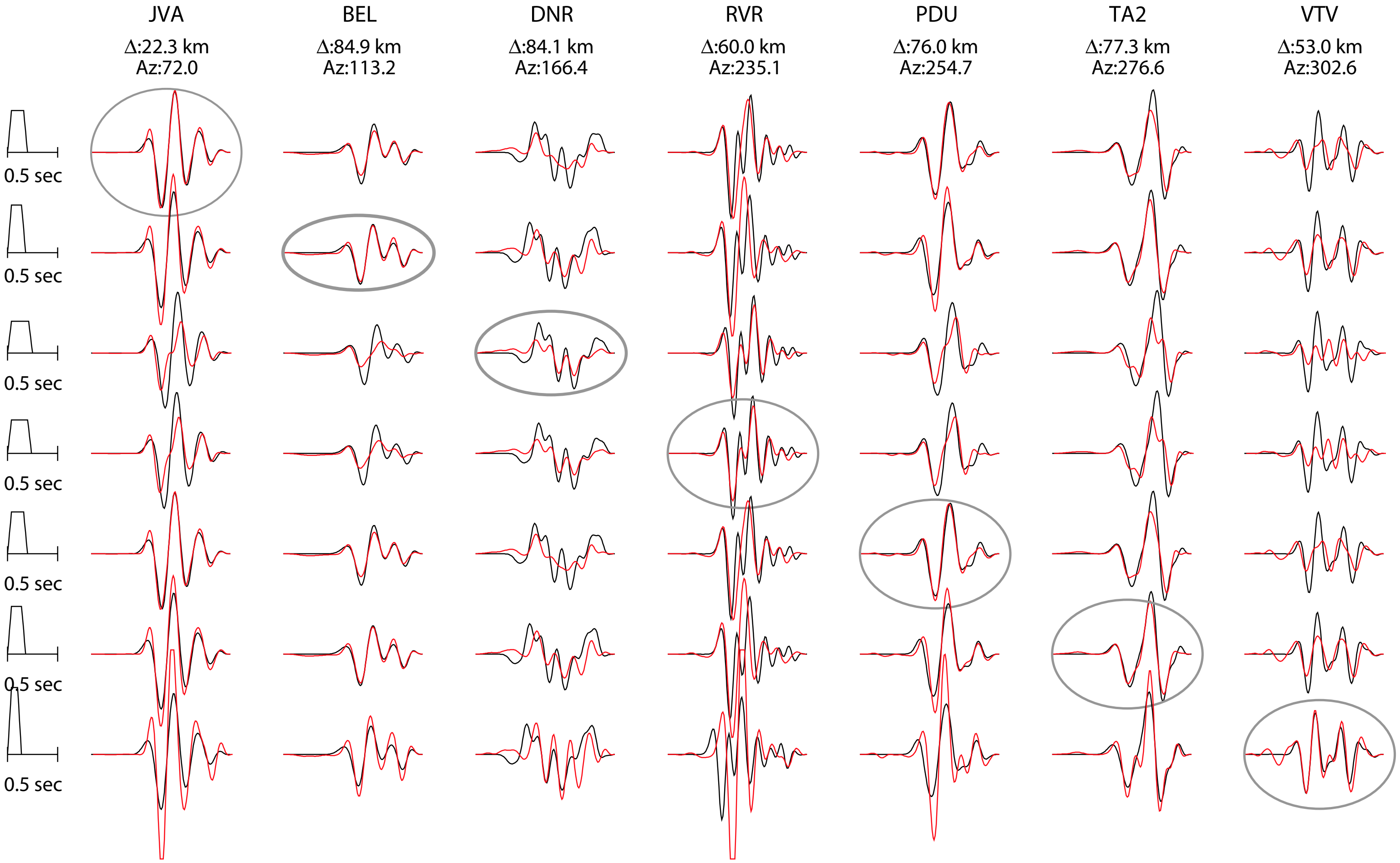

Figure 2.27: The selected waveform fits (Vertical P waves) between the records from event 13939856 (black) and the "synthetics" (red) constructed with EGFs from event 13951288. The relative source time functions (RSTFs) are given to the left. Plotted are the absolute amplitudes, except that a scaling factor of 1/4, 1/4, 1/3 and 1/3 has been applied to the stations JVA, PDU, TA2 and VTV respectively for display purposes. The obtained best RSTFs for the stations are circled. Note the apparent azimuthal pattern of the RSTFs.

The rupture time estimates for event 13939856 display large azimuthal variations (Fig. 2.26), which are in fact well resolved in the waveform comparisons (Fig. 2.27). The azimuthal pattern of τ_2 suggests either unilateral rupture on the NW-striking fault plane, propagating towards the southeast, or the bi-lateral rupture on the NE-striking fault plane, though the bi-lateral rupture explains the azimuthal trend of τ_2 better. However, the resulting fault length (~1.2 km) and the extremely large rupture velocity (~6.5 km/sec) from the bi-lateral fault cause some concerns. Moreover, such an azimuthal pattern is hardly discernible in the durations of the relative source time functions by deconvolution. Similar results have been obtained when we use other events for EGFs, suggesting the reality of event 13939856. Further study is therefore needed to clarify the discrepancy and explore the detailed rupture process of this event.

The rupture time estimates for event 13936432 display no systematic azimuthal variation (Fig.2.28(a)). In fact, the τ_2s tend to approximate a constant value (~0.07 sec), although there is some scatter. Such a uniform τ_2 is well confirmed when we directly compare the records from event 13936432 to the EGFs from event 13937200 (Fig. 2.29). Note the effectiveness of a uniform source time function in explaining the records from event 13936432 sampling the whole azimuthal range. Besides, the relative source time functions (RSTFs) of event 13936432 obtained by deconvolution (Fig. 2.28(b)) also suggest the lack of rupture directivity. Consequently, we are not able to resolve the primary and auxiliary fault plane ambiguity for event 13936432. However, a note worthy feature for this event (Fig. 2.28) is its relatively short source duration (~0.15 sec). This discovery is consistent with the measurement by energy ratio comparison (Fig. 2.18), where event 13936432 appears an outlier due to its short source duration, implying high stress drop of the event.

We summarize the inferred rupture directivities of our studied events in Fig. 2.30 together with the time evolution of the whole sequence. The main shock (13935988) that was discussed earlier (Fig. 2.6) has also been included. Apparently, unilateral ruptures dominate in Fig. 2.30. The inferred rupture planes have provided clear evidence for crossover faults at depth. There is in general good agreement between

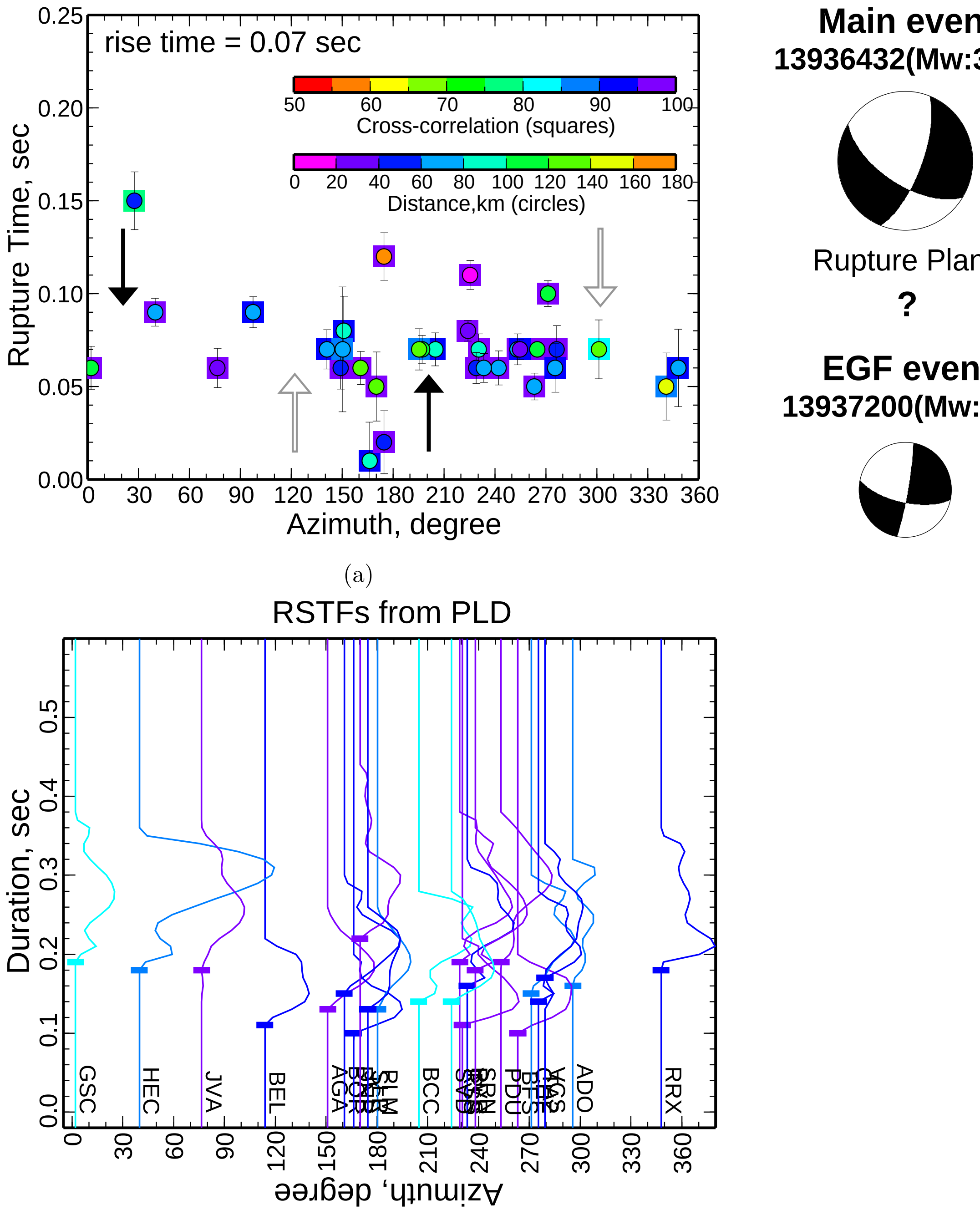

(a)

(b)

Figure 2.28: The rupture time τ_2 corresponding to the best τ_1 estimate of 0.07 sec from the forward modeling approach *vs.* azimuth for event 13936432. The black and gray arrows indicate the strikes of the two fault planes. (b) The source time functions (RSTFs) of event 13936432 relative to the EGF event 13937200 obtained by deconvolution.

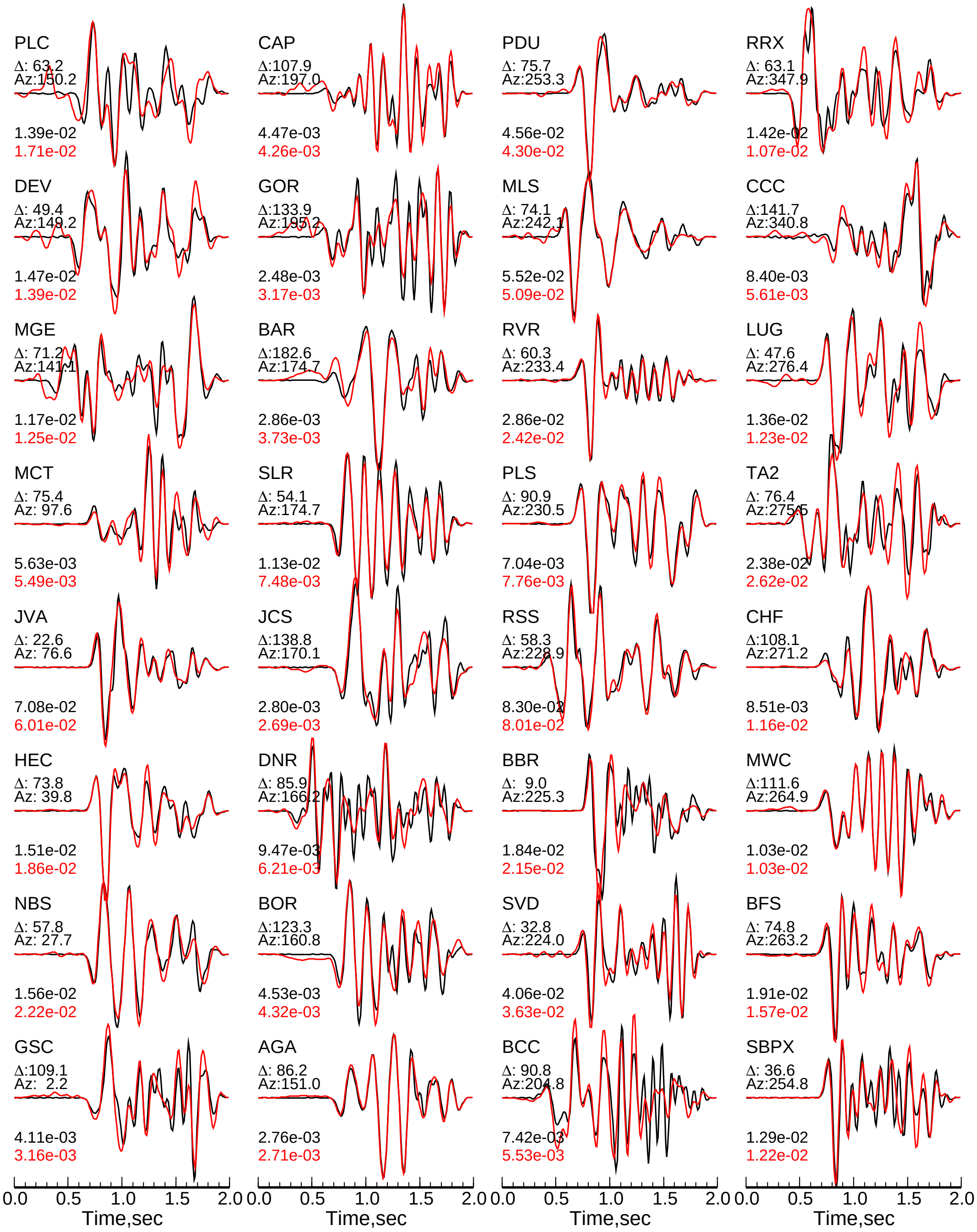

Figure 2.29: The records (vertical P waves) from event 13936432 (black) are compared with the "synthetics" (red) constructed from the EGFs assuming a uniform triangular (0.07–0.07 sec) source time function. A band-pass filter of 0.5–12 Hz has been applied. The amplitudes of the plotted traces are normalized by the maximum values given below the traces. Note the remarkable match between the shapes and amplitudes over the whole azimuthal range.

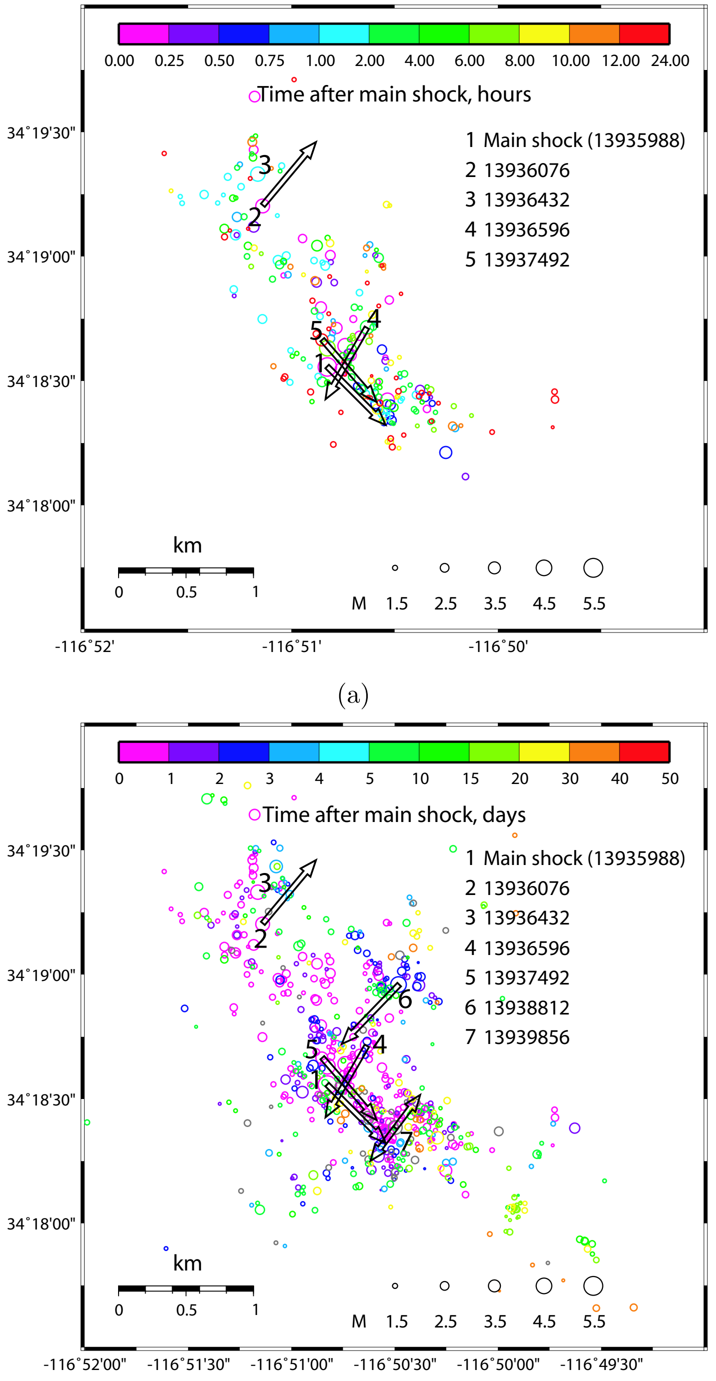

(a)

(b)

Figure 2.30: Time evolution of the 2003 Big Bear sequence for the first day after the main shock (a) and the first 50 days (b). Event locations are from *Chi and Hauksson* (2006) with a double-difference approach. Labeled according to their occurrence in time are the events that we have investigated for rupture directivity. The arrows indicate the strikes of the ruptured fault planes plus the rupture propagation directions.

the rupture planes and the seismicity lineations, except for the events 13936076 and 13938812. However, there is little correlation between rupture propagation and the aftershock activities, except for the main shock.

2.9 Conclusions

In this chapter, we developed a "two-way" calibration technique for studying clustered events, particularly their mechanisms and rupture processes. First, we demonstrate that the magnitude 4 events with known source mechanisms can be used to calibrate the path effects on the short-period (0.5-2 sec) P waves, so that the corrected P waves can be modeled for determining focal mechanisms of the smaller events within the cluster. The correction is formulated in terms of a station-specific "Amplitude Amplification Factor" (AAF), whose origin is mainly due to the site effect. Second, we show that the smaller events with radiation pattern corrections provide excellent empirical Green's functions (EGFs) for investigating the detailed rupture processes of the magnitude 4 events. In particular, we applied our methods to the 2003 Big Bear sequence. Our main results indicate that (1) Short-period (0.5-2 sec) P waves can be used for determining focal mechanisms of events as small as $M \sim 2$, provided necessary path calibration. (2) Magnitude 4 events display various detailed rupture processes.

Chapter 3

Locating and Modeling Regional Earthquakes with Two Stations

3.1 Abstract

We developed a new technique CAPloc to retrieve full source parameters of small seismic events from regional seismograms, which include origin time, epicenter location, depth, focal mechanism, and moment magnitude. Despite rather complicated propagation effects at short periods, a simple localized 1-D model can well explain signals of periods 3–10 sec if we break the three-component records into different segments and allow differential time shifts among them. These differential time shifts, once established from a calibration process or a well-determined tomographic map, can be used together with P wave travel times to refine an event's location. In this study, we tested whether our new method could produce satisfactory results with as few as two stations, so that we can improve source estimates of poorly monitored events with sparse waveform data. We conducted the test on 28 events in the Tibetan plateau. The focal mechanisms and locations determined from only two stations agree well with those determined from a whole PASSCAL array. In particular, our new method produces better locations than ISC, with the average mislocation error reduced from $\sim$16 km to $\sim$5 km. We also tested whether an event's depth and mechanism can be determined separately from its epicenter relocation in a two-step approach. We find that the two-step approach does not always give the correct solution, but the reliability of a solution can be evaluated using a reduced chi-square value.

3.2 Introduction

Rapid characterization of a seismically recorded event has been one of the major themes of seismic monitoring. An efficient and accurate way to retrieve the hypocenter, mechanism, origin time and size of a seismic event is important for understanding tectonic processes, and responding to earthquake hazards, as well as discriminating nuclear explosions from natural earthquakes.

Classic methods assume a good seismic velocity model and use travel times of certain seismic phases, usually the direct P and/or S wave, to locate an event's hypocenter, and phase polarities for determining the focal mechanism. Consequently, the accuracy of the solutions depends on the station coverage, since most velocity models used are good only for a global average. In that sense, large events with magnitude greater than $\sim$5.5, which are readily recorded globally, are usually well determined. However, a much larger population of smaller events, where only limited regional data ($\Delta <10°$) have adequate signal-to-noise ratio (SNR), are more prone to biases caused by structural heterogeneity.

A reinforced regional seismic network allows enough redundancy to average out some of the local complications. The implementation of TriNet with over 150 broadband stations in southern California is such an example, where an event's origin time, hypocenter, mechanism and size are well determined and reported on the Internet within minutes (*Hauksson*, 2001). Similar real-time systems have been developed in recent years in other seismically active regions to monitor seismic activity for rapid notification and damage assessment (e.g. *Teng et al.*, 1997; *Okada et al.*, 2004). In addition, temporarily deployed dense local seismic networks have provided rare opportunities to retrieve reliable regional source parameters in some geologically interesting, but remote areas (e.g. *Leitner et al.*, 2001; *Langin et al.*, 2003). However, although these well-determined regional events prove useful to constrain the thermal structure and understand the active tectonics, a substantial increase in their number is needed to further explore spatial and temporal variations. Therefore, a reliable method is needed to extract accurate source parameters from sparse recordings of poorly monitored events. These could be historical events that occurred before the modern era of dense instrumentation in southern California, or those in some remote areas, such as Southeastern Asia or the Middle East. Our method will also support the verification of the Comprehensive Nuclear Test-Ban Treaty (CTBT), which requires accurate location determination of global seismicity with a fixed teleseismic network (*Kennett and Ringdal*, 2001).

Better utilizing a limited data set becomes the major concern in developing such a method. Efforts are basically divided into two categories, focusing on accurate source location and focal mechanism, respectively. Tremendous work has been done to better locate a seismic event in the context of the CTBT. Various strategies include developing new techniques for more accurate travel time measurements, utilizing travel times together with slowness and azimuth information (e.g. *Bondár and North*, 1999; *Bondár et al.*, 1999; *Uhrhammer et al.*, 2001), implementing better regional velocity models (e.g. *Kremenetskaya et al.*, 2001), and deriving various source-specific station corrections (e.g. *Yang et al.*, 2001a,b; *Ryaboy et al.*, 2001). At the same time, rather than focusing on travel times of impulsive body wave phases, *Yacoub* (1996) reported locations of 16 nuclear explosions that were well determined by using arrival times of the maximum Rayleigh wave energy estimated over a narrow frequency band of 17–23 s, in the same manner as P-wave travel times are used. Similar experiments and results were reported later by *Stevens et al.* (2001). The improvement on epicenter location from various validation tests is encouraging. Accurate depth determination is, however, still an open issue.

On the other hand, modeling regional seismograms provides the only opportunity to constrain an event's source mechanism accurately when a reliable first motion focal plot cannot be constructed. Early work by *Langston* (1981) showed that the relative amplitudes of P, SH and SV waveforms from a WWSSN station are sufficient to discriminate between fault types. With the development of modern broadband seismic instrumentation and the success in modeling broadband records, *Dreger and Helmberger* (1993) demonstrated the feasibility of retrieving stable source orientations using long period body waves (mainly Pnl and S_n) from a couple of early southern

California broadband stations. Their work paralleled that of *Fan and Wallace* (1991) in New Mexico. Surface waves also prove useful in source mechanism determination as demonstrated by several authors addressing different periods ((*Thio and Kanamori*, 1995, 10–50 s); (*Romanowicz et al.*, 1993, 15–50 s); (*Ritsema and Lay*, 1993, >50 s)). However, the methods using surface waves alone require some azimuthal sampling around the source, which makes them less effective in cases, in which only a few stations are available. A step forward in using both body and surface waves was made in the so-called "cut and paste" method (CAP) (*Zhao and Helmberger*, 1994; *Zhu and Helmberger*, 1996), where body wave and surface waves from entire records are separated and modeled with differential time shifts between them allowed. This method desensitizes the timing between the principal crustal arrivals; hence, accurate source estimates could be achieved with imperfect Green's functions.

Here, based on an expansion of the CAP method, we present a joint effort to determine both event locations and focal mechanisms using complete 3-component regional seismograms. We call the new method CAPloc to distinguish it from the original CAP. The basis of the method lies in the fact that, as the waveforms of major seismic arrivals constrain an event's source depth and orientation, their differential travel times define the epicenter location. To put the method into practice requires calibration of the regional paths. In an earlier study, *Zhu et al.* (2006) conducted an effective calibration process with a temporary PASSCAL array on the Tibetan plateau. We will validate our method by demonstrating its ability to recover essentially the same source parameters derived from a well-distributed array with only two fixed stations.

3.3 Methodology

Let $u(t)$ be a recorded seismogram with instrument response removed. The corresponding synthetics $s(t)$ for a double-couple source can be expressed as a summation of contributions from three fundamental faults, namely, vertical strike slip, vertical dip slip and 45° dip slip:

$$s_j(t) = M_0 \sum_{i=1}^{3} A_{ij}(\phi - \varphi(\theta, \xi), \delta, \lambda) G_{ij}(h, \Delta(\theta, \xi), t), \tag{3.1}$$

where $j = 1, 2, 3$ denotes the vertical, radial and tangential component, respectively (*Helmberger*, 1983). The G_{ij}s are the Green's functions, and the A_{ij}s are the radiation coefficients. M_0 is the scalar moment. φ and Δ are the station azimuth and distance. The unknowns, h (depth), ϕ (strike), δ (dip) and λ (rake), which describe the source depth and orientation, together with θ (event latitude) and ξ (event longitude), which define the epicenter location, can be obtained by solving the equation

$$u(t) = s(t). \tag{3.2}$$

Since there are only limited unknowns and all of them are confined within a certain range of values, it is straightforward and convenient to solve the equation in a grid search manner.

However, solving Eq. 3.2 with an entire regional record is problematic. First, regional records are usually complicated by 3-D path and site effects. In particular, different portions of the records, e.g., the body wave (*Pnl*) and surface waves, which sample different parts of the crust, require different adjustments on the 1-D Green's functions over different frequency bands. Secondly, whole-waveform inversion is easily dominated by the strongest signals, usually the surface waves. To overcome these difficulties, we expand the original CAP source estimation technique (*Zhao and Helmberger*, 1994; *Zhu and Helmberger*, 1996), which breaks an entire record into *Pnl* and surface wave segments to be modeled separately.

We use the chi-square χ_w^2 as our object function:

$$\chi_w^2 = \frac{e_{Pnl}}{\sigma_{Pnl}^2} + \frac{e_{Sur}}{\sigma_{Sur}^2}, \tag{3.3}$$

where the waveform misfit errors

$$e_{Pnl} = \|u^{Pnl}(t) - s^{Pnl}(t - \Delta T)\|, \tag{3.4}$$

$$\begin{aligned} e_{Sur} = {} & \|u^{Rayleigh}(t) - s^{Rayleigh}(t - \Delta T - \delta t^{Rayleigh})\| \\ & + \|u^{Love}(t) - s^{Love}(t - \Delta T - \delta t^{Love})\|. \end{aligned} \tag{3.5}$$

Here $\|\|$ denotes the L_2 norm. ΔT is the time shift to align synthetics with data on the first P arrival. The $\delta t^{Rayleigh}$ and δt^{Love} are the path-specific timing corrections for the synthetic Rayleigh and Love wave segments with respect to the first P arrival, which can be derived from a simple calibration process as discussed by *Zhu et al.* (2006) or using a well-determined tomographic map. These δts account for the deviations of real crustal structure from the 1-D model. They are a prerequisite for an accurate epicenter relocation. If we set them as free parameters to be determined by waveform cross-correlation in the grid search, the source depth and orientation can still be determined but not the epicenter location, since the mislocation errors are absorbed by these time shifts.

The parameters σ^2_{Pnl} and σ^2_{Sur} in Eq. 3.3 are the variances of waveform residuals of Pnl and surface waves. They measure how well the velocity model can explain the observed waveforms. We distinguish Pnl and surface waves, because they sample the velocity structure differently. Since σ^2_{Pnl} and σ^2_{Sur} are usually not known *a priori*, we conduct a series of trial grid searches with a range of $\sigma_{Sur}/\sigma_{Pnl}$ ratios to minimize

$$\chi'^2_w = \sigma^2_{Sur}\chi^2_w = \frac{\sigma^2_{Sur}}{\sigma^2_{Pnl}} e_{Pnl} + e_{Sur}. \tag{3.6}$$

The best $\sigma_{Sur}/\sigma_{Pnl}$ ratio is selected when the misfit errors of Pnl and surface waves are "equal":

$$\frac{1}{\nu_{Sur}} \frac{e_{Sur}}{\sigma^2_{Sur}} = \frac{1}{\nu_{Pnl}} \frac{e_{Pnl}}{\sigma^2_{Pnl}}. \tag{3.7}$$

Here, ν_{Pnl} and ν_{Sur} are the numbers of measurements from Pnl and surface wave waveform data, respectively. Since an individual data point on a seismogram strongly correlates with its neighbors, we count every duration of the dominant period as one independent "data point".

By using Eq. 3.7 and Eq. (4.26) of *Bevington and Robinson* (2003), σ^2_{Pnl} and σ^2_{Sur} can then be estimated *a posteriori* from the misfit errors of *Pnl* and surface waves at the best solution:

$$\sigma^2_{Pnl} = \frac{\nu_{Pnl} + \nu_{Sur}}{\nu_{Pnl} + \nu_{Sur} - m} \frac{e_{Pnl}}{\nu_{Pnl}}, \tag{3.8}$$

$$\sigma^2_{Sur} = \frac{\nu_{Pnl} + \nu_{Sur}}{\nu_{Pnl} + \nu_{Sur} - m} \frac{e_{Sur}}{\nu_{Sur}}, \tag{3.9}$$

where m is the number of unknown source parameters.

Thus, the relative weight between *Pnl* and surface waves in our new CAPloc is adaptive as compared to a fixed value in the original CAP (*Zhu and Helmberger*, 1996). Later we will show that a static weighting factor of *Pnl* to surface waves is not appropriate, especially when few stations are used.

We can place an additional constraint on the event location by minimizing P wave travel-time residuals

$$\chi^2_t = \frac{1}{\sigma^2_t} \sum_{n=1}^{N} \left(\Delta T_n - \frac{1}{N} \sum_{n=1}^{N} \Delta T_n \right)^2, \tag{3.10}$$

where σ^2_t represents the variance of the residuals. Provided that structural effects on these travel-time residuals can be corrected by a path calibration or tomographic study, σ^2_t mainly measures uncertainty in picking P wave arrivals. The average of the travel-time residuals, $\frac{1}{N}\sum_{n=1}^{N} \Delta T_n$, implies an offset in the event's origin time.

We simply search through the whole parameter space of all the unknowns h, ϕ, δ, λ, θ and ξ, and determine the best solution of the source parameters where

$$\chi^2 = \chi^2_w + \chi^2_t, \tag{3.11}$$

is minimized. However, since the waveforms of *Pnl* and surface waves are mainly controlled by source depth and orientation, while their travel times only depend on event location, we can also separate the whole parameter space into two subspaces of (h, ϕ,

δ, λ) and (θ, ξ), and conduct two grid searches separately on them. The first one is to determine source depth and orientation with an event's preliminary epicenter location by minimizing χ_w^2, where $\delta t^{Rayleigh}$ and δt^{Love} are set as free parameters determined by waveform cross-correlation to account for both event mislocation and structural effects. Then, using the obtained source depth and mechanism, a second grid search is conducted for a better epicenter location, where the surface wave segments are no longer allowed to float, but fixed with predetermined time shifts from either path calibration or seismic tomography. Compared to the one-step approach, this two-step approach has the advantage of requiring less computation time. However, as might be predicted, a wrong source depth or mechanism from the first step could lead to a wrong relocation. In the next section, we will test both approaches.

3.4 Applications

3.4.1 Data

The Tibetan plateau was chosen as our test bed mainly based on two considerations. First, Tibet itself is a seismically active, but poorly monitored region with a sparse short-period network plus a couple of modern broadband instruments. Second, *Zhu et al.* (2006) obtained useful calibration information for various regional paths on the plateau using data collected by a temporary PASSCAL experiment in 1991–1992 (*Owens et al.*, 1993). Moreover, the events they have studied with locations, depths, and mechanisms well determined from the whole PASSCAL array are ideal for testing the validity of our new method. Fig. 3.1 displays locations of over 50 earthquakes investigated by *Zhu et al.* (2006). The average relocation offset with respect to the ISC locations is ∼16 km, excluding the two events mislocated by ISC by over hundreds of kilometers. The offsets generally correlate well with the ISC station coverage: smaller offsets are associated with better coverage.

To test our method, we choose two fixed stations, LHSA and TUNL, and the 28 events that were recorded by both. The two stations were separated by over

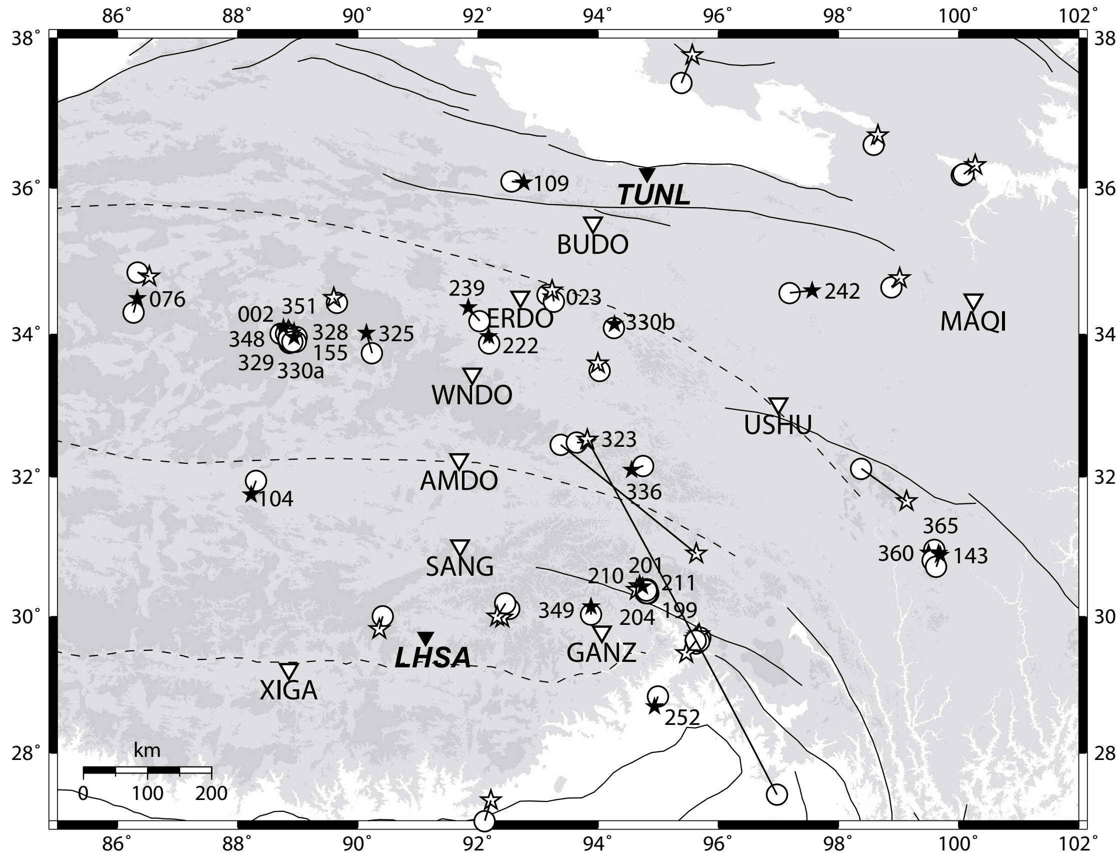

Figure 3.1: Temporary stations (inverted triangles) of the 1991-1992 PASSCAL experiment on the Tibetan plateau are displayed with 53 recorded earthquakes. The circles represent the events' ISC locations, and the stars represent their relocations using the full array by *Zhu et al.* (2006). The filled stars indicate the 28 events selected in this study, which were recorded by both stations LHSA and TUNL (solid triangles). Labeled are their Julian day numbers.

five hundred kilometers, so they provide nearly independent constraints for all of the selected events. Furthermore, they are the sites of two permanent broadband seismic stations in Tibet. Therefore, our study will benefit future earthquake source determination in the region. Using the same two stations for all the events can avoid possible biases in data selection and ensure a fair assessment of our method.

Three-component seismograms of an event 330b located between the two stations are displayed in Fig. 3.2 as an example. The data are shown in different frequency bands. Note that one advantage of having broadband waveform data is that several crustal phases can be well recognized when the waveforms are examined in different frequency bands. For example, while the long-period Pnl waves are weak, the short-period P waves are strong and useful for picking P wave arrival times and polarities. Different bandpass filters, 3–20 s for Pnl and 10–50 s for surface waves, are chosen mainly based on previous waveform modeling results. For example, *Zhu and Helmberger* (1996) found that allowing short-period energy ($\sim$ 3–20 s) into the Pnl window helped resolve the depth phases. Surface waves at short periods are heavily influenced by shallow crustal structures, but they are stable over a lower frequency band of 10–50 s (see also *Ritsema and Lay*, 1993). Although we have examined other frequency ranges, the filters applied on the records shown in Fig. 3.2 proved optimal, thus were used throughout this study.

In the following, we will apply the two approaches of our method to the selected 28 events using the two stations and compare the results with those determined from the whole PASSCAL array (*Zhu et al.*, 2006). We use the same 1-D Tibetan velocity model (T93) by *Zhu et al.* (2006) to facilitate the use of the path calibration they developed. The Green's functions are computed using a reflectivity code (*Zhu and Rivera*, 2002) with a 5 km interval in both depth and distance.

3.4.2 The one-step approach

We first test the one-step approach, where the source depth, mechanism and epicenter location are simultaneously determined in one grid search. The target parameter space of strike, dip, rake and depth is chosen as 0°–360°, 0°–90°, -90°–90°, and 0–40 km, respectively. For each event, we search the epicentral area of a $1^\circ \times 1^\circ$ square surrounding its ISC location. A searching step of 10° is used for the fault parameters, 5 km for the depth and 0.05° for both the latitude and longitude since our Green's functions are computed with a 5 km interval. The time shifts of Rayleigh and Love waves, i.e., $\delta t^{Rayleigh}$ and δt^{Love}, are fixed to the corresponding empirical-path-specific corrections (EPSCs) established by the relocated events (*Zhu et al.*, 2006). However, to account for the discreteness of the finite grid size, we allow the δts to vary within

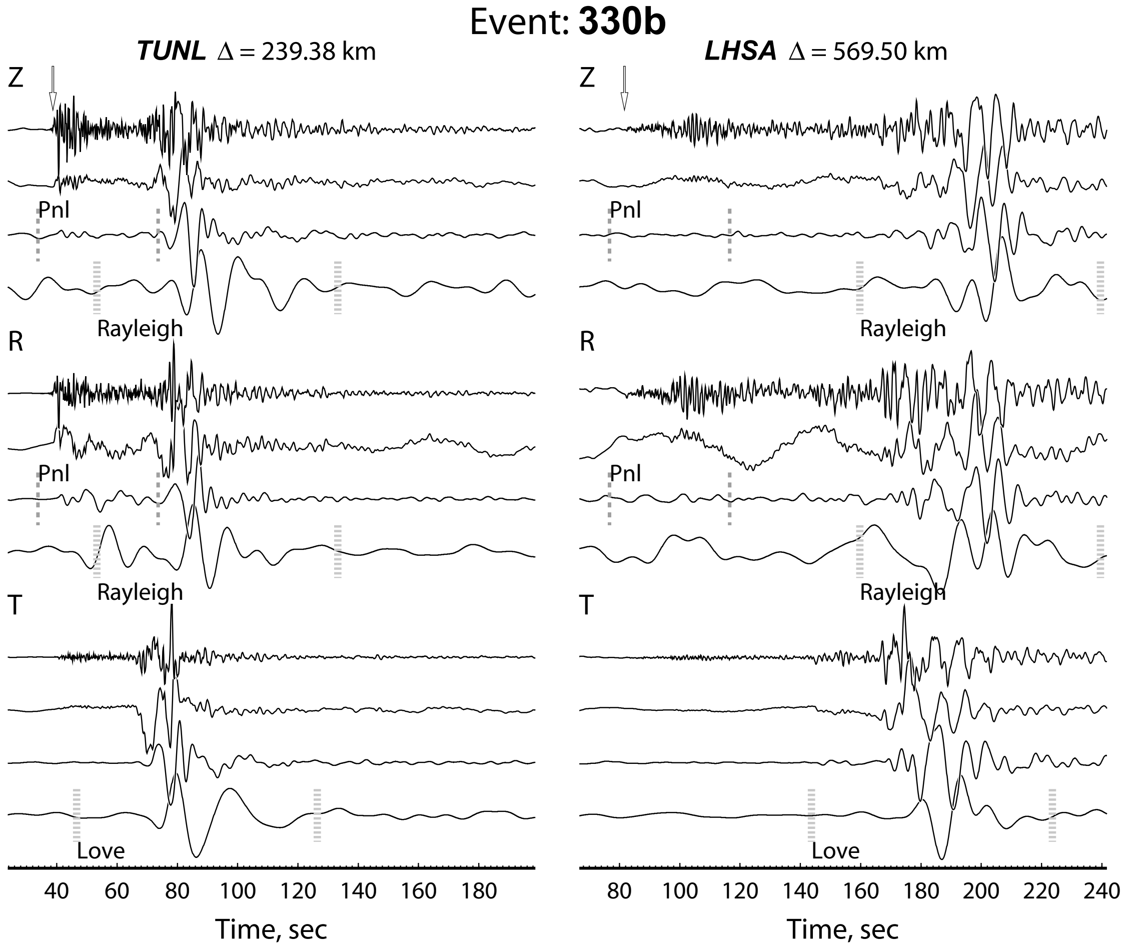

Figure 3.2: Three-component records from event 330b at the two stations, LHSA (left) and TUNL (right), are displayed in different frequency bands. The top trace of each component displays the broadband velocity record with an arrow on the vertical (Z) component indicating the onset of P wave. The following traces are the integrated displacements without filtering and with bandpass filters, 0.05–0.3 Hz and 0.02–0.1 Hz. The time windows of the Pnl and surface waves are determined by the epicentral distance using apparent velocities of P (6.5 km/s), S (3.8 km/s), Rayleigh (3.1 km/s), and Love (3.4 km/s) waves, as indicated by the dashed lines.

±0.5 s of the assigned values, as determined by waveform cross-correlation during the grid search. This is equivalent to assuming a 0.5 s uncertainty in the calibration result.

The whole procedure is illustrated in Figs. 3.3 and 3.4 with two events 222 and 104 as examples. We try a range of $\sigma_{Sur}/\sigma_{Pnl}$ ratios from 0.0 to 10.0 in the grid searches to minimize χ'^2_w in Eq. 3.6, and the best $\sigma_{Sur}/\sigma_{Pnl}$ ratio is selected when Eq. 3.7 is satisfied. Quite different $\sigma_{Sur}/\sigma_{Pnl}$ ratios, 1.6 for event 222 and 7.6 for event 104, are obtained (Figs. 3.3 and 3.4). The solutions of source parameters in the vicinity of the best $\sigma_{Sur}/\sigma_{Pnl}$ ratio appear rather stable. However, different depths, mechanisms, and epicentral locations are produced when the $\sigma_{Sur}/\sigma_{Pnl}$ ratio departs significantly from the best value. Consequently, the resulting waveform fits change. For event 222 (Fig. 3.3), as a $\sigma_{Sur}/\sigma_{Pnl}$ ratio of 4.0 over weights the *Pnl* waves, a shallower source of ∼5 km deep and northwestward by ∼15 km is produced compared to that with the best $\sigma_{Sur}/\sigma_{Pnl}$ ratio (1.6). Although the *Pnl* waves are slightly better fitted, the larger $\sigma_{Sur}/\sigma_{Pnl}$ ratio reduces the weight on the surface waves and causes apparently poorer Rayleigh wave waveform fits. Event 104 (Fig. 3.4) requires a much larger $\sigma_{Sur}/\sigma_{Pnl}$ ratio of 7.6. A small $\sigma_{Sur}/\sigma_{Pnl}$ ratio, such as 2.0, leads to a deeper source and a slightly changed mechanism. Though the waveform fits of surface waves remain similar, the larger $\sigma_{Sur}/\sigma_{Pnl}$ ratio puts more weight on the *Pnl* waves and subsequently improves the *Pnl* waveform fit at station LHSA, where the cross-correlation coefficients between the observed and synthetic *Pnl* waves are increased from 22/38 to 71/78 (Fig. 3.4). This underlines the importance of the adaptive weighting scheme between *Pnl* and surface waves in our CAPloc method. Since *Pnl* and surface waves provide nearly independent constraints in source characterization, and their amplitude ratio is a useful depth indicator, using both *Pnl* and surface waves is more effective and desired, particularly when few stations are used. An inappropriate relative weight between *Pnl* and surface waves, such as the static *Pnl* weight used in the original CAP by *Zhu and Helmberger* (1996), can easily cause an imbalance between the two, thus losing the constraint from the weaker component as shown in both Fig. 3.3 and 3.4. The large variation in $\sigma_{Sur}/\sigma_{Pnl}$ ratios obtained for

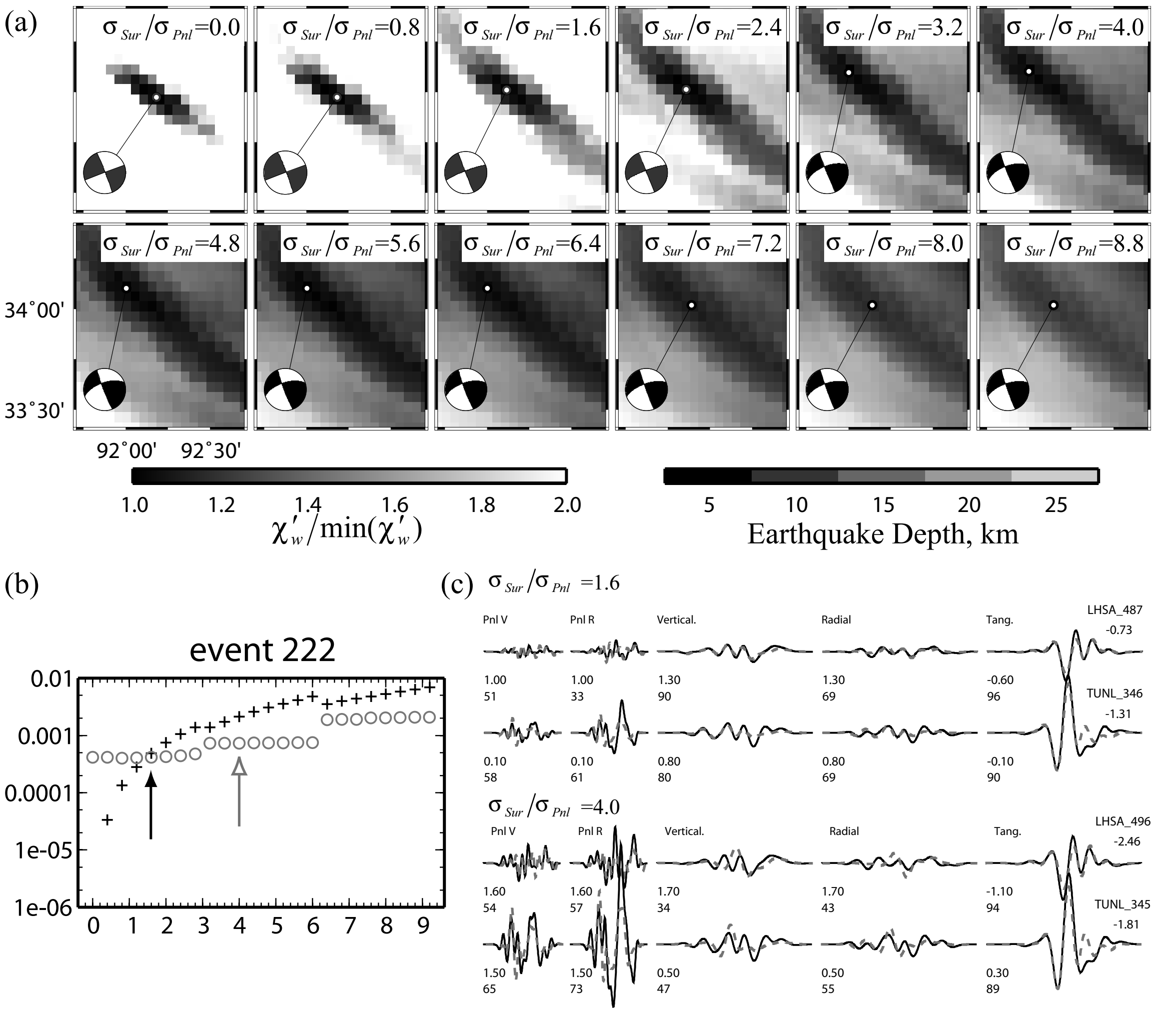

Figure 3.3: One-step grid-search results for Event 222. (a) The best solutions of source parameters with different $\sigma_{Sur}/\sigma_{Pnl}$ ratios. (b) The waveform misfit error as a function of $\sigma_{Sur}/\sigma_{Pnl}$ ratio. The crosses and circles display $\frac{\sigma^2_{Sur}}{\sigma^2_{Pnl}}\frac{\nu_{Sur}}{\nu_{Pnl}}e_{Pnl}$ and e_{Sur} respectively. The best $\sigma_{Sur}/\sigma_{Pnl}$ ratio is chosen when the two are equal (indicated by the black arrow). (c) The waveform fits from the solution with the best $\sigma_{Sur}/\sigma_{Pnl}$ ratio (1.6) are displayed in the upper panel. In the lower panel, we show those from the solution with a different $\sigma_{Sur}/\sigma_{Pnl}$ ratio of 4.0. The Pnl waves are plotted with the scaling factor of $\sigma_{Sur}/\sigma_{Pnl}$. The numbers below the traces are the differential time shifts in sec determined by cross-correlation (cc) and the corresponding cc coefficients.

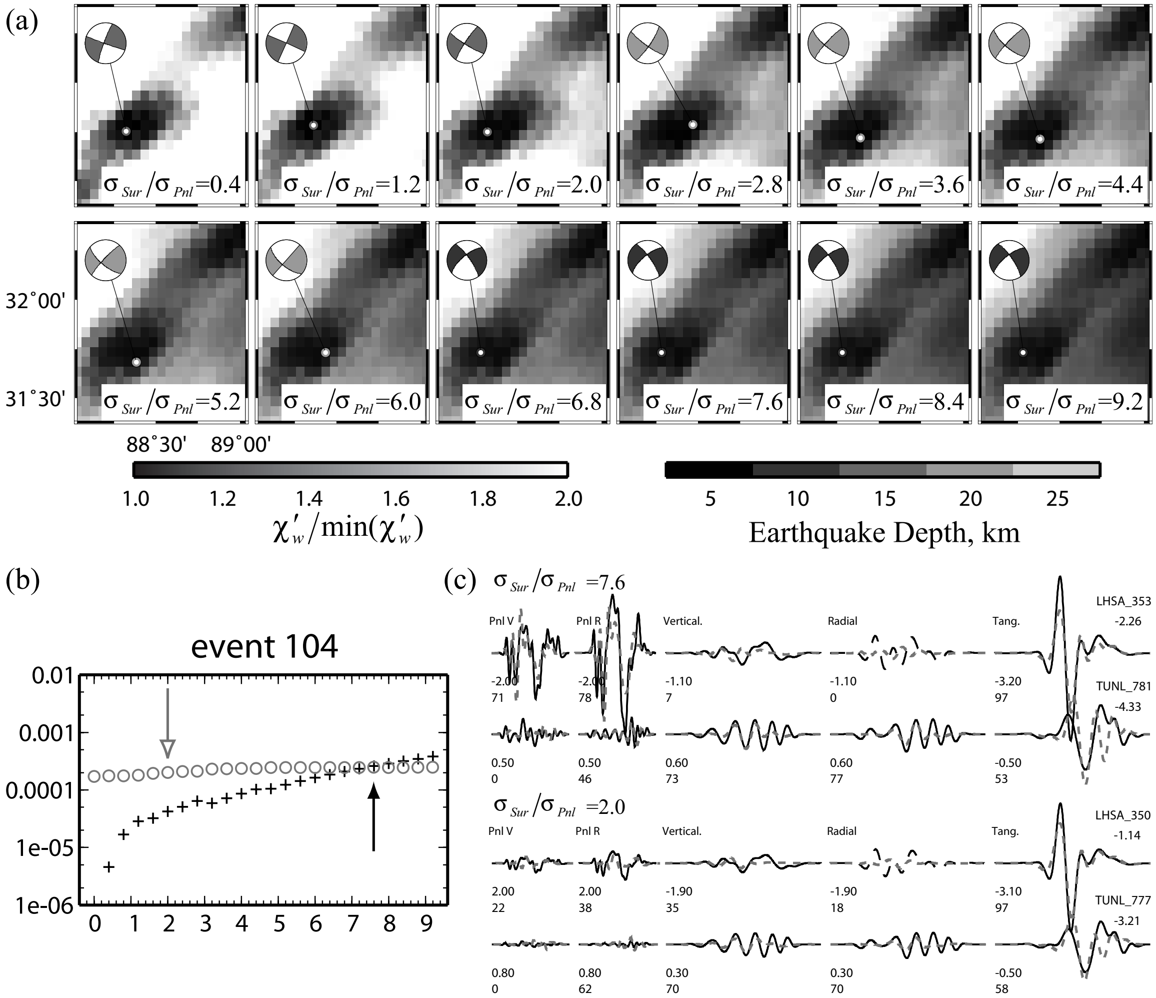

Figure 3.4: One-step grid-search results for Event 104. See the captions of Fig. 3.3 for details.

different events (see Table 3.1) is mainly due to the rather limited azimuthal coverage of the two stations.

We estimate the variances σ^2_{Pnl} and σ^2_{Sur} using the best $\sigma_{Sur}/\sigma_{Pnl}$ ratio from Eqs. 3.8 and 3.9. Then we add in the P-wave travel time constraint (Eq. 3.10) to find the best combination of source depth, mechanism and epicenter location that minimizes χ^2 in Eq. 3.11. A σ^2_t value of 0.09 s^2 is used by assuming an uncertainty of 0.3 s in reading P-wave arrival times. The results for all the 28 events are summarized in Table 3.1, and the details of 20 events are displayed in Fig. 3.5, where we choose two events from each event cluster as representatives. We use the reduced chi-square

χ^2/ν (Fig. 3.5) to estimate the uncertainties of the source parameters, where $\nu = \nu_{Sur} + \nu_{Pnl} - m$. The number of unknown parameters m equals 7 in our case, since we solve for h, ϕ, δ, λ, θ, ξ and the moment magnitude M_0 (see *Bevington and Robinson*, 2003). We choose a threshold of $\chi^2/\nu \leq 1.2$. If the minimum value of χ^2/ν exceeds 1.2, such as for event 349, there is a conflict between fitting both the waveform data and the P-wave travel times, suggesting an unreliable solution (denoted by "*n/a*" in Table 3.1). This is not surprising, considering the low SNR of surface waves from both stations for this event. Besides, for a few events, 325, 330a, 360, 104, and 143, a secondary solution exists (listed in Table 3.1 with a "$\star$"), which corresponds to a local minimum of $\chi^2/\nu \leq 1.2$. The existence of a secondary solution implies a trade-off between event location and mechanism, which is mainly due to the loose constraint from noisy Rayleigh waves at both stations.

In summary, the comparison between the two-station solutions from the one-step approach and the array solutions shows remarkable consistency for both source locations and focal mechanisms. Specifically, the average offset between the two-station locations and the whole-array locations is ~5 km.

3.4.3 The two-step approach

The above results from the one-step approach have demonstrated the ability of our new method to recover essentially the same source parameters by a distributed array using only two stations. However, this approach is a time-consuming process. It takes approximately one day on a Pentium-IV PC to find the location and focal mechanism for one event with the parameter ranges and searching steps we chose. An expedited alternative is the two-step approach, where we separate the single grid search into two, one for the source depth and mechanism, the other for the epicentral location. With the same source parameter space and the searching steps, the computation time required by the two-step approach drops by a factor of ~ 9.

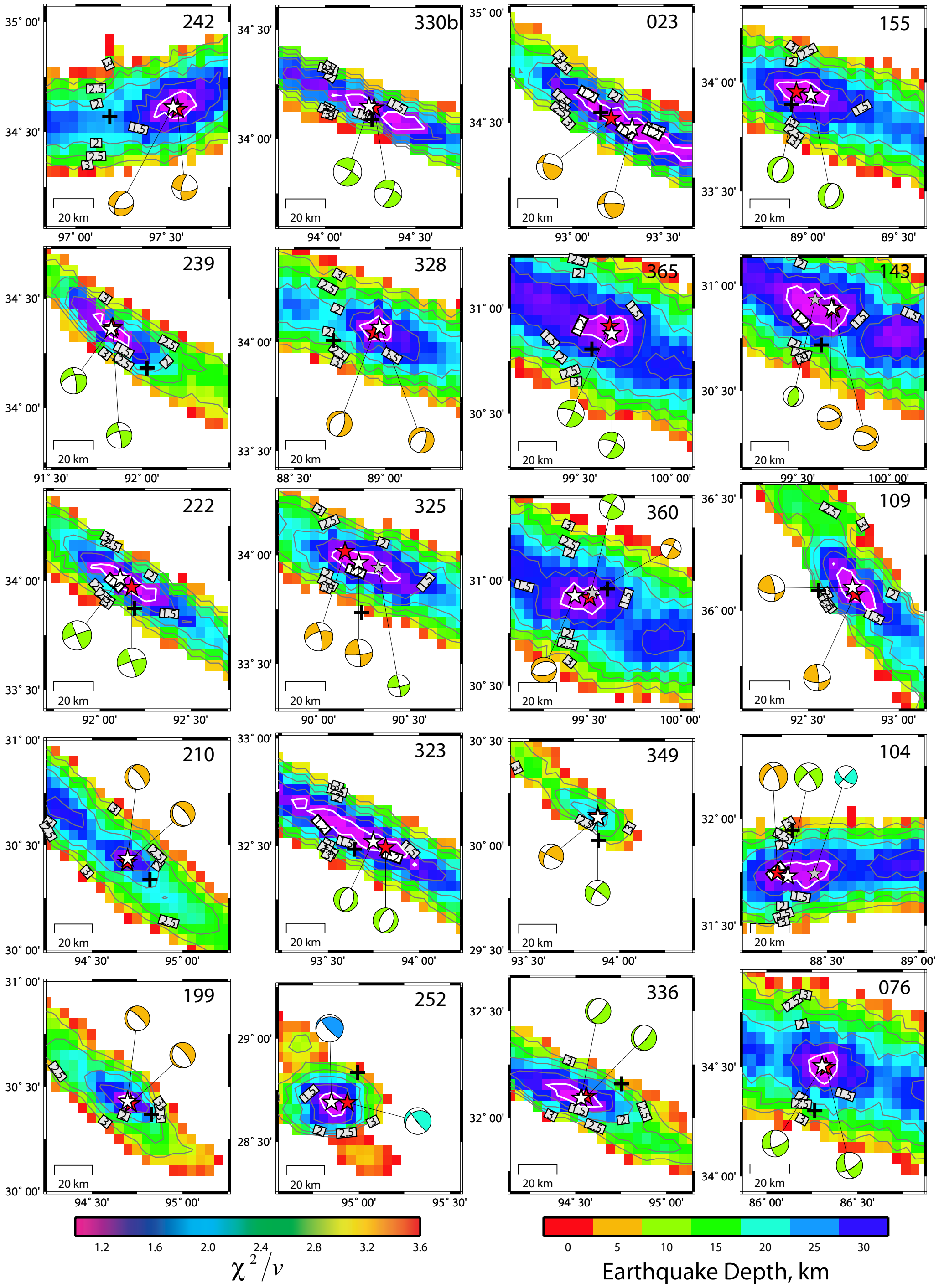

Figure 3.5: Results of the one-step approach for 20 events. Contours show the reduced chi-square χ^2/ν values with the 1.2 contour in the white color. For each event, the epicenter with the $min\left(\chi^2/\nu\right)$ is indicated by the white star, together with the obtained focal mechanism. The depth of the event is indicated by the color of the "beach ball". In the case of existence of a secondary solution, it is denoted by a smaller gray star, as shown for event 325, 360, 104, and 143. Also shown for comparison are the events' ISC locations (black crosses) and the array determined solutions (red stars) by *Zhu et al.* (2006).

We first search for an event's depth and mechanism assuming its ISC location, where the $\delta t^{Rayleigh}$ and δt^{Love} are set as free parameters to account for the location error and the structural effect. We follow a similar procedure as in the one-step approach to achieve the best relative weight between Pnl and surface waves. The obtained best $\sigma_{Sur}/\sigma_{Pnl}$ ratios are close to their counterparts from the one-step approach (see Table 3.1). However, discrepancies are revealed when we compare the depth and mechanism solutions with those determined by the whole array in Table 3.1. Besides, quite a few events have local minima with $\chi_w^2/\nu \leq 1.2$, as shown in Fig. 3.6 for event 242. These local minima are given in Table 3.1 with a "$\star$". Existence of these local minima is mainly due to cycle-skipping of the surface waves. However, a large number of them would indicate a poorly constrained solution, which could be caused by low SNR of the waveform data, an inappropriate velocity model, or a large event location error. It is worth mentioning that the three events, 242, 328 and 076, that appear to have the most number of local minima (>5, see Table 3.1) also have the largest errors in their ISC locations with respect to their relocations by *Zhu et al.* (2006). In fact, if we simply discard these solutions with a large number of local minima, the two-station solutions basically agree with the array solutions, even though they systematically have larger uncertainties.

We then take the obtained source depths and mechanisms to relocate the events, where the surface-wave segments are not allowed to float. The relocation results are summarized in Table 3.1, and Fig. 3.7 displays the details for the same 20 events shown in Fig. 3.5. Quite a few events in Fig. 3.7, such as 210, 242, 336, 360, 365, 076, 109, 143 and 155, show a minimum χ^2/ν value exceeding 1.2, which indicates the relocations with the assumed depth and mechanism fail to explain the travel times of P and surface waves. The discrepancies are due to the phase shifts of the synthetic surface waves from the fixed source depth and mechanism. Therefore, we mark such relocations as unreliable (denoted by "*n/a*" in Table 3.1). Correspondingly, the adopted source depths and mechanisms are also questionable.

For the relocations we trust ($\chi^2/\nu \leq 1.2$) in Fig. 3.7, their offsets with respect to the array locations are generally less than 10 km. Moreover, the adopted source

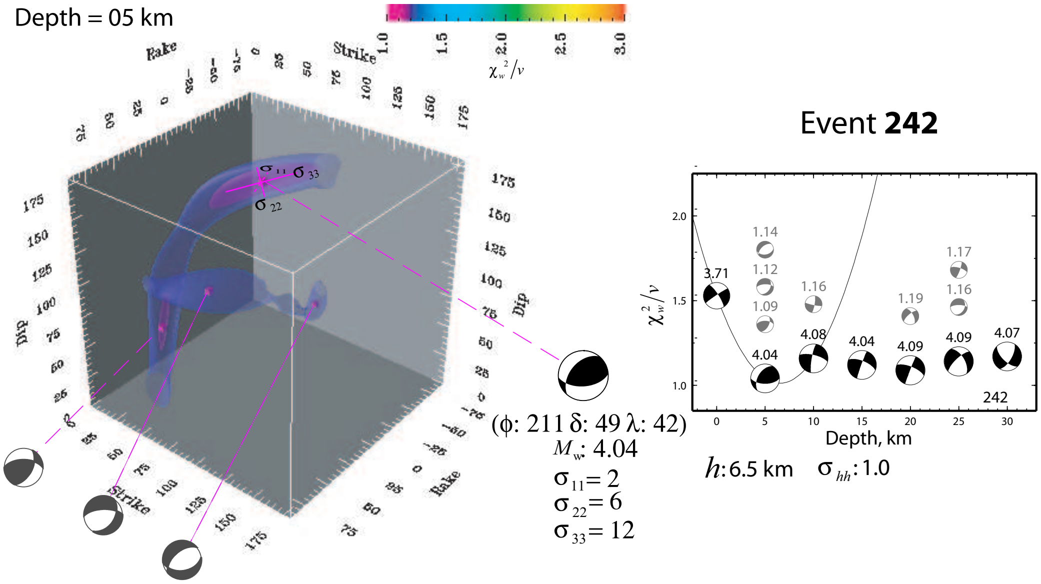

Figure 3.6: Resolution of the depth and focal mechanism for event 242. The left panel shows the reduced chi-square χ^2_w/ν in the fault parameter space for the best source depth of 5 km. Two iso-χ^2_w/ν surfaces of 1.1 and 1.2 are displayed together with the best focal mechanism (black beach ball) and local minima (gray beach balls). The uncertainties associated with the best solution can be quantified by the principal axis lengths (σ_{11}, σ_{22} and σ_{33}) of the ellipsoid that best fits the shape of the 1.2 iso-surfaces at the minimum. The right panel shows χ^2_w/ν as a function of source depth. At each depth, besides the best solution, local minima of different mechanisms are also shown as gray beach balls with the corresponding χ^2_w/ν values displayed at the top.

depths and mechanisms also agree well with the array solutions. Trade-offs between source depth, mechanism and epicenter location are rarely observed, except for events 239, 252, 325 and 023. However, the offset between an unreliable relocation and the array location generally exceeds 20 km, and the assumed source depth and mechanism also differ from the array solution. So, the two-step approach does not always give the correct solution, but the reliability of a solution can be evaluated by the reduced chi-square value. Also note the uncertainties of the relocations (the $\chi^2/\nu = 1.2$ contour) are systematically underestimated, since the correlation of the epicenter location with the source depth and mechanism has not been taken into account. If we discard the unreliable relocations, the two-step approach actually improves the locations of 15 events with an average mislocation error reduction from ~16 km in their initial ISC

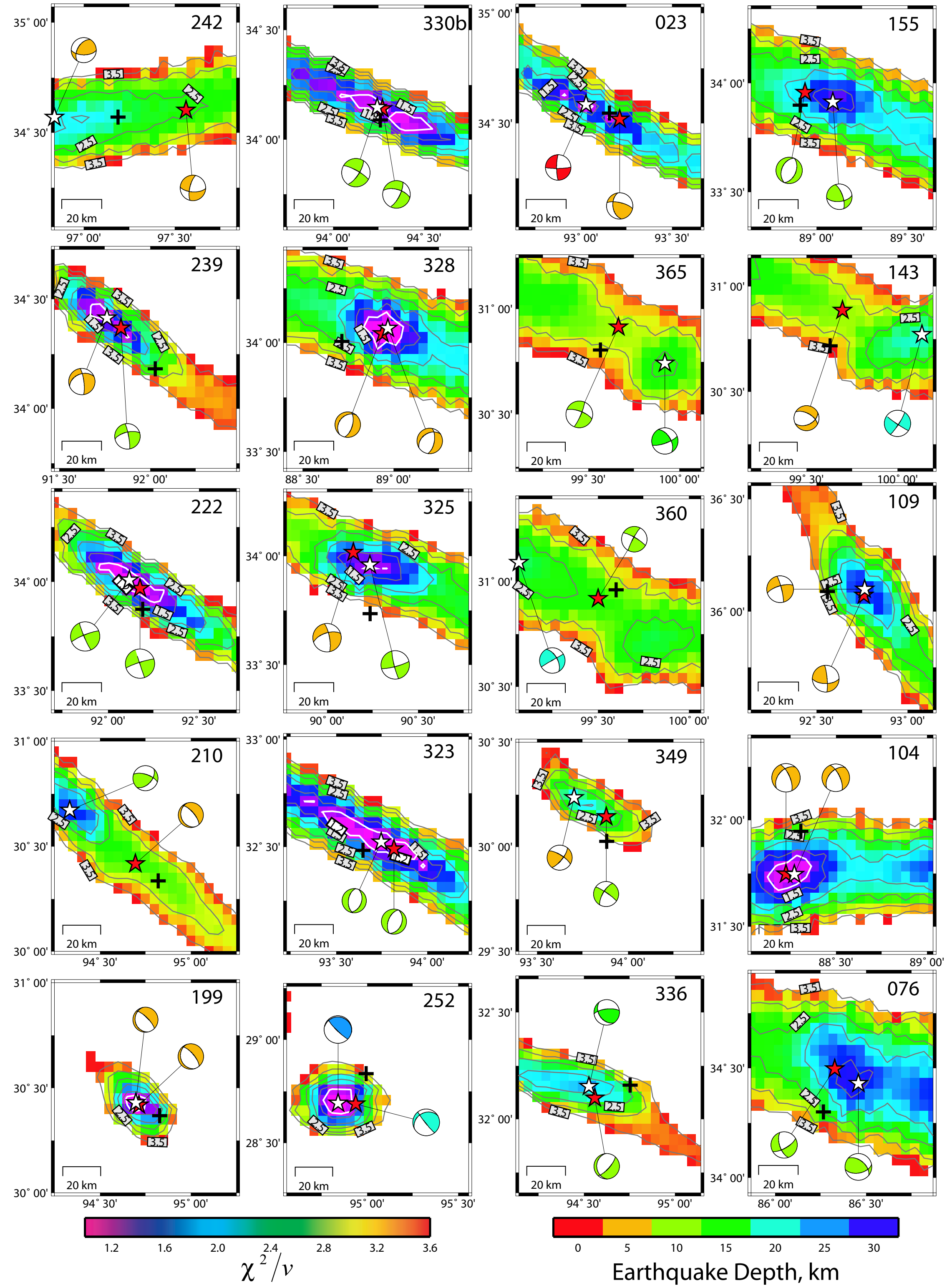

Figure 3.7: Results from the two-step approach for the same 20 events in Fig. 3.5. See Fig. 3.5 for details.

locations to ~7 km.

3.5 Discussion and conclusions

In this paper, we developed a new technique, CAPloc, to simultaneously determine source mechanism and location of a small regional event using complete 3-component seismograms. A similar effort was attempted by *Tajima et al.* (2002) using long period whole waveforms (20–50 mHz). Our method is superior in that both *Pnl* and surface waves are modeled to provide better constraints on source depth and orientation. Moreover, fitting differential travel times between *P* and surface waves helps eliminate the influence of a wrong event origin time. To take full advantage of both *Pnl* and surface waves, we introduced an adaptive weighting scheme. The relative weight between *Pnl* and surface waves is derived from the variances of their waveform residuals to balance their contributions. An appropriate weight of *Pnl* to surface waves is important, especially when few stations are available. We tested two approaches of CAPloc. They are essentially the same, in that the entire records are modeled with the separations between the *P* and surface waves adjusted from known calibration information. However, the two-step approach, though it requires much less computer time, is vulnerable in determining the source depth and mechanism using only two stations. The one-step approach better accounts for the trade-offs between an event location and mechanism; hence it gives better results.

The empirical-path-specific corrections (EPSCs) are essential to the success of the method, and their uncertainties directly affect the uncertainty of the source location. Since an event location is mainly constrained by the differential travel times between the *P* and surface waves, a 0.5 s uncertainty in the EPSCs would be mapped into an uncertainty of ~3 km in the events' epicentral distances. For the optimal case where the two stations differ in azimuth by ~90°, the event location could be well constrained within a radius of ~3 km. Otherwise the uncertainty range of the epicenter location tends to be elongated, suggesting a poorer constraint in a certain direction (e.g., Fig. 3.5 and 3.7). Note the relatively large uncertainties of the epicenter locations are due to the discrete Green's functions with a distance interval of 5 km. Since we use the closest Green's function for each station, a 2.5 km error in the epicentral distance could result. This suggests that a denser Green's function library should be used, or the distance error of the Green's functions should be corrected to achieve better location precision.

We assume a fixed 0.5 s uncertainty in the EPSCs. However, considering their possible variations over the spatial parameter space, especially the 3-D hypocenter space in the one-step approach, the 0.5 s uncertainty may represent a lower bound. Moreover, the uncertainties of the EPSCs might vary for different paths, depending on the goodness of the velocity model and how well the events for the calibration purpose are determined. A high resolution tomographic map will enable timely EPSC predictions plus better controlled uncertainty estimates, which will be pursued in a future effort.

We restrict ourselves to using data from only two stations to demonstrate that the complete 3-component seismograms from as few as two stations suffice in determining both location and mechanism of a regional event. However, additional arrival-time or first-motion polarity data of short-period stations, if available, can be incorporated easily into the approach. Adding arrival times can help constrain the event location. Moreover, polarities could be quite useful in narrowing the uncertainties of a focal mechanism solution, even if waveform data from only one station are available. Fig. 3.8 gives such an example for event 330b, where we use station TUNL alone to retrieve the source depth and orientation. We obtain a well-defined depth of 9.6 km, which agrees with the two-station as well as the array solutions. However, the focal mechanism is poorly constrained (Fig. 3.8A). Fig. 3.8B shows the remarkable improvement by adding the polarities from some other stations, where the first P wave motion is easily discernible. Similar results are obtained when we use another station or another event.

In summary, this study addresses the issue of modeling small regional events that are poorly monitored. A magnitude threshold of $\sim$3.5 is anticipated for the frequency band we currently use. We demonstrate that regional seismograms from as few as two

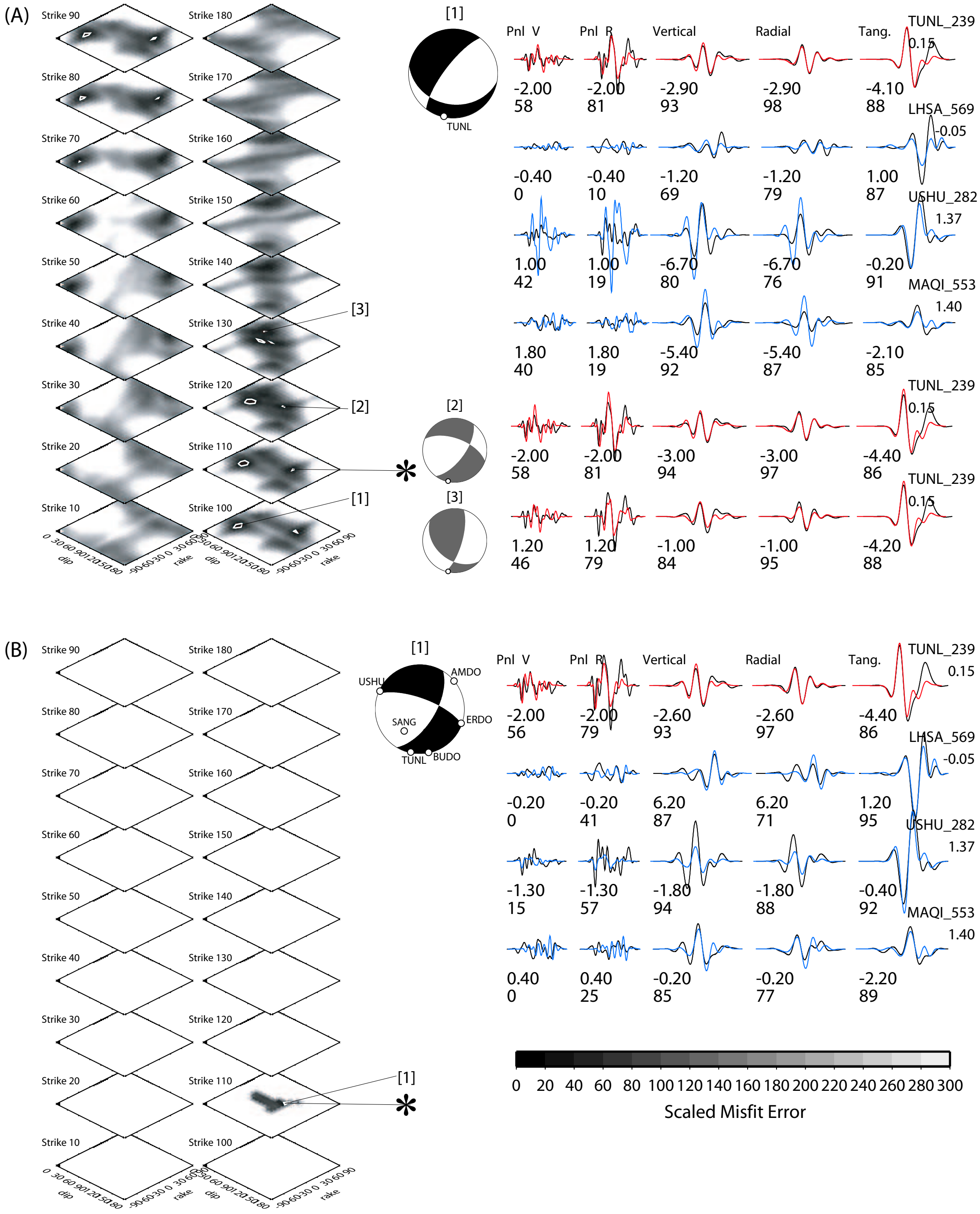

Figure 3.8: The focal mechanism solution using station TUNL only (A), and station TUNL plus first-motion polarities from additional stations USHU, AMDO, ERDO, BUDO, and SANG (B). A $\sigma_{Sur}/\sigma_{Pnl}$ ratio of 2.2 is used. The waveform misfit errors normalized by the minimum value are shown in the left. The best solution is denoted by [1] and local minima as [2] and [3]. The "$*$" indicates the array determined solution. The corresponding waveform fits are shown at right, together with the predictions for the three stations, LHSA, USHU, and MAQI.

stations suffice to determine both source location and mechanism provided that we have path calibration information. For the 28 events tested, the two-station solutions agree well with those determined from the whole PASSCAL array. In particular, we improve the events' ISC locations with an average mislocation error reduction from $\sim$16 km to $\sim$5 km.

Table 3.1: Source parameters of epicentral location, depth and focal mechanism in Tibet

	ISC		Array Solution by *Zhu et al. (2006)*		Two-station Solutions							
					One-step Approach				Two-step Approach			
ID	lat./long.	Δx	lat./long.	$h/\phi/\delta/\lambda/M_w$	lat./long.	Δx	$h/\phi/\delta/\lambda/M_w$	$\frac{\sigma_{Sur}}{\sigma_{Pnl}}$	lat./long.	Δx	$h/\phi/\delta/\lambda/M_w$	$\frac{\sigma_{Sur}}{\sigma_{Pnl}}$
199	30.37/94.83	12	30.42/94.71	5/160/21/-71/4.1	30.43/94.70	2	6.1/167/20/-58/4.0	0.2	30.43/94.70	2	6.7/168/19/-58/4.0	0.2
201	30.39/94.81	3	30.42/94.81	5/170/23/-63/4.0	30.44/94.78	4	6.1/180/30/-50/3.9	0.2	30.44/94.78	4	6.9/180/28/-50/3.9	0.2
									⋆ 15/39/66/64			
204	30.33/94.83	10	30.41/94.78	5/157/21/-70/4.0	30.44/94.74	5	6.9/172/21/-43/4.0	0.2	30.44/94.74	5	7.0/189/29/-29/4.0	0.2
									⋆ 15/50/70/90			
210	30.34/94.82	15	30.42/94.69	5/161/23/-71/4.0	30.44/94.70	2	5.6/180/27/-54/4.0	0.3	n/a		11.6/ 42/49/ 34/4.0	0.3
									⋆ 15/114/64/-37; 5/29/81/-49; 5/90/10/40; 5/210/50/-10			
211	30.37/94.81	9	30.43/94.74	5/161/21/-71/3.9	30.43/94.75	1	6.5/180/26/-49/3.8	0.4	n/a		14.8/128/52/ 9/3.9	0.4
									⋆ 5/99/21/-38; 10/80/20/-60; 20/70/60/50			
222	33.87/92.19	11	33.97/92.18	10/252/83/ 2/4.7	34.01/92.11	7	10.7/249/83/ 3/4.7	1.6	34.01/92.12	7	10.6/248/81/ 6/4.7	1.4
239	34.18/92.03	27	34.37/91.84	9/256/66/ -8/4.1	34.36/91.83	1	10.2/252/55/-16/4.2	1.4	34.41/91.76	9	7.2/249/42/-18/4.2	1.6
242	34.57/97.19	34	34.60/97.56	5/ 96/69/-15/4.0	34.61/97.54	3	5.3/ 88/52/-44/4.1	1.0	n/a		6.5/211/49/ 42/4.0	1.0
									⋆ 20/201/88/-21; 5/24/56/36; 5/268/64/-58; 5/82/42/-64; 25/227/72/-34			
252	28.84/95.00	17	28.69/94.94	21/241/29/ 12/4.3	28.69/94.85	9	22.8/262/19/ 37/4.4	1.6	28.69/94.84	9	23.4/282/10/ 58/4.4	1.6
323	32.48/93.65	16	32.49/93.82	8/ 21/38/-89/4.0	32.52/93.75	7	11.5/ 22/41/-84/3.9	1.2	32.52/93.75	7	10.8/ 19/41/-81/3.9	1.3
									⋆ 15/62/53/19; 5/30/50/-50			
325	33.74/90.24	32	34.02/90.14	5/251/60/-16/4.5	33.97/90.22	9	7.3/ 84/80/ 6/4.4	4.0	33.96/90.23	11	8.8/ 75/81/ -7/4.5	3.2
					⋆ 33.94/90.33 12.2/78/81/5							
328	34.01/88.72	21	34.04/88.94	5/221/31/-67/4.1	34.07/88.97	4	5.6/239/37/-50/4.1	1.8	34.07/88.97	4	6.5/238/39/-49/4.1	1.9

Continued on next page…

Table 3.1 – continued from previous page

	ISC		Array Solution		Two-station Solutions							
			by Zhu et al. (2006)		One-step Approach				Two-step Approach			
ID	lat./long.	Δx	lat./long.	$h/\phi/\delta/\lambda/M_w$	lat./long.	Δx	$h/\phi/\delta/\lambda/M_w$	$\frac{\sigma_{Sur}}{\sigma_{Pnl}}$	lat./long.	Δx	$h/\phi/\delta/\lambda/M_w$	$\frac{\sigma_{Sur}}{\sigma_{Pnl}}$
									⋆ 15/228/63/-28; 5/70/50/-40; 20/72/59/32; 35/269/83/51; 5/220/70/20			
329	34.01/88.81	8	34.02/88.89	5/222/33/-64/4.3	34.03/88.92	3	5.7/229/34/-61/4.2	2.8	*n*/a		7.2/ 79/70/-36/4.2	2.8
									⋆ 5/240/50/-40; 20/68/59/29; 10/270/70/10			
330a	33.88/88.86	13	33.99/88.92	5/211/32/-72/4.2	33.98/88.94	2	6.0/229/37/-61/4.1	2.6	*n*/a		7.2/ 89/89/-23/4.1	2.4
					⋆ 33.94/89.04		15.5/259/77/22		⋆ 25/232/72/24; 15/230/70/-20; 10/90/60/20			
330b	34.09/94.26	6	34.14/94.27	11/286/63/-21/4.4	34.15/94.24	3	9.1/299/77/-19/4.5	2.2	34.15/94.24	3	8.5/299/78/-19/4.5	2.2
									⋆ 5/127/69/32			
336	32.16/94.75	20	32.10/94.56	10/ 43/73/-74/4.1	32.09/94.53	3	11.5/ 43/73/-80/4.1	1.4	*n*/a		13.7/263/69/ 56/4.1	1.4
									⋆ 10/41/75/-80			
348	33.92/88.84	13	34.04/88.83	5/212/30/-72/4.8	34.08/88.83	4	5.7/230/39/-50/4.7	4.0	34.08/88.83	4	6.2/228/39/-48/4.7	4.0
									⋆ 15/69/75/-24; 20/70/58/27; 15/250/70/20			
349	30.03/93.88	13	30.14/93.88	8/211/69/ -9/4.0	*n*/a				*n*/a		6.4/ 38/72/ 18/4.1	1.2
									⋆ 5/220/60/20			
351	33.96/88.98	17	34.04/88.83	5/222/24/-61/4.2	34.03/88.84	2	6.5/239/28/-42/4.2	3.2	*n*/a		8.7/224/50/-18/4.2	3.2
									⋆ 5/239/28/-43; 20/79/47/35; 10/40/50/-10			
360	30.96/99.60	11	30.92/99.50	10/300/78/ 8/4.1	30.93/99.42	8	7.3/ 82/53/-83/4.1	2.8	*n*/a		20.4/240/89/-32/4.1	2.0
					⋆ 30.94/99.52		7.1/298/77/4					
365	30.81/99.57	15	30.91/99.67	12/294/67/ -2/4.2	30.88/99.67	4	11.0/ 3/ 7/ 15/4.2	2.8	*n*/a		16.1/ 70/74/ 37/4.2	1.9
002	33.94/88.85	19	34.09/88.76	5/221/30/-56/4.4	34.10/88.80	4	6.4/236/41/-39/4.3	2.4	34.09/88.80	4	7.0/227/36/-44/4.3	2.4
									⋆ 10/232/53/-7; 20/75/52/13; 5/10/60/-90; 10/70/60/-20			
023	34.55/93.16	6	34.52/93.21	5/280/67/ 43/4.2	34.48/93.33	12	5.7/270/79/ 42/4.3	0.8	34.59/93.03	19	0.0/ 89/83/-10/4.1	0.7
									⋆ 5/109/31/41; 5/280/70/50			

Continued on next page...

Table 3.1 – continued from previous page

	ISC		Array Solution *by Zhu et al. (2006)*		Two-station Solutions							
					One-step Approach				Two-step Approach			
ID	lat./long.	Δx	lat./long.	$h/\phi/\delta/\lambda/M_w$	lat./long.	Δx	$h/\phi/\delta/\lambda/M_w$	$\frac{\sigma_{Sur}}{\sigma_{Pnl}}$	lat./long.	Δx	$h/\phi/\delta/\lambda/M_w$	$\frac{\sigma_{Sur}}{\sigma_{Pnl}}$
076	34.30/86.27	23	34.50/86.33	9/63/68/-29/4.2	34.51/86.31	2	10.8/69/72/-33/4.3	4.4	*n*/a		11.0/79/52/53/4.3	4.4
									⋆ 10/70/70/-40; 10/260/70/10; 10/230/40/-50; 15/340/70/30; 15/320/50/-50			
104	31.95/88.31	24	31.75/88.22	5/227/49/-23/4.5	31.73/88.28	6	8.2/230/70/-13/4.5	7.6	31.75/88.27	4	7.1/223/48/-30/4.4	6.8
					⋆ 31.74/88.43	20.1/222/87/24			⋆ 20/229/79/27; 5/60/60/-10; 5/360/50/-80			
109	36.09/92.56	18	36.07/92.76	5/92/60/7/4.3	36.10/92.75	4	6.0/93/56/22/4.3	2.0	*n*/a		6.7/253/70/-9/4.3	1.8
									⋆ 5/80/60/10			
143	30.72/99.63	20	30.89/99.70	5/299/44/-52/4.0	30.89/99.69	1	7.0/301/34/-53/4.0	1.8	*n*/a		20.3/33/82/-5/4.2	1.2
					⋆ 30.94/99.60	12.1/8/42/78						
155	33.90/88.91	7	33.96/88.94	8/30/48/-79/4.2	33.94/89.02	8	11.2/27/39/-77/4.1	1.8	*n*/a		11.0/84/58/25/4.1	1.8
									⋆ 5/79/68/-40; 5/260/50/-20; 20/270/80/30			

The Δxs are the epicentral offsets in km with respect to the array locations. The unreliable solutions are denoted as "*n/a*" and the smallest local minima up to five are given following a "⋆" sign.

Chapter 4

Trans-Pacific Upper Mantle Shear Velocity Structure

4.1 Introduction

Seismic velocity structure provides the most important constraint on modeling the mineralogical composition and dynamics of the Earth's interior. Of particular interest is the oceanic upper mantle structure, due to its large departure from a global average (e.g., PREM by *Dziewonski and Anderson* (1981)). The origin of the characteristic high velocity lid, prominent low-velocity zone (LVZ) and the general lack of 220 km discontinuity has warranted a large number of investigations from the mineralogical point of view. The recent work by *Stixrude and Lithgow-Bertelloni* (2005) suggested a solid-state LVZ, which is the natural consequence of a thermal boundary layer and the effects of pressure and temperature on the elastic wave velocity of subsolidus mantle assemblages. The properties atypical of the mantle, such as partial melt and bound water, would be permissible, but not required. However, the quantitative comparison of their "null" hypothesis with seismological models revealed discrepancies in the negative velocity gradient, the absolute value of velocity in the LVZ, and the high velocity gradient below the LVZ. To reconcile these discrepancies forced them to examine variants of the "null" hypothesis as well as include the effects of partial melt, attenuation, and anisotropy.

Such mineralogical studies have been matched in seismology. In particular, the last decade has seen the remarkable progress of seismic tomography, mostly driven by the advancement of theory and computational power, where global 3-D models have spanned the entire depth range of the Earth's mantle and achieved lateral resolution of less than 1000 km (*Romanowicz*, 2003). However, many oceanic areas remain unsampled or poorly resolved in most high resolution P velocity models. The other type of long wavelength velocity models based on surface waves generally have good coverage across the oceans, but most of them lack radial resolution. The current generation of global models, therefore, is not capable of resolving the hypotheses regarding the layering of the oceanic upper mantle. Instead, "pure path" regional models can provide significant information complementary to the tomographic models (*Gaherty et al.*, 1999).

Although there is increasing evidence for short-length scale variations in lithospheric thickness across plate boundaries where subduction has occurred or is occurring (e.g., *Melbourne and Helmberger*, 2001), structures away from plate boundaries display much smoother lateral variations of smaller scale, where simple corridors appear one dimensional (1-D). Here we will investigate one such strip that runs nearly across the central Pacific ocean connecting the Tonga-Fiji source region to TriNet, southern California. Cross sections from global tomographic models display laterally homogeneous features along this corridor, where the largest anomalies are associated with adjustments made to eliminate the 220 km discontinuity in the reference model PREM (*Dziewonski and Anderson*, 1981). The plate history along the corridor is relatively simple, with the sea floor developed by the spreading of the ancient Pacific-Farallon ridge. The lithospheric age spans a relatively wide range from approximately 100 Ma near the source region to ∼20 Ma approaching the California coastal line, where the lithosphere is about 50 km thick (*Melbourne and Helmberger*, 2001). Pure surface wave study by *Nishimura and Forsyth* (1989) indicated progressive increase of lithosphere thickness with increasing plate age, qualitatively mimicking isotherms of theoretical thermal cooling models. However, their results solely from fundamental-mode surface wave data are debatable, due to their poor vertical resolution. In contrast, *Gaherty et al.* (1999) suggested little age dependence of the lithosphere thickness when they compared regional models of the old Pacific ocean (100-125 Ma) and the younger Philippine Sea (15-50 Ma), where the transitions from the high velocity lid to the underlying LVZ (the G discontinuity) were mainly determined from ScS

reverberation observations (*Revenaugh and Jordan*, 1991b). They interpreted the G discontinuity mainly as a compositional boundary rather than a thermal boundary.

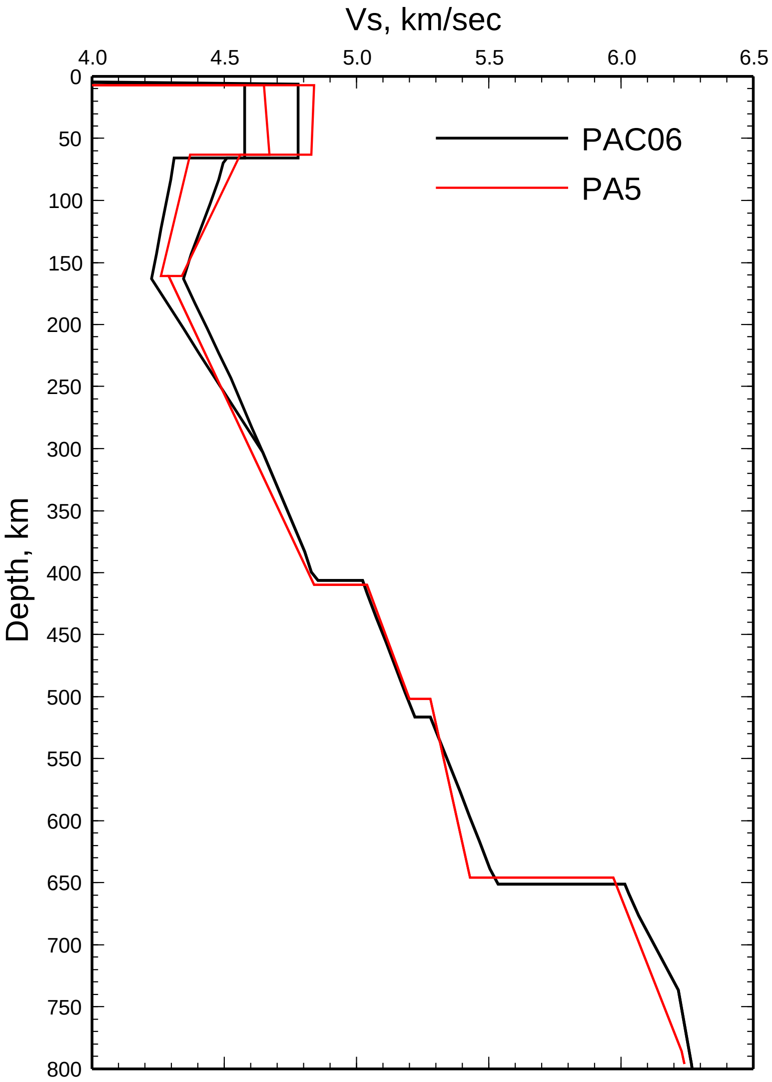

Figure 4.1: Comparison of $PA5$ (red) developed by *Gaherty and Jordan* (1996) for the corridor from Fiji-Tonga to Hawaii with our preferred model $PAC06$ (black).

The whole corridor has been included in an early 2-D study from Tonga to Newfoundland (*Graves and Helmberger*, 1988), where multi-bounce S waves from a single event were modeled with a 2-D WKB code and the emphasis was given to the sharp transition across the Pacific–North America boundary. More recently, *Gaherty and Jordan* (1996) investigated the older half of the corridor from Tonga-Fiji to Hawaii with a combined data set of ScS reverberations and measured frequency-dependent (10-45 mHz) phase delays for body and surface waves recorded on the island stations KIP and HON. Their 1-D radial-anisotropic model (PA5) features a high velocity lid, a prominent LVZ, and a high-gradient zone extending to the 410 km discontinuity (Fig. 4.1).

In this study, we use a novel data set of broadband seismograms from the dense TriNet array in southern California. At the epicentral distances of 70°–95°, multi-bounce S waves up to S^5 sampling over the upper mantle triplication range are observed, including the guided waves from shallow events transversing the LVZ, such as the G phase. Simultaneously modeling the move outs of all these S wave multiplets that bottom out at different depths produces strong constraints on the radial velocity structure.

Because velocity anomalies localized to a single leg of a multiple bounce phase will be mapped into the whole path, we interpret our model as an effective average along the corridor. However, it well explains record sections from a large number of events at different depths, spanning a distance range of 70°–95°. Moreover, the fair agreement between our model and PA5 developed for the older half path with different data and methods (*Gaherty and Jordan*, 1996) (Fig. 4.1) indicates a relatively simple, uniform structure along the corridor, which proves particularly useful for mineralogical investigations.

4.2 Data

Since early 1999, when the southern California TriNet array was expanded into a dense broadband network with over 120 stations, hundreds of large events (M > 5.5) that occurred in the Tonga-Fiji seismic zone have been recorded. Among them, we selected 49 events (Fig. 4.2), whose seismic sources are relatively simple, and whose multi-bounce phases are rich. We assumed the event locations and origin times from Harvard CMT solutions (see Table 4.1 for the events discussed here) (*Dziewonski et al.*, 1981). However, the exact event locations and origin times are not critical, since

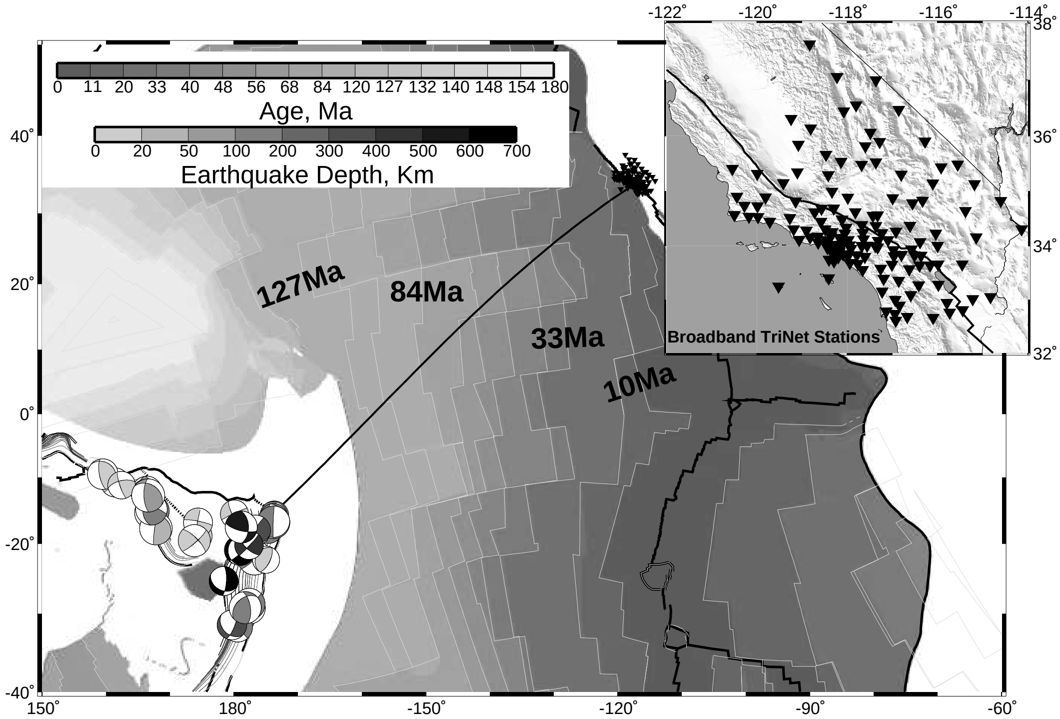

Figure 4.2: The source-receiver geometry is displayed on a sea-floor age map.

we model differential times between S multiplets, and the effects of event location or origin time become second order (*Grand and Helmberger*, 1984b).

Due to the small aperture of TriNet, a single event provides limited lateral coverage. However, the problem gets well compensated as we study a large number of events spanning a wide distance range of 70°–95° (Fig. 4.3). Moreover, modeling multiple events of different mechanisms, at different depths, provides an effective way to eliminate contaminations of source effects on the velocity structure. Particularly within the studied distance range, both SSS and S^4 become triplicated by the 410 km and 660 km discontinuities. A sketch of their triplication patterns is displayed in Fig. 4.4.

We rotated the original horizontal-component (N-S and E-W) data into radial (SV) and tangential (SH) motions, although we generally found the SV waves on the vertical component to be the most useful for modeling purposes. An example of the tangential records from a shallow event (9533473) is displayed as a distance cross section in Fig. 4.5, where the various S wave multiplets are labeled. The dense array produces coherent seismograms, which warrants a simple stacking procedure and facilitates identification of triplications or phase interference. At the shown distance range (∼82°–87°), SSS is triplicated due to the 660 km discontinuity, resulting in a forward branch (S^3_{ef}) turning below the discontinuity and a shallower backward branch (S^3_{cd}). S^4 contains more complexity, in that the triplications are interfering with the shallow guided waves. The apparent interference in Fig. 4.5, however, is mainly due to the guided waves that are most sensitive to different shallow depths, since the amplitude of S^4 is much smaller due to the radiation pattern effect. Modeling such guided waves at their natural frequencies (> 10 sec) provides powerful constraints on the shallow part of the velocity model. However, the whole group becomes simpler and the so called "G-phase" when filtered to longer periods (> 30 sec), which is normally used in tomographic studies.

Table 4.1: Source parameters of the Tonga-Fiji events used in this study (from Harvard's CMT catalog)

Event ID	Date	Origin Time	Location Lat./Long.	Depth (km)	Mw	FM (stk/dip/rake)	Δ corr. (km)
13980540	2003/07/27	02:04:15.6	-21.09/-176.12	216	6.6	294/22/-3	-30
9942373	2003/09/02	18:28:10.9	-15.14/-172.92	15	6.4	210/28/171	–
9982833	2004/02/12	13:47:35.9	-19.41/-172.80	12	5.7	213/26/96	-60
10100677	2005/05/18	10:27:15.0	-15.22/-172.69	12	6.2	144/33/48	–
9927909	2003/07/03	06:21:57.3	-21.46/-173.80	16	5.9	192/24/83	-70
9685024	2000/01/08	16:47:30.2	-16.84/-173.81	162	7.2	79 / 8/-13	–
9658105	2001/05/26	10:57:31.0	-20.25/-177.65	414	6.3	134/68/-176	–
9648517	2001/04/28	04:50:1.9	-18.07/-176.68	367	6.8	106/16/161	–
9533473	2000/02/25	01:44:5.2	-19.55/174.17	17	7.1	315/74/169	–
9026350	1997/10/14	09:53:32.7	-21.94/-176.15	166	7.7	257/17/-30	-50
9687900	2000/01/09	21:54:44.8	-18.78/174.52	18	6.4	49 /83/0	–
9564185	2000/09/14	15:00:2.3	-15.59/-179.92	15	6.2	154/77/176	–
9743493	2002/01/03	10:17:49.6	-17.84/167.82	20	6.6	359/30/97	–
9792597	2002/06/17	21:26:33.9	-12.49/166.25	44	6.6	163/38/81	–
9611653	2001/01/09	16:49:37.9	-14.90/167.11	115	7.0	183/44/160	–
9557761	2000/08/09	22:56:4.9	-16.88/174.54	15	6.4	281/82/4	–

Continued on next page...

Table 4.1 – continued from previous page

Event ID	Date	Origin Time	Location Lat./Long.	Depth (km)	Mw	FM (stk/dip/rake)	Δ corr. (km)
14170576	2005/08/06	09:56:19.3	-19.57/-175.35	218	6.6	266/33/-24	–
14132616	2005/03/19	15:02:47.9	-20.60/-173.58	18	6.1	199/27/85	–
9557029	2000/08/03	01:09:48.6	-11.93/166.17	51	6.6	169/40/87	–

Δ *corr.* applies to the events that appear mislocated as discussed in section 4.3.3. The correction is simply an average distance shift for all the stations from a particular event.

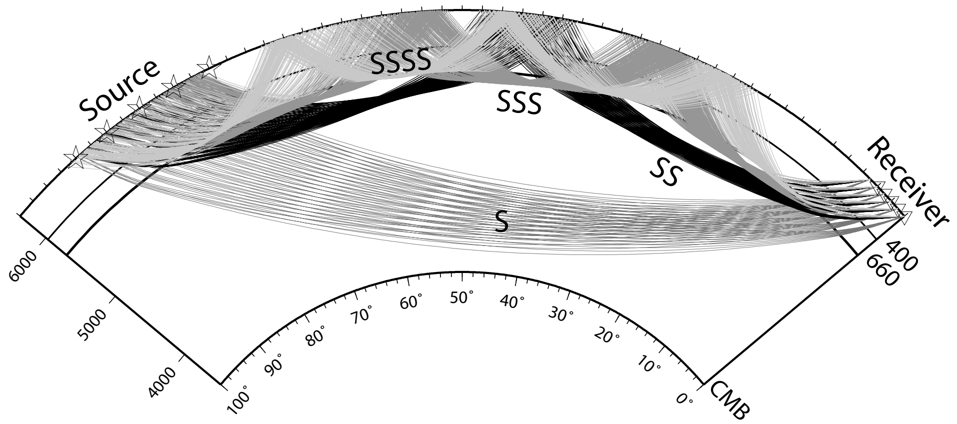

Figure 4.3: Schematic ray paths of multi-bounce S waves at epicentral distances of 70°–95°used in this study.

4.3 Waveform modeling

Our modeling effort involves matching the differential travel times between multi-bounce S waves and simulating their waveforms, particularly the waveforms of the higher-order multiplets, S^3 and S^4, plus shallow guided waves, which are triplicated or interfering in the upper mantle. Since the different multiplets have their own turning depths, simultaneously modeling their travel times provides unique estimates of velocity at various depths. Moreover, finer-scale structures can be inferred by simulating their subtle triplication or interference patterns.

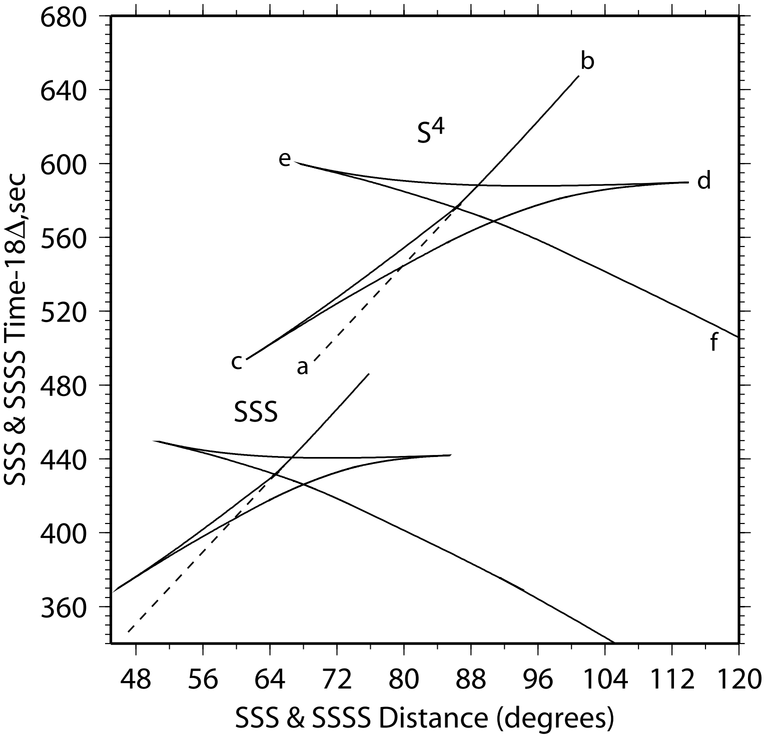

Figure 4.4: Triplication plot for a trial model with a 10 km deep source. The dashed lines indicate the positions of diffractions.

Because of the complexity in the waveforms to be modeled, we take a "trial and error" approach which has proven effective in previous similar studies (e.g. *Grand and Helmberger*, 1984b; *Melbourne and Helmberger*, 2002). In addition, we parameterize the velocity model as a composite of a high velocity lid, a negative-gradient zone, a positive-gradient zone and the transition zone, according to *a priori* information from previous oceanic models (e.g. *Grand and Helmberger*, 1984a; *Gaherty and Jordan*, 1996). This simple parameterization enables us to efficiently investigate possible interdependencies among the thicknesses, average velocities and gradients of the sublayers in a grid-search manner, and hence to resolve the main characteristics of the model.

We construct full synthetics with a reflectivity code (*Zhu and Rivera*, 2002) while we use generalized ray theory to help identify individual arrivals in cases where ambiguity exists. We model both the *SH* (tangential) and *SV* (vertical) components

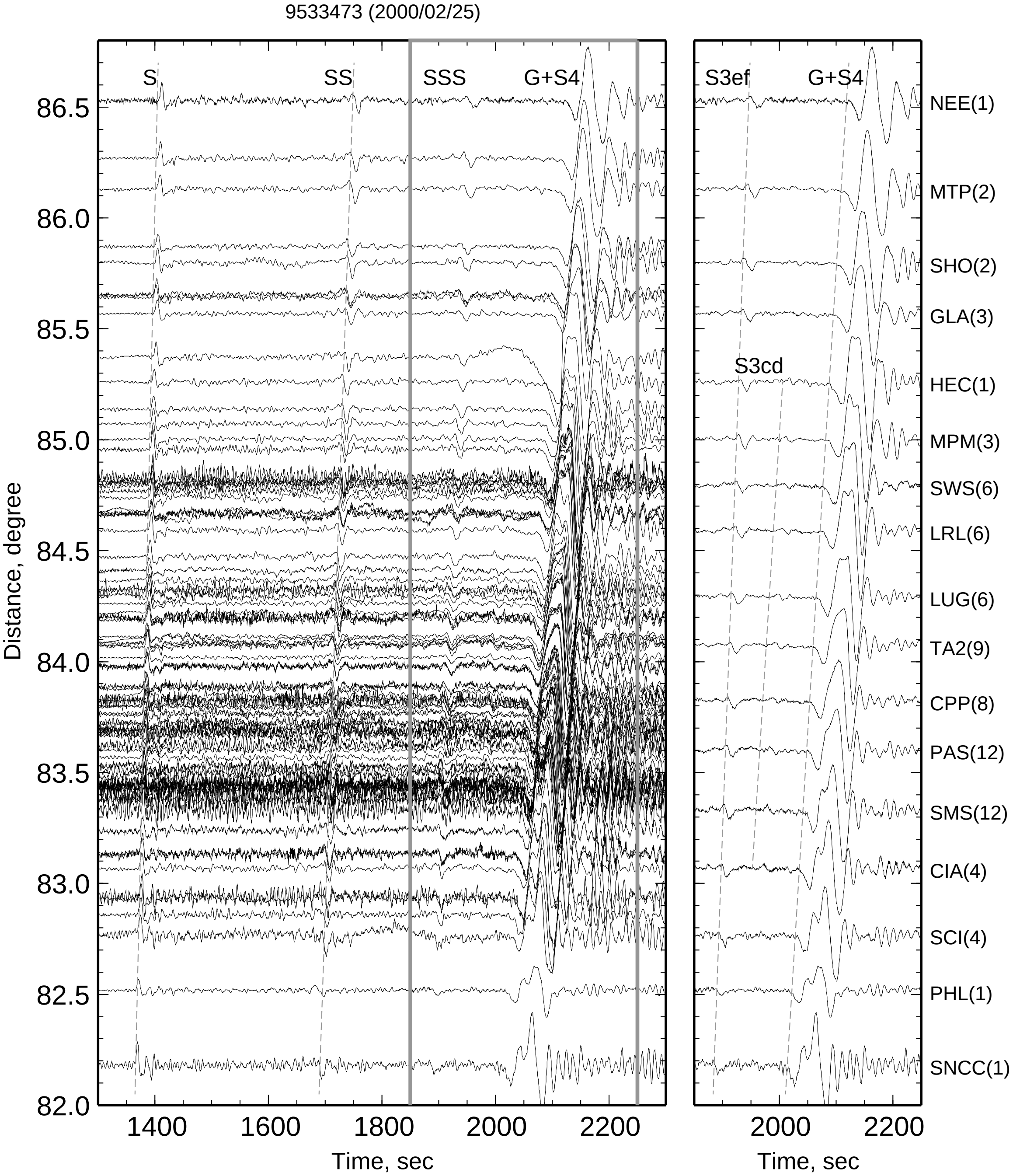

Figure 4.5: (left) The velocity cross section of the tangential component from a shallow event (9533473). The original records are desampled down to 1 Hz for display purpose. Labeled are the *S* wave multiples. (right) The selected records after a simple running-stack process, where the record at each station has been replaced by the average of the nearest records within 10 km. The number following a station name indicates how many records have been stacked for the particular station.

with a uniform approach, which enabled us to address the discrepancy due to seismic anisotropy directly.

We started with the attenuation model developed by *Ding and Grand* (1993) for the East Pacific Rise (EPR) using multi-bounce S waves. This model has proved effective in a later study by *Melbourne and Helmberger* (2002) for EPR events recorded at TriNet. However, we found that nearly doubled Q values in the upper 200 km of the model are required to explain the progressive amplitude decay of the S multiplets (see Table 4.2). This adjustment is reasonable considering *Ding and Grand* (1993)'s Q model, sampling one of the hottest structures on the Earth, was probably a lower bound.

For example, we display the waveform comparison between the data shown in Fig. 4.5 and the synthetics from our best SH model $PAC06_{sh}$ (Fig. 4.6). We align both the data and synthetics on SS to minimize the source region complexity, since SS has a take off angle close to those of the higher-order multiplets, while the direct S wave leaves the source at a much steeper angle (see Fig. 4.3). The whole cross section is nicely reproduced with the simple 1-D model (Fig. 4.6), particularly the waveforms of the guided waves overriding the S^4 triplications. There is a slight tendency for the coastal stations to be matched better than the in land ones, such as hec, gla, dan, mtp and nee. Moreover, the time lags of the synthetic "$G + S^4$" waves relative to the observations are systematically increasing with station distance (Fig. 4.6(c)). This "unmodeled" feature is consistent with the lithospheric thickness change across the Pacific-North America boundary reported by *Melbourne and Helmberger* (2001). Similar sharp transitions are also seen in recent tomographic models (e.g., *Tanimoto and Sheldrake*, 2002). The major discrepancy of the comparison in Fig. 4.6 is the time lags of the synthetic S phases (~ 5 sec) relative to the observations. We attribute this advancement of the observed S waves to the fast slabs in the source region, mainly because the same problem does not exist for the deeper events.

By contrast, we display in Figs. 4.7 and 4.8 the waveform fits for the same event 9533473 shown in Fig. 4.6 with the preliminary Earth reference model ($PREM_{sh}$) (*Dziewonski and Anderson*, 1981) and the path average of a typical tomographic

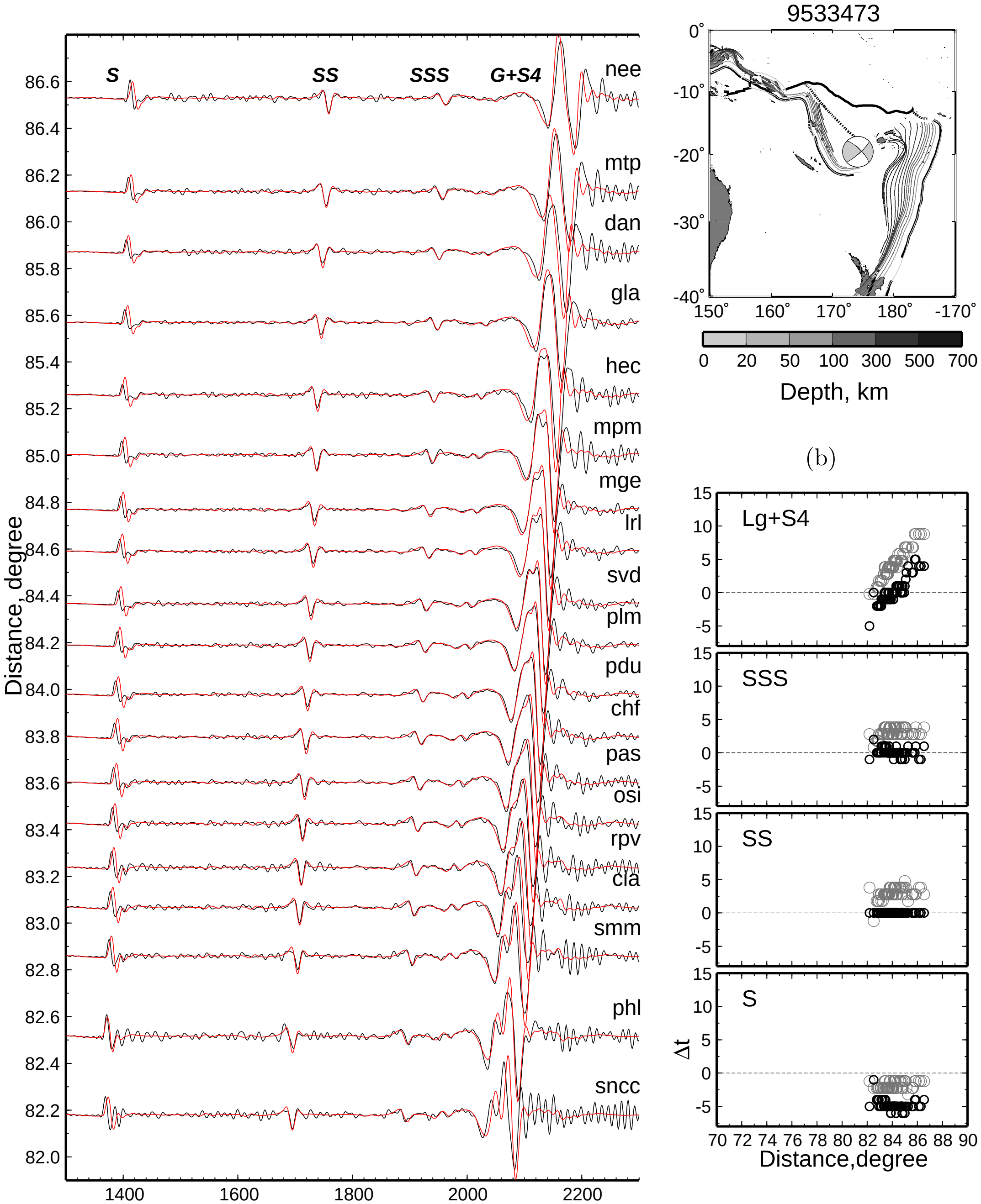

(a)

(b)

(c)

Figure 4.6: (a) Waveform comparison between the SH data (black) from event 9533473 and the synthetics with $PAC06_{sh}$ (red). Time axis is relative to the event origin time. (b) The source parameters of the event from Harvard's CMT catalog. (c) The gray circles are the time delays of the synthetic S multiplets relative to the observations measured by waveform cross correlation. The black ones are the residuals after the synthetics and data are aligned on SS.

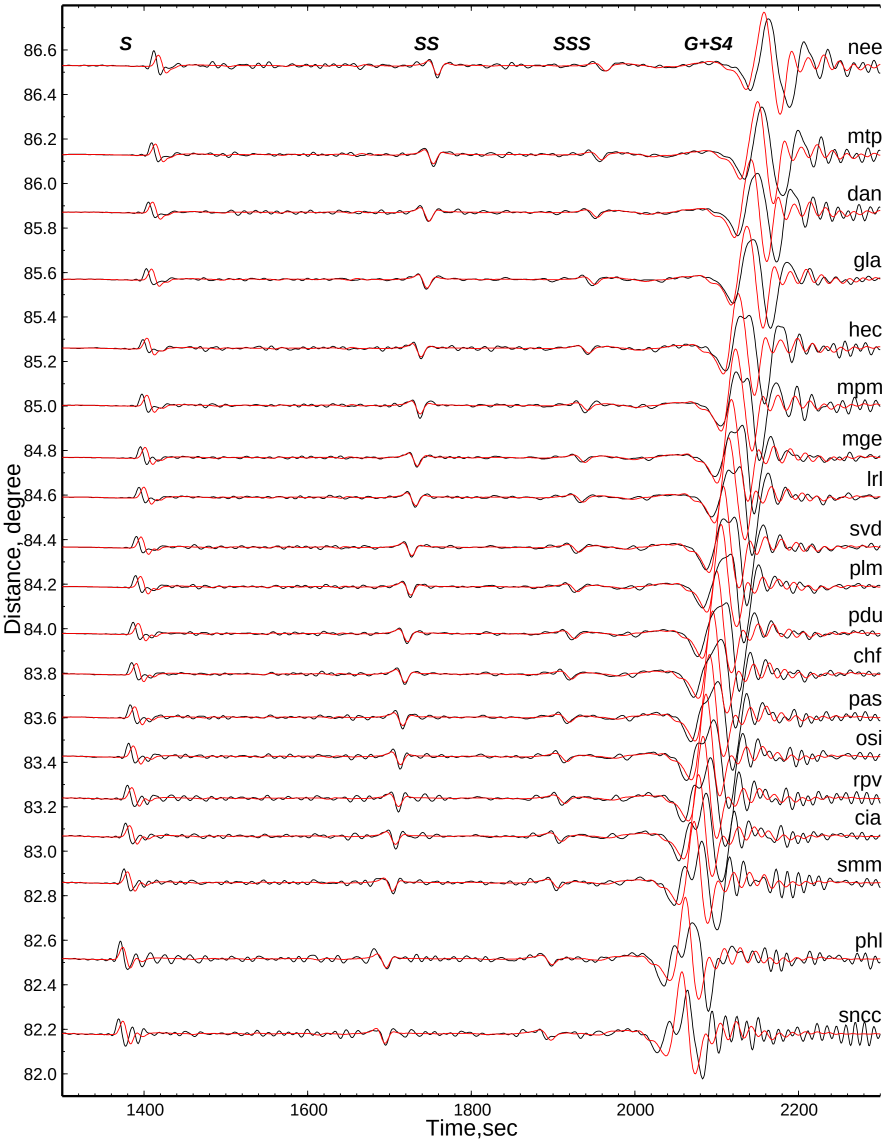

Figure 4.7: The selected waveform fits for event 9533473 as shown in Fig. 4.6 with the preliminary Earth reference model ($PREM_{sh}$). Both the data (black) and synthetics (red) are aligned on SS.

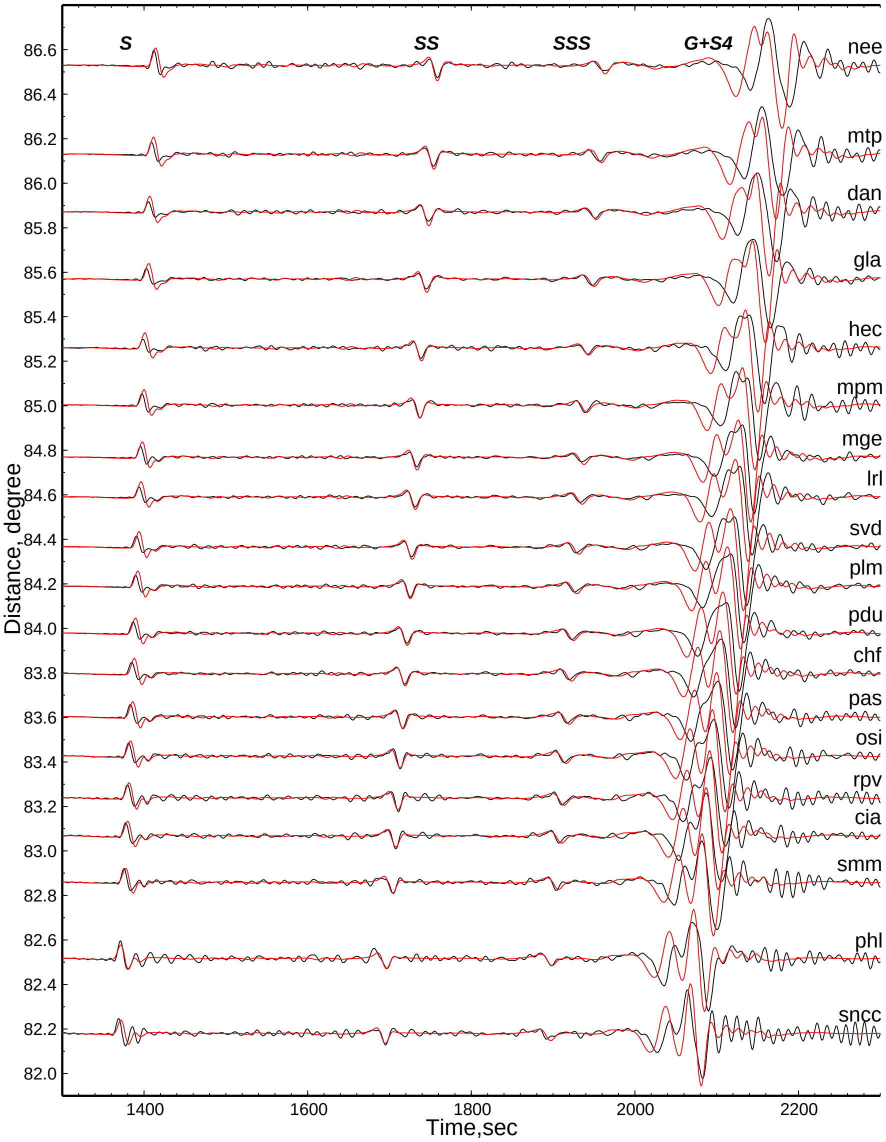

Figure 4.8: The selected waveform fits for event 9533473 as shown in Fig. 4.6 with the path average of a typical tomographic model S20RTS by *Ritsema et al.* (1999).

model S20RTS by *Ritsema et al.* (1999). Because S20RTS was developed mainly with Rayleigh wave dispersion data, we extrapolated the SH counterpart of the path averaged S20RTS assuming the same anisotropy as in the reference model PREM. The comparison between PREM, the path average of S20RTS and our preferred model $PAC06_{sh}$ is given in Fig. 4.9. Moreover, to correct the crustal effect in $PREM_{sh}$ and $S20RTS_{sh}$, we have replaced their thick crust (∼21 km) with the much thinner one (∼6 km) in our model $PAC06_{sh}$. As a consequence, the underlying mantle layers in the two models have been thickened to conserve the overall travel time. The synthetics from $PREM_{sh}$ and $S20RTS_{sh}$ with their original thick crust are compared with data in Appendix B. As shown in Fig. 4.7, PREM failed to predict both the interference pattern of the guided waves and their travel times. The tomographic model (S20RTS) containing a well developed LVZ produces the two interfering branches; however, their travel times plus their separations are apparently off. These comparisons suggest strong dependence of the guided waves on the shallow part of the model, which we will explore in the next section.

Although there is some redundancy, the selected 49 events contain extensive sampling of SSS and S^4 triplications (Fig. 4.4), plus their interference with the guided waves for shallow events. Therefore, they provide the most stringent constraint for different depth ranges of the model. For example, as the guided waves traversing the LVZ provides a means of estimating the shallow part of the model, the triplications of SSS or S^4 mainly constrain the transition zone. In the following, we will give typical examples of the events that we use to refine the velocity structure at different depths, where we will also address representative sensitivity tests in an attempt to quantify the model resolution. Our discussion will be restricted to the tangential (SH) component alone, since the adequate SV observations are rather limited.

4.3.1 Lid and LVZ

The velocity in the shallow part of the model, such as the Lid or the low velocity zone (LVZ) has the most effect on the differential travel times of the multi-bounce

S waves, since the higher-order multiplets systematically spend more time traveling there. Moreover, the shallow radial structure largely controls the waveforms of the guided waves traversing the LVZ. However, its influence becomes significantly less on the triplication patterns of SSS or S^4. In particular, it can hardly change the time separations between the triplicated branches, except for a small overall shift. This allows us to separate the effect of the shallow part from that of the underlying transition zone when modeling the records. The transition zone, however, mainly controls the triplications.

The shallow events (depth $<$ 50 km) are the most suitable for determining the Lid and LVZ structure, since they generate the most guided waves. Moreover, their seismograms are relatively simple without obvious depth phases. Fig. 4.10 displays a composite cross section of four shallow events together with synthetics overlain from our preferred SH model $PAC06_{sh}$. The four events have different source mechanisms, however, their records are well explained with a single model, suggesting the source effects on the velocity structure are eliminated. The radial structure of the Lid and LVZ heavily shapes the waveforms of the guided waves tunneled in the LVZ. However, such influences are rather difficult to quantify or predict, since they generally involve both timing and phase changes in the complex waveform pockets. Therefore, we have parameterized the model as a composite of three simple layers (the lid, negative gradient zone and a positive gradient zone) and deliberately conducted extensive “grid searches” for the basic parameters, such as thickness, average velocity and gradient of each sublayer. Our preferred model $PAC06_{sh}$ produces the best waveform fits to the observations. The basic characteristics of $PAC06_{sh}$ include a 60 km thick high velocity lid ($V_{sh} = 4.78$ km), a prominent LVZ with the lowest velocity of 4.34 km/sec at the depth of ~160 km, and a high gradient (~0.002 sec^{-1}) zone underneath. There is small room for trade-offs among the model parameters, but not much. In the next few figures (Figs. 4.11 to 4.14), we will compare the waveform fits for the composite cross section as shown in Fig. 4.10 with the perturbed lid, G discontinuity, and the high gradient zone respectively, where the apparently increasing waveform misfits with the perturbations suggest the robustness of these features.

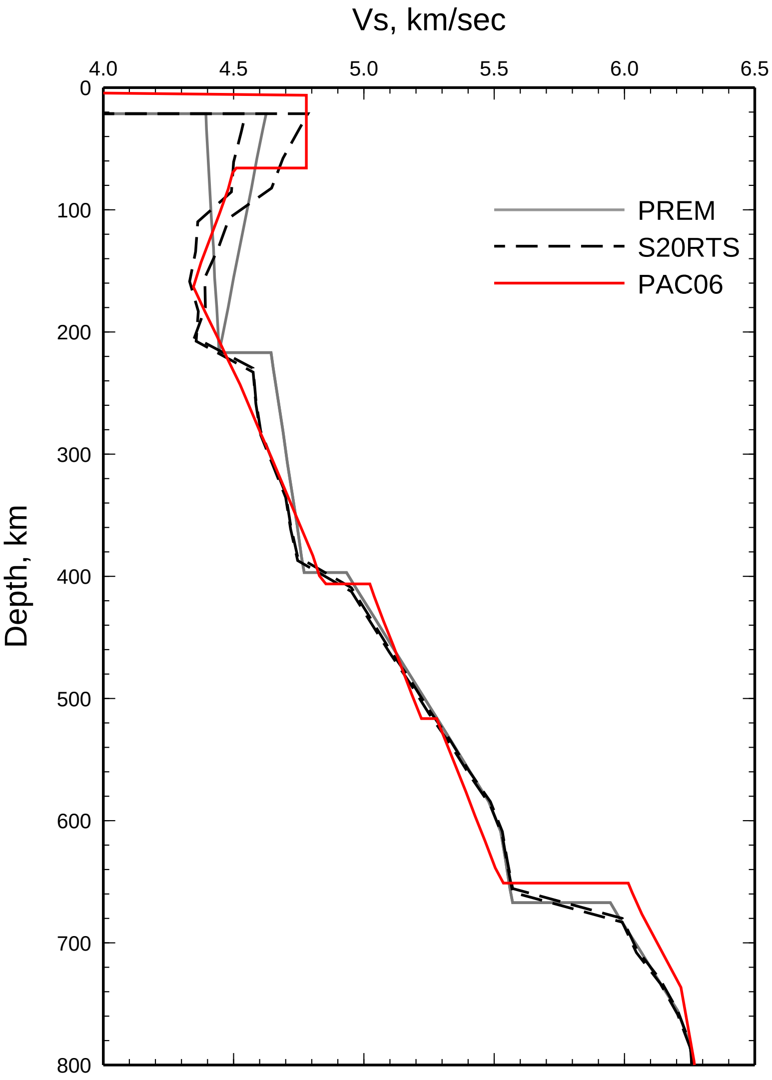

Figure 4.9: Comparison of our preferred SH model $PAC06_{sh}$ with PREM and the path average of the tomographic model S20RTS by *Ritsema et al.* (1999). Since S20RTS was developed mainly with Rayleigh wave data, we have extrapolated its SH counterpart assuming exactly the same anisotropy as in PREM.

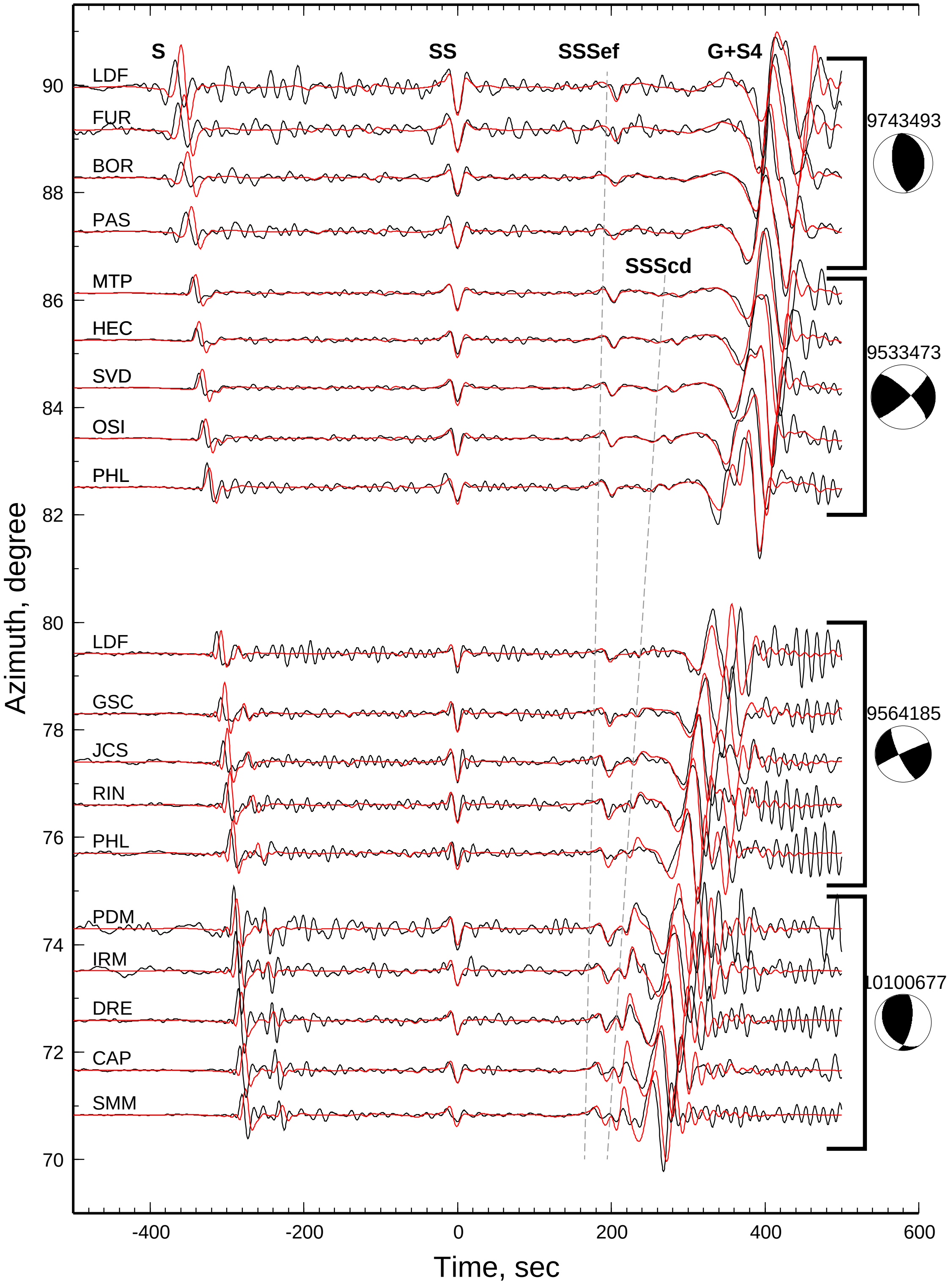

Figure 4.10: Waveform comparison between data (black) and the synthetics (red) from our preferred SH model $PAC06_{sh}$. Both the data and synthetics are aligned on SS. The traces for the two thrust events 10100677 and 9743493 have been multiplied by a factor of "-1" for display purposes.

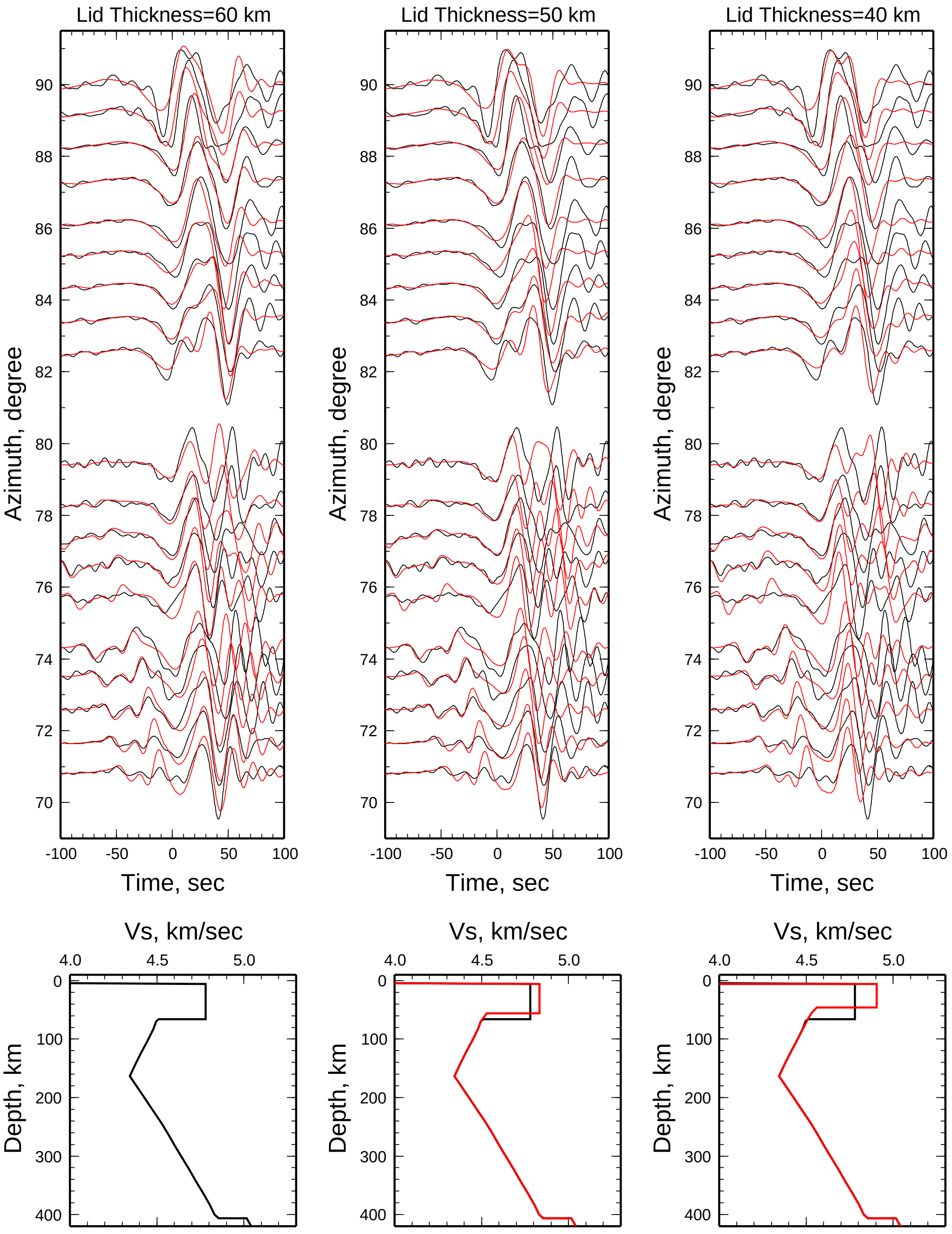

(a) (b) (c)

Figure 4.11: The waveform fits from Fig. 4.10 with our preferred SH model $PAC06_{sh}$ (a) are compared to those from the perturbed models, particularly of a thinner lid (b) and (c). The perturbed models are shown in red with $PAC06$ in black. We display only the guided waves from the composite cross section in Fig. 4.10, since the tested perturbations have little effect on the earlier arrivals. Time axis is reduced by $Dist.(km)/4.5(km/sec)$.

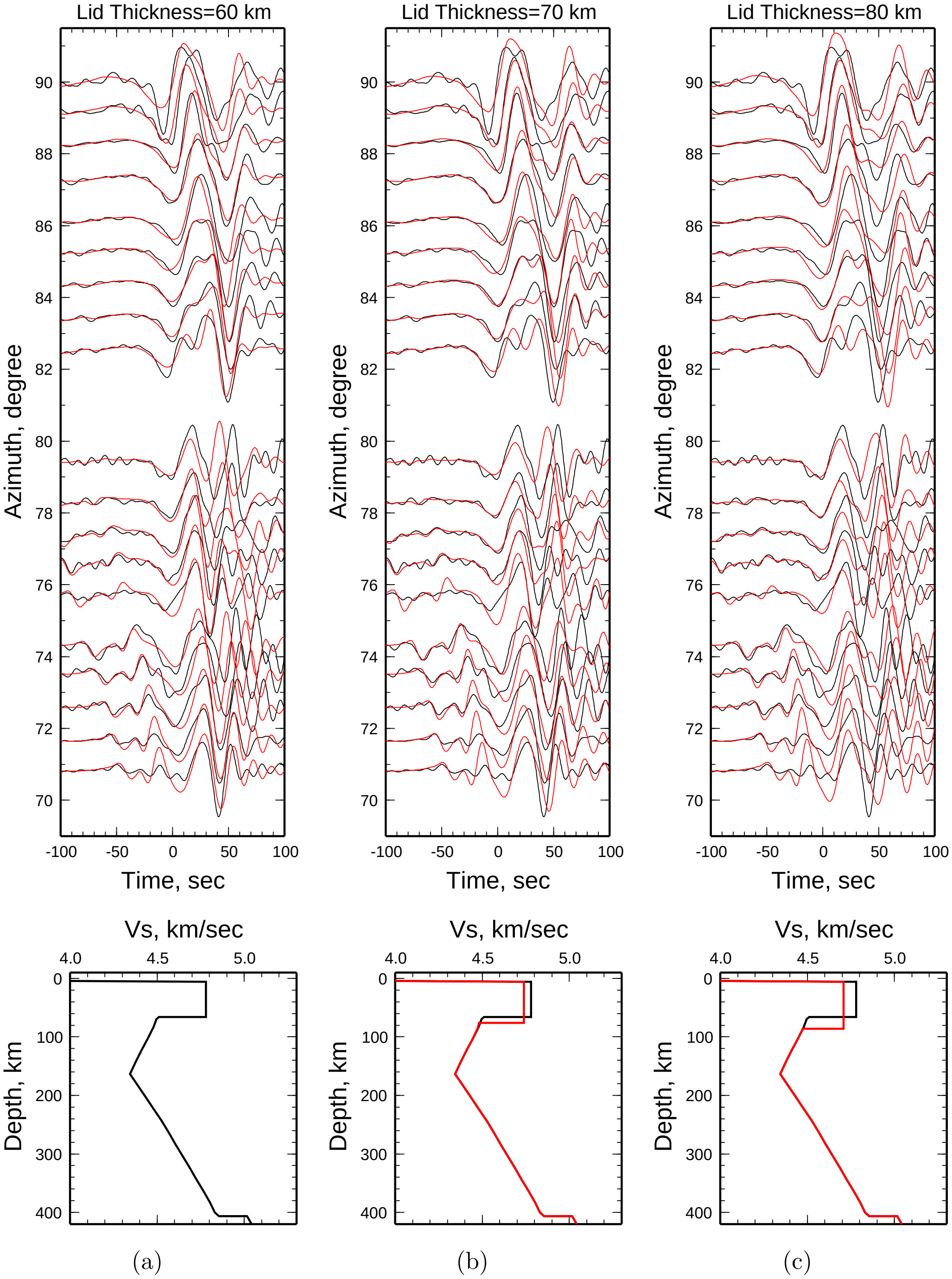

Figure 4.12: The waveform fits from Fig. 4.10 with our preferred SH model $PAC06_{sh}$ (a) are compared to those from the perturbed models, particularly of a thicker lid (b) and (c). The perturbed models are shown in red with $PAC06$ in black. We display only the guided waves from the composite cross section in Fig. 4.10, since the tested perturbations have little effect on the earlier arrivals. Time axis as in Fig. 4.11.

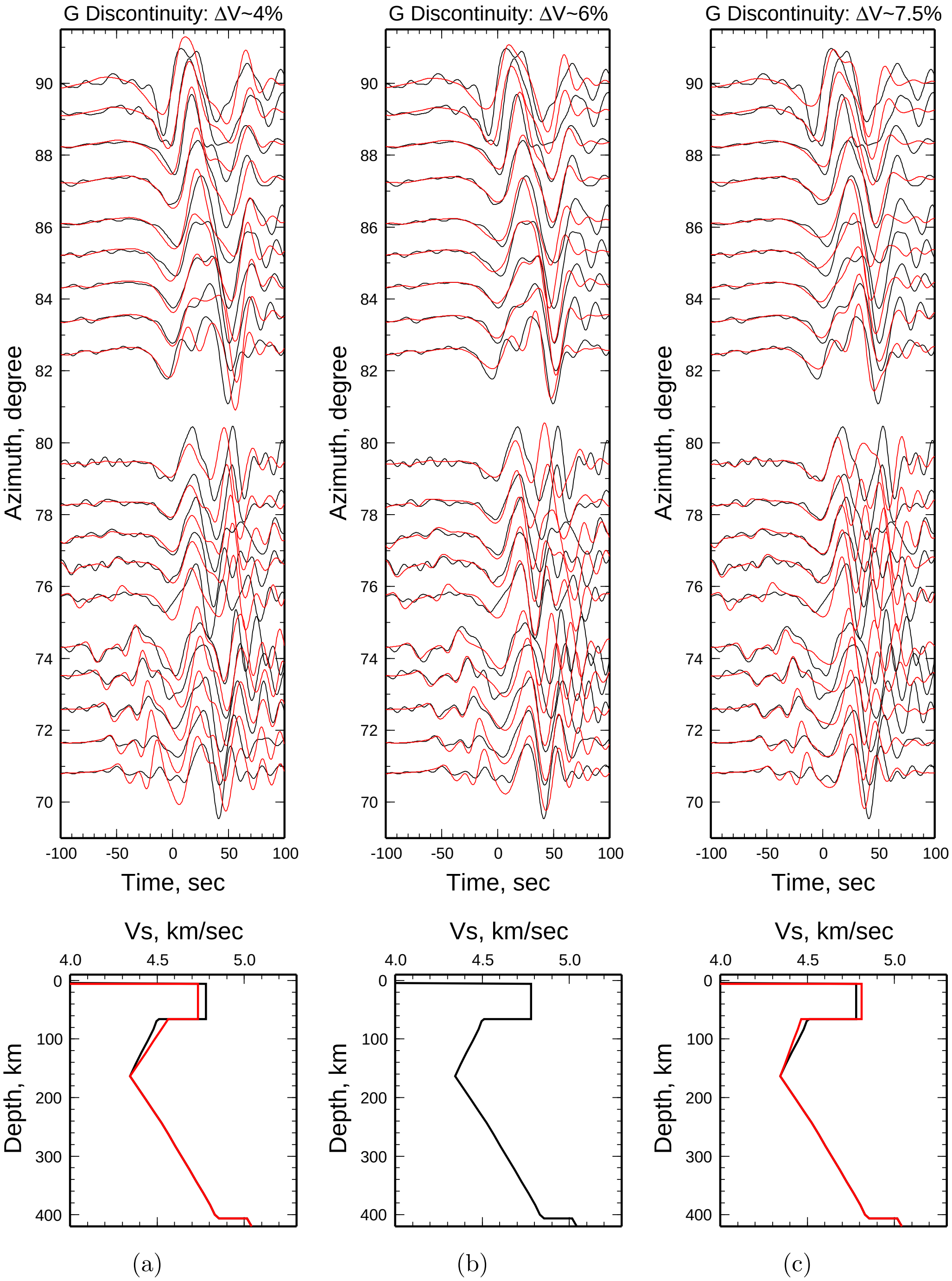

Figure 4.13: The waveform fits with our preferred SH model $PAC06_{sh}$ (b) are compared to those from the perturbed models, particularly of a smaller velocity jump at "G" discontinuity (a) and a larger one (c). The perturbed models are shown in red with $PAC06$ in black. We display only the guided waves from the composite cross section in Fig. 4.10, since the tested perturbations have little effect on the earlier arrivals. Time axis as in Fig. 4.11.

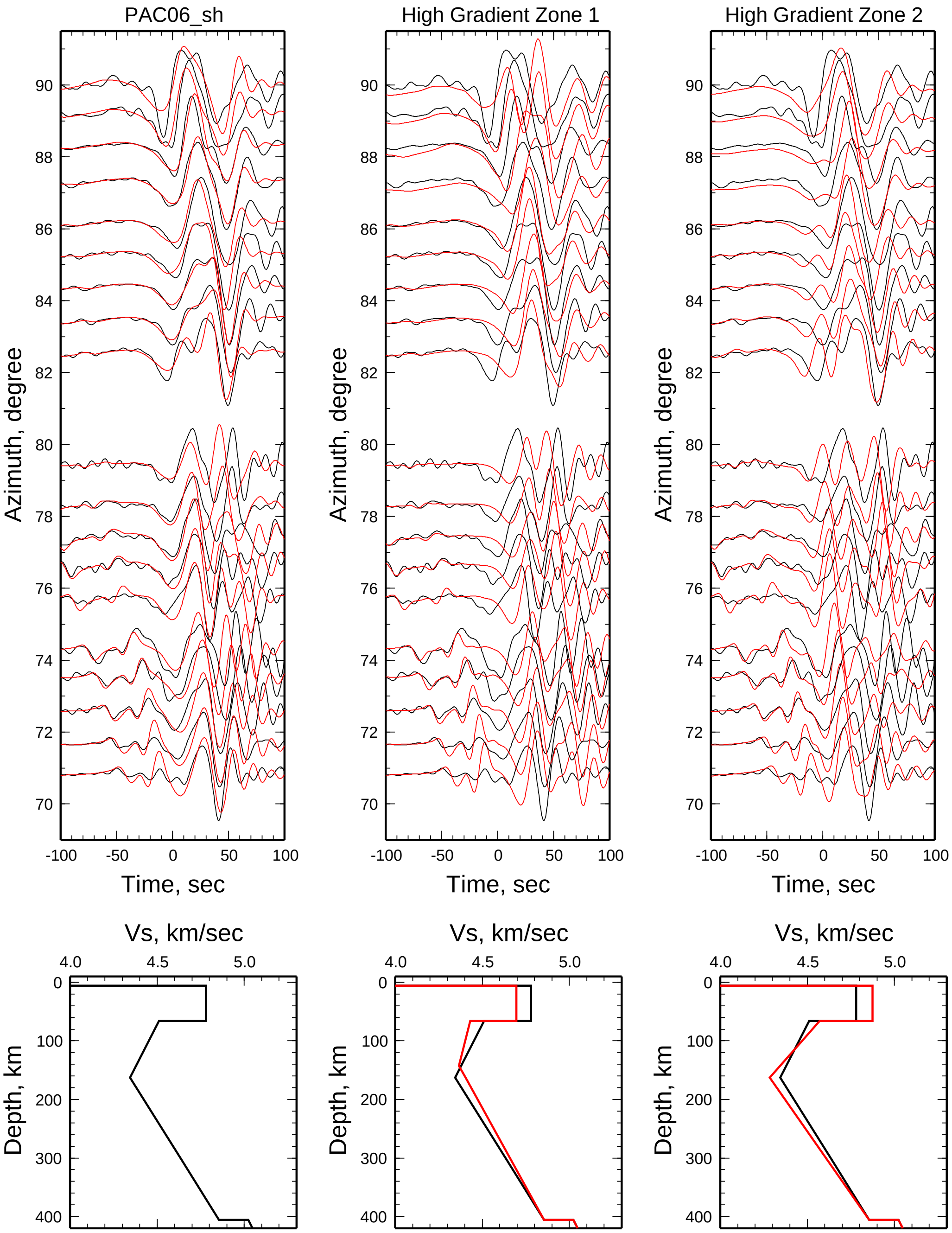

(a) (b) (c)

Figure 4.14: The waveform fits with our preferred SH model $PAC06_{sh}$ (a) are compared to those from the perturbed models, particularly of higher velocities in the high gradient zone (HGZ) (b) and lower velocities in the HGZ (c) The perturbed models are shown in red with $PAC06$ in black. The perturbations are mainly used to investigate possible trade offs between the velocities of the first two layers and the HGZ. We display only the guided waves from the composite cross section in Fig. 4.10, since the tested perturbations have little effect on the earlier arrivals. Time axis as in Fig. 4.11.

4.3.2 Transition zone

The transition zone comprising the two major mantle discontinuities plays the most significant role in shaping the triplication patterns, since the triplicated branches travel nearly the same paths except in the vicinity of the discontinuities. Therefore, modeling the separation, the cross over and the relative amplitudes of the triplicated branches provides tight constraints on the transition zone (e.g. *Grand and Helmberger*, 1984b; *Melbourne and Helmberger*, 1998). In this study, we widely observe the triplications of the higher-order multiplets SSS and S^4. Among them, those of S^4 are mainly from intermediate and deep events, where the guided waves are well suppressed. We started with a trial structure for the transition zone from the tectonic North America model (TNA) (*Grand and Helmberger*, 1984b) (Fig. 4.15), and used a large number of the observed triplications to examine the details. We let the TNA model stand unless modifications were required to better explain our observations, since the transition zone structure of TNA is particularly well constrained with good sampling of all the triplicated branches due to both the 410 km and 660 km discontinuities. The resulting transition zone structure in our preferred model $PAC06$ turned out to be very similar to that of TNA, and the major difference is that $PAC06$ has a small velocity jump ($\Delta V_s \sim 1\%$) at approximately 516 km. Although we did not observe clear triplications due to such a small discontinuity, it is needed mainly to explain the amplitudes of the triplicated "*cd*" branches (Fig. 4.4) that bottom out within the transition zone.

Our model $PAC06$ inherited a ∼406 km discontinuity from TNA. The velocity jump, however, is smaller (∼4%), mainly due to the generally larger velocities in the shallower part of the model (see Fig. 4.15), which are required to explain the differential travel times between the multiplets and the guided waves. We have conducted various tests on the fine structures of the discontinuity, to examine the exact depth, velocity jump and sharpness of the discontinuity. However, these fine-scale features cannot be well resolved with our data set. In particular the synthetics constructed with the perturbations produce nearly equal waveform fits to most of the observations.

This is because our data set does not contain sampling of the 410 km triplications as good as those addressed in *Melbourne and Helmberger* (1998) or *Song et al.* (2004).

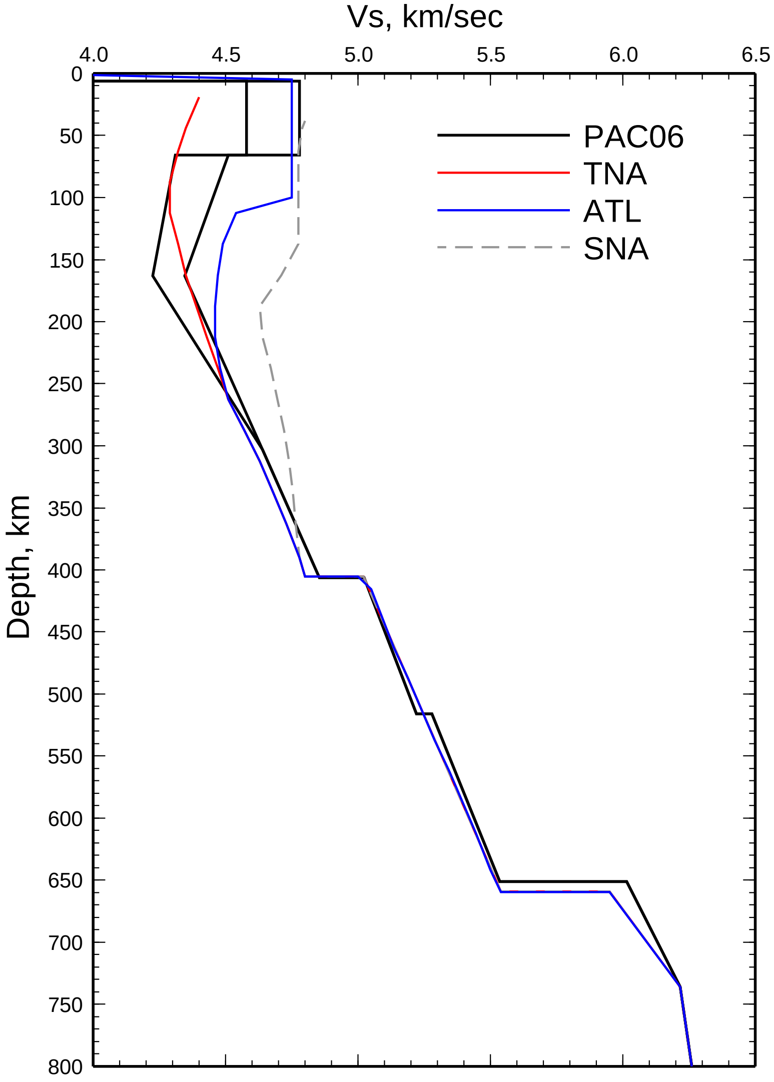

Figure 4.15: Comparison of $PAC06$ with the earlier pure path upper-mantle models, TNA, SNA (*Grand and Helmberger*, 1984b) and ATL (*Grand and Helmberger*, 1984a), developed by modeling similar multi-bounce S wave data sets.

However, the radial structure within the transition zone is well determined, particularly, the average velocity gradient and the ∼1% velocity jump at approximately ∼516 km. The constraint is mainly from modeling the relative behavior of the "*cd*" and "ef" branches (see Fig. 4.4). Figure 4.16 gives such an example, where we compare selected SSS waveform fits with our preferred model $PAC06$ and the perturbed

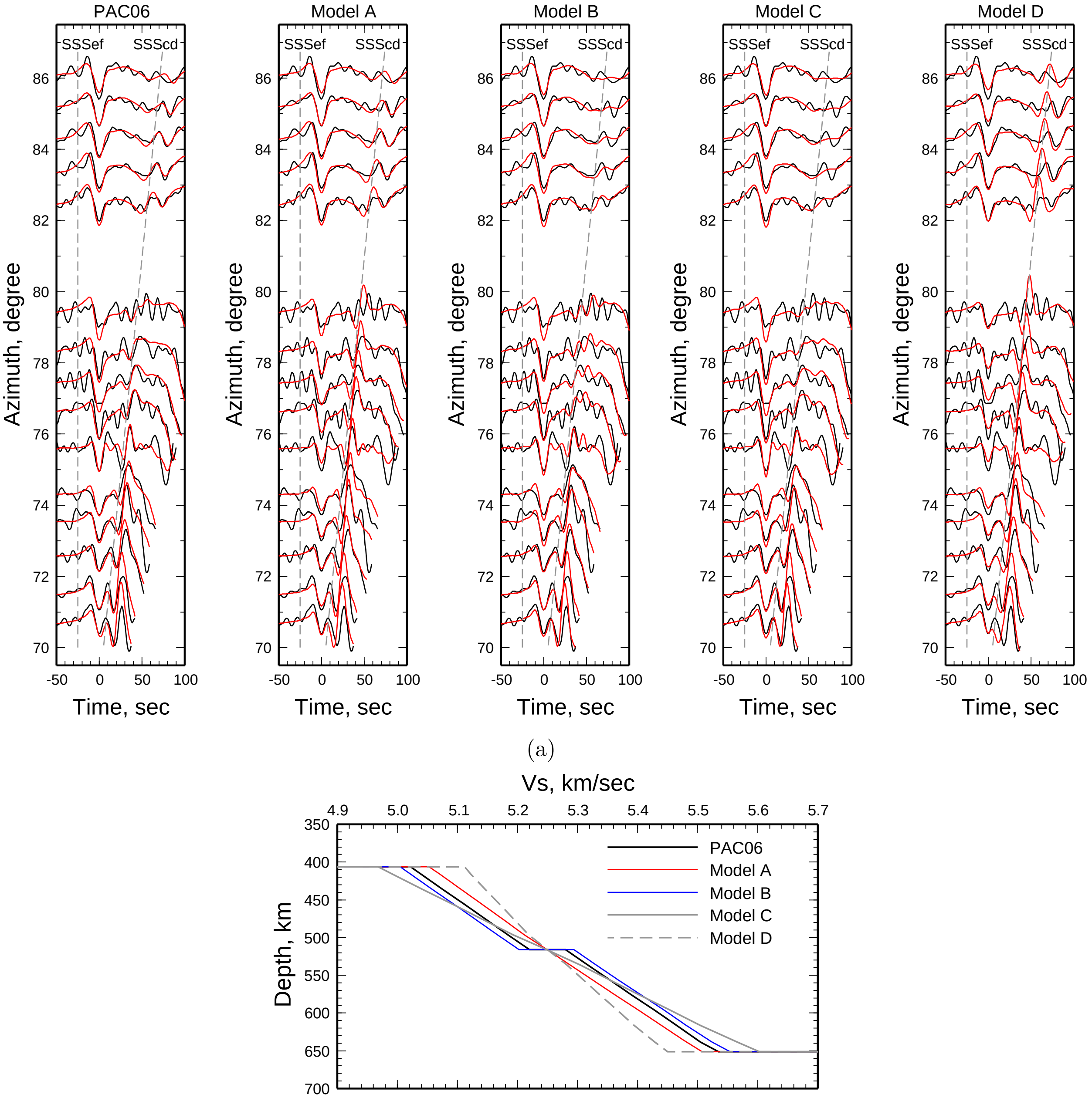

(a)

(b)

Figure 4.16: The selected SSS waveform fits from four shallow events (10100677, 9982833, 9564185 and 9533473 from the bottom to top) with our preferred model $PAC06_{sh}$ and the perturbed models (a). The perturbations are particularly concentrated in the transition zone (b), which is the most sensitive to the triplicated branch SSS_{cd}. Both the data (black) and synthetics (red) are aligned on SSS_{ef}, and the normalized amplitudes by the maxima on the records are plotted. Note the different behavior of the synthetic SSS from the perturbed models, in particular, the amplitude contrast between SSS_{ef} and SSS_{cd}.

ones. The data shown are all selected from shallow events to avoid complications caused by the depth phases. As the distance increases, SSS_{cd} systematically moves backwards relative to the forward branch SSS_{ef}. Although there are small perturbations on the individual observations, the stability of the triplication pattern indicates little significant lateral variation along the path. Our model $PAC06$ accurately produces both the differential times and relative amplitudes between the triplicated branches SSS_{ef} and SSS_{cd} (Fig. 4.16), while the perturbed model "A" with a similar gradient, but no 516 km velocity jump, significantly over-predicts the amplitudes of the backward branch SSS_{cd}. On the contrary, the bigger 516 km discontinuity in the perturbed model "B" (Fig. 4.16) exaggerates the triplication in SSS_{cd}, and causes SSS_{cd} to fade away beyond 82°. Also in Fig. 4.16, we included two models "C" and "D" with different velocity gradients. As the larger gradient in model "C" tends to suppress the "*cd*" branch, model "D" with the smaller gradient produces the magnified and advanced SSS_{cd}. We have also investigated the depth resolution of the small discontinuity in the transition zone of $PAC06$. Varying the discontinuity depth mainly changes the position of the triplication on the "*cd*" branch. Although there is some uncertainty, a depth of approximately 516 km proved the best estimate.

$PAC06$ contains a slightly shallower 651 km discontinuity and a faster high gradient zone right below the discontinuity compared to TNA (see Fig. 4.15). These features were well examined with our data. Synthetic experiments showed significant advancement of the "ef" branches, particularly of SSS and S^4 by the elevated discontinuity and faster high gradient zone, which however, were required by our observations.

4.3.3 Summary: SH component

In the previous sections, 4.3.1 and 4.3.2, we mainly concentrated on the derivation of the model, where we showed complete waveform comparisons only for a small fraction of the studied events. Although we will not add more such comparisons here, we summarize the overall fit of the differential travel times between the S multiplets for all the events in Fig. 4.17. We use differences between synthetics and data of the differential travel times, ΔT_{S-SS}, ΔT_{SSS-SS} and $\Delta T_{SSSS-SS}$ (Fig. 4.17). To calculate these timing differences, we have measured the time lags between the synthetics and data for S, SS, SSS and S^4 respectively by waveform cross correlation. In cases for which SSS or S^4 is triplicated, the emphasis has been given to the early branch. The alignment of synthetics and data on SS has eliminated possible origin time problems. Moreover, we have also applied event mislocation corrections (see Table 4.1) for the few events that displayed relatively large, systematic discrepancies in the differential time measurements. In particular, the observed higher-order multiplets from these events are increasingly faster or slower than the synthetic predictions, which can be easily explained by the events' mislocation error. The data points in Fig. 4.17 are color-coded by the depths of the events, while the overlain waveform comparisons for the selected events are given in Appendix B.

The most apparent anomaly in Fig. 4.17 occurs for ΔT_{S-SS}, where large negative values of ΔT_{S-SS} up to ∼-7 sec are observed. This implies that the observed direct S waves are faster than the model would predict. We attribute the anomaly to the fast slab effects (see the earlier discussion of Fig. 4.6). Although this warrants further investigation, there are two main lines of evidence that favor our argument. First, nearly all the problematic events are shallow or slightly deeper, sampling a particular distance range (∼80°–85°). Moreover, most of these events are located along the complex New Hebrides subduction slab (see Appendix B). Secondly, the upper mantle structure is not an effective modifier on the differential travel times between S and the higher-order multiplets. Another note worthy feature in Fig. 4.17 is the linear trend for ΔT_{S^4-SS}, where ΔT_{S^4-SS} systematically increases from the westernmost coastal stations to the easternmost in land ones. Such a tendency becomes particularly obvious when the guided waves are involved for the shallow events, due to the sharp transition from fast oceanic lithosphere to thick continental crust across the Pacific–North America boundary.

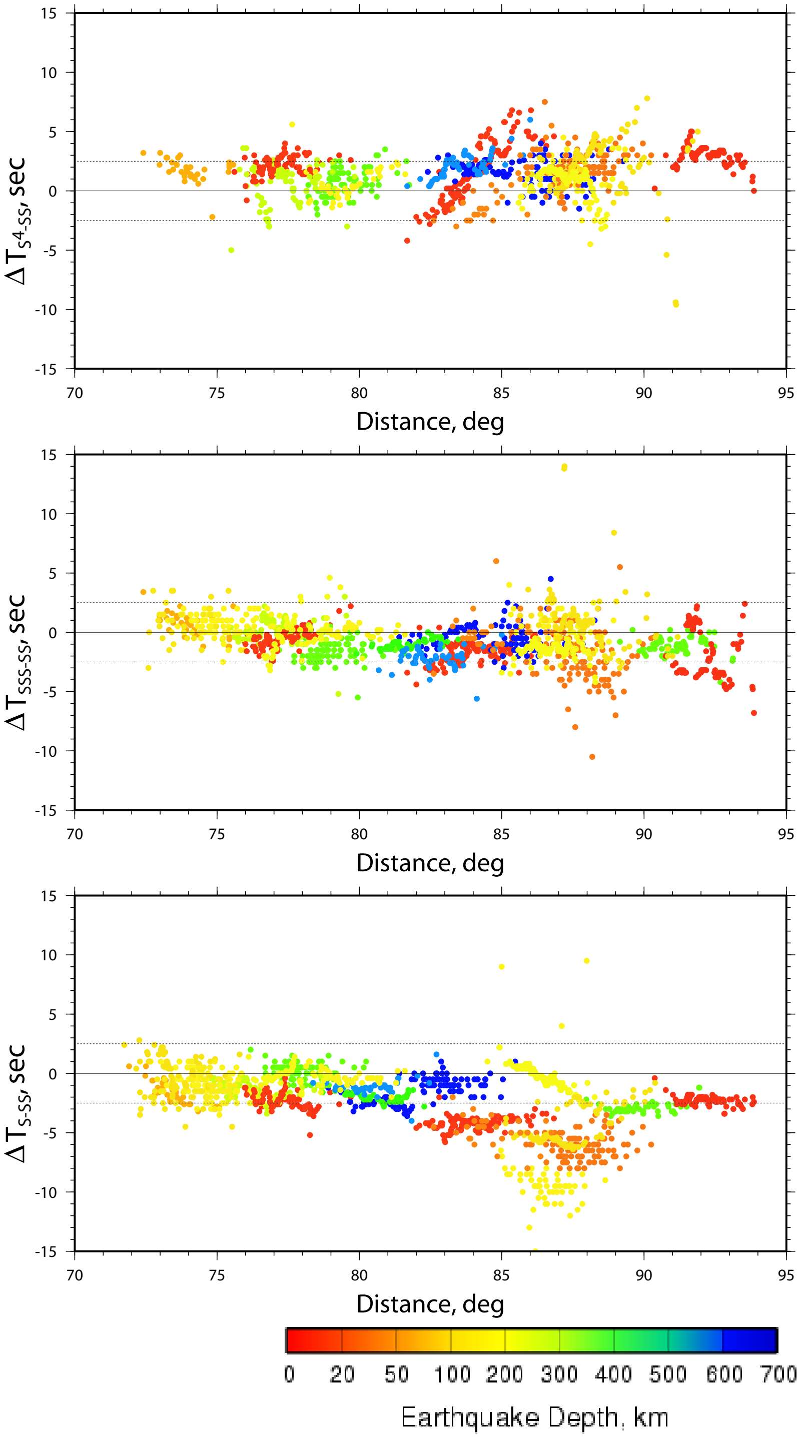

Figure 4.17: S wave multiplets' differential times, particularly ΔT_{S-SS}, ΔT_{SSS-SS} and $\Delta T_{SSSS-SS}$, between the data and synthetics. A positive value implies the separation between the multiplets on the data is smaller than that on the synthetics, while a negative value suggests the opposite. The data points from different events are color-coded by the events' depths.

4.3.4 SV component

The above discussion was restricted to the transverse (SH) component, while in this section, we will address the SV wave observations. We will particularly focus on the vertical component, since it generally produces better signal to noise ratios than the radial component. The greatest difficulty in modeling the SV waves is caused by the SV–P wave coupling. The problem can get overwhelming, especially when the SV-coupled PL waves are developed, and mainly controlled by the crustal waveguide for continental paths (e.g. *Helmberger and Engen*, 1974). However, although we widely observe the energy leakage of SV waves into P waves in this study, their coupling effect is not significant, which implies that the shallow oceanic structure is more uniform. For an example, we display the cross section of the vertical component from a shallow event in Fig. 4.18, where the multi-bounce SV waves are easily recognized and labeled. Among them, S^4 is the strongest due to the constructive interference of the triplicated branches at the sampled distance range (see Fig. 4.4). On the SV records, even S^5 can be clearly observed, since the Rayleigh waves are much slower. As we will address later in this section, these S^5 waves that bottom out from approximately 300 km deep provide a good constraint on the depth extent of the observed seismic anisotropy.

Many investigators have reported radial anisotropy (or transverse isotropy) from surface wave studies in the upper mantle beneath the Pacific ocean (e.g., *Ekström and Dziewonski*, 1998). However, it is not appropriate for us to contrast the SH and SV observations directly, since the multi-bounce SH and SV waves contain different phase shifts from the bounce points and the station-side receiver functions. One way to bypass the problem is to compare the SV observations with the synthetics from our well-constrained SH model (Fig. 4.18). Since there is some contamination of SS, we have chosen to align the synthetics and data on S^3 instead. The alignment resulted in a large shift of over 20 sec for the synthetics relative to the data, which cannot easily be attributed to an origin time problem, since the observed direct S waves are apparently advanced by about that amount. Moreover, the higher-order multiplets S^4 and S^5

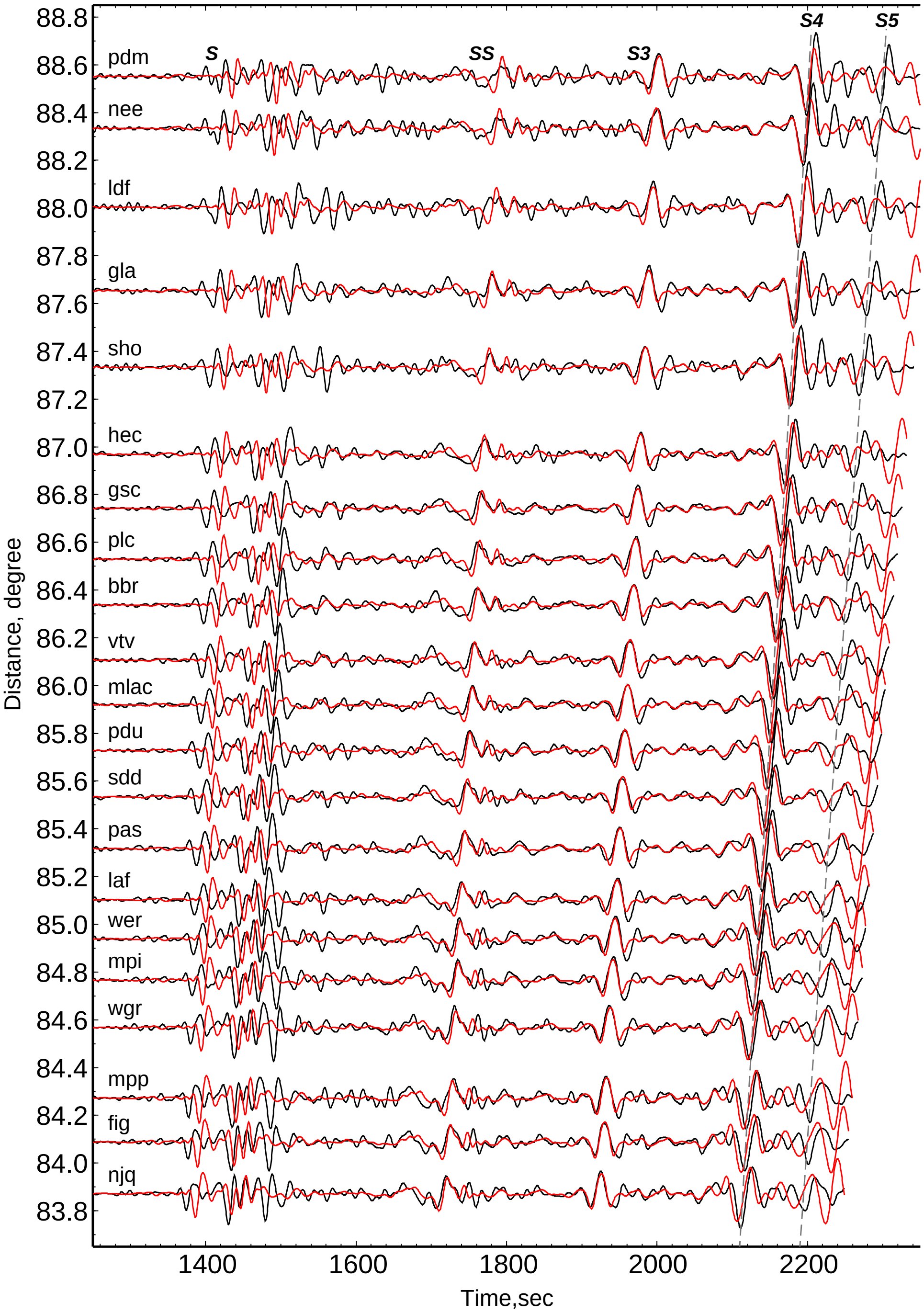

Figure 4.18: The selected waveform fits for the vertical component of a shallow event 9792597 (see Table 4.1) with our preferred SH model $PAC06_{sh}$. The data are shown in black with synthetics in red. We chose to align the synthetics and data on "$S3$", since there is some contamination on "SS". Labeled are the S wave multiplets up to S^5 that can be easily recognized. Note the synthetics have been shifted by approximately 20 sec for such an alignment. However, that is about the amount the observed direct S waves are advanced. Moreover, the higher-order multiplets S^4 and S^5 are delayed on the data relative to the synthetics.

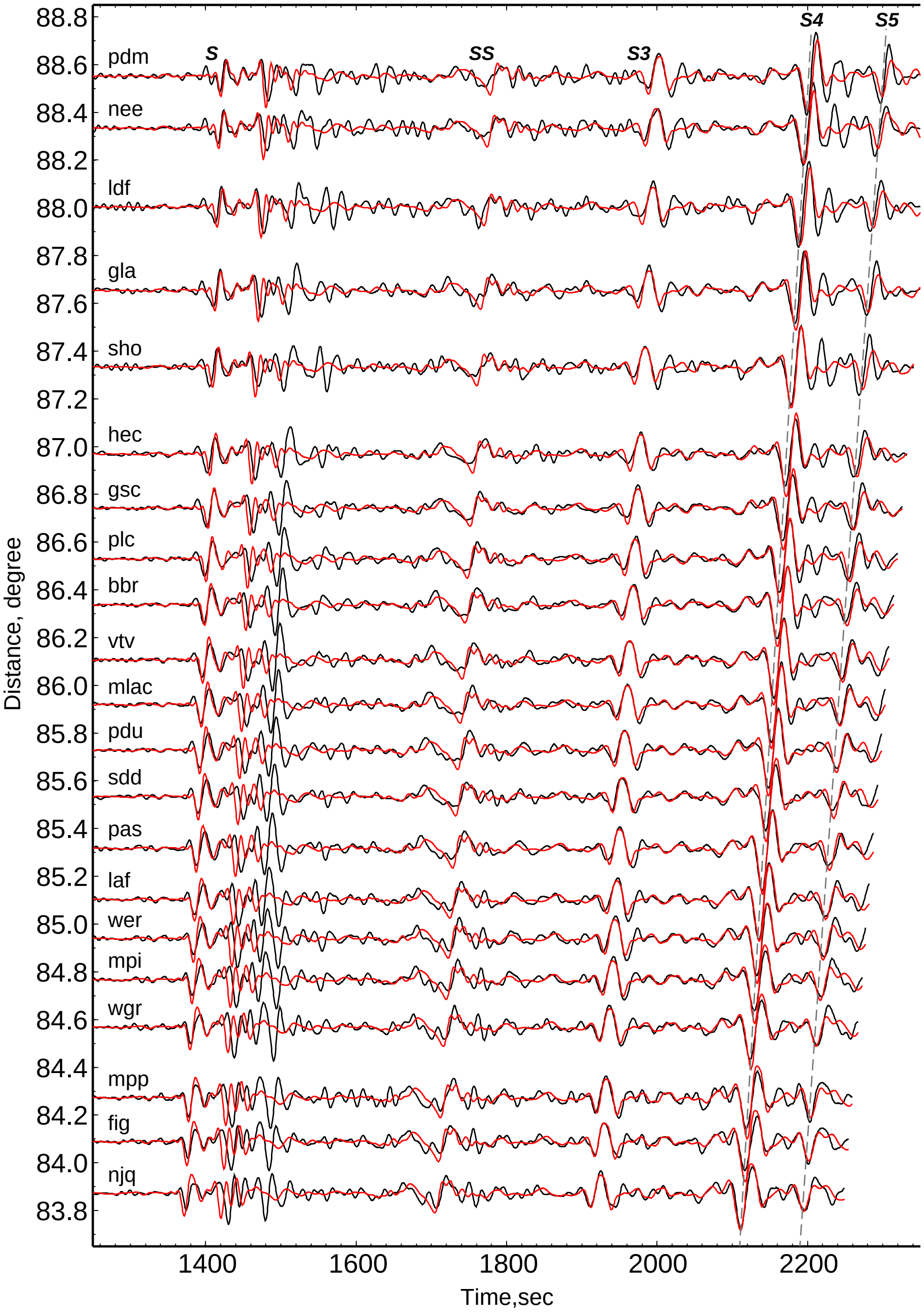

Figure 4.19: The selected waveform fits for the vertical component of the same event as shown in Fig. 4.18 with our preferred SV model $PAC06_{sv}$.The data are shown in black with synthetics in red. We aligned the synthetics and data on "S3", which resulted in an average shift of $\sim$ 2 sec for the synthetics relative to the data. Note the nice fits for all the labeled S wave multiplets.

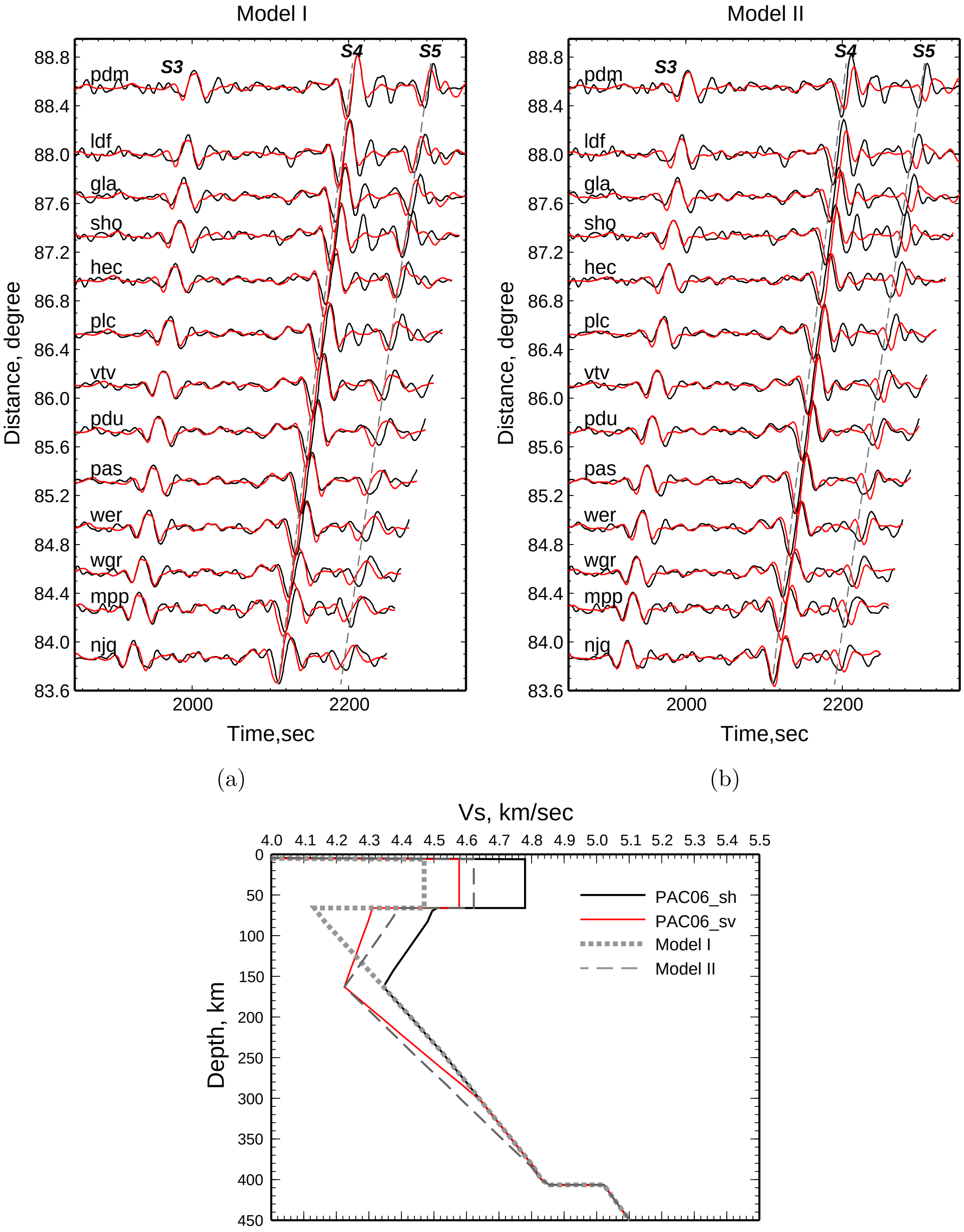

(a) (b)

(c)

Figure 4.20: The comparison of the waveform fits for the same event as shown in Fig. 4.19 with the perturbed *SV* models, Model I in (a) and Model II in (b). The model perturbations are mainly to investigate the depth extent of the observed anisotropy ($V\_sv < V\_sh$). Note in particular the synthetic S^5 is advanced with perturbed Model I, while slowed by Model II.

are progressively slower than the synthetic predictions. In particular, the observed S^5 are delayed by over 10 sec relative to the synthetics. All these discrepancies suggest the SV model is slower than the SH counterpart, especially in the shallow part, such as the Lid or LVZ, since the higher-order multiplets increasingly spend more time there.

We have concentrated on the shallow part in deriving the SV model due to the lack of good triplication data in the SV observations. The same structure below the 406 km discontinuity as in the SH model is assumed. Besides, we intended to retain the well-constrained features in the SH model, such as the Lid thickness and the large "G" discontinuity, in parameterizing the SV model. These features, however, are not well resolved with the SV data. Figure 4.19 displays the waveform fits for the same observations as shown in Fig. 4.18, with our preferred SV model $PAC06_{sv}$. The comparison between the SV and SH model is given in Fig. 4.20(c). $PAC06_{sv}$ accurately produces both the waveforms and travel times of the SV wave multiplets (Fig. 4.19).

$PAC06_{sv}$ features slower velocities than the SH model down to a depth of approximately 300 km (Fig. 4.20(c)). Although there is some trade off between the Lid and LVZ velocities for the SV model, the depth extent of anisotropy ($V_{sv} < V_{sh}$) is well determined, where the major constraint is attributed to the S^5 turning at approximately 300 km deep. For an example, we display in Fig. 4.20 the waveform comparisons with two trial models, where the anisotropy is confined to the top ∼170 km (Model I) or extends to the 406 km discontinuity (Model II). The perturbations have little effect on the deeper phases, such as S^4, S^3, SS or S, since their travel times are conserved. However, the influences on S^5 are significant, because S^5 travels nearly flat at about 300 km deep; thus it is rather sensitive to the velocity perturbations there. Our experiments with various perturbed models suggest significant anisotropy ($\Delta V_{sh-sv} > 1\%$) extending below 220 km depth.

4.4 Results and discussions

In this study, we concentrated on resolving the upper mantle layering by constructing simple models with as few parameters as possible. In particular, if a linear gradient between two depths proved effective in explaining most observations, we did not add any other *posterior* constraints. Our preferred 1D model, $PAC06$ (Table 4.2), however, provides excellent fits to both the waveforms and travel times of the observed S wave multiplets from a large number of events.

Table 4.2: Model $PAC06$

Depth (km)	V_{sh} (km/sec)	V_{sv} (km/sec)	Q_s
0.2	1.00	1.00	20
0.2	3.20	3.20	20
6	3.20	3.20	20
6	4.78	4.58	160
66	4.78	4.58	160
66	4.51	4.31	100
163	4.34	4.22	100
303	4.64	4.64	120
406	4.86	4.86	160
406	5.02	5.02	180
516	5.22	5.22	180
516	5.28	5.28	180
651	5.54	5.54	180
651	6.01	6.01	310
736	6.22	6.22	310
900	6.33	6.33	310

Figure 4.1 displays the interesting comparison between the model $PAC06$ from this study and the model $PA5$ developed by *Gaherty and Jordan* (1996) for the older half of the corridor from Fiji-Tonga to Hawaii. In their study, *Gaherty and Jordan* (1996) mainly utilized relatively long period ($>$ 25 sec) body and surface waves plus the ScS reverberations (e.g. *Revenaugh and Jordan*, 1991b) for determining the discontinuities. Although $PA5$ samples relatively old oceanic lithosphere (100-125 Ma), while our studied path covers a wider range from 125 Ma to ∼10 Ma at the receiver side, the two models display remarkable agreement (Fig. 4.1), which suggests that the whole path is highly uniform. In particular, $PAC06$ and $PA5$ both contain a

high-velocity lid of ∼60 km with a large Lid-LVZ boundary (the "G" discontinuity). There is no clear evidence of a progressively thinning lithosphere as the crustal age gets younger. Also the sharp "G" discontinuity contradicts the smeared transitions predicted from theoretic thermal cooling models. However, they favorably support the argument by *Gaherty et al.* (1999) that the "G" discontinuity rather represents a compositional boundary than a solely thermal boundary. A note worthy discrepancy in the comparison is that $PA5$ has a faster lid, with a slower high-gradient zone (HGZ) below ∼160 km compared to $PAC06$. Future work is needed to quantify how much difference there is a reality. However, as we have seen earlier (Fig. 4.14), the velocity contrast between the shallower part and the HGZ is well constrained in $PAC06$. The biggest discrepancy between $PAC06$ and $PA5$ occurs around the 660 km discontinuity, where the major constraints for $PA5$ were from the ScS reverberations.

$PAC06$ contains radial anisotropy down to a depth of ∼300 km, which is consistent with the results from previous studies (e.g. *Nishimura and Forsyth*, 1989; *Ekström and Dziewonski*, 1998). The shallow cutoff (∼160 km) of anisotropy in $PA5$ is probably mainly an artifact from the model parameterization. The anisotropy of $V_{sh} > V_{sv}$ in the lid can be attributed to the lattice preferred orientation (LPO) in olivine when the lid was formed (e.g. *Nicolas and Christensen*, 1987), since the studied path is consistently oblique to the ancient spreading direction. The anisotropy in the LVZ could be caused by the preferred orientation of melt-filled pockets (e.g. *Schlue and Knopoff*, 1977) or shearing in the asthenosphere due to mantle flow or plate motions (e.g. *Zhang and Karato*, 1995; *Montagner and Tanimoto*, 1991). However, due to the limited azimuthal sampling, the anisotropy in $PAC06$ only represents a projection of the full (3D) anisotropy onto the particular path.

Figure 4.15 compares $PAC06$ to the earlier pure path models developed with similar multi-bounce S wave data, particularly, TNA, SNA for the North America shield (*Grand and Helmberger*, 1984b) and ATL featuring the old Atlantic (∼ 70–150 Ma) (*Grand and Helmberger*, 1984a). Except for SNA, the other three models all contain a well-developed LVZ. Moreover, the high gradient zone (HGZ) beneath the smallest velocities in the LVZs appear unique for the oceanic paths, in contrast with the continental model SNA. The steep gradient in the HGZ is intriguing, since it cannot be easily explained with a subadiabatic thermal gradient or decreasing partial melt with depth. However, a depth-dependent increase in the amount of pyroxenite could produce such an enhanced velocity gradient, though a plausible dynamical picture is absent (e.g. *Stixrude and Lithgow-Bertelloni*, 2005). Also note in Fig. 4.15 the lowest velocities in the LVZ migrate upward below the ridges (TNA) and downward beneath the old oceans (ATL). This might suggest that possible flows in the LVZ are not confined within a certain depth range.

Compared to the other models, $PAC06$ contains a velocity jump at ~516 km (Fig. 4.15). This is in good agreement with global stacks of SS precursors (*Shearer*, 1990, 1993) or ScS reverberations (*Revenaugh and Jordan*, 1991a). The small velocity jump at the discontinuity is consistent with the $\beta-\gamma$ transition in $(Mg, Fe)_2SiO_4$ of the mineralogical models (e.g. *Rigden et al.*, 1991).

4.5 Conclusion

In this study, we developed a pure path shear velocity model $PAC06$ along the corridor from Tonga-Fiji to California. The model contains a fast lid ($V_{sh} = 4.78$ km/sec, $V_{sv} = 4.58$ km/sec) ~60 km thick. The underlying low velocity zone (LVZ) is prominent with the lowest velocities $V_{sh} = 4.34$ km/sec, and $V_{sv} = 4.22$ km/sec. Besides the 406 km and 651 km discontinuities, $PAC06$ also has a small (~1%) velocity jump at ~516 km. We consider these main features of $PAC06$ to be well determined, since $PAC06$ explains a large data set from various events. Therefore, it is ideally suited for comparing with mineralogical models.

Appendix A

Source Parameters of 159 Southern Califonia Events (1998.4-2004.10)

	SCSN				Fault Parameters		
Event id	origin date-time	lat/lon	*h*	mb	FM:$\phi/\delta/\lambda$	*h*	Mw
10964587	2001/07/14,17:30:39.	36.02/-117.87	3.7	3.8	81/88/12	5.1	4.4
10972299	2001/07/19,20:42:36.	34.27/-117.46	10.9	3.8	92/62/56	9.8	3.8
10992159	2001/07/20,12:53:07.	35.99/-117.88	3.4	4.4	80/79/-20	5.1	4.1
12887732	2002/05/02,06:00:15.	35.71/-118.08	3.1	3.8	218/80/9	5.1	3.6
13657604	2002/06/14,12:40:46.	36.69/-116.34	7.0	4.9	212/29/-92	10.6	4.5
13692644	2002/07/25,00:43:15.	34.16/-117.43	6.5	3.7	229/69/-16	6.5	3.6
13917260	2002/12/10,21:04:00.	32.23/-115.80	7.0	4.8	42/51/-42	7.2	4.6
13945908	2003/03/11,19:28:17.	34.36/-116.13	3.9	4.6	47/81/-6	8.2	4.3
14065544	2004/06/15,22:28:48.	32.33/-117.92	10.0	5.3	234/72/-31	17.1	5.0
3298170	1998/03/06,05:54:21.	36.07/-117.62	1.1	4.5	71/85/9	9.0	4.4
3298292	1998/03/11,12:18:51.	34.02/-117.23	14.9	4.5	236/66/-79	17.4	4.2
3317364	1999/05/14,10:52:35.	34.03/-116.36	1.8	4.2	61/84/10	4.5	4.1
3319204	1999/08/01,16:27:18.	37.40/-117.09	6.0	4.0	92/75/-3	9.2	4.8
7112721	1998/10/01,18:18:15.	34.11/-116.92	4.4	4.6	229/73/34	7.0	4.3
7177729	2000/02/14,09:57:42.	34.80/-116.37	2.3	4.4	98/90/38	5.0	4.0
7179710	2000/02/28,23:08:42.	36.07/-117.60	0.2	4.2	217/70/4	4.2	4.2
9038699	1998/01/05,18:14:06.	33.95/-117.71	11.5	4.3	40/83/34	9.9	3.9
9044494	1998/03/06,05:47:40.	36.07/-117.64	1.8	5.2	228/77/-24	7.7	5.0
9044650	1998/03/06,07:36:35.	36.06/-117.65	2.1	4.4	220/74/-18	9.8	4.2
9045109	1998/03/07,00:36:46.	36.08/-117.62	1.7	5.0	69/89/-6	6.3	4.7
9058934	1998/07/02,03:39:50.	36.95/-117.53	6.0	4.8	242/81/-11	3.4	4.7
9064093	1998/08/16,13:34:40.	34.12/-116.93	6.2	4.8	47/90/-35	6.7	4.5
9064568	1998/08/20,23:49:58.	34.37/-117.65	9.0	4.4	109/36/91	10.6	4.1
9069997	1998/10/27,01:08:40.	34.32/-116.84	5.9	4.8	43/73/-15	7.0	4.4
9070083	1998/10/27,15:40:17.	34.32/-116.85	4.3	4.1	51/79/-21	5.6	3.8
9075803	1999/01/13,13:20:55.	32.71/-115.92	10.5	4.4	219/90/-30	8.2	4.2
9087073	1999/05/15,13:22:11.	37.53/-118.82	6.0	5.4	28/70/36	5.0	5.5
9090617	1999/06/03,21:36:28.	37.53/-118.80	0.0	4.4	188/58/16	3.8	4.2

Continued on next page...

Table A.1 – continued from previous page

	SCSN				Fault Parameters		
Event id	origin date-time	lat/lon	h	mb	FM:$\phi/\delta/\lambda$	h	Mw
9095528	1999/07/11,18:20:46.	35.73/-118.48	5.7	4.3	-1/36/-66	5.6	4.2
9096656	1999/07/19,22:09:27.	33.63/-116.72	14.1	4.2	57/52/33	14.9	3.8
9098566	1999/08/01,16:06:20.	37.53/-116.97	6.0	5.9	78/40/-39	8.5	5.7
9098867	1999/08/02,05:40:26.	37.42/-117.06	6.0	4.1	81/56/-18	7.3	4.1
9105672	1999/09/20,07:02:49.	34.32/-116.85	2.8	4.1	51/83/-22	5.5	3.9
9106250	1999/09/26,16:15:37.	37.44/-117.04	6.0	4.5	99/30/-49	5.8	4.2
9109131	1999/10/16,16:08:24.	34.68/-116.31	0.8	4.0	241/67/-30	3.9	3.9
9109254	1999/10/16,17:38:48.	34.43/-116.25	0.0	4.9	261/32/10	6.5	4.6
9109287	1999/10/16,18:01:57.	34.70/-116.29	3.6	4.3	83/79/-28	3.6	4.0
9109636	1999/10/16,22:53:41.	34.71/-116.36	6.0	4.5	250/76/-21	8.8	4.1
9110685	1999/10/17,16:22:48.	34.35/-116.14	0.2	4.2	49/82/-3	5.3	4.1
9113909	1999/10/21,01:25:42.	34.87/-116.40	3.2	4.2	111/70/15	5.2	4.0
9114763	1999/10/22,12:40:52.	34.34/-116.21	9.5	4.2	75/79/8	15.9	3.8
9114812	1999/10/22,16:08:48.	34.87/-116.41	0.9	5.0	90/84/22	4.0	5.0
9114858	1999/10/22,16:48:23.	34.83/-116.38	4.2	4.1	262/80/16	4.2	3.8
9119414	1999/11/03,03:27:56.	34.84/-116.36	7.0	4.1	82/78/-17	5.9	3.9
9120741	1999/11/07,06:47:49.	34.79/-116.29	5.1	4.0	100/87/-20	6.8	4.0
9122706	1999/11/14,14:20:09.	34.84/-116.41	6.3	4.4	81/82/-13	7.3	4.3
9130422	1999/12/23,14:30:54.	34.59/-116.27	7.4	4.0	100/69/14	9.2	3.8
9140050	2000/02/21,13:49:43.	34.05/-117.25	15.0	4.3	272/82/-1	17.7	4.2
9151000	2000/05/18,09:41:37.	35.10/-118.30	6.8	3.9	31/75/40	7.5	3.7
9151609	2000/05/23,04:42:43.	36.32/-118.07	1.7	3.9	81/69/-39	9.2	3.9
9152038	2000/05/27,03:35:34.	35.78/-117.65	0.8	4.0	79/77/-26	3.5	3.8
9155518	2000/06/26,15:43:07.	34.78/-116.30	4.3	4.5	282/87/-18	7.3	4.4
9169867	2000/12/02,08:28:07.	34.27/-116.78	3.4	4.0	41/77/-7	5.9	3.8
9171679	2000/12/24,01:04:21.	34.92/-119.02	13.9	4.4	22/90/-22	17.1	4.1
9613229	2001/01/14,02:26:14.	34.28/-118.40	8.8	4.3	121/40/72	8.8	4.2
9613261	2001/01/14,02:50:53.	34.29/-118.40	8.4	4.0	79/58/33	7.6	3.9
9627721	2001/02/10,21:05:05.	34.29/-116.95	9.1	5.1	205/76/4	8.4	4.7
9627953	2001/02/11,00:39:15.	34.29/-116.94	8.1	4.2	198/46/-12	7.8	3.8
9644345	2001/04/14,14:51:22.	35.99/-118.33	5.6	3.8	181/51/-84	4.9	4.1
9652545	2001/05/14,17:13:30.	34.23/-117.44	8.7	3.8	50/49/-1	7.1	3.7
9653349	2001/05/17,21:53:45.	35.80/-118.04	8.7	4.2	214/80/-26	10.8	4.0
9653493	2001/05/17,22:56:45.	35.80/-118.05	8.4	4.1	212/74/-38	12.1	4.1
9655209	2001/05/23,19:10:34.	34.02/-116.76	14.4	3.8	31/67/43	16.8	3.7
9666905	2001/07/03,11:40:48.	34.26/-116.76	3.3	3.9	43/55/13	6.2	3.8
9674049	2001/07/17,12:07:26.	36.01/-117.86	7.0	4.8	259/90/-11	5.6	5.1
9674097	2001/07/17,12:25:18.	36.04/-117.87	5.6	4.1	30/47/-75	5.3	4.1

Continued on next page...

Table A.1 – continued from previous page

	SCSN				Fault Parameters		
Event id	origin date-time	lat/lon	h	mb	FM:$\phi/\delta/\lambda$	h	Mw
9674213	2001/07/17,12:59:59.	36.02/-117.88	0.4	4.7	243/71/-23	3.2	4.9
9686565	2001/07/28,01:09:29.	36.06/-117.87	1.7	4.0	49/63/-29	3.2	4.0
9689717	2001/08/02,16:21:18.	37.22/-117.79	10.1	3.7	2/22/-92	10.3	4.0
9716853	2001/10/28,16:27:45.	33.92/-118.27	21.1	4.0	110/74/81	15.8	3.8
9718013	2001/10/31,07:56:16.	33.51/-116.51	15.2	5.1	221/80/-48	17.0	5.0
9735129	2001/12/14,12:01:35.	33.95/-117.75	13.8	4.0	40/82/-26	8.3	3.7
9742277	2002/01/02,12:11:28.	33.38/-116.43	12.6	4.2	46/90/21	14.7	4.0
9753485	2002/01/29,05:53:28.	34.36/-118.66	14.2	4.2	94/66/85	13.1	4.3
9753497	2002/01/29,06:08:01.	34.37/-118.66	14.4	3.8	74/58/71	11.6	3.9
9753949	2002/01/29,20:23:07.	34.36/-118.67	12.6	3.6	61/70/85	10.2	3.8
9774569	2002/03/30,13:50:51.	33.19/-116.73	9.3	3.8	68/77/13	10.3	3.7
9775765	2002/04/05,08:02:56.	34.52/-116.29	5.6	4.4	331/43/-63	4.7	4.1
9805021	2002/07/31,08:31:47.	34.57/-116.44	3.0	3.7	137/60/61	8.5	3.5
9818433	2002/09/03,07:08:51.	33.92/-117.78	12.9	4.8	29/87/-6	7.6	4.3
9826789	2002/09/21,21:26:16.	33.22/-116.11	14.6	4.3	58/86/-12	12.8	4.0
9828889	2002/09/28,10:34:47.	35.95/-117.30	3.7	4.1	252/56/20	6.4	4.0
9829213	2002/09/28,18:11:29.	35.95/-117.31	3.5	4.0	246/69/18	5.9	3.8
9854597	2002/10/29,14:16:54.	34.80/-116.27	4.6	4.8	84/80/-10	7.6	4.5
9882325	2003/01/25,09:11:02.	35.32/-118.66	5.6	3.9	182/26/-42	3.5	4.1
9882329	2003/01/25,09:16:10.	35.32/-118.65	5.6	4.5	200/50/-34	3.9	4.3
9915709	2003/05/14,22:47:18.	33.75/-116.02	8.2	3.9	262/43/-36	7.4	3.6
9930549	2003/07/15,06:15:50.	34.62/-116.67	7.6	4.2	186/71/30	10.0	3.8
9941081	2003/08/27,06:02:22.	34.40/-118.65	17.9	3.9	263/87/-72	15.8	3.9
9966033	2003/12/20,16:35:23.	37.18/-117.86	9.3	4.0	230/59/-36	8.8	4.0
9983429	2004/02/14,12:43:11.	35.04/-119.13	12.1	4.3	72/38/87	12.9	4.5
3320884	1999/10/21,01:57:38.	34.86/-116.39	3.5	5.0	69/90/32	4.9	4.5
3320940	1999/10/22,20:16:01.	34.87/-116.40	1.3	4.1	250/65/-29	5.9	3.8
3320954	1999/10/22,20:17:30.	34.86/-116.39	2.9	4.2	110/63/37	3.3	4.0
3321590	1999/10/21,01:54:34.	34.87/-116.39	1.0	5.1	68/84/6	5.4	5.0
7210945	2000/12/27,00:27:14.	32.73/-118.07	6.0	4.0	265/89/-62	11.6	4.0
9109442	1999/10/16,20:13:37.	34.69/-116.28	1.3	4.6	81/71/-23	4.9	4.3
9141142	2000/02/29,22:08:05.	36.09/-117.60	0.1	4.0	223/82/-20	3.8	4.0
10023841	2004/06/29,10:20:43.	36.07/-117.90	5.3	3.7	70/77/34	8.1	3.7
10970835	2001/07/17,12:22:19.	36.03/-117.88	1.9	3.6	80/89/-36	7.0	3.9
13813696	2002/09/17,15:00:05.	33.50/-116.78	16.0	3.7	227/59/3	21.0	3.5
14000376	2003/10/29,23:44:48.	34.27/-118.75	13.8	3.6	238/58/43	9.2	3.6
14072464	2004/07/09,04:43:45.	32.51/-115.74	5.5	3.7	226/79/-50	7.7	3.7
14079184	2004/07/28,20:19:42.	34.13/-117.45	6.4	3.8	226/90/-20	5.2	3.6

Continued on next page...

Table A.1 – continued from previous page

	SCSN				Fault Parameters		
Event id	origin date-time	lat/lon	h	mb	FM:$\phi/\delta/\lambda$	h	Mw
3320951	1999/10/22,16:51:36.	34.82/-116.39	2.6	3.7	258/68/-26	5.2	3.6
3321426	1999/11/03,02:55:05.	34.80/-116.28	4.5	3.8	291/90/10	5.6	3.8
3324595	1999/10/22,11:34:23.	34.60/-116.27	0.0	3.8	151/44/88	5.9	3.7
7180136	2000/03/02,15:00:34.	36.08/-117.60	0.4	3.9	41/87/21	3.5	4.0
9045697	1998/03/08,15:28:41.	36.08/-117.62	1.1	3.9	58/82/-11	5.6	3.7
9059586	1998/07/05,16:25:14.	36.94/-117.54	6.0	3.7	251/23/9	4.7	3.9
9075784	1999/01/13,10:02:05.	32.72/-115.92	10.0	3.8	227/83/-36	8.8	3.8
9085734	1999/05/05,02:17:46.	34.07/-116.37	1.8	3.6	69/61/-12	2.6	3.6
9086693	1999/05/14,08:22:07.	34.03/-116.36	1.4	3.9	232/87/-12	4.8	3.9
9093975	1999/06/29,12:55:00.	34.01/-118.22	9.5	3.8	102/58/63	6.1	3.7
9094270	1999/07/01,12:43:07.	35.09/-118.31	6.9	3.8	34/74/31	9.0	3.6
9096972	1999/07/22,09:57:24.	34.40/-118.61	11.3	4.0	291/58/66	10.5	3.8
9109496	1999/10/16,21:10:50.	34.67/-116.34	2.9	3.9	257/72/-47	4.8	3.8
9114042	1999/10/21,05:47:38.	34.53/-116.27	0.0	3.8	179/40/92	6.2	3.6
9114612	1999/10/22,05:54:01.	34.70/-116.36	3.0	3.7	282/69/-63	5.9	3.5
9114775	1999/10/22,13:43:14.	34.85/-116.40	4.2	3.8	247/71/-29	3.7	3.6
9116921	1999/10/26,22:59:36.	36.45/-117.90	0.0	3.9	228/89/-26	4.4	4.0
9128775	1999/12/13,13:20:16.	34.10/-117.01	3.3	3.8	216/70/13	5.2	4.0
9147453	2000/04/16,01:15:57.	34.80/-116.27	4.1	3.8	279/71/8	6.5	3.6
9148510	2000/04/25,18:36:07.	33.16/-115.64	4.9	3.7	57/90/-36	6.5	3.8
9150059	2000/05/10,23:25:42.	33.16/-115.64	4.0	3.9	61/79/-34	12.0	4.0
9151375	2000/05/21,06:27:37.	34.29/-116.87	5.9	3.6	48/90/-22	7.7	3.5
9152745	2000/06/02,14:24:14.	33.18/-115.60	1.8	3.5	17/62/-61	11.4	3.8
9153800	2000/06/12,03:15:02.	34.68/-116.36	7.3	3.9	261/66/7	8.7	3.6
9154179	2000/06/14,22:39:27.	32.87/-115.51	8.8	3.6	249/60/-27	16.1	3.9
9158503	2000/07/26,03:01:46.	32.15/-115.11	6.0	3.8	121/77/14	14.3	3.9
9163702	2000/09/20,16:10:33.	36.05/-117.87	2.8	3.7	70/64/-41	2.4	3.7
9164821	2000/10/01,04:46:19.	32.12/-115.15	6.0	3.9	22/29/-31	11.7	3.9
9165019	2000/10/03,02:44:02.	35.78/-117.65	3.6	3.5	39/71/-57	6.2	3.5
9165761	2000/10/12,16:51:19.	34.56/-118.90	25.7	3.9	84/68/79	7.8	3.8
9627557	2001/02/10,17:50:22.	33.82/-116.15	8.2	3.9	69/90/-21	9.0	3.7
9642941	2001/04/08,01:25:28.	36.02/-117.81	3.6	3.8	51/60/-47	3.3	3.9
9646589	2001/04/23,16:33:48.	36.02/-117.88	4.8	3.5	71/83/-17	5.4	3.7
9653293	2001/05/17,20:47:58.	35.80/-118.04	5.6	3.6	240/66/-32	9.5	3.7
9671933	2001/07/14,17:30:28.	36.03/-117.88	2.7	3.6	263/89/-13	7.7	4.3
9673577	2001/07/16,15:55:28.	36.02/-117.88	2.9	3.5	242/68/-46	3.3	3.6
9674093	2001/07/17,12:22:28.	36.03/-117.86	5.5	3.8	258/78/-38	7.5	4.0
9674205	2001/07/17,12:56:31.	36.03/-117.88	2.7	3.7	250/79/-36	5.3	3.8

Continued on next page. . .

Table A.1 – continued from previous page

	SCSN				Fault Parameters		
Event id	origin date-time	lat/lon	h	mb	FM:$\phi/\delta/\lambda$	h	Mw
9674653	2001/07/17,14:59:50.	36.03/-117.88	2.6	3.7	267/82/-21	4.3	3.7
9688025	2001/07/30,23:34:17.	36.05/-117.88	2.8	3.7	21/37/-58	5.2	4.0
9688709	2001/08/01,03:05:15.	35.99/-117.88	3.5	3.6	72/77/-25	3.9	3.9
9734033	2001/12/11,21:40:35.	34.11/-116.72	9.3	3.6	218/57/-2	6.9	3.8
9817605	2002/08/31,16:24:33.	33.05/-115.61	14.2	3.8	311/67/-27	9.9	3.8
9827109	2002/09/23,08:13:16.	32.18/-115.38	7.0	3.6	30/71/-21	11.3	3.8
9875657	2003/01/02,16:11:37.	35.32/-118.66	3.6	3.6	150/31/-70	6.6	3.8
9875665	2003/01/02,16:15:44.	35.31/-118.66	3.6	3.6	213/55/-10	5.2	3.7
9915909	2003/05/15,17:58:02.	35.84/-118.11	10.7	3.6	241/48/-23	15.8	3.5
9994573	2004/03/28,07:20:02.	36.18/-118.16	7.7	3.8	173/66/-63	7.2	3.7
13935988	2003/02/22,12:19:10.	34.31/-116.85	1.2	5.4	41/79/-21	6.3	5.0
13936812	2003/02/22,19:33:45.	34.31/-116.85	3.0	4.5	90/46/90	5.3	4.3
13936432	2003/02/22,14:16:08.	34.32/-116.86	4.2	4.1	21/72/-28	5.5	3.8
13938812	2003/02/25,04:03:04.	34.32/-116.84	2.7	4.6	44/84/-11	4.8	4.2
13936596	2003/02/22,16:12:16.	34.31/-116.85	4.3	3.9	28/86/-18	5.9	3.7
13939856	2003/02/27,05:00:21.	34.30/-116.84	4.6	4.0	37/80/-21	6.2	3.8
14095628	2004/09/29,22:54:54.	35.39/-118.62	3.5	5.0	202/72/-2	8.6	4.9

Appendix B

More Waveform Comparisons along Tonga-Fiji, California Corridor

The waveform comparisons for more events studied in Chapter 4 are displayed here, where representative events of various source types, at different depths are selected. For each event, the subfigure (a) displays the overlain waveform comparison, (b) shows the source parameter, and the measured time lags of the S multiplets are given in (c). The last two figures are the waveform comparisons for event 9533473 as shown in Fig. 4.6 with the preliminary earth reference model (PREM), and the path average of the tomographic model $S20RTS$ containing a thick crust ($\sim$ 21 km).

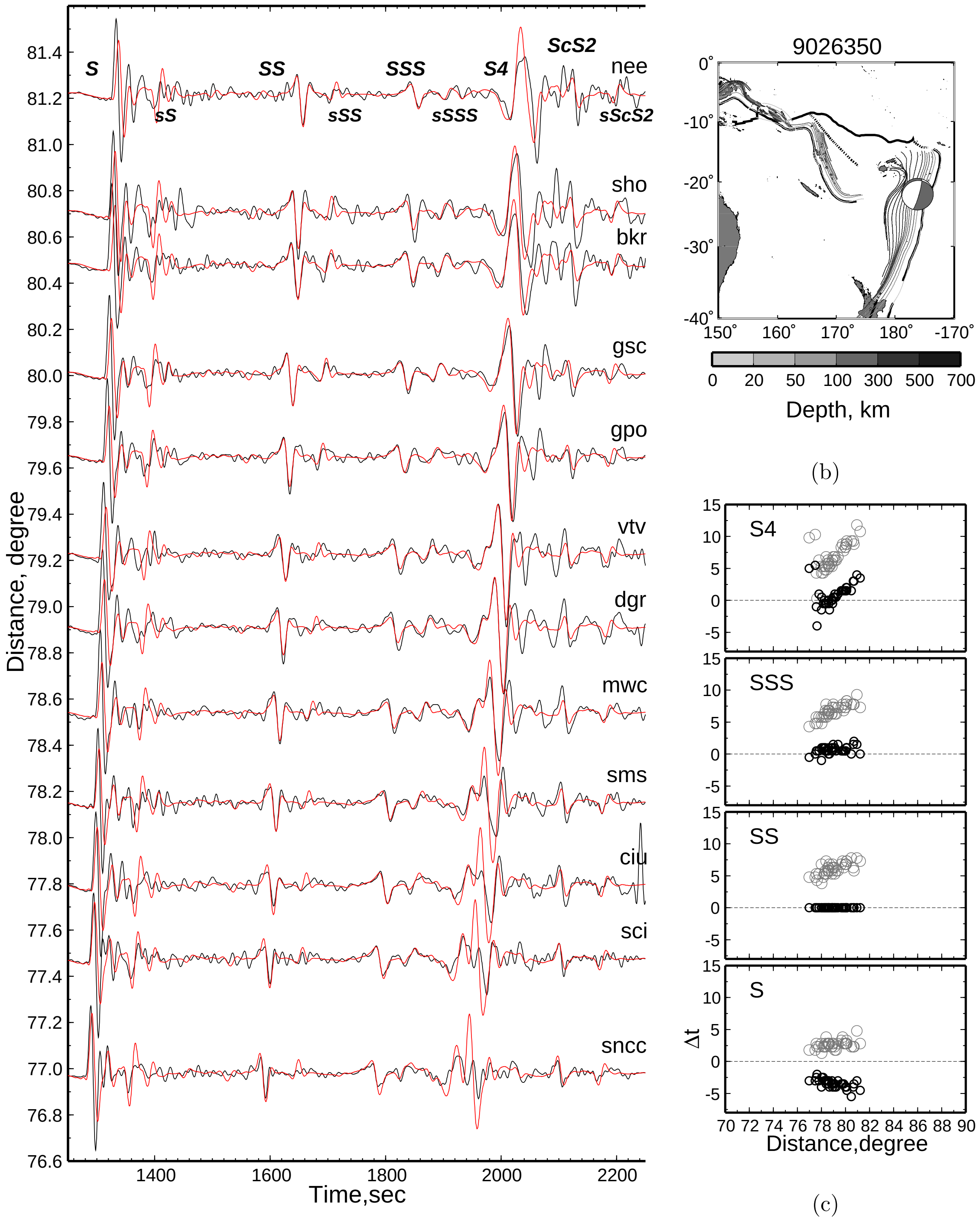

(a)

(b)

(c)

Figure B.1: Event 9026350.

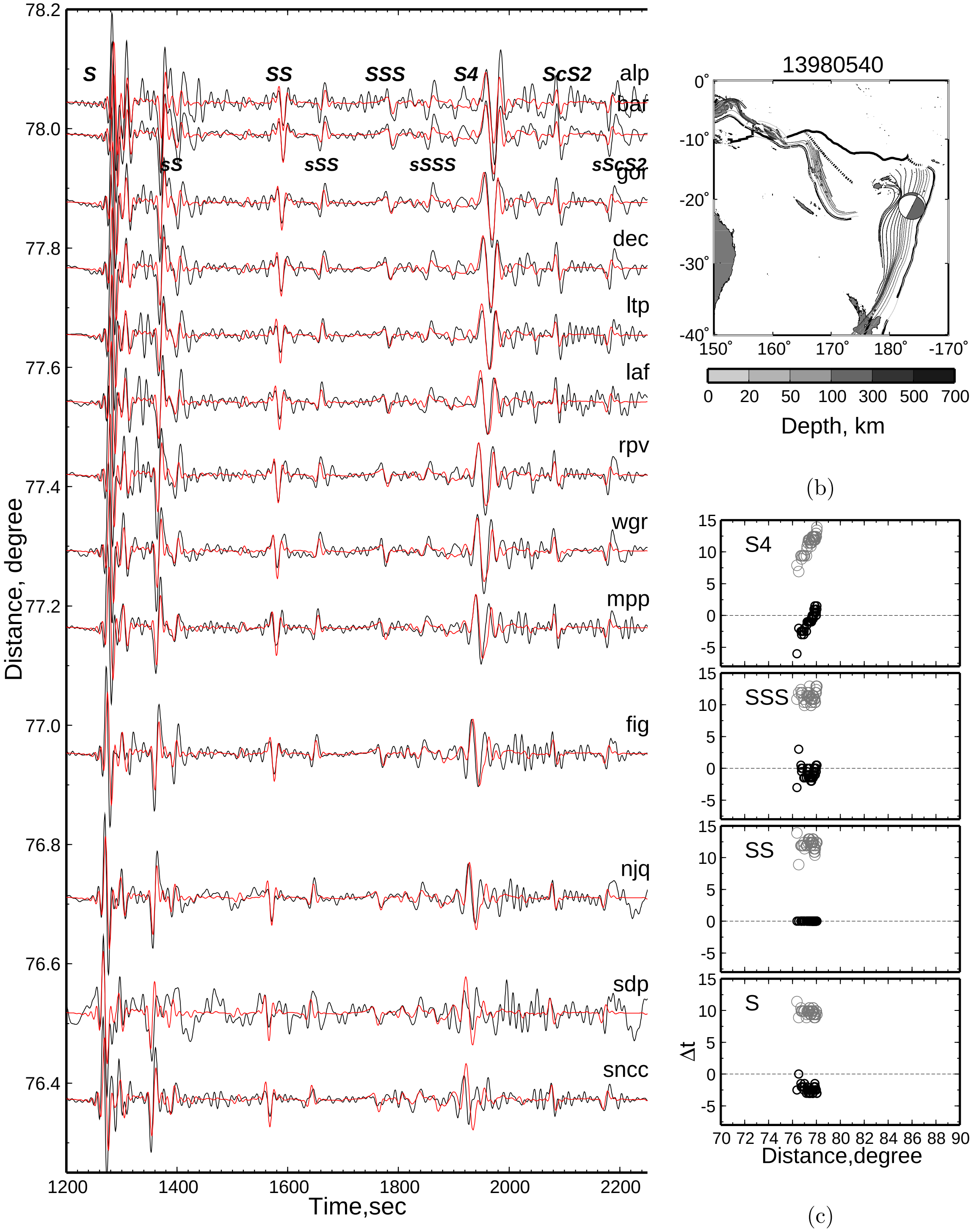

(a)

(b)

(c)

Figure B.2: Event 13980540.

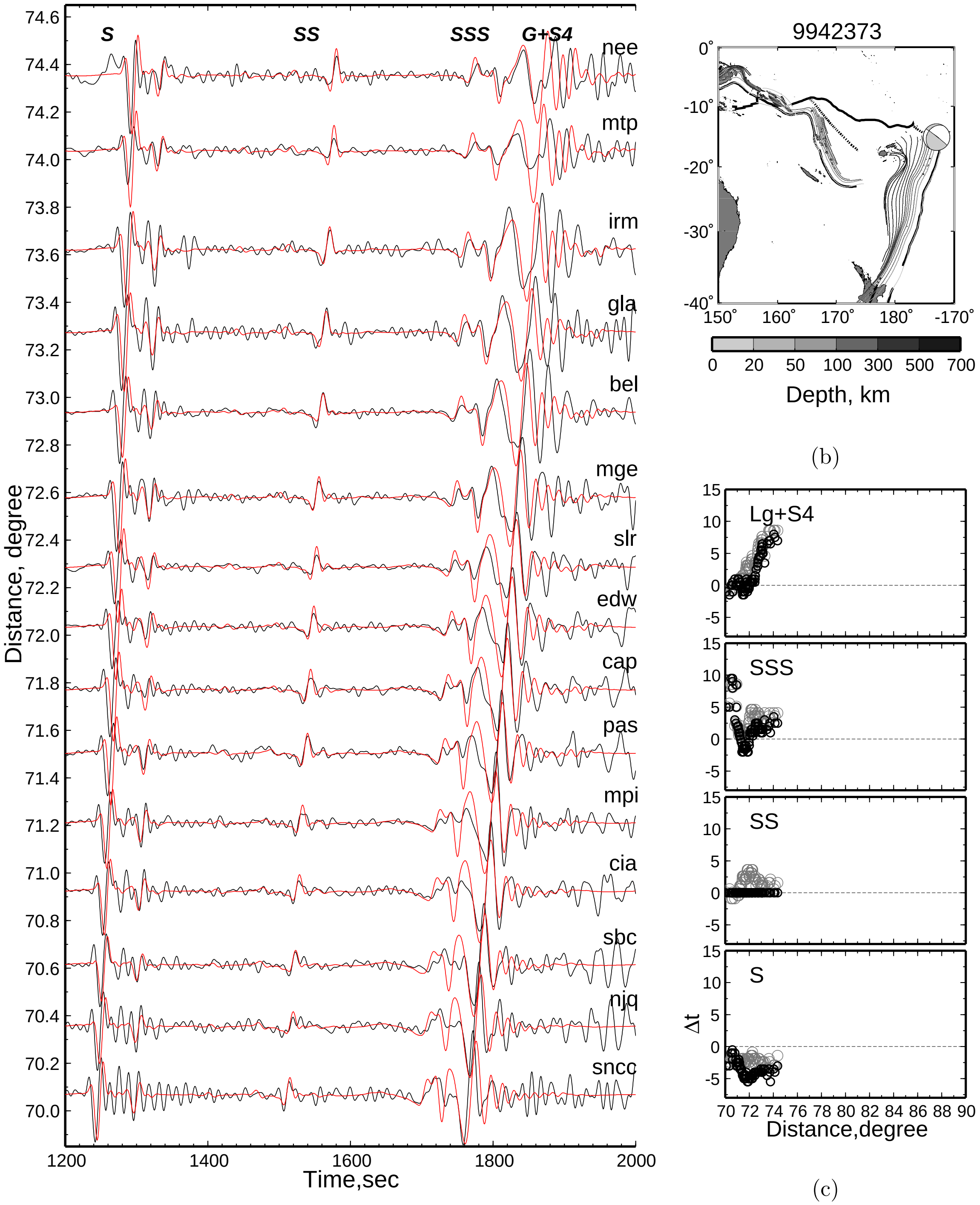

(b)

(c)

(a)

Figure B.3: Event 9942373.

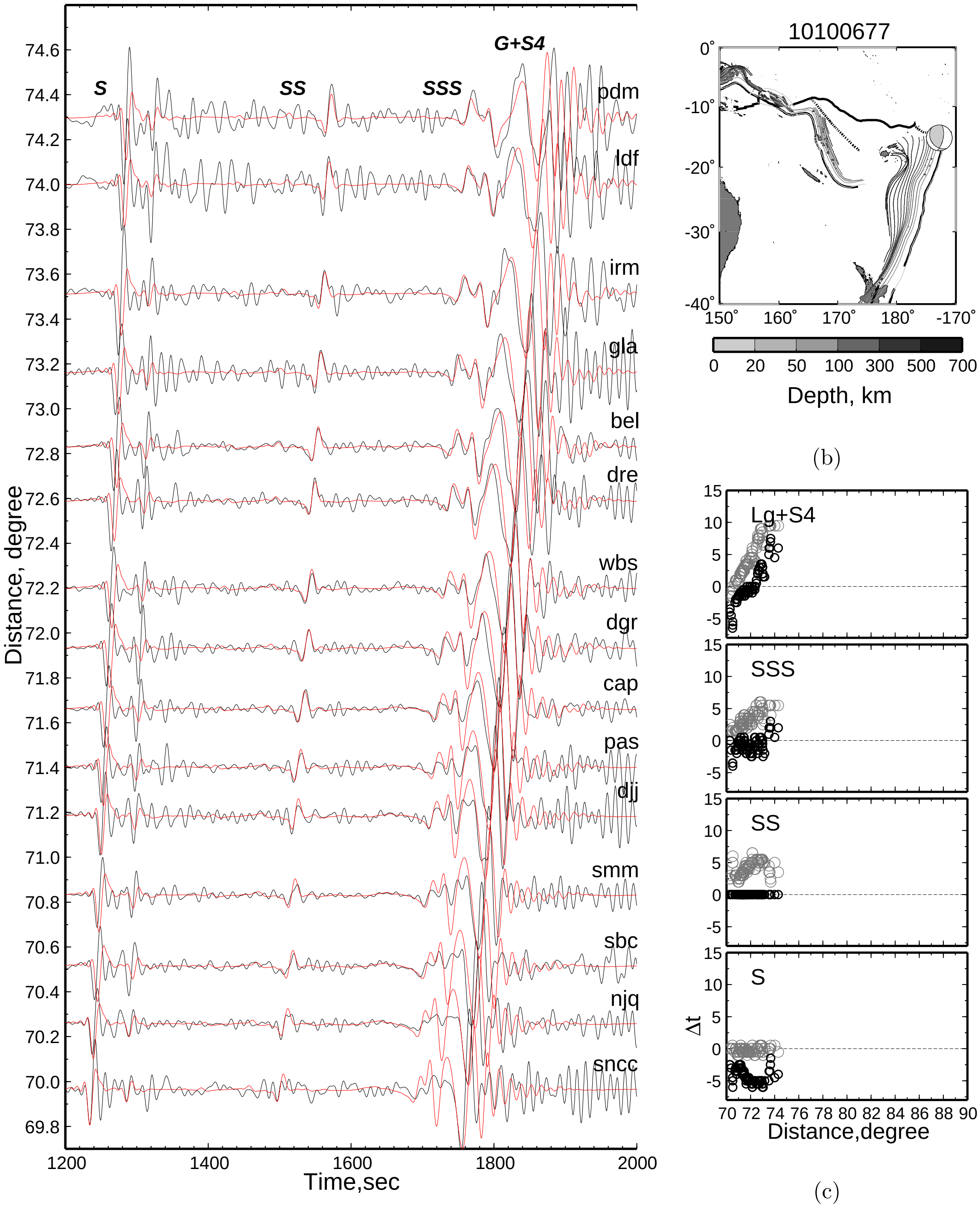

(a)

(b)

(c)

Figure B.4: Event 10100677.

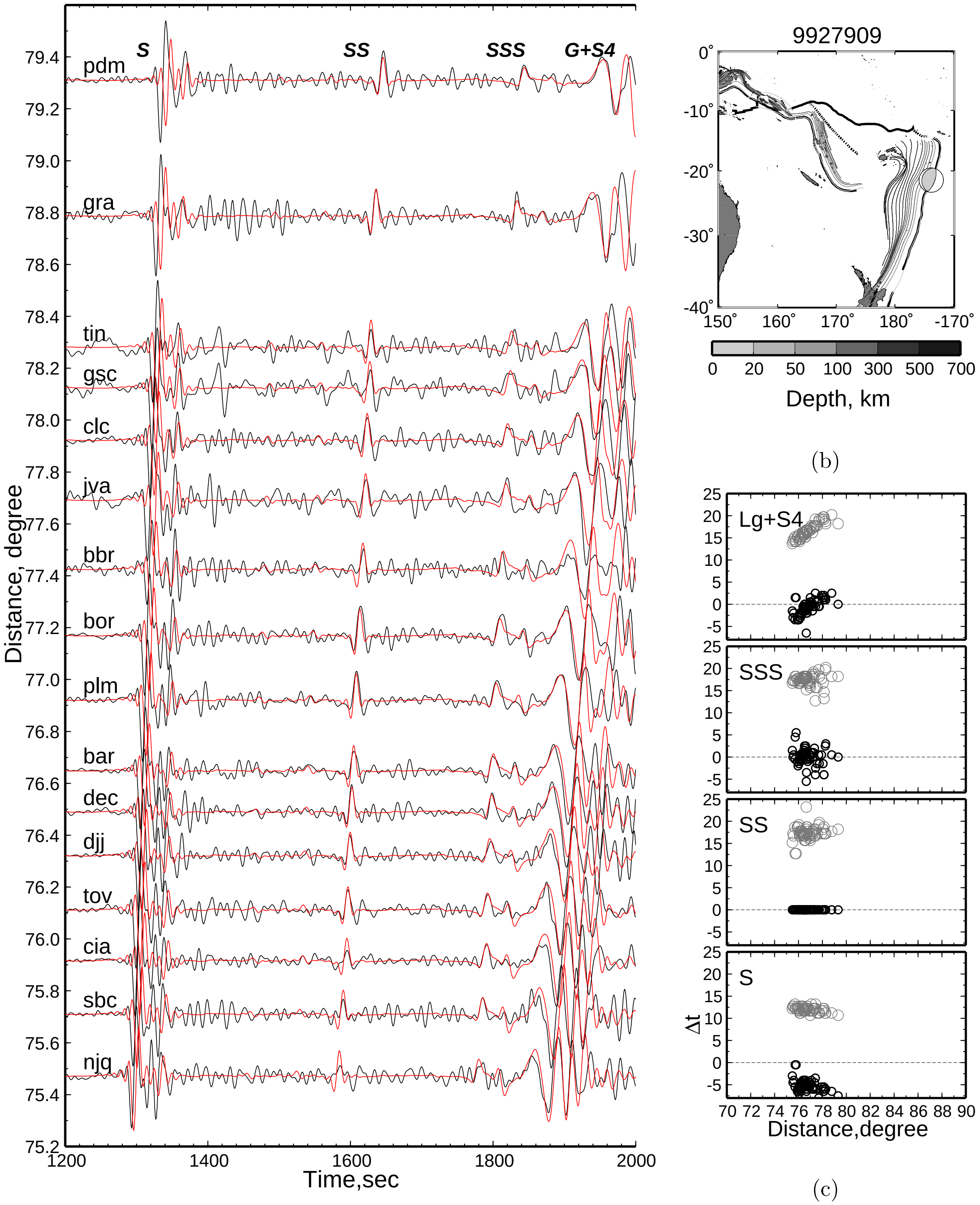

(a)

(b)

(c)

Figure B.5: Event 9927909.

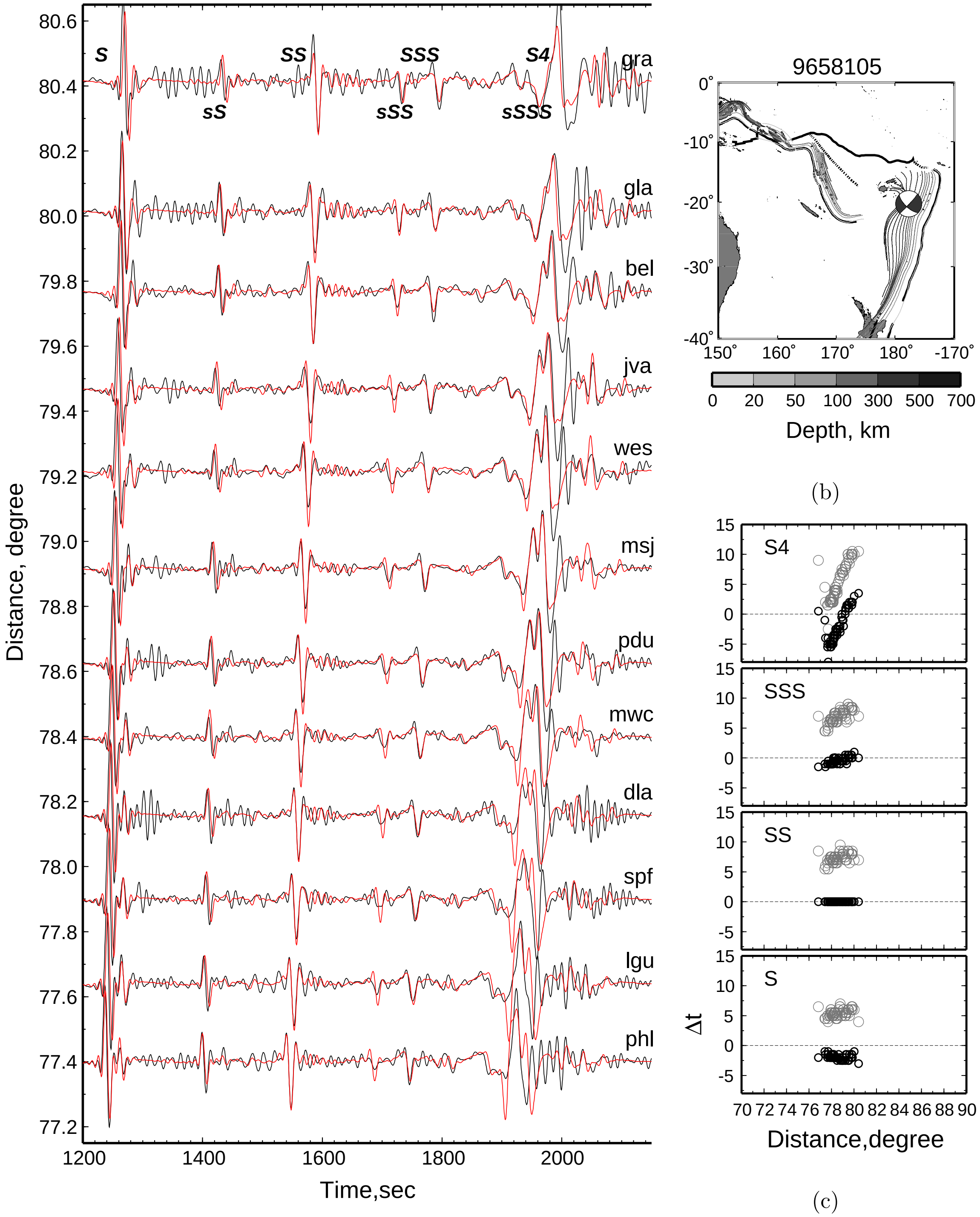

(a)

(b)

(c)

Figure B.6: Event 9658105.

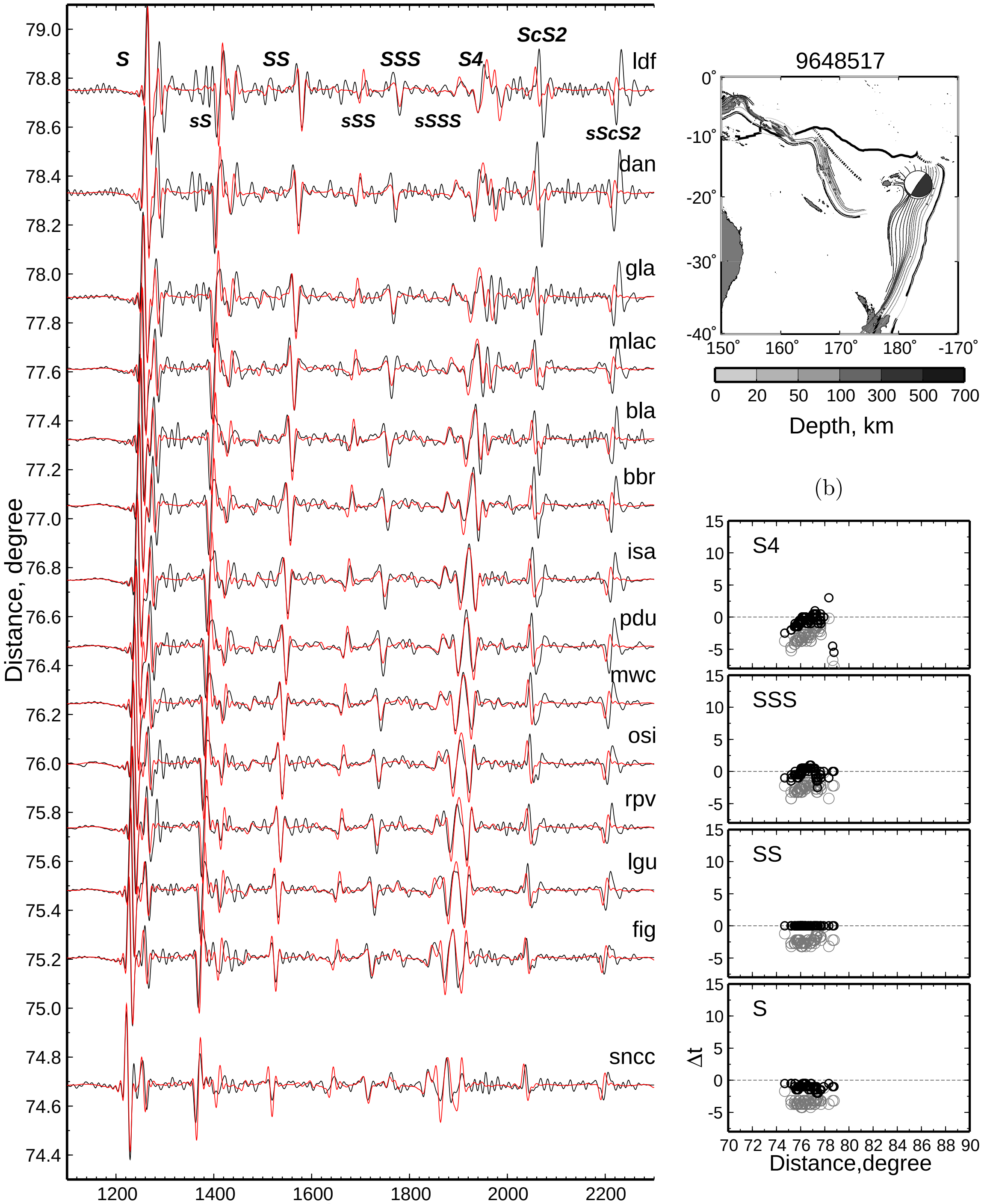

(a)

(b)

(c)

Figure B.7: Event 9648517.

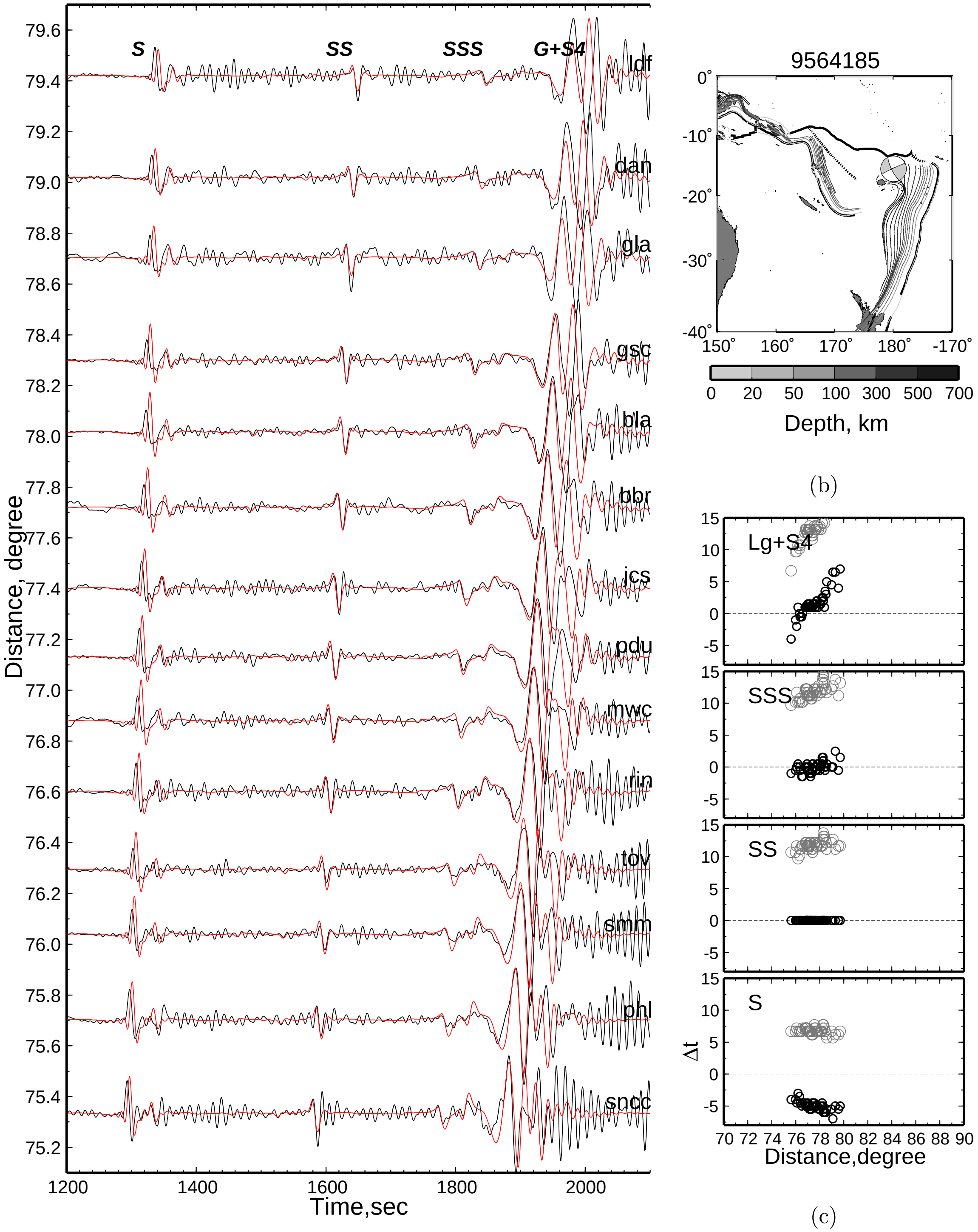

(a)

(b)

(c)

Figure B.8: Event 9564185.

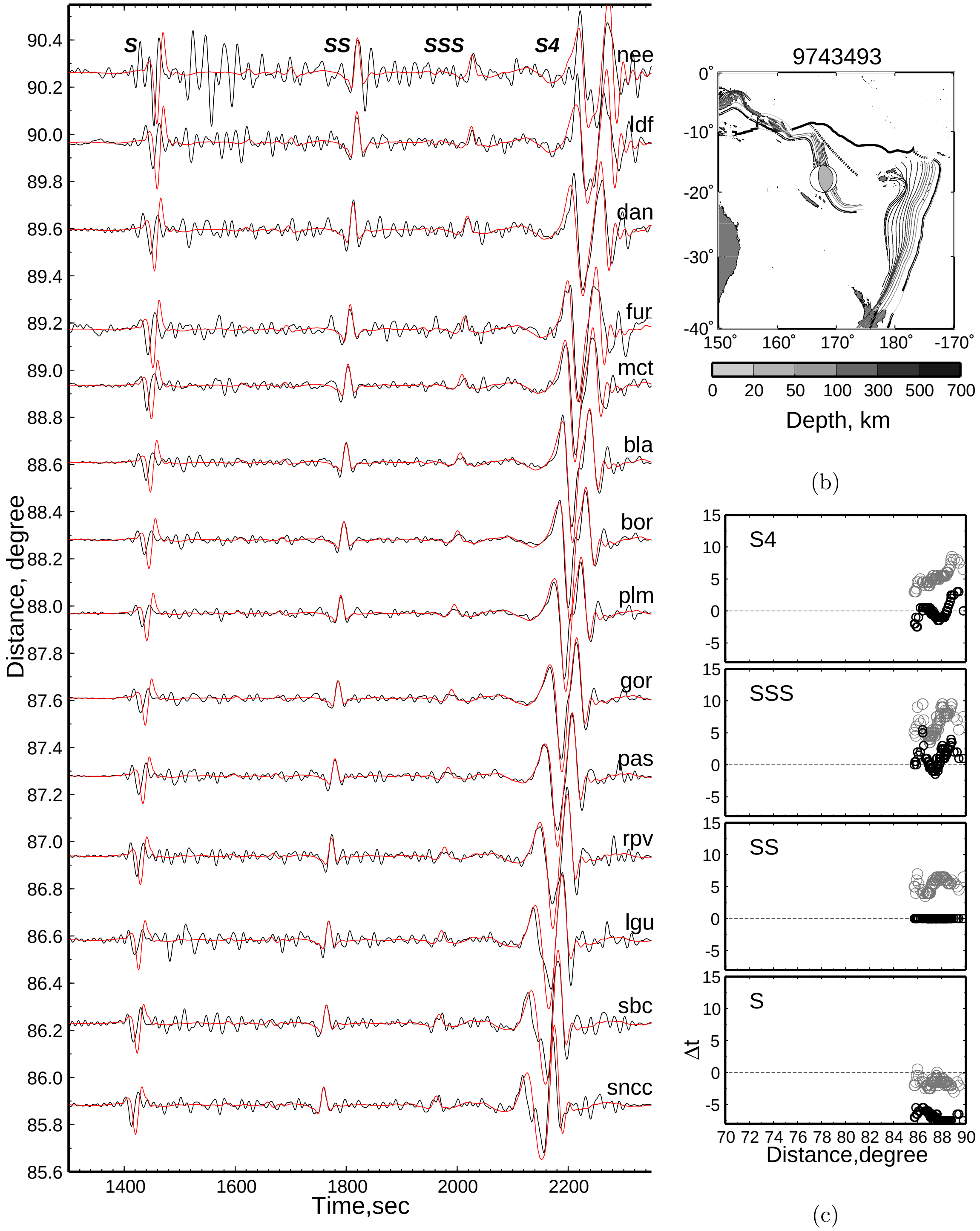

(a)

(b)

(c)

Figure B.9: Event 9743493.

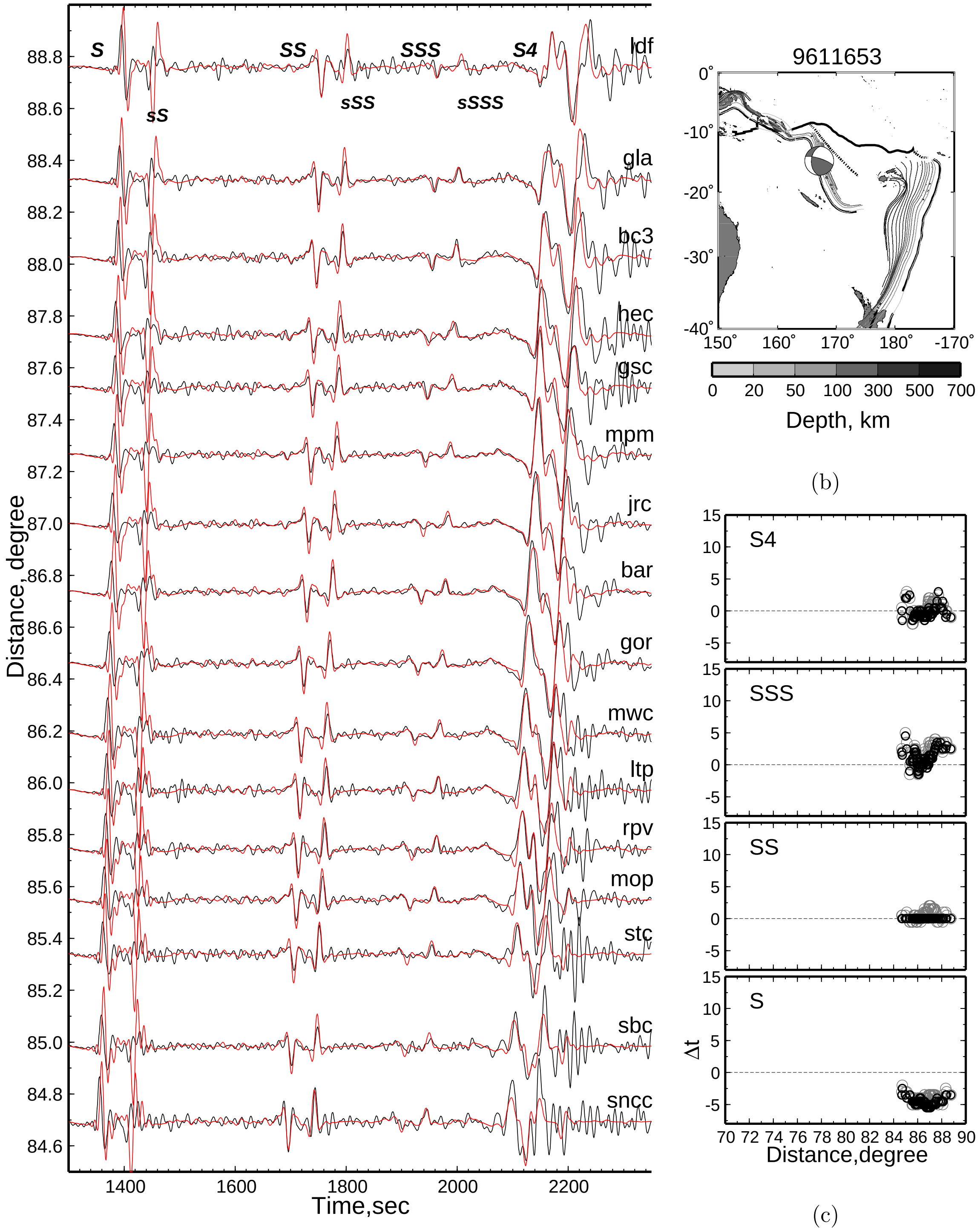

(a)

(b)

(c)

Figure B.10: Event 9611653.

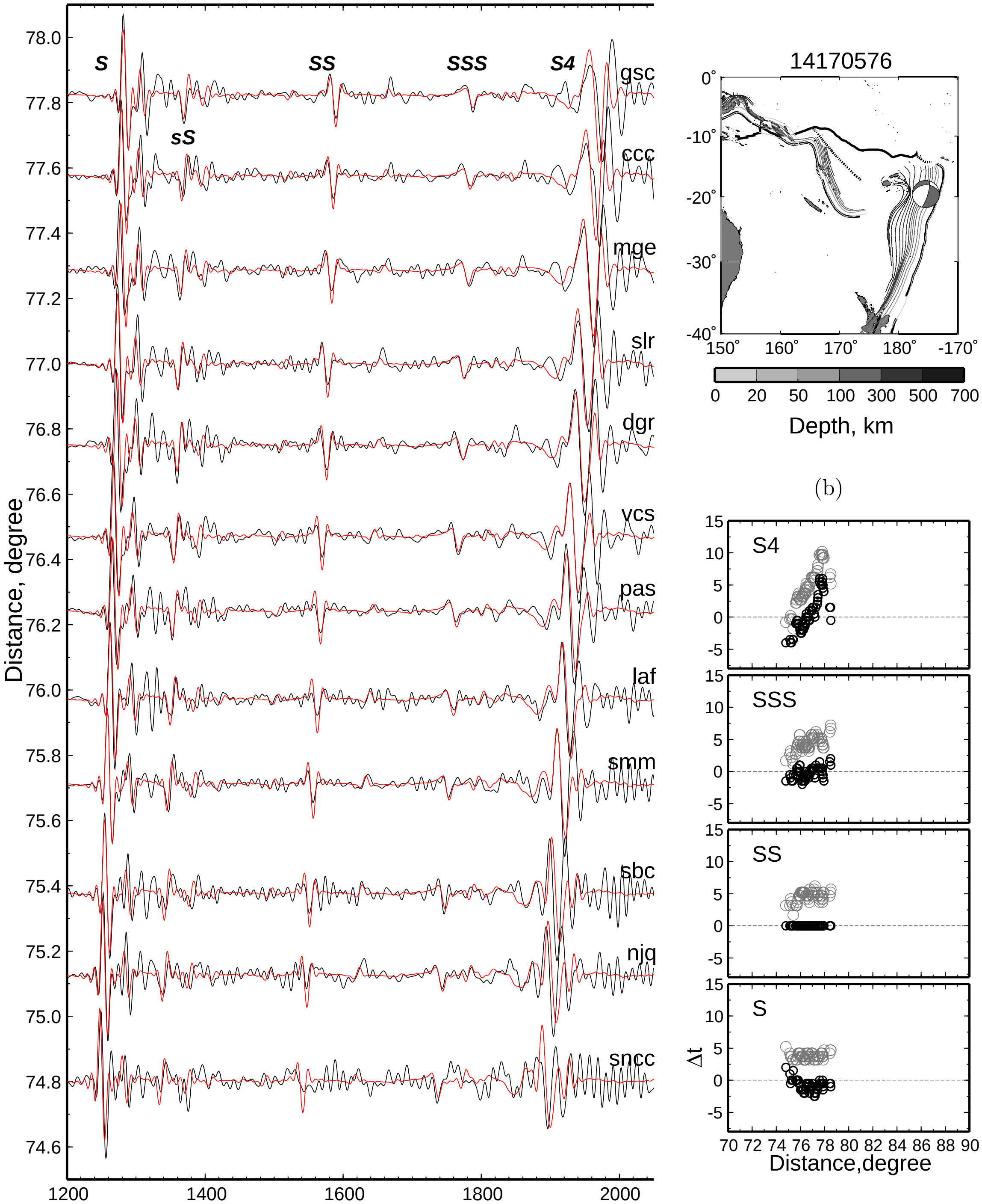

(a)

(b)

(c)

Figure B.11: Event 14170576.

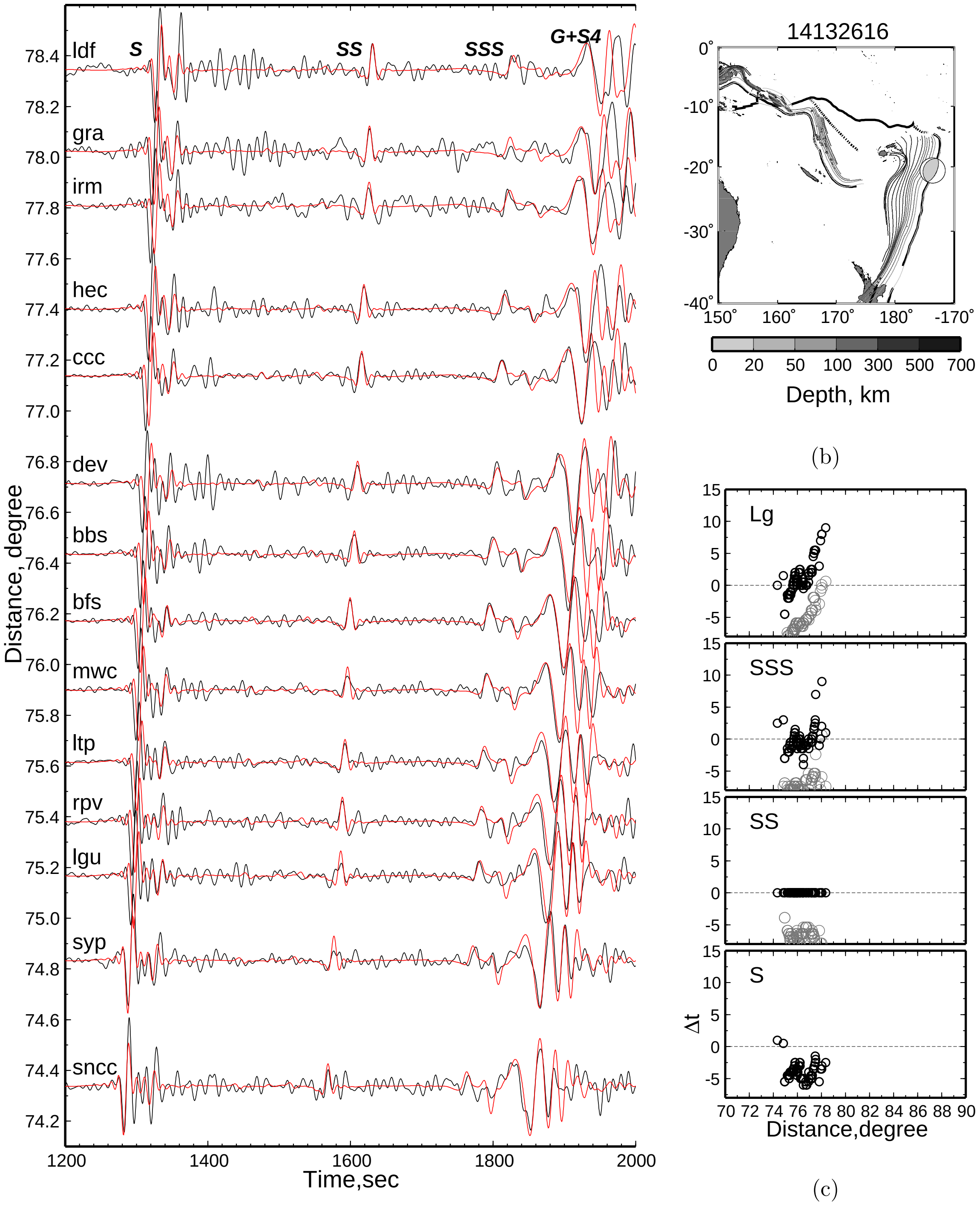

(a)

(b)

(c)

Figure B.12: Event 14132616.

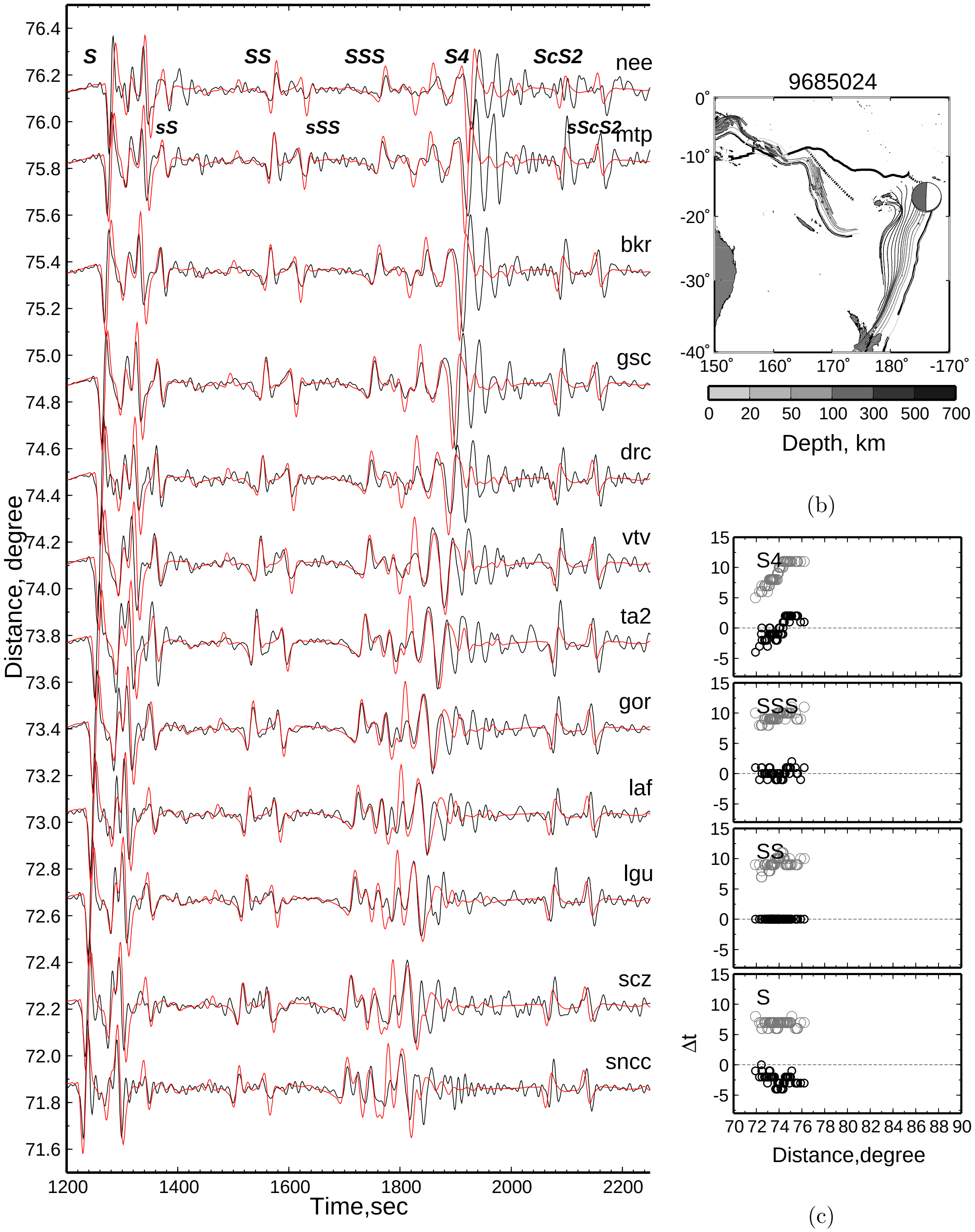

(a)

(b)

(c)

Figure B.13: Event 9685024.

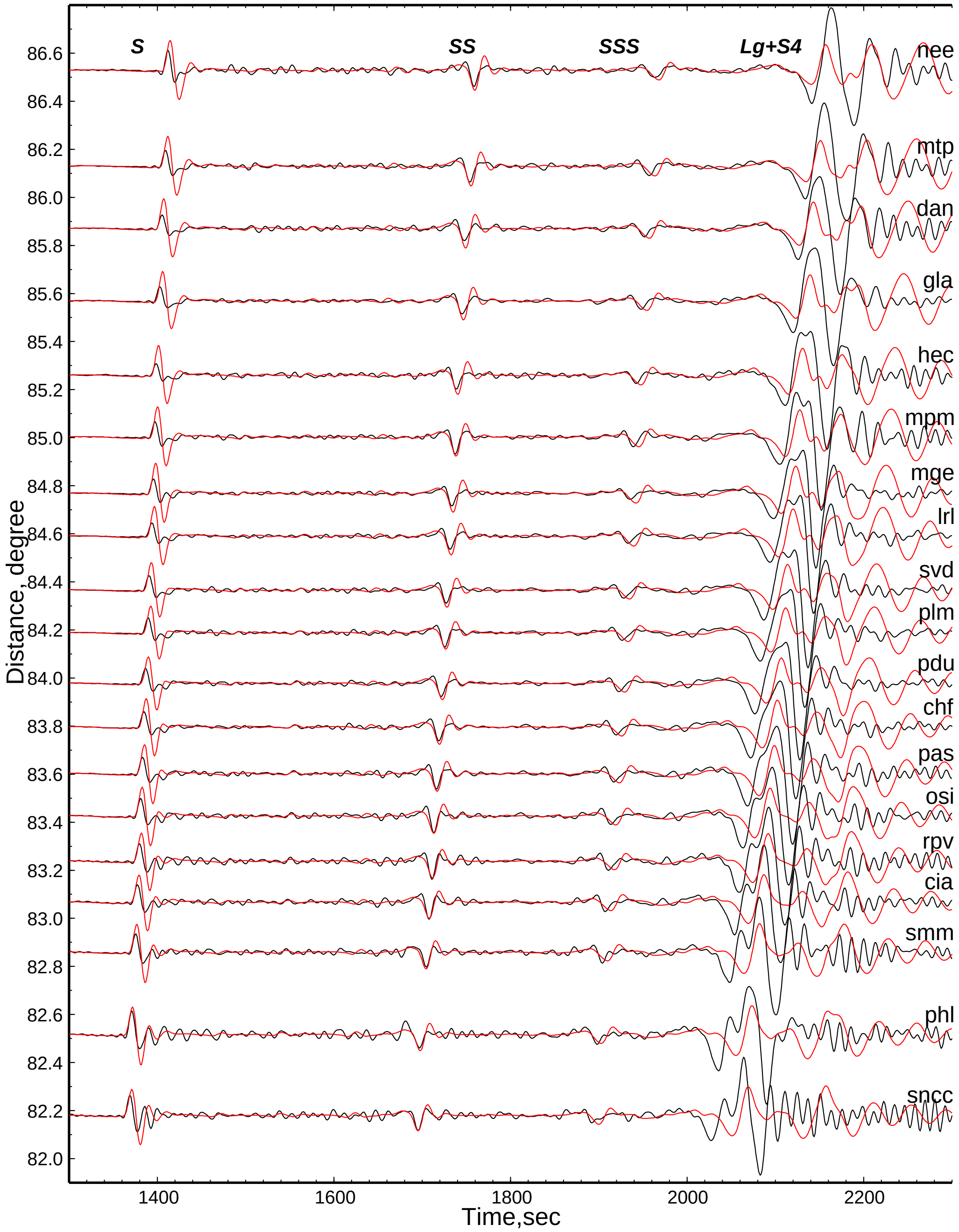

Figure B.14: The selected waveform fits for event 9533473 as shown in Fig. 4.6 with the preliminary Earth reference model ($PREM_{sh}$) containing a thick crust (∼21 km). Both the data (black) and synthetics (red) are aligned on SS.

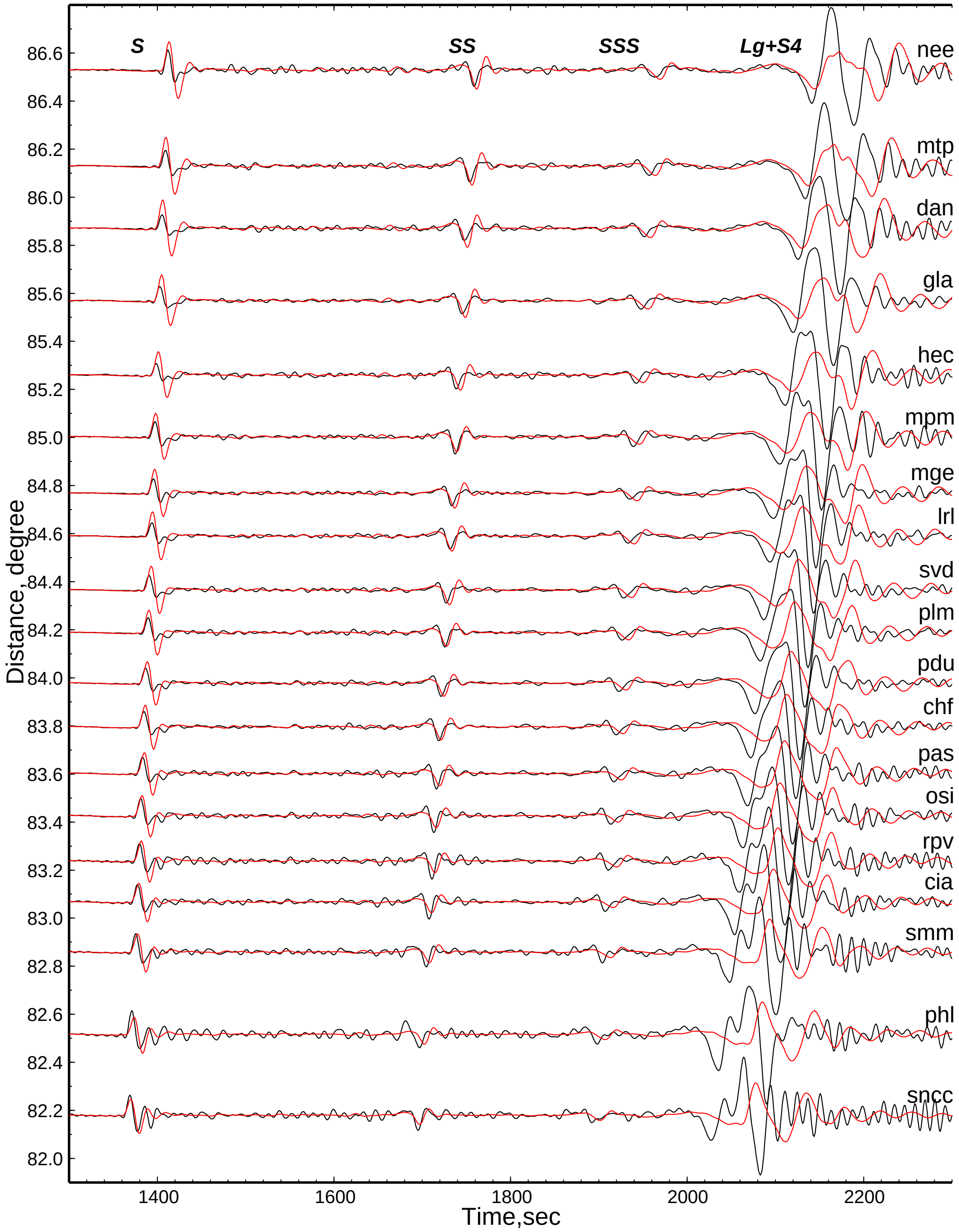

Figure B.15: The selected waveform fits for event 9533473 as shown in Fig. 4.6 with the path average of a typical tomographic model S20RTS by *Ritsema et al.* (1999) containing a thick crust from PREM (~21 km). Both the data (black) and synthetics (red) are aligned on SS.

Bibliography

Abercrombie, R. E. (1995), Earthquake source scaling relationships from -1 to 5 m_l using seismgrams recorded at 2.5-km depth, *J. Geophys. Res.*, *100*(B12), 24,015–24,036.

Abers, G. A., and J. W. Gephart (2001), Direct inversion of earthquake first motions for both the stress tensor and focal mechanisms and application to southern California, *J. Geophys. Res.*, *106*(B11), 26,523–26,540.

Bakun, W. H. (1984), Seismic moments, local magnitudes, and coda-duration magnitudes for earthquakes in central California, *Bull. Seismol. Soc. Am.*, *74*(2), 439–458.

Ben-Zion, Y., and J. R. Rice (1993), Earthquake failure sequences along a cellular fault zone in a three-dimensional elastic solid containing asperity and nonasperity regions, *J. Geophys. Res.*, *98*, 14,109–14,131.

Ben-Zion, Y., and L. Zhu (2002), Potency-magnitude scaling relations for southern California earthquakes with $1.0 < m_l < 7.0$, *Geophys. J. Int.*, *148*, F1–F5.

Bevington, P. R., and D. K. Robinson (2003), *Data reduction and error analysis*, McGraw-Hill.

Bondár, I., and R. G. North (1999), Development of calibration techniques for the comprehensive nuclear-test-ban treaty (CTBT) international monitoring system, *Physics of the Earth and Planetary Interiors*, *113*, 11–24.

Bondár, I., R. G. North, and G. Beall (1999), Teleseismic slowness-azimuth station corrections for the international monitoring system seismic network, *Bull. Seismol. Soc. Am.*, *89*(4), 989–1003.

Boore, D. M. (1983), Stochastic simulation of high-frequency ground motions based on seismological models of the radiated spectra, *Bull. Seismol. Soc. Am.*, *73*(6), 1865–1894.

Chi, W.-C., and E. Hauksson (2006), Fault-perpendicular seismicity after 2003 Mw=4.9 Big Bear , California earthquake: Implications for static stress triggering, *Geophys. Res. Lett.*, *submitted.*

Clinton, J. F., E. Hauksson, and K. Solanki (2006), Automatically generated moment tensor solutions for southern California: Robustness of the m_w magnitude scale and style of faulting, *Bull. Seismol. Soc. Am.*, *submitted.*

Ding, X. Y., and S. P. Grand (1993), Upper mantle q structure beneath the east pacific rise, *J. Geophys. Res.*, *98*(B2), 1973–1985.

Dreger, D., and D. V. Helmberger (1993), Determination of source parameters at regional distances with three-component sparse network data, *J. Geophys. Res.*, *98*(B5), 8107–8125.

Dziewonski, A. M., and D. L. Anderson (1981), Preliminary reference earth model, *Physics of the Earth and Planetary Interiors*, *25*, 297–356.

Dziewonski, A. M., T. A. Chou, and J. H. Woodhouse (1981), Determination of earthquake source parameters form waveform data for studies of global and regional seismicity, *J. Geophys. Res.*, *86*, 2825–2952.

Ebel, J. E., and K.-P. Bonjer (1990), Moment tensor inversion of small earthquakes in southwestern Germany for the fault plane solution, *Geophys. J. Int.*, *101*, 133–146.

Ekström, G., and A. M. Dziewonski (1998), The unique anisotropy of the Pacific upper mantle, *Nature*, *394*, 168–172.

Fan, G., and T. Wallace (1991), The determination of source parameters for small earthquakes from a single, very broadband seismic station, *Geophys. Res. Lett.*, *18*(8), 1385–1388.

Frankel, A., and H. Kanamori (1983), Determination of rupture duration and stress drop for earthquakes in southern California, *Bull. Seismol. Soc. Am.*, *73*(6), 1527–1551.

Frohlich, C. (1992), Triangle diagrams: ternary graphs to display similarity and diversity of earthquake focal mechanisms, *Physics of the Earth and Planetary Interiors*, *75*, 193–198.

Gaherty, J. B., and T. H. Jordan (1996), Seismic structure of the upper mantle in a central pacific corridor, *J. Geophys. Res.*, *101*(B10), 22,291–22,309.

Gaherty, J. B., M. Kato, and T. H. Jordan (1999), Seismological structure of the upper mantle: a regional comparison of seismic layering, *Physics of the Earth and Planetary Interiors*, *110*, 21–41.

Gephart, J. W., and D. W. Forsyth (1984), An improved method for determining the regional stress tensor using earthquake focal mechanism data: application to the San Fernando earthquake sequence, *J. Geophys. Res.*, *89*(B11), 9305–9320.

Grand, S. P., and D. V. Helmberger (1984a), Upper mantle shear structure beneath the north atlantic ocean, *J. Geophys. Res.*, *89*(B13), 11,465–11,475.

Grand, S. P., and D. V. Helmberger (1984b), Upper mantle shear structure of north america, *Geophys. J. R. astr. Soc.*, *76*, 399–438.

Graves, R. W., and D. V. Helmberger (1988), Upper mantle cross section from Tonga to Newfoundland, *J. Geophys. Res.*, *93*, 4701–4711.

Hanks, T. C., and D. M. Boore (1984), Moment-magnitude relations in theory and practice, *J. Geophys. Res.*, *89*(B7), 6229–6235.

Hanks, T. C., and H. Kanamori (1979), A moment magnitude scale, *J. Geophys. Res.*, *84*, 2348–2350.

Hardebeck, J. L., and E. Hauksson (2001a), Crustal stress field in southern California and its implications for fault mechanics, *J. Geophys. Res.*, *106*(B10), 21,859–21,882.

Hardebeck, J. L., and E. Hauksson (2001b), Stress orientations obtained from earthquake focal mechanisms: What are appropriate uncertainty estimates, *Bull. Seismol. Soc. Am.*, *91*, 250–262.

Hardebeck, J. L., and P. M. Shearer (2002), A new method for determining first-motion focal mechanisms, *Bull. Seismol. Soc. Am.*, *92*(6), 2264–2276.

Hardebeck, J. L., and P. M. Shearer (2003), Using S/P amplitude ratios to constrain the focal mechanisms of small earthquakes, *Bull. Seismol. Soc. Am.*, *93*(6), 2434–2444.

Hartzell, S. H. (1978), Earthquake aftershocks as Green's functions, *Geophys. Res. Lett.*, *5*(1), 1–4.

Haskell, N. A. (1964), Total energy and energy spectra density of elastic waves from propagating faults, *Bull. Seismol. Soc. Am.*, *54*, 1811–1841.

Hauksson, E. (1994), State of stress from focal mechanisms before and after the 1992 Landers earthquake sequence, *Bull. Seismol. Soc. Am.*, *84*(3), 917–934.

Hauksson, E. (2000), Crustal structure and seismicity distribution adjacent to the Pacific and North America plate boundary in southern California, *J. Geophys. Res.*, *105*, 13,875–13,903.

Hauksson, E. (2001), Southern California seismic network: Caltech/USGS element of TriNet 1997-2001, *Seismol. res. Lett.*, *72*(6).

Hauksson, E., L. M. Jones, K. Hutton, and D. Eberhart-Phillips (1993), The 1992 Landers earthquake sequence: Seismological observations, *J. Geophys. Res.*, *98*(B11), 19,835–19,858.

Helmberger, D. V. (1983), Theory and application of synthetic seismograms, in *Earthquakes: Observation, Theory and Interpretation*, pp. 174–222, Soc. Italiana di Fisica, Bolgna, Italy.

Helmberger, D. V., and G. R. Engen (1974), Upper mantle shear structure, *J. Geophys. Res.*, *79*(26), 4017–4028.

Hough, S. E., and D. S. Dreger (1995), Source parameters of the 23 April 1992 m 6.1 Joshua Tree, California, earthquake and its aftershocks: empirical Green's function analysis of GEOS and TERRAscope data, *Bull. Seismol. Soc. Am.*, *85*, 1576–1590.

Jones, L. E., and D. V. Helmberger (1998), Earthquake source parameters and fault kinematics in the eastern California shear zone, *Bull. Seismol. Soc. Am.*, *88*(6), 1337–1352.

Kanamori, H., and D. L. Anderson (1975), Theoretical basis of some empirical relations in seismology, *Bull. Seismol. Soc. Am.*, *65*, 1073–1095.

Kennett, B. L. N., and F. Ringdal (2001), Locating seismic events in the CTBT context, *Pure Appl. Geophys.*, *158*, 7–18.

Kilb, D., and A. M. Rubin (2002), Implications of diverse fault orientations imaged in relocated aftershocks of the Mount Lewis, M_L 5.7, California,earthquake, *J. Geophys. Res.*, *107*(B11).

Kisslinger, C. (1980), Evaluation of s to p amplitude ratios for determining focal mechanisms from regional network observations, *Bull. Seismol. Soc. Am.*, *70*(4), 999–1014.

Kisslinger, C., J. R. Bowman, and K. Koch (1981), Procedures for computing focal mechanisms from local $(SV/P)_z$ data, *Bull. Seismol. Soc. Am.*, *71*(6), 1719–1729.

Kremenetskaya, E., V. Asming, and F. Ringdal (2001), Seismic location calibration of the European Arctic, *Pure Appl. Geophys.*, *158*, 117–128.

Langin, W. R., L. D. Brown, and E. A. Sandvol (2003), Seismicity of central Tibet from project INDEPTH III seismic recordings, *Bull. Seismol. Soc. Am.*, *93*, 2146–2159.

Langston, C. A. (1981), Source inversion of seismic waveforms: the Koyna, India, earthquakes of 13 September 1967, *Bull. Seismol. Soc. Am.*, *71*, 1–24.

Lanza, V., D. Spallarossa, M. Cattaneo, D. Bindi, and P. Augliera (1999), Source parameters of small events using constrained deconvolution with empirical Green's functions, *Geophys. J. Int.*, *137*, 651–662.

Lay, T., and T. C. Wallace (1995), *Modern global seismology*, ACADEMIC PRESS.

Leitner, B., D. Eberhart-Phillips, H. Anderson, and J. L. Nábělek (2001), A focused look at the Alpine fault, New Zealand: Seismicity, focal mechanisms, and stress observations, *J. Geophys. Res.*, *106*(B2), 2193–2220.

Li, H., and L. Zhu (2006), High-resolution structures of the Landers fault zone inferred from aftershock waveform data, *Geophys. J. Int.*, *Submitted*.

Liu, Q., J. Polet, D. Komatitsch, and J. Tromp (2004), Spectral-element moment tensor inversions for earthquakes in southern California, *Bull. Seismol. Soc. Am.*, *94*(5), 1748–1761.

McGuire, J. J. (2004), Estimating finite source properties of small earthquake ruptures, *Bull. Seismol. Soc. Am.*, *94*(2), 377–393.

McKenzie, D. P. (1969), The relationship between fault plane solutions for earthquakes and the directions of the principal stresses, *Bull. Seismol. Soc. Am.*, *59*, 591–601.

Melbourne, T., and D. V. Helmberger (1998), Fine structure of the 410km discontinuity, *J. Geophys. Res.*, *103*(B5), 10,091–10,102.

Melbourne, T., and D. V. Helmberger (2001), Mantle control of plate boundary deformation, *Geophys. Res. Lett.*, *28*(20), 4003–4006.

Melbourne, T. I., and D. V. Helmberger (2002), Whole mantle shear structure beneath the East Pacific Rise, *J. Geophys. Res.*, *107*(B9), 2204–.

Michael, A. J. (1984), Determination of stress from slip data: faults and folds, *J. Geophys. Res.*, *89*, 11,517–11,526.

Michael, A. J. (1987), The use of focal mechanisms to determine stress: A control study, *J. Geophys. Res.*, *92*, 357–368.

Michael, A. J. (1991), Spatial variations in stress within the 1987 Whittier Narrows, California, aftershock sequence: new techniques and results, *J. Geophys. Res.*, *96*(B4), 6303–6319.

Montagner, J.-P., and T. Tanimoto (1991), Global upper-mantle mantle tomography of seismic velocitites and anisotropy, *J. Geophys. Res.*, *96*, 20,337–20,351.

Nakamura, A., S. Horiuchi, and A. Hasegawa (1999), Joint focal mechanism determination with source–region station corrections using short-period body-wave amplitude data, *Bull. Seismol. Soc. Am.*, *89*(2), 373–383.

Nicolas, A., and N. I. Christensen (1987), Formation of anisotropy in upper mantle peridotites: A review, in Composition, Structure, and Dynamics of Lithosphere-Asthenosphere System, in *Geodyn. Ser.*, vol. 16, pp. 111–123, American Geophysical Union.

Nishimura, C. E., and D. W. Forsyth (1989), The anisotropic structure of the upper mantle in the Pacific, *Geophys. J.*, *96*, 203–229.

Okada, Y., K. Kasahara, S. Hori, K. Obara, S. Sekiguchi, H. Fujiwara, and A. Yamamoto (2004), Recent progress of seismic observation networks in Japan – Hi-net, F-net, K-net and KiK-net, *Earth Planets Space*, *56*(8), xv–xxviii.

Owens, T. J., G. E. Randall, F. T. Wu, and R. S. Zeng (1993), PASSCAL instrument performance during the Tibetan plateau passive seismic experiment, *Bull. Seismol. Soc. Am.*, *83*, 1959–1970.

Prejean, S., W. L. Ellsworth, M. Zoback, and F. Waldhauser (2002), Fault structure and kinematics of the Long Valley Caldera region, California, revealed by high-accuracy earthquake hypocenters and focal mechanism stress inversions, *J. Geophys. Res.*, *107*(B12).

Prieto, G. A., P. M. Shearer, F. L. Vernon, and D. Kilb (2004), Earthquake source scaling and self-similarity estimation from stacking p and s spectra, *J. Geophys. Res.*, *109*.

Rau, R.-J., F. T. Wu, and T.-C. Shin (1996), Regional network focal mechanism determination using 3D velocity model and sh/p amplitude ratio, *Bull. Seismol. Soc. Am.*, *86*(5), 1270–1283.

Reasenberg, P., and D. Oppenheimer (1985), FPFIT, FPPLOT, and FPPAGE: FORTRAN computer programs for calculating and displaying earthquake fault-plane solutions, in *U.S. Geol. Surv. Open-File Rept.*, pp. 85–739.

Revenaugh, J., and T. H. Jordan (1991a), Mantle layering from scs reverberations 2. the transition zone, *J. Geophys. Res.*, *96*(B12), 19,763–19,780.

Revenaugh, J., and T. H. Jordan (1991b), Mantle layering from scs reverberations 3. the upper mantle, *J. Geophys. Res.*, *96*(B12), 19,781–19,810.

Richter, C. F. (1935), An instrumental earthquake magnitude scale, *Bull. Seismol. Soc. Am.*, *25*, 1–32.

Rigden, S. M., G. D. Gwanmesia, J. D. Fitzgerald, I. Jackson, and R. C. Lieberman (1991), Spinel elasticity and the seismic structure of the transition zone of the mantle, *Nature*, *345*, 143–145.

Ritsema, J., and T. Lay (1993), Rapid source mechanism determination of large (Mw $\geq$ 5) earthquakes in the western United States, *Geophys. Res. Lett.*, *20*(15), 1611–1614.

Ritsema, J., H. J. van Heijst, and J. H. Woodhouse (1999), Complex shear velocity structure imaged beneath Africa and Iceland, *Science*, *286*, 1925–1928.

Rivera, L., and A. Cisternas (1990), Stess tensor and fault plane solutions for a population of earthquakes, *Bull. Seismol. Soc. Am.*, *80*, 600–614.

Romanowicz, B. (2003), Global mantle tomography: Progress status in the past 10 years, *Annual Review of Earth and Planetary Sciences*, *31*, 303–328.

Romanowicz, B., D. S. Dreger, M. Pasyanos, and R. Uhrhammer (1993), Monitoring of strain release in central and northern California, *Geophys. Res. Lett.*, *20*(15), 1643–1646.

Ryaboy, V., D. R. Baumagardt, P. Firbas, and A. M. Dainty (2001), Application of 3-D crustal and upper mantle velocity model of North America for location of regional seismic events, *Pure Appl. Geophys.*, *158*, 79–103.

Savage, B., and D. V. Helmberger (2004), Site response from incident *pnl* waves, *Bull. Seismol. Soc. Am.*, *94*(1), 357–362.

Schaff, D. P., G. H. R. Bokelmann, G. C. Beroza, F. Waldhauser, and W. L. Ellsworth (2002), High-resolution image of Calaveras Fault seismicity, *J. Geophys. Res.*, *107*(B9).

Schaff, D. P., G. H. R. Bokelmann, W. L. Ellsworth, E. Zanzerkia, F. Waldhauser, and G. C. Beroza (2004), Optimizing correlation techniques for improved earthquake location, *Bull. Seismol. Soc. Am.*, *94*(2), 705–721.

Schlue, J. W., and L. Knopoff (1977), Shear-wave polarization anisotropy in the Pacific basin, *Geophys. J. R. astr. Soc.*, *49*, 145–165.

Shearer, P. M. (1990), Seismic imaging of upper mantle structure with new evidence for a 520-km discontinuity, *Nature*, *344*, 121–126.

Shearer, P. M. (1993), Global mapping of upper mantle reflectors from long-period *ss* precursors, *Geophys. J. Int.*, *115*, 878–904.

Shearer, P. M. (1998), Evidence from a cluster of small earthquakes for a fault at 18 km depth beneath Oak Ridge, southern California, *Bull. Seismol. Soc. Am.*, *88*, 1327–1336.

Shearer, P. M., J. L. Hardebeck, L. Astiz, and K. B. Richards-Dinger (2003), Analysis of similar event clusters in aftershocks of the 1994 Northridge, California, earthquake, *J. Geophys. Res.*, *108*(B1).

Song, T.-R. A., D. V. Helmberger, and S. P. Grand (2004), Low-velocity zone atop the 410-km seismic discontinuity in the northwestern United States, *Nature*, *427*, 530–533.

Song, X. J., and D. V. Helmberger (1997), Northridge aftershocks, a source study with TERRAscope data, *Bull. Seismol. Soc. Am.*, *87*(4), 1024–1034.

Song, X. J., and D. V. Helmberger (1998), Pseudo Green's functions and waveform tomography, *Bull. Seismol. Soc. Am.*, *88*(1), 304–312.

Stevens, J. L., D. A. Adams, and G. E. Baker (2001), Improved surface wave detection and measurement using phase-matched filtering with a global one-degree dispersion model, in *Proceedings of the 23rd Seismic Research Review: Worldwide Monitoring of Nuclear Explosions – Octorber 2-5, 2001*, pp. 420–430.

Stixrude, L., and C. Lithgow-Bertelloni (2005), Mineralogy and elasticity of the oceanic upper mantle: Origin of the low-velocity zone, *J. Geophys. Res.*, *110*(B3), B03,204.

Tajima, F., C. Megnin, D. S. Dreger, and B. Romanowicz (2002), Feasibility of real-time broadband waveform inversion for simultaneous moment tensor and centroid location determination, *Bull. Seismol. Soc. Am.*, *92*(2), 739–750.

Tan, Y., L. Zhu, D. V. Helmberger, and C. K. Saikia (2006), Locating and modeling regional earthquakes with two stations, *J. Geophys. Res.*, *111*(B01), 306–.

Tanimoto, T., and K. P. Sheldrake (2002), Three-dimensional s-wave velocity structure in southern California, *Geophys. Res. Lett.*, *29*(8), 1223–.

Teng, T., L. Wu, T. Shin, Y. Tsai, and W. H. K. Lee (1997), One minute after: strong-motion map, effective epicenter, and effective magnitude, *Bull. Seismol. Soc. Am.*, *87*, 1209–1219.

Thio, H.-K., and H. Kanamori (1995), Moment-tensor inversion for local earthquakes using surface waves recorded at TERRAscope, *Bull. Seismol. Soc. Am.*, *85*, 1021–1038.

Uhrhammer, R., D. S. Dreger, and B. Romanowicz (2001), Best practice in earthquake location using broadband three-component seismic waveform data, *Pure Appl. Geophys.*, *158*, 259–276.

Venkataraman, A., J. Mori, H. Kanamori, and L. Zhu (2000), Fine structure of the rupture zone of the Apirl 26 and 27, 1997, Northridge aftershocks, *J. Geophys. Res.*, *105*(B8), 19,085–19,093.

Vidal, A., and L. Mungúia (1991), Local magnitude and source parameters for earthquakes in the Peninsular Ranges of Baja California, Mexico, *Bull. Seismol. Soc. Am.*, *81*(6), 2254–2267.

Waldhauser, F., and W. L. Ellsworth (2000), A double-difference earthquake location algorithm: Method and application to the northern hayward fault, California, *Bull. Seismol. Soc. Am.*, *90*(6), 1353–1368.

Waldhauser, F., and W. L. Ellsworth (2002), Fault structure and mechanics of the Hayward Fault, California,from double-difference earthquake locations, *J. Geophys. Res.*, *107*(B3).

Yacoub, N. K. (1996), Maximum spectral energy arrival time for epicenter estimation. Part I: Rayleigh waves, *Seismol. res. Lett.*, *67*(2), 62.

Yang, X., I. Bondár, K. McLaughlin, R. North, and W. Nagy (2001a), Path-dependent regional phase travel-time corrections for the International Monitoring System in North America, *Bull. Seismol. Soc. Am.*, *91*, 1831–1850.

Yang, X., I. Bondár, K. McLaughlin, R. North, and W. Nagy (2001b), Source specific station corrections for regional phases at Fennoscandian stations, *Pure Appl. Geophys.*, *168*, 35–57.

Zanzerkia, E. E., G. C. Beroza, and J. E. Vidale (2003), Waveform analysis of the 1999 Hector Mine foreshock sequence, *Geophys. Res. Lett.*, *30*(8).

Zhang, S., and S. Karato (1995), Lattice preferred orientation of olivine aggregates deformed in simple shear, *Nature*, *375*, 774–777.

Zhao, L. S., and D. V. Helmberger (1994), Source estimation from broadband regional seismograms, *Bull. Seismol. Soc. Am.*, *84*, 91–104.

Zhao, L.-S., and D. V. Helmberger (1996), Regional moments,energy levels, and a new discriminant, *Pure Appl. Geophys.*, *146*(2), 281–304.

Zhu, L., and D. V. Helmberger (1996), Advancement in source estimation techniques using broadband regional seismograms, *Bull. Seismol. Soc. Am.*, *86*, 1634–1641.

Zhu, L., and L. A. Rivera (2002), A note on the dynamic dand static displacements from a point source in multi-layered media, *Geophys. J. Int.*, *148*, 619–627.

Zhu, L., Y. Tan, D. V. Helmberger, and C. K. Saikia (2006), Calibration of the Tibetan plateau using regional seismic waveforms, *Pure Appl. Geophys.*, *In press.*